UNIVERSITY OF SOUTHAMPTON

FACULTY OF NATURAL AND ENVIRONMENTAL SCIENCES

SCHOOL OF OCEAN AND EARTH SCIENCES

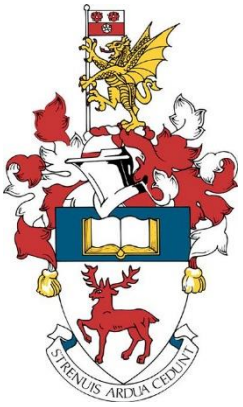

Rise and fall of a hydrothermal system: A tale of metalliferous sediments (TAG hydrothermal field, MAR, 26°N)

by

ADELINE MARIE DUTRIEUX

Thesis for the degree of Doctor of Philosophy

September 2020

UNIVERSITY OF SOUTHAMPTON
FACULTY OF NATURAL AND ENVIRONMENTAL SCIENCES
SCHOOL OF OCEAN AND EARTH SCIENCES

Thesis for the degree of Doctor of Philosophy

Rise and fall of a hydrothermal system: A tale of metalliferous sediments (TAG hydrothermal field, MAR, 26°N)

By Adeline Marie Dutrieux

Abstract

Hydrothermal sediments, or metalliferous sediments, are linked to hydrothermal activity and are found in the vicinity of seafloor hydrothermal systems. Their study allows for the geochronological reconstruction of hydrothermal systems and further understanding of the geochemical alteration processes of seafloor massive sulphides (SMS). As they are rich in copper, zinc and gold, hydrothermal sediments are also potential mineral resources and excellent indicators for SMS ore deposits in deep-sea mineral exploration. Furthermore, formation of these sediments and the subsequent diagenesis, have an impact on global elemental cycles and budgets as they retain or release metals. This study investigates the origin, nature and diagenesis of metalliferous sediments present at the TAG hydrothermal field (TAGHF, 26°N, Mid-Atlantic Ridge) in order to address the geochronological evolution of the hydrothermal system. For this, metalliferous sediments have been collected using gravity coring, rock drilling and mega-coring in distinct seafloor environments at the TAGHF: from the top of inactive hydrothermal mounds, at the base of hydrothermal mounds and in several hundred meters-distant depositional basins and channels. Dating by radiocarbon isotopes, oxygen isotopes and palaeomagnetism shows that high-temperature hydrothermal activity from a number of individual vent sites across the TAGHF was synchronously suppressed. This suppression coincides with the last glacial termination, *ca*. 12,500 years ago, when the sea-level rose. In addition to the synchronous cessation, at least three vent sites show signs of synchronous rejuvenation in the last 10,000 years. These synchronous suppression and reactivation support the hypothesis that a unique heat source below the ridge feeds several vents simultaneously. After the cessation of high-temperature hydrothermal activity, sediments underwent diagenesis and are influenced by low-temperature hydrothermal fluids. The mineralogical and geochemical analyses of these sediments and their pore waters demonstrate that post-deposition processes vary according to their environments of deposition. In distal depositional basins,

metals are rapidly buried in thick turbiditic deposits up to several metres thick. Copper, cobalt and manganese are mobilized by diagenetic redox processes, and re-distributed to be eventually preserved in sulphides, or oxides closer to the sediment/seawater interface. These processes surpress metal release into the ocean and help preserve the metal tenor, resulting in a considerable resource potential in the sediments of this area. On the flanks and at the base of extinct hydrothermal sites (mounds), recurrent sulphidic debris-flows also hold a high metal tenor (*e.g.* up to 28 wt% Cu), yet exposure to seawater dissolves and mobilises these metals into pore waters, which are eventually released into the ocean. On the top of the extinct hydrothermal mounds, oxidised hydrothermal sediments, here referred to as seafloor gossans, are dominantly derived from sulphide chimney material. They have experienced complete oxidative weathering by seawater, slow burial, and are capped by pelagic carbonate sediments. Down-core changes in their lithology suggest deeper sediments, close to the SMS ore body, are dominantly composed of fine hematite and quartz, which precipitated from low to moderate temperature hydrothermal fluids that are themselves implemented in the formation of a subjacent silicified layer of jasper that preserves the underlying main ore body. This thesis explores the fate of seafloor massive sulphides from a well-known area on the Mid-Atlantic Ridge, and hence aims to increase the knowledge of metal preservation in hydrothermal sediments in general, and the controls on fluctuation of hydrothermal activity and mineralisation.

Table of Contents

Table of Tables

Table of Figures

List of Accompanying Digital Materials

0. Introduction to the accompanying digital materials
1. Sediment and pore water sample list during the JC138 expedition
2. Photography of the cores
3. 12 Stratigraphy logs from JC138 gravity cores and sediment drilling cores
4. Grain size by Malvern Analyzer in sediments
5. Density, porosity in sediments
6. Photography by microscopy
7. Mineralogy by X Ray diffraction in sediments
8. Mineralogy and chemical mapping by Scanning Electron Microscope in sediments
9. ITRAX data for sediment chemostratigraphy
10. Geochemistry with ICP in sediments (included Au, Ag and REE)
11. Calcium carbonate by coulometry in sediments
12. Stable oxygen isotopes in sediments
13. Radiocarbon dating in sediments
14. Paleomagnetism in sediments
15. Geochemistry for cations with ICP in pore waters
16. Chromatography data for the anions in pore waters
17. Autoanalyzer data for Nutrients in pore waters
18. Titrator measurements for total alkalinity in pore waters

Research Thesis: Declaration of Authorship

I, Adeline Dutrieux, declare that this thesis and the work presented in it are my own and has been generated by me as the result of my own original research.

Rise and fall of a hydrothermal system: A tale of the metalliferous sediments (TAG hydrothermal field, MAR, 26°N)

I confirm that:

This work was done wholly or mainly while in candidature for a research degree at this University;

Where any part of this thesis has previously been submitted for a degree or any other qualification at this University or any other institution, this has been clearly stated;

Where I have consulted the published work of others, this is always clearly attributed;

Where I have quoted from the work of others, the source is always given. With the exception of such quotations, this thesis is entirely my own work;

I have acknowledged all main sources of help;

Where the thesis is based on work done by myself jointly with others, I have made clear exactly what was done by others and what I have contributed myself;

Parts of this work has been published before submission as:

- B.J. Murton, B. Lehrmann, **A.M. Dutrieux**, S. Martins, A. Gil de la Iglesia, I.J. Stobbs, F. J.A.S. Barriga, J. Bialas, A. Dannowski, Mark.E. Vardy, L.J. North, I. A.L.M. Yeo, P.A.J. Lusty, S. Petersen (2019). Geological fate of seafloor massive sulphides at the TAG hydrothermal field (Mid-Atlantic Ridge), *Ore Geology Reviews* 107. 905-923.
- Petersen S. and Scientific Party (2016) RV METEOR Fahrtbericht / Cruise Report M127 - Extended Version: Metal fluxes and Resource Potential at the Slow-spreading TAG Mid ocean Ridge Segment (26°N, MAR) – Blue Mining@Sea, GEOMAR report 32, Kiel, 163p.
- Murton B. J. and Scientific Party (2018) Cruise Report : Expedition JC 138 : 29th June – 8th August 2016, Mid Atlantic Ridge, 26° 8.38'N; 44° 49.92'W.

Signature:		Date:	

Acknowledgements

While writing these acknowledgements, I am overwhelmed with gratitude for being given the incredible opportunity to have lived this PhD adventure. I joined a remarkable network of brilliant scientists and have developed dear friendship. Over the past four years this invaluably rewarding experience has allowed me to develop professionally and emotionally, thank you.

To begin with, I wish to thank my supervisor, Dr Anna Lichtschlag for her help and guidance. While undoubtedly my heart remains with lab and field work, and not sat at a desk, I finally came to terms with it and I hope I didn't let you down.

A huge thank you goes to my second supervisor, Professor Bramley Murton. I am particularly grateful for the opportunity of having worked on hydrothermal systems, which I have long been fascinated with. I am also grateful to him for providing me with seagoing opportunities and sharing an interest in marine mineral resources. And, while I may have shown a little resistance to not working with rocks or sulphides at first, I now admit loud and clear that I wouldn't have changed my PhD subject for anything in the world, and I truly believe that metalliferous sediments rock the most!

This thesis is inspired by many scientific discussions exchanged with Doug Connelly and Phyllis Lam, Steve Roberts and Rachel Mills. Thank you for your valuable insights. Thanks also to the Deep-sea Mineral Resources team at NOCS for the scientific discussions and most importantly for their friendship. Soon to be Dr. Iain Stobbs, these old times sharing an office with you, never complaining about my dumb questions on English language and our endless discussions on the how and the why have made you a valuable partner in this journey. With you, Dr Izzie Yeo and Sarah Howarth, I enjoyed those great times on field or in a bar (or both at the same time). You are strong, determined and the present and the future feminine representatives in the marine mineral world. Keep rising your voices for gender equality in academic research. Dr. Berit Lehrmann, thank you for your help and your original character entertaining the team. With respect to the material in this report, thanks are due to the Blue Mining's seagoing teams for providing help, bathymetry, advice and discussions on board the *Meteor* M127 and the *James Cook* JC138. This includes John Jamieson, Sven Petersen, Sofia Martins, Fernando Barriga, Paul Lusty, Romina Gehrmann, Eric Atias, Laurence North and Gavin Haughton. This project would not have been possible without the support of many people who helped me with the analytical work, and thanks

go to Kate Peel, Matt Cooper, the BOSCORF team (Suzie, Miros, Mike, and Millie), Richard Pearce, Ross Williams, Megan Wilding, Dan Doran and Matt Beverley-Smith. I thank Yuxi Jin and Chuang Xuan for revealing the world of paleomagnetism, and Steve Moreton for introducing me to radiocarbon dating.

Thanks to my two examiners, Professors Frances Wall and Rachel James who pointed the weaknesses of my study during my viva and help me bringing this thesis at its best.

I am profoundly filled with joy, love and gratitude when I write these names: Sophie Hage, Maria de la Fuente Ruiz, Aude Lavayssière and Delphine Lobelle. Four superwomen, without whom I can barely imagine my life in Southampton. A warm heartfelt thank you and see you all very soon. Other loyal friends have too earned a very special thanks for sharing my life, James, Amaya, Jeremy, David, Elwyn, Marla, Bhargav and Despo. I shall stop here although this list could include many more special people which I have met in my four years in Southampton. Merci également à mes amis belges, Marie, Hélène, Marie, Philippe, Virginie, Sarah et Clémentine de ne pas m'oublier loin de vous.

Most importantly, I deeply thank my family. Maman, Papa, Laurent, Maïté, Tyméo, merci pour le support émotionnel et vos encouragements dans mes choix de carrière, pour apprendre la nouvelle technologie afin de rester unis, pour les nombreuses visites et pour le plein de bières outre-manche. Ma dernière pensée est spécialement adressée à mon extraordinaire filleule, Elyne, pour ton bonheur intarissable partagé lors de nos retrouvailles et ta patience pendant ces 4 ans d'absence. J'ai commencé cette aventure en « pomme de terre » au lendemain de tes 2 ans, et il me tarde de rattraper le temps en partageant avec toi les aventures d'une exploratrice océanographe.

Finally, I would like to thank the Graduate School of the National Oceanography Centre for providing me with a PhD scholarship in the first instance and for welcoming me as a foreign student. From the rolling hills and vertiginous cliffs of Dorset to the fells and lakes of the North, from ciders to folk ceilidhs, I have enjoyed Britain's embrace.

This work was funded by a PhD joint-scholarship from the Graduate School of the National Oceanography Centre and the National Oceanography Centre. The data collection, analyses and conferences attendance were also supplemented by a further grant from the European Union Seventh Framework Program (EU-FP7) "Blue Mining: breakthrough solutions for the sustainable deep-sea mining value chain" under grant No. 604500. A grant from the NERC Radiocarbon Facility NRCF010001 (allocation number 2142.1018) allocated to Dr. Anna Lichtschlag supported the radiocarbon dating work.

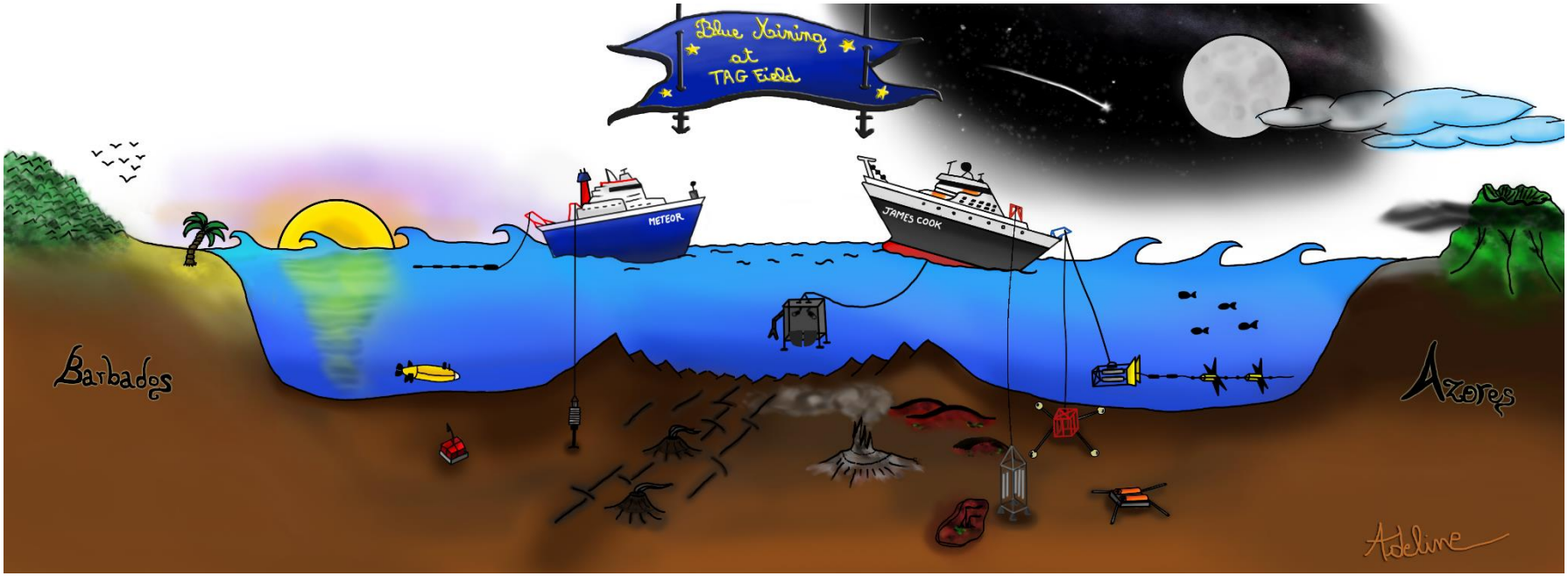

"This is how I represent my three months of expedition! Plenty of geophysical and geological instruments deployed on the seafloor, HyBIS surveying the hydrothermal field, red iron sediment on the inactive mounds (and its stubborn stains), plenty of wonderful sunsets and sunrises on the Meteor, bright and exceptional Perseid meteor shower in the endless James Cook night shifts! Sandy beaches and jungle in Barbados, a cloudy caldera in the Azores, the flat sea surface on the mid-Atlantic ridge, and an eagerly active black smoker … Thank you all." August 2016.

Definitions and Abbreviations

ARM Anhysteretic remanent magnetization

BOSCORF British Ocean Sediment Cores Research facility based at the National Oceanography Centre

CRM Certified reference material

calBP Calibrated years before present (before 1950).

EDS Energy dispersive X-Ray spectroscopy

eSMS Extinct seafloor massive sulphides

Eu/Eu* Europium anomaly

GC **G**ravity core

Gossan Iron-containing secondary deposit, largely consisting of oxides and typically reddish, occurring above a deposit of a terrestrial or marine metallic ore

ICP-MS Inductively coupled plasma mass spectrometry

ICP-OES Inductively coupled plasma optical emission spectrometry

ITRAX Micro X-ray Fluorescence core scanner designed and marketed by Cox analytical systems, available at BOSCORF.

ka kilo-annum, as known as thousand years

kcps kilo-counts

(μ)M (micro)moles/litre (solute concentration unit)

M1 to M4 Lithostratigraphic units used in the sediments on the top of the mound (M1 being the shallowest, M4 the deepest).

MAR Mid-Atlantic Ridge

MIS Marine isotope stage related to glaciation and interglaciation periods.

MSE Mean standard error (for ITRAX measurements)

NERC Natural environment research council, now UKRI

NOCS National Oceanography Centre Southampton

NRCF NERC Radiocarbon Facility, East Kilbride, UK

NRM Natural remanent magnetization

REE Rare earth element

SEM Scanning electron microscopy

SMS Seafloor massive sulphides

TA Total alkalinity

TAG Trans-Atlantic Geotraverse. Transect followed during the 1972 and 1973 cruises of the National oceanic and Atmospheric Administration (NOAA).

TAGHF Trans-Atlantic Geotraverse hydrothermal field

RPI Relative paleomagnetic intensity

wt% Weight percentage

XRF X-ray fluorescence

Y-REE Rare earth elements and yttrium

%RE Percent of relative error (for accuracy)

%RSD Percent of relative standard deviation (for precision)

Chapter 1 Introduction

1.1 General introduction

The search for hydrothermal vents and their associated oases of endemic life began in the early 1960's. Scientists sampled metal-rich sediments in regions where the seafloor was spreading apart, and measured warm temperatures in metalliferous sediments from the Red Sea (Miller *et al.*, 1966; Boström *et al.*, 1969). On land, ophiolites and associated volcanogenic massive sulphides (VMS) pointed out to an origin within a seafloor geological environment (Constantinou and Govett, 1973). In the early 70's, hydrothermal venting was suggested to occur at mid-ocean ridges (MOR) to account for the missing heat that scientists noticed when they measured a heat flow at mid-oceanic ridges lower than the predicted heat flow. In these geological settings, a higher heat flow was predicted due to hot mantle material rising near and to the seafloor. Consequently, it was suggested that hydrothermal vents release fluids carrying off the excess heat originally accumulated from the percolation and convection of seawater through a permeable oceanic crust. Finally, in 1977, visual observation during an oceanographic expedition at the Galapagos Rift confirmed the existence of hydrothermal vents (*'the thermal springs'*) and revealed a unique biological community (Corliss *et al.*, 1979). Two years later, the submersible Alvin took the first photographic evidence of a high-temperature black smoker on the East-Pacific Rise, and scientists recognised the importance of the associated polymetallic seafloor massive sulphides (SMS) rich in zinc, copper and with traces of lead and silver (Spiess *et al.*, 1980). In forty years, more than 700 hydrothermal sites have been identified or inferred by oceanographic surveys in the world ocean (FIGURE 1.1). Hydrothermal systems have now been found in all oceans occurring in various geological settings (Hannington *et al.*, 2005) and their remarkable geological, chemical, and biological diversity does not cease to increase (Beaulieu and Szafranski, 2018, InterRidge vent database; http://vents-data.interridge.org).. Research initially focused on fast-spreading ridges, but hydrothermal systems in slow-spreading ridges were also rapidly reported (*e.g.* Mid-Atlantic Ridge; MAR; Rona, 1980), in back-arc basins (*e.g.* Okinawa Trough; Kimura *et al.*, 1988), on active submarine volcanic arcs (*e.g.* Aeolian Arc; Gamberi *et al.*, 1997), or at intra-plate volcanic hot spots (*e.g.* Society Islands in French Polynesia; Michard *et al.*, 1993). In 2015, Beaulieu *et al.* estimated from the actual worldwide distribution that approximately 900 hydrothermal fields remained to be discovered, with a major concentration at the

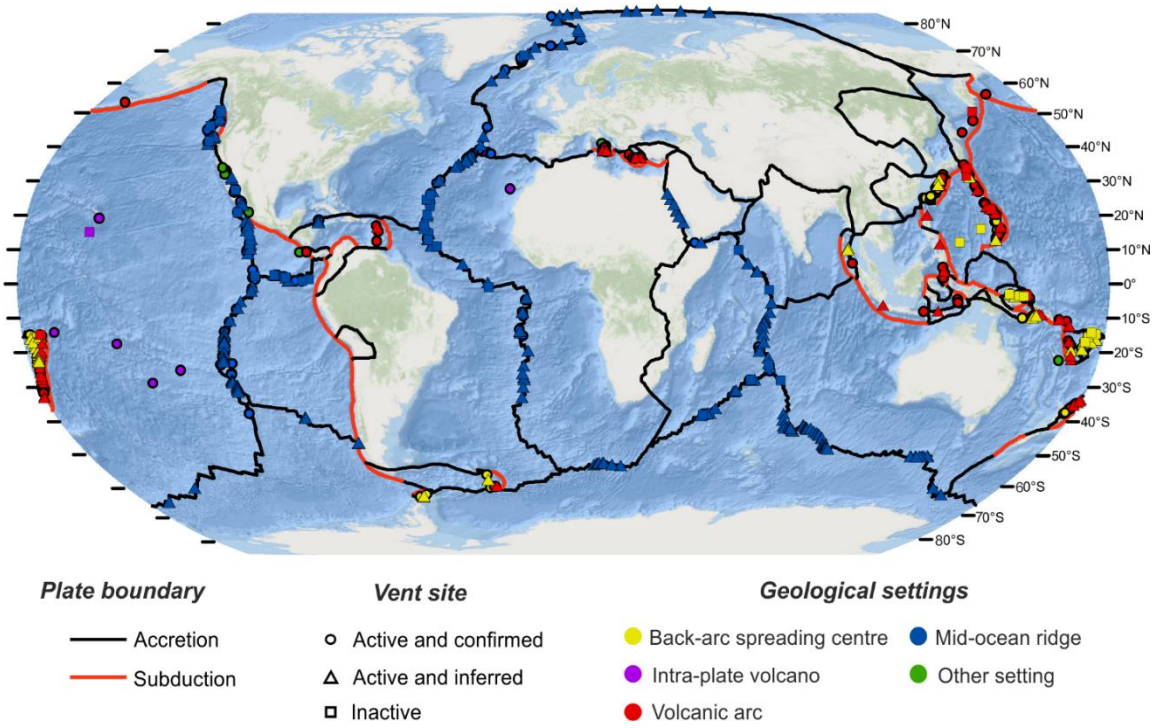

FIGURE 1.1 Worldwide distribution of submarine hydrothermal fields along the plate boundaries. Vent sites are distinguished between confirmed (circle) or inferred (triangle) active and inactive sites (square). Geological settings are colour-coded (mid-oceanic spreading centres, back-arc spreading centres, volcanic arcs, intra-plate volcanoes and other miscellaneous). The tectonic plate boundaries are provided by Bird (2003) and vent site information are provided by the global InterRidge Vents Database http://vents-data.interridge.org. Credits for the ocean base map go to GEBCO, ESRI and other contributors.

slow-spreading MORs. Evidence suggests that there are many more inactive (also called extinct or relict) sites than active sites (Hannington *et al.*, 2011), however, present-day exploration techniques mainly identify hydrothermal systems and their deposits from water column anomalies produced by active vent systems, leaving considerable potential for the discovery of the vast majority of inactive systems.

1.1.1 Aim of the study

The discovery of hydrothermal systems solved a mystery, *i.e.* the missing heat, yet opened doors to numerous questions on the understanding of our Earth system: what role does hydrothermal venting play in the oceanic geochemical budget (*cf.* section 1.2.2.2)? What role does hydrothermal circulation play in the cooling of oceanic crust (*cf.* section 1.2.2.1)? How are the seafloor ore deposits formed (*cf.* section 1.3.1.1)? How did an ecosystem develop in a sunless and chemically hostile environment? How does a hydrothermal

system evolve over geological time (*cf.* section 1.5)? Nowadays, hydrothermal research is mainly motivated by academic studies to provide answers to those questions, but is also driven by national and commercial interests in the mineral resource potential of seafloor hydrothermal deposits (*cf.* section 1.3.1.2).

With the goal to add to a better understanding of the Earth System, my thesis aims to address the following specific research questions:

- How does hydrothermal activity vary over time at a specific hydrothermal field and are there external factors influencing the activity?
- How efficient is the subsurface trapping mechanism for metals in sediments in the vicinity of a hydrothermal site?
- How do hydrothermal sites evolve after the high-temperature hydrothermal flow has ceased?

To answer these questions, this thesis presents geochronological, geological, mineralogical and geochemical results obtained on metalliferous sediments from the TAG hydrothermal field at 26°N on the Mid-Atlantic Ridge.

1.2 Seafloor hydrothermal systems

1.2.1 Formation of hydrothermal vent systems

Seafloor hydrothermal circulation, or hydrothermalism (Jamieson *et al.*, 2016), is the major mechanism for the cooling of the interior of the Earth and the transfer of chemical elements from the crust and mantle to the oceans (Hajash, 1975). Cold seawater percolates downward through a fractured ocean crust. During its downward percolation into the recharge zone, seawater is heated by a heat source (*e.g.* a magma body) reaching maximum temperatures and super-critical conditions where the density of the fluid reduces rapidly causing it to rise buoyantly (> 400°C) (FIGURE 1.2). The fluids are chemically modified through exchange with the host rock: *e.g.* they progressively lose Mg^{2+}, SO_4^{2-}, and OH^- ions and become enriched in Ca^{2+} and H^+ ions. The underlying heat source, derived from magmatic activity, drives the convection of hydrothermal fluids towards the ocean floor and results in both high-temperature venting and lower temperature diffuse flows in the discharge zone. On the way to the surface, many chemicals species (Fe, Mn, Cu, Zn, Pb, Si, and S) are leached from the host rocks and magmatic volatiles are added to the fluids (^3He, CO_2, CH_4, H_2S, H_2). The oceanic crust, originally composed of fresh basalt and gabbro (plagioclase, olivine and

pyroxene assemblages), once in contact with hydrothermal fluids, acquires a secondary mineral assemblage containing chlorite, amphibole, secondary plagioclase, quartz, epidote and possibly anhydrite. High-temperature fluids are rich in numerous elements, chemically reduced and acidic, that escape into the overlying water column at black and white smokers (vents); the colour resulting from the precipitating mineral assemblage that depend on the venting fluids compositions as they mix with ambient seawater (German and Seyfried, 2014). White smokers are dominated by a sulphate assemblage, while black smokers contain more sulphide minerals. Temperatures at the exit reach usually around 300-350°C, although records indicate 401°C at the Beebe Vent field (Mid-Cayman Spreading Centre) (Webber *et al.*, 2015) and 464°C at 5°S on the MAR (Koschinsky *et al.*, 2008), both hydrothermal systems displaying supercritical venting conditions (*i.e.* high pressure and temperature conditions where liquid and gas merge into one). The escaped fluids immediately form a buoyant plume that rises above the seafloor in the water column until it becomes neutrally buoyant through mixing with ambient colder seawater. The hydrothermal fluids are diluted by a factor of ~10^4 by this entrainment of ambient seawater in the first 5 to 10 meters, and the dilution increases with the rise height (Lupton, 1995). Once the plume has reached its density equilibrium with the ambient seawater, it spreads out laterally on an isopycnal horizon above the hydrothermal source, following the oceanic currents (Lupton, 1995). The composition of the expelled, hot vent fluids reflects several factors: the initial fluid composition (seawater), the composition of the rock that reacted

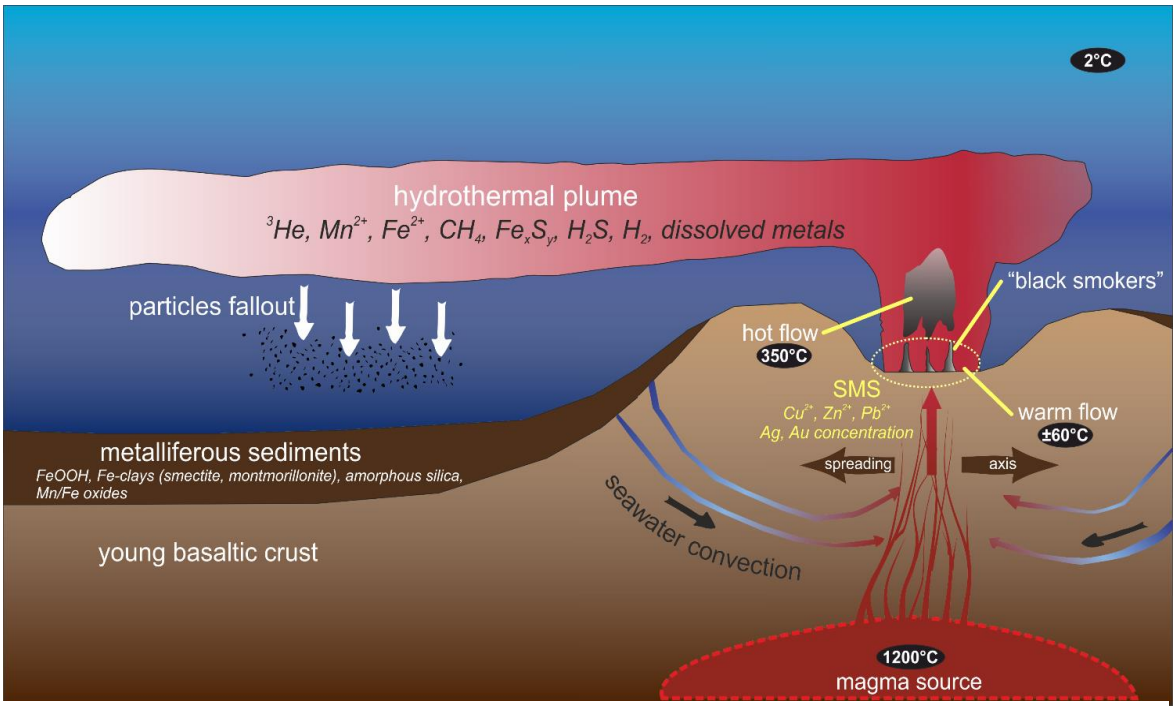

FIGURE 1.2 Schematic representation of hydrothermal circulation at a mid-oceanic spreading ridge and its principal components. SMS refers to the seafloor massive sulphides.

with the fluid as it circulated, the structure of the host rock (*e.g.* a fault system) and the depth, size and shape of the heat source (Tivey, 2007). For instance, if the hosting rocks are ultramafic, serpentinization of the lower part of the ocean crust or the upper-mantle zone can occur (Miyashiro *et al.*, 1969; Zonenshain *et al.*, 1989) which can, in turn, provide a source of Ca to hydrothermal fluids through enhanced and rapid reaction of pyroxene compared with olivine (Bach and Fruh-Green, 2010). Another example is the sediment-hosted hydrothermal vents in the Gulf of California. Those vents generate distinct chemistry reflecting a biogenic and carbon-rich component in the system, *i.e.* ammonium-rich and "ore deposit" metals depleted fluids (Von Damm *et al.*, 1985).

Where the mineral-laden fluids reach the seafloor, they mix with cold ambient seawater and induce a sudden change in temperature, redox conditions and precipitation of sulphide, oxide, silicate and carbonate minerals forming spires or chimneys. The continuous collapse, as the chimneys grow, coalesces to form the sulphide mounds, referred to as the seafloor massive sulphides (SMS) (*cf.* section 1.3.1). The SMS deposits found associated with inactive hydrothermal vents are consequently called inactive, or extinct SMS (eSMS). Two other types of mineral deposits encountered in hydrothermal systems are: i) accumulations of Fe-Mn oxyhydroxides and silicates from low-temperature diffuse discharge (*cf.* section 1.3.2), and ii) fine-grained particles precipitated from hydrothermal plumes, known as the plume fall-out (*cf.* section 1.3.3) (German and Seyfried, 2014).

Slow-spreading ridges have been observed to host larger and more mature hydrothermal deposits than those on fast spreading ridges. This is thought to arise because slow-spreading ridges have discontinuous magmatic supply, hence, less frequent lava eruptions burying the SMS deposits. This discontinuity also leads to magmatic events of greater magnitude. Furthermore, a more localised tectonic regime develops large and long-lived faults that penetrate the seafloor from the top of rift valley walls to the base of the lithosphere, providing long-term sustained focused conduits for fluid flow and mineralisation. On fast spreading ridges, deposits are smaller but more numerous because of the relatively short-lived tectonic-controlled upflow zone for hydrothermal circulation and frequent burial by eruptions of lava (Fouquet, 1997; Bach and Fruh-Green, 2010).

1.2.2 Heat and chemical flows through the oceanic lithosphere

Characterizing the heat and chemical flows associated with hydrothermal systems remains an important scientific focus to understand the impact of these systems in supporting microbial communities and modifying ocean chemistry.

1.2.2.1 Hydrothermal heat flows

About 60% of the worldwide heat loss from the Earth interior is focused in the newly formed lithosphere, at volcanic hot spots, and mid-ocean spreading ridges (Sclater *et al*., 1980). Stein and Stein (1994) estimate the total heat dissipated via hydrothermal circulation is 11 x 10^{12} watts. This heat is inferred to be the discrepancy between the total predicted heat flux and the measured conductive heat flux through oceanic lithosphere (Sclater *et al*., 1980; Stein and Stein, 1994). Elderfield and Schultz (1996) suggest that axial regions (*i.e.* young crusts) account for a removal of 2 ± 1 x 10^{12} watts by advection while off-axis flows (along ridge flanks) account for removal of 7 to 9 x 10^{12} watts by advection. Therefore, high-temperature venting may only represent a small fraction of the heat (perhaps 10-15%) lost from the interior of the earth to the ocean (Murton *et al*., 1999; Nielsen *et al*., 2006).

Low-temperature diffuse flow (usually < 35°C), which discharges over much larger spatial scales on the ridges or volcanic flanks, most likely plays a greater role than high-temperature flow in the global geochemical and heat balance although it is not responsible for large mineral deposits (Fisher and Wheat, 2011). The diffuse flow contribution is estimated to be about 25% of the total Earth heat loss and 70% of the total hydrothermal heat loss associated with spreading plate boundaries. (Mottl and Wheat, 1994; Mottl, 2003; Nielsen *et al*., 2006; Wheat and Fisher, 2008).

1.2.2.2 Hydrothermal chemical flows

Chemical exchange between the lithosphere and the ocean occurs at the high-temperature vents via the expulsion of hydrothermal fluids; in off-axis settings via low-temperature diffuse flows and in oceanic crust alteration through the convective hydrothermal circulation.

Chemical fluxes from discrete high-temperature hydrothermal sources are determined by direct sampling of the hydrothermal fluids (*e.g.* Campbell *et al*., 1988) or calculated by balancing Sr or He isotope ratios in seawater (Elderfield and Schultz, 1996). Elements such as He, Mn, Fe, Li, K, Rb and Cs are enriched in hydrothermal fluids compared to *e.g.* river

inputs (FIGURE 1.3) or to average seawater concentrations (FIGURE 1.4). On the other hand, hydrothermal fluids are depleted in Mg and SO_4 (Elderfield *et al.*, 1993; Elderfield and Schultz, 1996). The differences to the seawater and river inputs result from the chemical reactions occurring during the hydrothermal circulation in the oceanic crust.

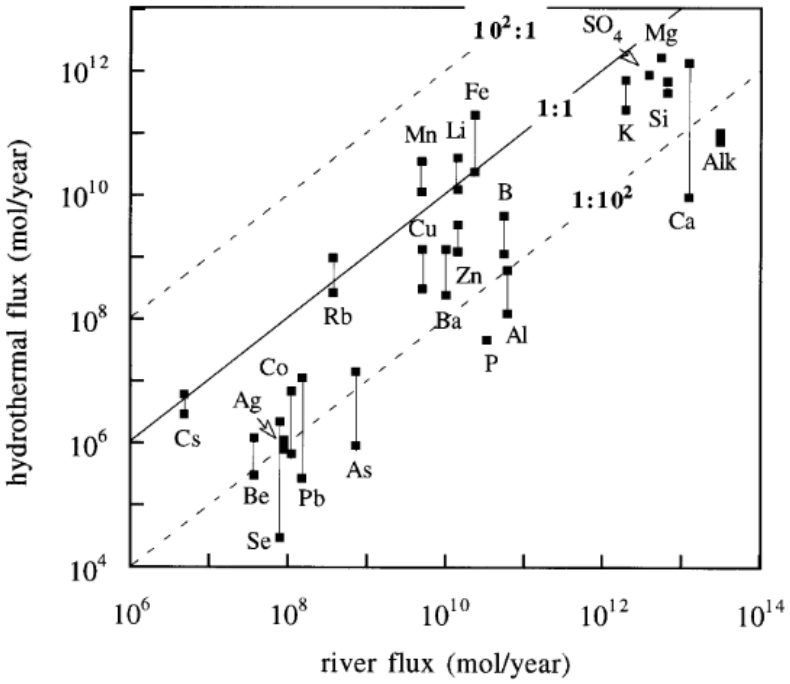

FIGURE 1.3 Comparison of hydrothermal fluxes and river fluxes. Dashed lines represent the concentration and dilution by a factor 100. From Elderfield and Schultz (1996).

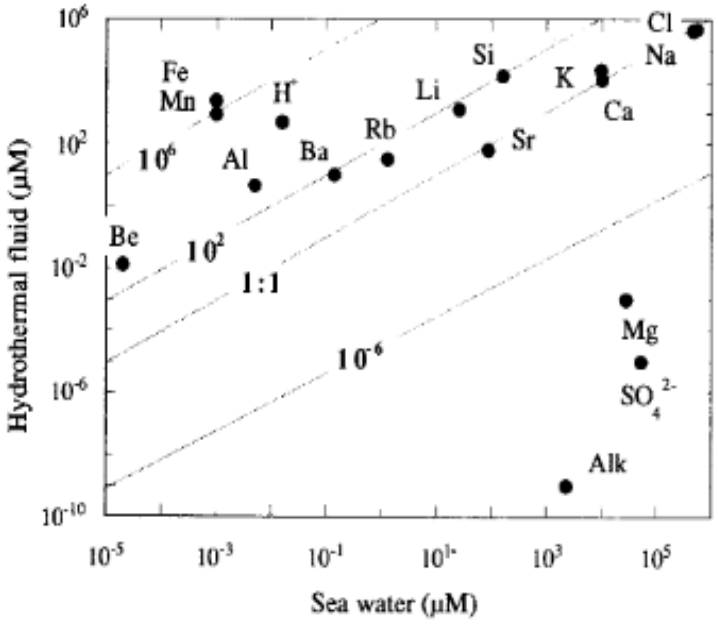

FIGURE 1.4 Concentrations of major and some minor elements in hydrothermal fluids compared to seawater. From Elderfield *et al.* (1993), compiling data from Von Damm (1985).

Hydrothermal chemical fluxes related to low-temperature diffuse flows are, however, poorly quantified and two behaviours are observed. The first behaviour is observed on ridge flanks and seamounts from off-axis regions. As the crust is older and cooler in those regions than in the high-temperature fluid circulation systems, the composition of discharging fluids is not or only slightly altered from bottom seawater (Fisher and Wheat, 2011; Le Gal *et al*., 2018). For instance, in the cool hydrothermal springs at the Cocos Plate, only Rb, Mo, V, U, Mg, Si, Li and PO_4 have distinctively different concentration (Mills and Dunk, 2010; Wheat *et al*., 2017).

The second behaviour is observed near active vent fields, and also during the closing period of a hydrothermal system where fluids are depleted in most metals except Fe and Mn. Those low-temperature fluids reach the seafloor to deposit low-temperature hydrothermal products (*cf.* section 1.3.2). Their contribution to hydrothermal Fe and Mn fluxes is estimated to be less than 10% and less than 40%, respectively (Massoth *et al*., 1994).

1.3 Hydrothermal deposits

Hydrothermal deposits are the focus of scientific research as they provide geological samples to assess the importance of hydrothermal systems in the global geochemical budget, and they provide insight into the fundamental question of how hydrothermal systems form. Several types of deposits are distinguished based on their formation processes, i) seafloor massive sulphides, ii) low-temperature hydrothermal deposits, and finally iii) hydrothermal plume fall-out. Sediments that contain component of weathered massive sulphides, low temperature hydrothermal deposits and/or plume fall-out are known as hydrothermal sediments. An extensive review of hydrothermal sediments is necessary to comprehend the work of this thesis and is provided in the SECTION 1.4.

1.3.1 Seafloor massive sulphides

1.3.1.1 Formation and dimension

SMS deposits are formed by the combination of collapse and growth of hydrothermal chimneys and spires, as well as replacement within and below the mounds resulting in the formation of mixtures of sulphides (pyrite, chalcopyrite, galena, pyrrhotite, marcasite and sphalerite), sulphates (anhydrite and barite), amorphous silica and altered host rock. (Hannington *et al*., 2005). The outer rim of a deposit consists usually of minerals rich in Fe and Zn (pyrite, marcasite and sphalerite) precipitating at lower temperature as the

hydrothermal fluid mixes with seawater; while Cu-rich minerals are typically found in the upflow fluid conduits (Hannington *et al.*, 2005). Because precipitation also occurs below the surface, deposits must be considered in three-dimension and, in addition, the geochemistry of the surface expression (*i.e.* chimneys) is rarely representative of the sub-seafloor deposits. Drilling into the deposits provides a third dimension to their structure and of the chemical distribution within the mounds. Only a few SMS deposits have been drilled, however, and these all show different sub-seafloor SMS geology. For example, a sediment-hosted SMS deposit was drilled at the Bent Hill site in the Middle Valley at the Juan de Fuca Ridge (Zierenberg *et al.*, 1998; Zierenberg and Miller, 2000; Houghton *et al.*, 2004) (FIGURE 1.5C). Here, the deep structure shows a stratified zone of high-grade copper-rich replacement mineralisation lying below the massive sulphide deposit and the feeder zone. The feeder zone, or stockwork, is the host rock cut by numerous subvertical veins of sulphides that were presumably pipes through which the hydrothermal fluids ascended towards the seafloor (Zierenberg *et al.*, 1998). The active TAG hydrothermal field at the MAR, 26°N (Humphris *et al.*, 1996; Herzig *et al.*, 1998a) was the first MOR-hosted and sediment-depleted, active system to be drilled. At the TAG active hydrothermal mound, the stockwork consists of breccias of sulphide, silica, and an unexpected concentration of anhydrite, mixed with altered wall rock fragments (Humphris *et al.*, 1995; Petersen *et al.*, 2000). However no deeper Cu-rich replacement zone was encountered (FIGURE 1.5B). Further South, the Irina II-Logatchev at MAR 14°N (Augustin, 2007; Petersen *et al.*, 2009) is an ultramafic-hosted field for which sub-seafloor investigation suggested the massive sulphide deposits are spatially restricted to the immediate surrounding of the active vent sites with a distinct Au-Cu enrichment (Petersen *et al.*, 2007) (FIGURE 1.5D). More recently, volcanic-arc-settings massive sulphides were investigated at the Palinuro volcanic complex (Aeolian Island Arc) (Petersen *et al.*, 2014). The structure is also stratified, with abundant barite, a greater variability in sulphide mineralogy (*e.g.* enargite, covellite, galena, *etc.*) and anomalously high contents of As, Hg, Sb, Bi, Te and Se.

Most SMS deposits are small in size and tonnage. The largest deposits are found where hydrothermal activity occurred for long periods of time (*e.g.* at slow spreading ridges). Some examples of the largest tonnage deposits (> 2 million tonnes) are the TAG hydrothermal mound, the Middle Valley and Solwara 1 (Hannington *et al.*, 2011). However estimation of the tonnage is may be biased due to the lack of consideration of the third-dimension that extends sub-surface. A recent sub-seafloor drilling, seismic and electromagnetic study (Murton et al., 2019) at an inactive hydrothermal mound at the TAG

hydrothermal field estimated a much larger tonnage of 19 Mt, much higher than the active mound estimates (2.7 Mt).

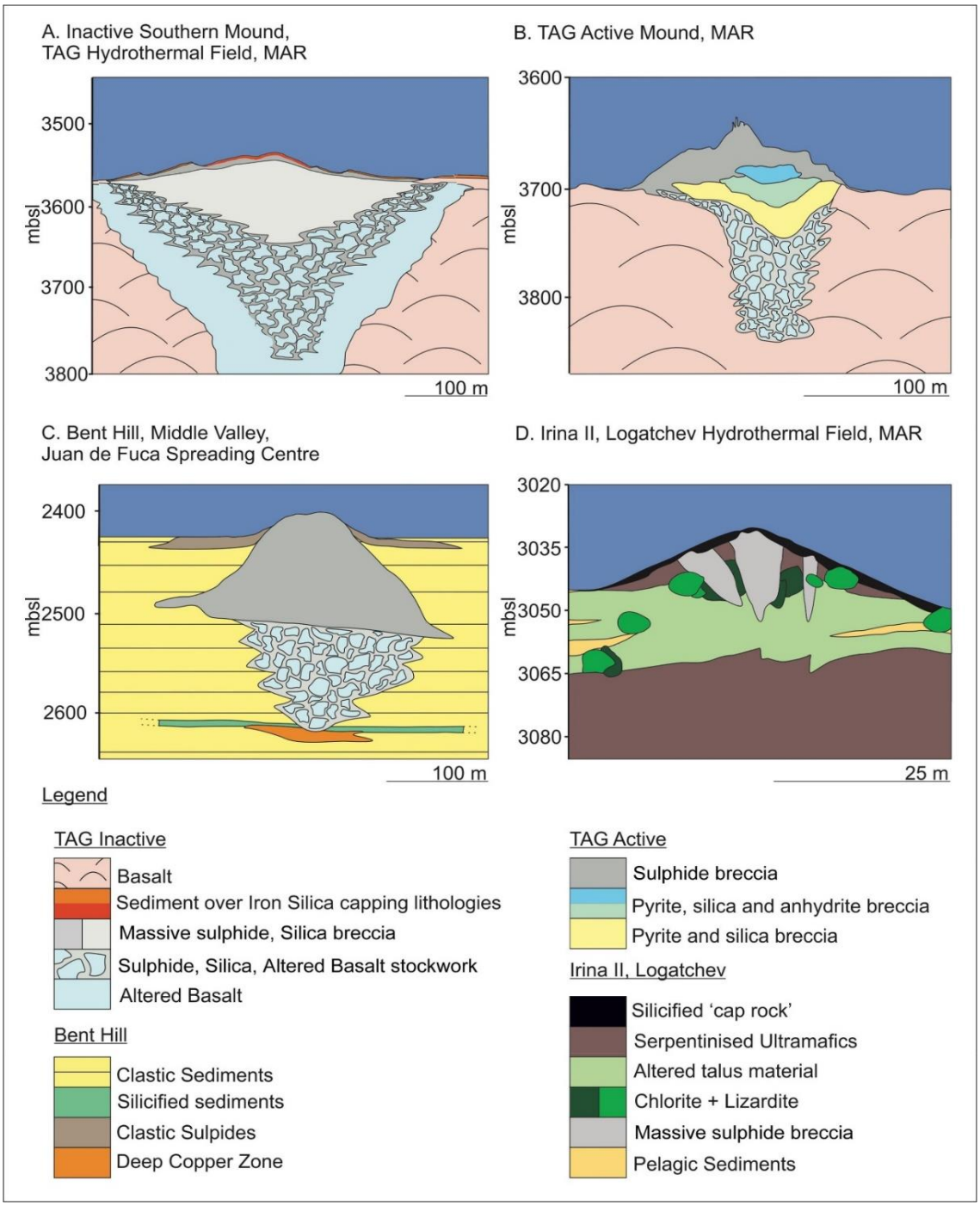

FIGURE 1.5 Cross-sections of four hydrothermal mounds based on drilling interpretation: (A) Inactive Southern Mound at the TAG hydrothermal field on the MAR, (B) the active TAG hydrothermal field, (C) Bent Hill at the Juan de Fuca Spreading centre, and (D) Irina II at the Logatchev hydrothermal field on the MAR. From Murton *et al*. (2019). Structures are modified from Humphris *et al*. (1995) for the active TAG Hydrothermal mound, Zierenberg *et al*. (1998) for Bent Hill and Augustin (2007) and Petersen *et al*. (2009) for Irina II.

In conclusion, differences between drilling results, in addition to the large geological disparity at volcanogenic massive sulphides, *i.e.* their terrestrial and ancient analogous, suggest that seafloor occurrences are more variable than previously thought (Petersen *et al.*, 2018).

1.3.1.2 Deep-sea mining of SMS deposits

As demand for raw metals increases, mining companies exploit lower-grade ores and deeper deposits. SMS are rich in Cu, Zn, Pb, Ag and Au (FIGURE 1.6), and their resource potentials are frequently compared to the volcanogenic massive sulphides mined on land (Cathles, 2011; Hannington *et al.*, 2011). Therefore, future resources could include marine minerals. Based on known and predicted vent site abundance and size, about 600 million tons of sulphide with about 30 million tons of copper and zinc could potentially to be found along the global neovolcanic zones at mid-ocean ridges (Hannington *et al.*, 2011).

To date, exploration activity has started, but exploitation may be challenging and is only expected to start in the next ten years. Factors affecting the current commercial viability are water depth, distance to land and sovereign jurisdiction (Clark *et al.*, 2013). About 60% of

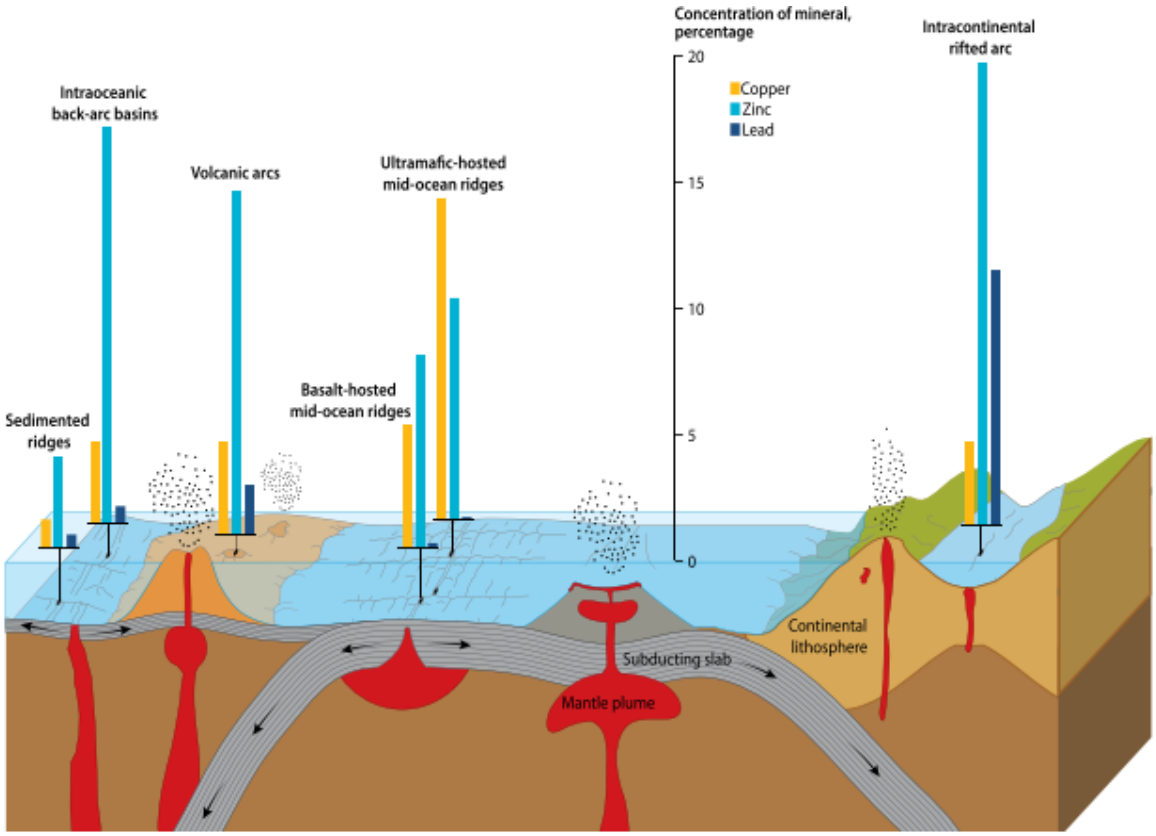

FIGURE 1.6 Geochemistry of massive sulphides in various tectonic settings. Zinc is concentrated in volcanic arcs, rifted arcs and back-arc basins, while Cu is concentrated at mid-ocean ridges. Source GEOMAR (Clark *et al.*, 2013).

known hydrothermal systems occur in international waters beyond national jurisdictions, and the majority of these at 2-3 km water depth on mid-ocean ridges. Those systems present the highest concentration in copper (FIGURE 1.6). On the other hand, sites at intra-plate volcanoes, back-arc basins and submarine volcanic arcs are more likely to be located within the economic exclusive zones of coastal states (Petersen *et al.*, 2016) and are richer in zinc and lead (FIGURE 1.6). Since 2002, exploration contracts have been issued by the International Seabed Authority in international waters. The two leading companies are *Nautilus Minerals* in the Bismark Sea, Papua New-Guinea and *Manafa International* for the Atlantis II project in the Red Sea.

Apart from mineral resources, a diverse array of unique and exotic animals, called vent-endemic species, live exclusively at hydrothermal vents. Many species have evolved to tolerate a habitat without sunlight and developed a symbiotic, or mutually beneficial, relationship with chemoautotrophic microbes. Those microbes get energy through chemical processes, rather than by photosynthesis, directly from the chemicals released by hydrothermal fluids (Fisher *et al.*, 2013). This ecosystem is threatened by the exploitation of hydrothermally active SMS. The environmental impact of deep-sea mining is likely to be significant, but has yet not been fully assessed. Therefore, regulations for exploitation (the "*Mining Code*") are now in development (Van Dover *et al.*, 2018). Numerous scientific studies agree that active vents are vulnerable and unique and must be protected until we have a full understanding of the biodiversity and evidence that active hydrothermal vent ecosystems are not at risk of serious harm from mining activities (Hannington *et al.*, 2017; Van Dover *et al.*, 2018). Following the International Seabed Authority regulations, inactive SMS deposits are most likely accessible for mining, reducing the potential ecosystem impacts. There are also believed to be far more inactive eSMS than active ones (Hannington *et al.*, 2011), and metal accumulations associated with eSMS deposits are expected to be larger than active deposits because they have undergone a complete formation cycle (German *et al.*, 2016b). These are the three reasons (reducing ecosystem impacts, larger distribution and larger metal accumulation) why the EC-funded project Blue Mining focused on the exploration and assessment program on the eSMS mounds at the TAG hydrothermal field (Blue Mining Eu-7th FP, 2018; Murton *et al.*, 2019).

1.3.2 Low-temperature hydrothermal mineralisation

Low-temperature, diffuse flow results from the mixing of upwelling hydrothermal fluids with seawater below the seafloor and can lead to sub-surface mineralisation within the

overlying sediments. The dominant mineralogy includes Mn and Fe oxyhydroxides but also silica (Hein *et al*., 2008) and clays including illite-smectite (Alt and Jiang, 1991) and nontronite, a Al-poor Fe-rich smectite (Corliss *et al*., 1979; Severmann *et al*., 2004; Dekov *et al*., 2007; Ta *et al*., 2017). Low-temperature fluid flows are also responsible for alteration of the sediments and rocks, enhancing weathering of sulphides and oceanic crust, generating ochreous gossan type material (Mills *et al*., 1996).

1.3.3 **Plume fall-out**

When hydrothermal fluids escape from the vent orifices, they rise and mix with seawater to form buoyant plumes. The two dissolved metals most enriched (up to 10^6-fold higher than ambient seawater) in the hydrothermal fluids are Fe and Mn. In the plumes, Fe and Mn are present as soluble or colloidal ions, or oxidised as oxyhydroxide particulates (Resing *et al*., 2015; Lough *et al*., 2019). Up to 99.9% of those respective elements are transported away by plume (Feely *et al*., 1994b) to eventually settle distally in pelagic sediments. As the dispersion distance from the hydrothermal vents increases up to several thousands of kilometres, Fe and Mn contents in the sediment decrease to background values (FIGURE 1.7) (Boström *et al*., 1969). Mn oxidation is slower than Fe oxidation; therefore, particulate Fe increases faster in the plume with respect to particulate Mn (Cowen *et al*., 1990; Massoth *et al*., 1994).

Novel insights brought by the GEOTRACES program (German *et al*., 2016a) confirm that hydrothermal plumes inject vent-sourced trace elements and isotopes (*e.g*. Fe, Mn, Al, ^{230}Th, ^{231}Pa) into the ocean by particle formation or scavenging or dissolution, and that they play an important role in global-scale trace element and isotope ocean biogeochemical cycles. Most chemical elements will not behave conservatively (*i.e.* concentrations determined by dilution only) and are removed by particle flocculation and settling or increase by absorption on hydrothermal plume particles and flocculation. The only true conservative hydrothermal chemical component is He, in addition to the physical tracers, salinity and

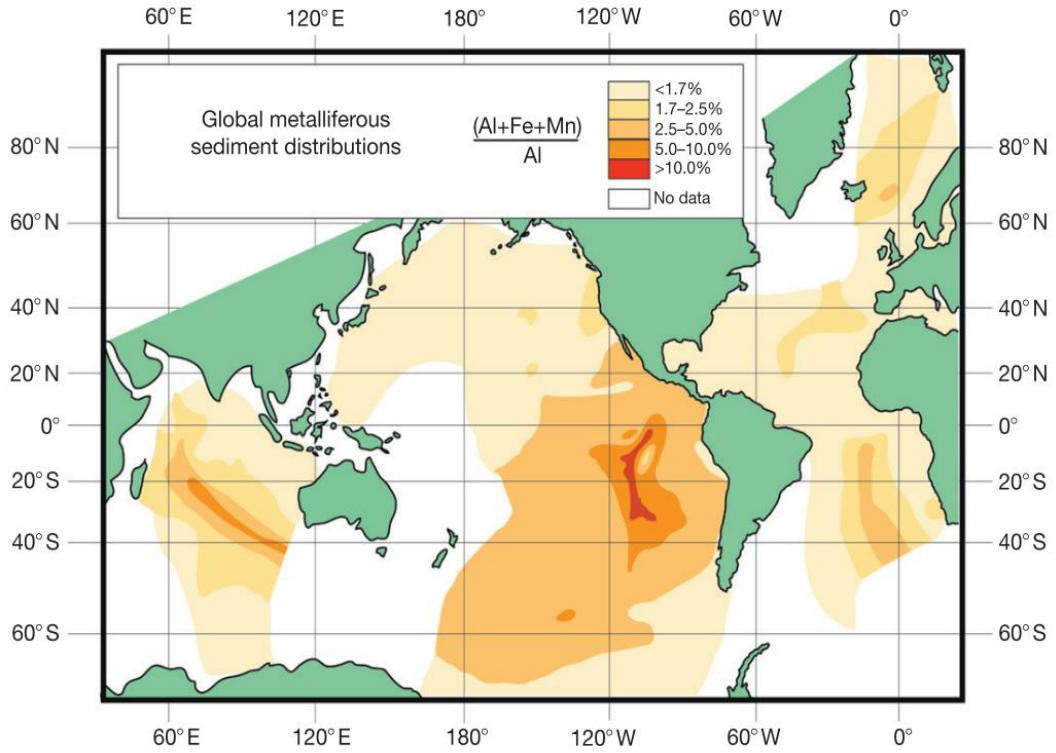

FIGURE 1.7 Global map of the (Al+Fe+Mn)/Al ratio for surficial marine sediments. The highest ratio delineate the mid-oceanic ridges, while low ratio represent pelagic sediments. From Boström *et al.* (1969), adapted by German and Seyfried (2014).

temperature (Lupton, 1995). The hydrothermal plumes initially take up large quantities of oxyanions due to chemical affinities with the oxyhydroxides (*i.e.* P, V, As, Cr) from seawater via adsorption onto or co-precipitation with the fine-grained plume particles (Feely *et al.*, 1992; Metz and Trefry, 1993; Feely *et al.*, 1994b). Suspended hydrothermal Fe-oxyhydroxides also scavenge Th (German *et al.*, 2002), other radionuclides (Hayes *et al.*, 2015), and rare earth elements (REEs) (German *et al.*, 1990), while chalcophile metals (Cu, Zn and Pb) co-precipitate with sulphide particles (German *et al.*, 2002).

At slow-spreading MORs, the height of a neutrally buoyant plume is often less than the steep wall elevation of the axial valley, and thus the plume is constrained and particles settle within the valley (Klinkhammer *et al.*, 1986; Gurvich, 2006). On the other hand, at fast-spreading MORs, the neutrally buoyant plumes are able to disperse up to 2000 km off-axis due to the flatter ridge morphology, with an elevated axial crest (Klinkhammer and Hudson, 1986; Lupton, 1995). The ridge morphology, therefore, has a crucial importance for the concentration of hydrothermal-derived particles settling within the pelagic sediments.

1.4 Hydrothermal sediments

Hydrothermal sediments, or hydrothermally-derived metalliferous sediments, are sediments characterized by a high concentration of metals originating from a hydrothermal source (mainly Fe and Mn, but also economically viable metals such as Cu, Zn, Au) (Shearme *et al.*, 1983; Gurvich, 2006). Different geochemical classifications have been proposed in order to distinguish metalliferous from non-metalliferous sediments, although these are not well-defined. In this thesis, I use a simplified classification from Lisitzin *et al.* (1976), based on the Boström index (Boström *et al.*, 1969). According to Lisitzin *et al.* (1976), sediments with 10 wt% or more of elemental Fe in the abiogenic fraction and depleted in Al and Ti are metalliferous sediments, while sediments with less than 10 wt% Fe are considered as pelagic sediments. The Boström index is defined as 100*Al/(Al+Fe+Mn) (without unit) and discriminates metalliferous sediments (with an index tending towards 0, usually less than 10) from non-metalliferous pelagic sediments (with an index > 60).

1.4.1 Worldwide distribution

The very first hydrothermal sediments from the deep-sea were recovered during the expedition of the *H.M.S Challenger* (1872-1876), at the eastern flank of the East Pacific Rise (Murray and Renard, 1891). However, no detailed investigations were carried out until the discovery of seafloor hydrothermal systems a century later (Dekov *et al.*, 2010). Following the discovery of new hydrothermal systems in various geological settings. Over the last 40 years, their associated metalliferous sediments were also investigated. Hydrothermal deposits are almost ubiquitous in marine sediments, distributed from the immediate vicinity of the hydrothermal vents up to thousands of kilometres distant (FIGURE 1.7) (Boström *et al.*, 1969).

The next paragraphs provide a non-exhaustive list of world metalliferous sediments for which the Boström Index tends towards zero, due to their close distance to an active hydrothermal system. Their disparity in geochemistry and accumulation processes suggest that numerous factors are influencing their formation and deposition, such as seafloor geomorphology, geochemistry of hydrothermal systems and surrounding water column and current active/waning stage of the hydrothermal system.

At the Mid-Atlantic Ridge, metalliferous sediments were extensively studied, including from North to South at the Grimsey Icelandic vent field (66°N) (Dekov *et al.*, 2008), Lucky Strike hydrothermal field (37°N) (Dias *et al.*, 2008), Rainbow hydrothermal field (36°N)

(Cave *et al*., 2002; Chavagnac *et al*., 2005), the Saldanha hydrothermal field (36°N) (Dias and Barriga, 2006), TAG hydrothermal field (26°N) (Scott *et al*., 1978; Shearme *et al*., 1983; Metz *et al*., 1988; German *et al*., 1993; Mills *et al*., 1993; Mills and Elderfield, 1995a; Mills *et al*., 1996; Damyanov *et al*., 1998; Goulding *et al*., 1998; Dekov *et al*., 1999; Mills *et al*., 2001; Severmann *et al*., 2004; German *et al*., 2016a), the MARK site (23°N) (Cherkashov, 1995), the Logatchev hydrothermal field (14°N) (Gablina *et al*., 2006) and Semenov hydrothermal field (13°N) (Rusakov *et al*., 2013).

On the ultra-slow spreading Mid-Cayman Spreading Centre, highly enriched base metal and talc sediments are found in the vicinity of the Beebe hydrothermal field in the Cayman Trough (Hodgkinson *et al*., 2015; Webber *et al*., 2015), which is the deepest known. The fast-spreading East Pacific Rise is also an excellent location to study dispersion of hydrothermal plume fall-out because of the elevated ridge morphology (*cf*. section 1.3.3) (Skornyakova, 1965; Cronan, 1976; Heath and Dymond, 1977; Barrett *et al*., 1987; German *et al*., 2002; Dunk and Mills, 2006), in addition to the near-field sediments (Dash *et al*., 1971; Ruhlin and Owen, 1986; Khripounoff and Alberic, 1991; Dill, 1994; German *et al*., 1999), including some with low-temperature mineralisation (Alt, 1988). The intermediate-spreading Juan de Fuca Ridge is suggested to account for a small proportion of sulphide particles within the sediments in the North Pacific (Hrischeva and Scott, 2007; Costa *et al*., 2017). Low-temperature mineralisation was also observed, non-exhaustively, in the Costa Rica margin (Bodeï *et al*., 2008; Steinmann *et al*., 2012), the Guaymas basin (Kurnosov, 2018) in detachment faults associated to the MORs (Tucholke *et al*., 2013) and on the ridge flanks of the Antarctic East Scotia and the Hook ridges (Aquilina *et al*., 2013; Aquilina *et al*., 2014). Other metalliferous sediments were found also in the Woodlark Basin Centre of the Papuan Peninsula (Bogdanov *et al*., 1997), at the Galapagos Rift (Walter and Stoffers, 1985), on the Indian Ridge (Iyer *et al*., 1997; Liao *et al*., 2018; Pan *et al*., 2018; Yu *et al*., 2018), Okinawa Trough (Hu *et al*., 2017), in volcanic arcs (Cronan, 1981; Hodkinson *et al*., 1986; Iizasa, 1993; Cronan *et al*., 2000; Johnson and Cronan, 2001; Dekov *et al*., 2007; Brathwaite *et al*., 2008; Dubinin *et al*., 2009; Pelleter *et al*., 2017) and in volcanic islands (Rouxel *et al*., 2018).

The Atlantis II Deep is a unique metalliferous sediment basin, hosted in a warm brine and warm pool on the floor of the Red Sea, and it is the only metalliferous sediment deposit to have been evaluated as a mineral resource with 90 Mt of salt-free ore deposit (Anschutz and Blanc, 1995; Anschutz *et al*., 2000; Bertram *et al*., 2011). It is also the only known modern deposit that is analogous to laminated Fe-rich chemical sediments, such as banded iron

formations, which provides evidence of the importance of non-sulphide metal-bearing components (Laurila *et al*., 2014; Laurila *et al*., 2015).

1.4.2 Origin and formation of the metalliferous sediments

Metalliferous sediments result from a combination of multiple processes. It is now known that their accumulation is directly controlled by the collapse and mass wasting of hydrothermally derived deposits (Metz *et al*., 1988; German *et al*., 1993; Mills *et al*., 1993; Halbach *et al*., 1998; Webber *et al*., 2015), *in situ* authigenic mineralisation from low-temperature fluids (*cf.* section 1.2.2; *e.g.* Alt, 1988; Mills *et al*., 1996; Goulding *et al*., 1998; Hein *et al*., 2008; Laurila *et al*., 2014) and the settling of hydrothermal plume fall-out from the neutrally buoyant plume migrating past the ridge axis (*cf.* section 1.2.3; *e.g.* Dymond and Roth, 1988; German *et al*., 1993; Mills *et al*., 1993). The composition of metalliferous sediments is, therefore, directly dependent on the host rock and the vent fluid composition. Once metalliferous sediments are accumulated, breakdown and weathering of the SMS deposits occur together with post-depositional diagenetic processes within the sedimentary column. Consequent to the combination of accumulation and post-depositional physical or chemical alteration processes of metalliferous sediments, their mineralogical and geochemical composition is highly variable between and within individual hydrothermal systems, as it will be demonstrated in the CHAPTER 5.

1.4.2.1 Sulphide weathering

Sulphide weathering is a chemical modification process of sulphides that occurs after the collapse of hydrothermal chimney material. Pyrite (FeS_2) reacts with the neutral pH and oxygenated seawater to precipitate metastable ferrihydrite (Eq. 1.1), which will transform into hematite and goethite (*cf.* section 1.4.2.2). Marcasite, a FeS_2 polymorph, is metastable and subject to decay into pyrite. Fe^{2+} also contributes to form jarosite, an orange-brown secondary mineral (Fallon *et al*., 2017). Cu sulphides (chalcopyrite, and in lesser proportion bornite) also undergo weathering, leaching Cu^{2+} (Eq. 1.2) to precipitate the secondary Cu mineral atacamite, $Cu_2Cl(OH)_3$, and its polymorphs (Eq. 1.3). Sulphide dissolution occurs under acidic pore water conditions (pH <5) within the mounds during the initial stages of deposit oxidation. In the presence of pyrite, sphalerite is preferentially dissolved through galvanic reactions (*i.e.* whereby different minerals may act as cathodes and anodes, and be cathodically protected or preferentially dissolved, respectively) (Fallon *et al*., 2017; Knight *et al*., 2017), releasing Zn in pore waters and its dissolution is pH-independent (Eq. 1.4).

Anhydrite, $Ca(SO)_4$, is unstable under cold seawater conditions and below 150°C, and rapidly dissolves. Finally, in comparison to anhydrite, barite, $Ba(SO)_4$ and quartz (or amorphous silica) have low solubility and are highly resistant to alteration.

$$2\,FeS_2 + 7.75O_2(aq) + 8\,H_2O \rightarrow Fe_2O_3 \cdot 4.5\,H_2O + 4\,SO_4^{2-} + 7H^+ \quad \text{(Eq. 1.1)}$$

$$CuFeS_2 + 3.75O_2(aq) + 0.5H_2O \rightarrow Cu^{2+} + Fe^{2+} + 2SO_4^{2-} + H^+ \quad \text{(Eq. 1.2)}$$

$$2\,Cu^{2+} + Cl^- + 3\,H_2O \rightarrow Cu_2Cl(OH)_3 + 3\,H^+ \quad \text{(Eq. 1.3)}$$

$$ZnS + 2O_2(aq) \rightarrow Zn^{2+} + SO_4^{2-} \quad \text{(Eq. 1.4)}$$

1.4.2.2 Post-depositional processes

The post-depositional fate of the near- and far-field hydrothermal sediment deposits remains poorly understood. To date, three processes are confirmed and consist of: i) microbially-mediated diagenesis, ii) ferrihydrite to goethite transformation and iii) redox cycling of transition metals.

The first process, microbially-mediated diagenesis, is available thanks to the electron donors (Fe(II), Mn(II), H_2 and CH_4) and acceptors (FeO(OH), MnO_2, CH_4 and CO_2) provided by the metalliferous substrate, the pore fluids and the low-temperature hydrothermal fluids commonly circulating through the periphery of the hydrothermal system. Prokaryotes remobilise some metal species through the sedimentary column (Glynn *et al*., 2006; Severmann *et al*., 2006). Microbial processes at hydrothermal fields have received the most attention lately (*e.g.* Edwards *et al*., 2003; Suzuki *et al*., 2004; Severmann *et al*., 2006; Toner *et al*., 2009; Müller *et al*., 2010; Lin *et al*., 2016; Ta *et al*., 2017) and are beyond the scope of this thesis.

The second process describes the ferrihydrite as a metastable hydrous Fe oxide either directly precipitating within the plume or a weathering product of sulphides (Eq. 1.1). Ferrihydrite undergoes transformation during oxic and suboxic diagenesis to a range of more crystalline Fe-rich phases (Dunk and Mills, 2006).

The third process suggests that transition metals are prone to be mobilized when the depth of oxidation front in the sediments moves downward or upward. The depth of the oxidation front is controlled by fluctuations in the relative balance of bottom water oxygen and electron donor input (organic matter and hydrothermal sulphides) (Mills *et al*., 2010).

1.4.3 Terrestrial analogues for metalliferous sediments

Once hydrothermal sediments undergo diagenesis, lithification and uplift, they may be found on land where they are more accessible to study. Regions like Troodos in Cyprus are excellent locations to investigate hydrothermal deposits, as the Troodos ophiolite was once part of the Tethyan seafloor associated with a supra-subduction zone or back-arc spreading ridge and contains VMS and associated metalliferous sedimentary rocks.

In Troodos, there are two distinct types of metalliferous sedimentary rocks associated with the massive sulphide deposits: umbers and ochres. Umbers are a Fe and Mn-rich sediment facies that accumulated above the extrusive lavas of the Troodos ophiolitic massif during the Mesozoic (Robertson, 1975). They are characterized by an enrichment in trace metals, including REEs and Yttrium (Robertson and Fleet, 1976; Josso *et al*., 2018). The sediment formed during late-stage hydrothermal activity of a seafloor hydrothermal system releasing amorphous Fe and Mn-oxides particle into plumes ('*a dilute metalliferous brine*'; Robertson, 1975; Boyle, 1984). Less widespread than umbers, are ochres, a yellow, iron-rich, unmetamorphosed mudstone, found closely associated with some of the VMS deposits resulting from the submarine weathering of sulphide ore. Those ochres are evidence that the ores were exposed and partly weathered on the ocean floor (Cann and Gillis, 2004). There is also abundant terrestrial evidence for moderate to low-temperature hydrothermal circulation that occurred in the ridge flank deposits, as umbers, but also a lava facies with silicification and gold enrichment (Prichard and Maliotis, 2007).

Despite the fact that hydrothermal sedimentary rocks are excellent exploration tools for targeting mineral deposits, comprehensive studies on these rocks are rather limited (Revan *et al*., 2019). Other terrestrial hydrothermal deposits include, but are not limited to: the Vani deposits in the Greek island Milos, ophiolite-associated deposits in Greece, and other ferruginous and/or manganiferous rocks proximal to VMS. The Vani Mn-Ba-Pb deposit is a fossil inhalative-exhalative hydrothermal mineralisation taking place in a sub-seafloor and/or seafloor environment, most likely alternating with cycles of deposition of sulphides (Papavassiliou *et al*., 2017). In mainland Greece, Mn-rich sediments are numerous, and while some are associated with mid-ocean ridges and their ophiolites (Robertson and Varnavas, 1993), others are thought to be related to hydrothermal activity associated with off-axis volcanism rather than to a spreading ridge source (Robertson and Degnan, 2008). According to Maslennikov *et al*. (2012) studying the Ural VMS deposits, the proximal rocks forming haloes around massive sulphide deposits are subdivided into jasperites, gossanites

and cherts. Jasperite mainly consists of hematite and quartz with a microbreccia-like texture, while a gossanite is a lithified analogue of the ochres, therefore derived from submarine hydrothermal gossans. A gossanite consists of oxidised clastic sulphides mixed with hematitized carbonate and/or hyaloclastic material, but may be entirely replaced by silica, chlorite and hematite. Cherts are quartz-dominant rocks and often contain sulphides (Maslennikov *et al*., 2012). The metalliferous sedimentary rocks from the Eastern Pontides in Turkey are extremely well preserved due to the non-metamorphosed nature of the region, largely composed of quartz and hematite, and are associated to VMS deposits (Revan *et al*., 2019).

1.4.4 Relevance of metalliferous sediments studies

The study of hydrothermal sediments is relevant to a number of in different aspects, all of which are considered in this thesis:

- Metalliferous sediments are excellent indicators of the presence, intensity and history of hydrothermal activity (Gurvich, 2006). The **geochronological evolution** of vent fields is recorded in the proximal and distal sediments that contain distinct, metal-rich layers reflecting discharge of hydrothermal material during active hydrothermal periods. Variation of hydrothermal activity is directly related to the variation of the heat and mass fluxes of the hydrothermal circulation. Therefore geochronological studies of sediments investigate the processes causing the change in hydrothermal activity to understand the variation of heat and mass fluxes over geological time.
- Hydrothermal sedimentation impacts the **global element cycles and budgets**. The distal marine sediments deposited from hydrothermal plumes may account for a large fraction of the metals discharged at the black smoker vents. Models estimated that the global flux of metals (in particularly Fe and Mn) and sulphur released by hydrothermal activity is ~10^6 tonnes per year which would mean that in just a few hundred years, the discharge would be higher than the estimated tonnage occurring in all the world's known SMS deposits (Hannington *et al*., 2011). Therefore, the discrepancy of discharged metals from hydrothermal venting could accumulate in the distal marine sediments. Hydrothermal plumes also have an impact on the budget and cycles of U, V and As as the hydrothermal particles scavenge the oxyanions from seawater (Mills and Elderfield, 1995a).

- Metalliferous sediments could be used as proxies to locate hydrothermal systems in **deep-sea mineral exploration** (*e.g.* Liao *et al.*, 2018). Halos of dispersion around hydrothermal sources and the study of their spatial distribution are useful vectors in the same way geochemical gradients are used for mineral exploration in land-based mining.
- Finally, hydrothermal sediments may be of similar economic interest to the SMS deposits themselves for **deep-sea mining** because they contain Cu and Zn sulphides, and show Au enrichment (Herzig *et al.*, 1991). For example, in the Red Sea, recent estimates of the metalliferous sediments could be as much as ~90 Mt of salt free mineral resources for the Atlantis II Deep hydrothermal system (Bertram *et al.*, 2011). However, to date, little is known about the spatial distribution of metalliferous sediments within a hydrothermal system, their weathering and diagenesis and their grade assessment as mineral resources.

1.5 Temporal evolution of a MOR hydrothermal system

Due to their location on a spreading ridge, MOR hydrothermal systems are ultimately carried away from their magmatic source below the ridge axis. Eventually, the hydrothermal activity at a specific field fades and ceases leaving behind a deserted, inactive and off-axis sulphidic mound, slowly buried in sediment while the hydrothermal circulation exits at a new vent emerging closer to the heat source and on the younger oceanic crust.

Petersen *et al.* (2000) propose a general genetic model for seafloor deposits based on observations at the active TAG hydrothermal mound. In the early cycle, the beginning of hydrothermal activity consists of precipitation of sulphides within a talus slope or volcanic cone, and hydrothermal brecciation of the host rock (FIGURE 1.8). Pyrite is precipitated and Cu, Zn and trace elements are evenly distributed while high-temperature fluid flow exits at the vent and diffuse, low-temperature fluid flow diffuses around the mounds. Anhydrite precipitates where the hydrothermal fluids mix with the penetrating seawater and exits through chimneys. The mound slowly starts to build up and sulphide debris constantly collapses. Rapid changes of vent-fluid composition can occur responding to a variation in the nature of the underlying heat source or the tectonic dynamics of the region (Von Damm, 1995).

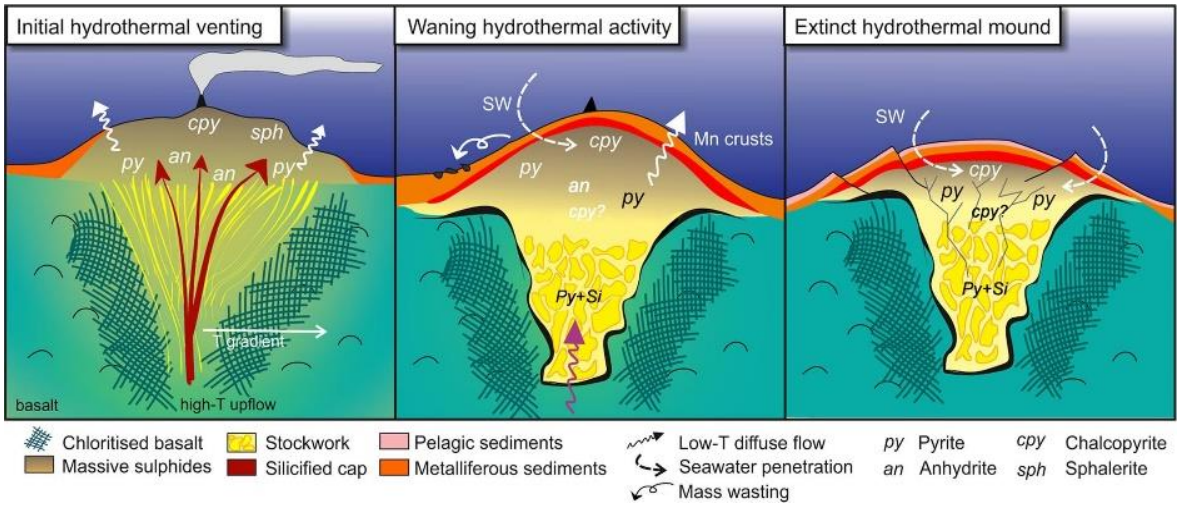

FIGURE 1.8 Generic geological evolution of a hydrothermal mound from the early stage of venting to their inactivity.

Numerous studies suggest most hydrothermal activity is episodic and therefore a hydrothermal mound can become inactive for short or long periods of time, much the same way as a dormant volcano. During the inactive periods, seawater infiltrates into the mound, cooling the interior leading to the dissolution of anhydrite that induces internal brecciation and collapse. Low-temperature mineralisation occurring at the waning stage of the hydrothermal activity, also precipitates clays, Mn oxides, and a lower-temperature retrograde mineral assemblages (*e.g.* amorphous silica and sphalerite) (Petersen *et al.*, 2000) and can lead to a Cu and Au enrichment (Halbach *et al.*, 1998).

At long-extinct inactive SMS deposits, the chimney structures are degraded by chemical dissolution and mass wasting and show various stages of weathering (Halbach *et al.*, 1998). Drilling into extinct hydrothermal mounds in 2016, as part as the Blue Mining project, at the TAG hydrothermal field, revealed the internal structure of a long-inactive field (Lehrmann *et al.*, 2018; Murton *et al.*, 2019) (FIGURE 1.5 and FIGURE 1.8). The main differences observed between this and active site are the complete absence of anhydrite, the thick and impermeable 1 to 5 m cap of Fe-rich silica (jasper) cap, protecting the sub-seafloor deposit from seawater penetration and formed during a late waning (cooling) stage, and an enrichment of Cu in the upper-ten meters of the ore body (Lehrmann *et al.*, 2018). In addition, circulation of seawater into SMS deposits can modify their composition by oxidising sulphides into oxyhydroxides and mobilising of metals (by mineral dissolution and release of heavy metals into the water column) (Fallon *et al.*, 2017; Knight *et al.*, 2017). Oxidation leaves behind submarine gossans with residual material and supergene enrichment capping the underlying, less altered primary deposit (Herzig *et al.*, 1991; Galley

and Koski, 1997). The process of weathering into gossans, however, is still poorly understood in terms of metal release into the ocean (Bennett *et al.*, 2008).

The oldest active hydrothermal field known started *c.* 223 ka ago at the Peterburgskoye field on the MAR (Cherkashov *et al.*, 2017). In addition, tens of thousands of years are most likely needed to form the largest known deposits, such as the Semyenov and Krasnov deposits, also on the slow-spreading MAR (Cherkashov *et al.*, 2017). The further evolution of an inactive hydrothermal mound becomes more complicated to investigate as hydrothermal systems are buried under sediments off-axis. To date, no deeply buried inactive fields outside the ridge flanks have been reported and post-activity modification studies rely on the occurrences opportunely brought on land by orogenesis (*i.e.* volcanogenic massive sulphides).

1.6 Thesis rationale and outline

The rationale of this thesis is to use metalliferous sediments to explore the geochemical evolution of a hydrothermal system from its start to its evanescence into residual sediments. Although metalliferous sediments begin to form as soon as hydrothermal activity starts, they are also the ultimate fate for these hydrothermal products. By studying their occurrence at the TAG hydrothermal field (MAR, 26°N), and especially their geochemistry, weathering and metal mobilisation, this study investigates how the eSMS deposits evolve after hydrothermal fluid flow has ceased and what processes drive the hydrothermal activity.

1.6.1 Thesis structure

The core of this thesis is presented in three science chapters that have been produced independently as manuscripts to be submitted for publication. Each chapter can be read independently. These chapters are wrapped in additional chapters providing an introduction and overview of the concepts discussed (CHAPTER 1). CHAPTER 2 describes the geological setting of the study area, the TAG hydrothermal field. This chapter also summarizes previous published studies on rock, sediment and fluid geochemistry, and mineralogy. CHAPTER 3 describes the sampling procedure, deployed during the *James Cook* JC138 and *Meteor* M127 expeditions in summer 2016, and the analytical methods used to obtain my data sets, of which the majority are presented in the three results chapters.

CHAPTER 4 establishes a geochronological history of hydrothermal activity at the TAGHF for three different sites, based on age-depth models produced by radiocarbon dating, palaeomagnetism and stable oxygen isotopes in the overlying pelagic sediments. This chapter uses the results to discuss the spatial and temporal distribution of hydrothermal activity at the TAGHF and among other hydrothermal systems around the world in relation to glacial-interglacial cycles. The study finds, with some limitations, that external factors influence the heat and energy fluxes resulting from hydrothermal activity.

CHAPTER 5 describes and discusses the results obtained from the mineralogy and geochemistry of hydrothermal sediments and their associated pore waters. The aim of this chapter is to extend the knowledge of sediment accumulation in different geological settings from extinct hydrothermal mounds to more distal locations. This chapter also explores the relationship between the depositional environments and the ongoing diagenetic processes inducing metal mobilisation and preservation. These diagenetic processes cause some environments to act as sources of metals to the ocean such as slopes and young deposit settings, or to act as sinks for metals such as distal depositional channels and basins. This chapter assesses the efficiency of sub-seafloor trapping mechanism for metals.

CHAPTER 6 presents the results obtained from mineralogy and geochemistry on the top of extinct seafloor hydrothermal mounds (the 'gossans'). This chapter discusses the physical and chemical processes occurring in a hydrothermal deposit when a high-temperature hydrothermal fluid flow ceases to understand the implications for the weathering and preservation of the massive sulphide ore bodies. The results are also compared to analogue terrestrial metalliferous sedimentary rocks to address the hypothetical evolution of a hydrothermal system once this system is off-axis and until it is subducted or uplifted on land.

CHAPTER 7 revisits the research questions addressed that form the core of this thesis, and provides a synthesis of the findings of this study that constructs a narrative describing the history and processes of geochemical evolution of a hydrothermal system, from its rise to its eventual evanescence into sediments. In addition, it provides new research questions that rose from this work and that should be addressed in the future.

Chapter 2 Geological setting: the TAG hydrothermal field

The Trans-Atlantic Geotraverse Hydrothermal Field (TAGHF) is a tectonically-driven hydrothermal field located on an active detachment fault on the eastern flank of the MAR at a depth ~3650 m (Rona, 1980; Humphris *et al.*, 2015) (FIGURE 2.1). The TAG segment of the MAR is located between the Kane Fracture Zone (24°N) and the Atlantic Fracture zone (30°N) and extends for 40 km, from 25°55'N to 26°17'N (FIGURE 2.2A). It is terminated to the north and the south by non-transform discontinuities (Sempéré *et al.*, 1990; Purdy *et al.*, 1990; Sempéré *et al.*, 1993).

It was discovered in 1972, during the Trans-Atlantic Geotraverse programme (Scott *et al.*, 1974) of the National Oceanic and Atmospheric Administration, when hydrothermal sediments were found on the seafloor and anomalies of thermal and Fe and Mn-rich particles were found in the water column (Scott *et al.*, 1978; Shearme *et al.*, 1983; Thompson *et al.*, 1985). It was not until 1985, however, that the currently active black smoker complex was discovered 2 km away from the neovolcanic axis (Klinkhammer *et al.*, 1986; Rona *et al.*, 1986; Thompson *et al.*, 1988). The TAGHF was the first hydrothermal field discovered on the slow-spreading MAR and confirmed that the distribution of hydrothermal systems is not restricted to intermediate-to-fast spreading oceanic ridges (Rona *et al.*, 1986). Since its

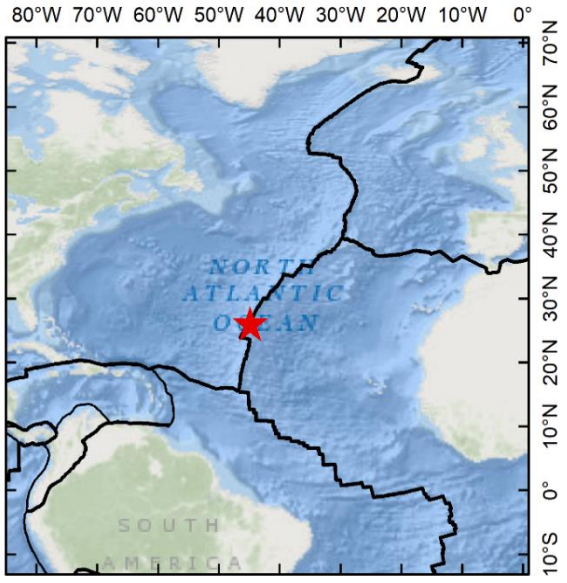

FIGURE 2.1 Location of the study area (red star), the TAGHF, on the MAR. The base map is provided by GEBCO, and the tectonic plate boundaries are provided by Bird *et al.* (2003).

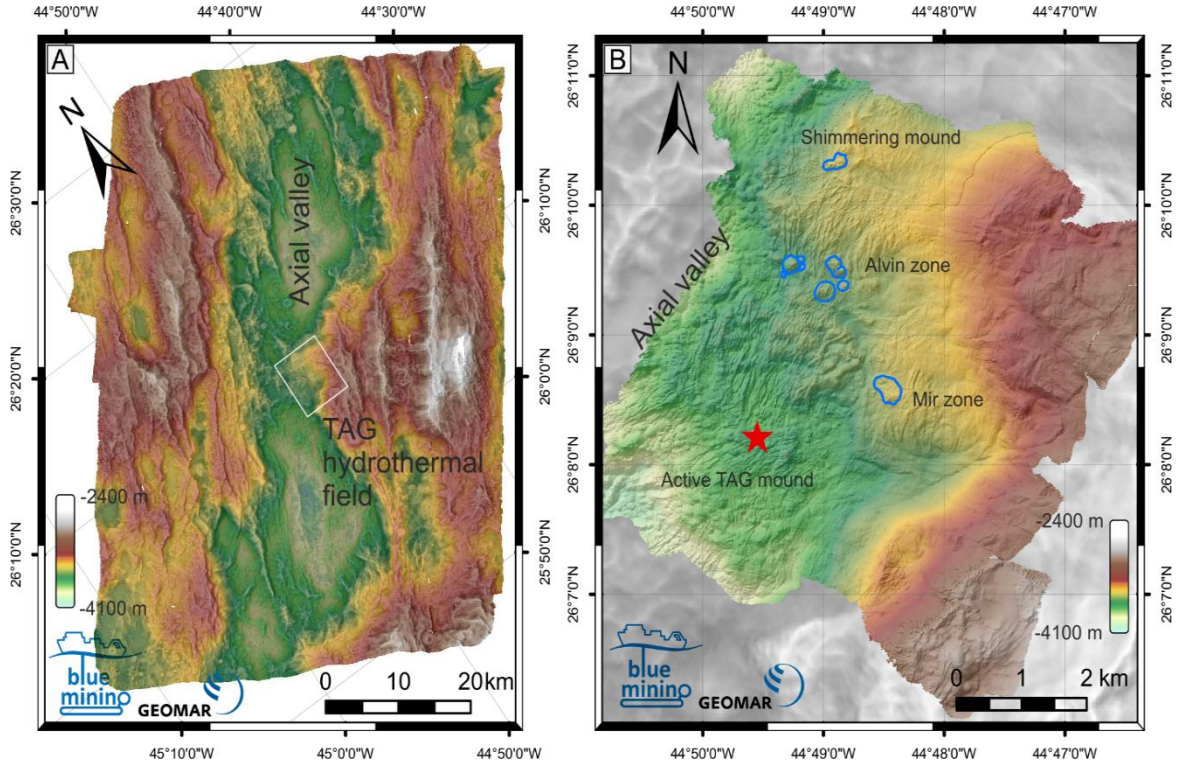

FIGURE 2.2 Bathymetry maps. (A) Ship-board multibeam swath bathymetry map of the TAG ridge segment (40 km extend from 25°55'N to 26°17'N) of the Mid-Atlantic Ridge including the TAGHF. The inset white outlined box is the location of (B). (B). AUV-derived, near bottom multibeam swath bathymetry map of the TAGHF showing location of the active TAG mound and other eSMS (outlined in blue).

discovery, the TAGHF has been extensively studied with dredging, photographic imagery, high-resolution side-scan sonar and *in situ* observations with the submersibles Alvin and remotely operated vehicles (ROV) (Becker and Von Herzen, 1996), Mir (BRAVEX programme, 1994), Shinkai (Gamo *et al.*, 1996) and Nautile (Hermine expedition, IFREMER, 2017). During these expeditions, direct visual observations assessed the extent of the active venting complex, the distribution and pattern of hydrothermal mineral deposition, identified the white smoker Kremlin area, and confirmed the existence of inactive hydrothermal mounds to which the MIR, Shinkai and Alvin submersibles gave their names.

In 1993, ODP Leg 158 drilled into the active vent complex to reveal the internal structure of the mound (Humphris *et al.*, 1995; Herzig *et al.*, 1998a). More recently, the EU-FP7 programme Blue Mining conducted seabed drilling operations, during the *RSS James Cook* expedition JC138, to study the internal structure of extinct hydrothermal mounds (Blue Mining Eu-7th FP, 2018; Murton and Scientific Party, 2018). High-resolution (~50 cm and ~2 m) multi-beam swath bathymetry mapping of several eSMS areas, and ship-board multibeam mapping (50 m resolution) of the axial valley between 26 and 26°35'N were

acquired on *RV Meteor* expedition M127, also part of the EU-FP7 project Blue mining (Petersen and Scientific Party, 2016) (FIGURE 2.2).

The major features of the TAGHF consist of: the active black smoker complex, completely covered by hydrothermal precipitates, sulphide talus and manganese crusts; the low-temperature hydrothermal zones in the eastern part including the Shimmering mound on the northern side of the field, and several extinct hydrothermal mounds, largely covered by pelagic carbonate ooze (FIGURE 2.2B) (Rona *et al.*, 1993a).

2.1. The TAG active hydrothermal mound

The TAG active mound (26°08'N, 44°49'W, at 3620 m depth) is a ~200 m diameter, 60 m high, black smoker complex with chimneys at the summit and a cover of sulphide talus and manganese oxide encrustations. The mound complex consists of concentric inner and outer levels and lies on oceanic crust at least 100,000 years old. The outer mound is covered predominantly with carbonate ooze and metalliferous sediments, basalt talus, occasional massive sulphide blocks, and a few relict chimneys (Rona *et al.*, 1986; Thompson *et al.*, 1988). The inner mound rises about 30 m above the outer mound and is composed of sulphide blocks and relict and active chimneys (FIGURE 2.3). The centre of the mound consists of high

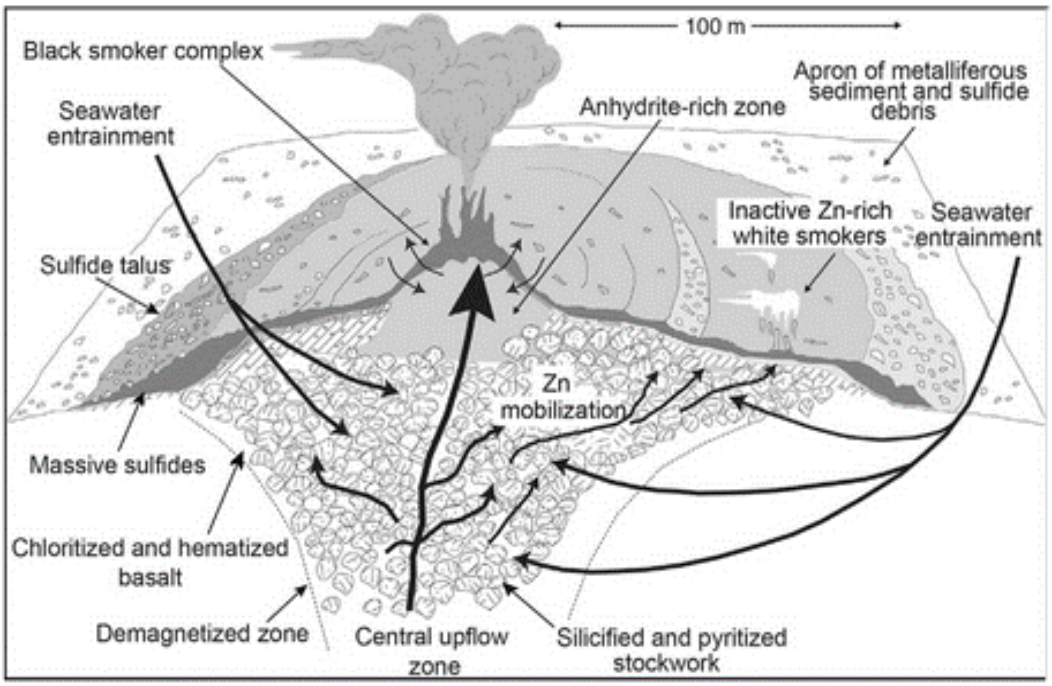

FIGURE 2.3 Schematic diagram of the TAG active mound. The geomorphology, surficial features and inferred patterns of fluid upflow and seawater entrainment in the internal structure are shown. The inactive Zn-rich white smokers represents the Kremlin area. From Humphris *et al.* (2015).

temperature 'black smoker' chimneys that are at least 10 m tall. Their mineralogy consists of anhydrite, pyrite and chalcopyrite, while on the seafloor blocks of anhydrite and massive sulphides are interspersed.

The chemistry of the black smoker fluid appears to be similar in composition and temperature (290-321°C) to fluids collected from the EPR (Campbell *et al*., 1988). Chimneys across the main edifice exit exactly the same fluid composition and suggest that they are all supplied from a single reservoir (Edmonds *et al*., 1996; Chiba *et al*., 2001). The chemistry shows also the same temporal stability (from 1986 to 2001) as observed on the EPR and Guaymas Basin (Edmond *et al*., 1995; Chiba *et al*., 2001) although there are small temporal changes in pH, alkalinity and Fe values. These variations suggest a subsurface FeS precipitation with entrainment of seawater in the system (Gamo *et al*., 1996). Analyses of the fluids prior and after ODP drilling, show that major dissolved ionic species concentrations are stable indicating that the drilling did not disturb the primary plumbing system (Campbell *et al*., 1988; Gamo *et al*., 1996; Chiba *et al*., 2001). However, venting patterns changed and new chimneys built-up after the drilling (Edmonds *et al*., 1996).

In addition to the main venting chimneys, shimmering water and smoke emanate from cracks and fissures in the slope of the mounds and on the outer mound plateau. A few bulbous active 1 to 2 m tall chimneys cluster in the southern part of the outer mound, the Kremlin area (Thompson *et al*., 1988). White to blue-grey smoke emanates from the top of the chimneys and anhydrite and sphalerite dominate the mineralogy, which is characteristic of lower temperatures venting (< 300°C) (Thompson *et al*., 1988). All surfaces where hot water emanates are covered with shrimps, anemones, crabs, eels, gastropods and small worm tubes, although the biota is largely restricted to the inner mound.

The internal structure, as determined by drilling during ODP Leg 158 is composed of a sulphide-anhydrite-silica breccia (FIGURE 2.4) indicating that the deposit grows largely *in situ* (Humphris *et al*., 1995). At each active event, new precipitates are formed and cement the older deposits (Humphris *et al*., 1995). Numerous anhydrite veins crosscut the inner mound and contribute to its internal growth. In the deepest part the basalt host rock is progressively silicified and replaced by a pyrite/quartz assemblage also contributing to the internal growth and stockwork formation (Fouquet *et al*., 1998). During inactive periods, anhydrite dissolves, and the mound undergoes collapse and fault disruption (Humphris *et al*., 1995). Fouquet *et al*. (1998) also suggested that surface sulphides building the chimneys are progressively buried and recrystallized, contributing to the surface growth of the massive sulphide mound.

ODP drilling revealed that metals (Zn, Cu and trace metals) have very low concentrations within the mound and in the stockwork zone. Instead, most are enriched closer to the surface of the mound (Herzig *et al*., 1998b). These features may be explained by the leaching of the primary sulphides during hydrothermal activity in conjunction with zone refining whereby Cu, Zn, Pb, Ag, and other trace metals are mobilised (Fouquet *et al*., 1998; Herzig *et al*., 1998b). Zn mobilisation probably occurs also in the eastern rim of the active mound producing the Zn-rich 'white smokers', although no Zn-rich zones were found at depth (Fouquet *et al*., 1998). The wall-rock consists of basaltic breccia, largely paragonitized and chloritized, grading into silicified basalt (Herzig *et al*., 1998b).

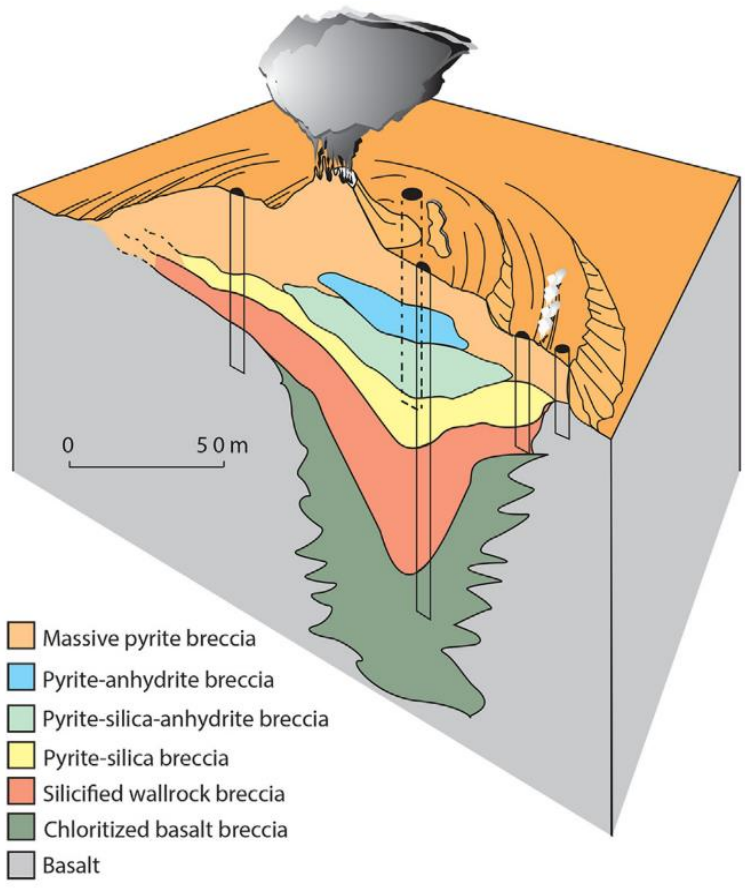

FIGURE 2.4 Subsurface stratigraphy of the TAG active hydrothermal mound determined by drilling during ODP Leg 158. All units are dominated by breccias composed of mixtures of clasts of different lithologies. From Humphris *et al*. 2015.

2.2. Relict hydrothermal deposits (inactive hydrothermal mounds)

In this section, a description of the geology of the inactive hydrothermal mounds is provided. The presence of inactive zones indicates the hydrothermal regime has not been constant over geological time and that the fluid pathways within the crust have evolved.

2.2.1. Alvin zone

The Alvin zone, located 4 km NNE of the active TAG mound, contains several 100-300 m diameter, 30-60 m high, sulphide mounds. These are dome shaped, with discontinuous sulphide outcrops, standing and toppled chimneys, and a thin (<2 m) cover of pelagic carbonate sediment (Rona *et al.*, 1993b; Rona *et al.*, 1993a). The mounds identified in the Alvin zone include the Shinkai mound (Rona *et al.*, 1998; White *et al.*, 1998), Southern mound (Rona *et al.*, 1993a), Double mound (Rona *et al.*, 1993a) and Rona mound (Petersen and Scientific Party, 2016; Murton *et al.*, 2019) (TABLE 2.1).

The internal structure of an inactive hydrothermal mound is distinctly different from the TAG active hydrothermal mound. The main differences are the absence of anhydrite, replaced by a massive sulphide ore body dominated by pyrite, and the presence of a 3-6 m thick impermeable silica cap (Murton *et al.*, 2019). The dimensions, depth and tonnage tend to increase compared to the active mound with up to 200 m sub-surface of ore body and stockwork surrounded by an altered basalt wall-rock (Murton *et al.*, 2019).

TABLE 2.1 Summary of the active and inactive hydrothermal mounds of the TAGHF with their key features, compiled from different literature referenced in the text.

Name	Coordinates of the mound centre	Water depth (m)	Height (m)	Diameter (m)	Morphology	Active/Inactive
TAG mound	26°08'13''N 44°49'34''W	3620	~60	~200	Concentric inner and outer levels	Active
Southern Mound	26°09'20''N 44°48'58''W	3525	~70	~300	Intersected with faults Ravines	Inactive, although some shimmering water was observed
Rona Mound	26°09'22''N 44°48'50''W	3524	~40	~150	The smallest mound. Smooth	Inactive
Shinkai Mound	26°09'32''N 44°49'15''W	3540	~100	~300	One main mound and three adjacent smaller monticules Steep with ravines	Inactive
Double mound	26°09'30''N 44°48'53''W	3490	~70	~300	Two similar mounds, intersected with faults and ravines	Inactive
Shimmering zone	26°10'20''N 44°48'51''W	3410	~100	~300	Crest in an L shape, located on the edge of a steep slope	Inactive although some shimmering water was observed
Mir zone	26°08'33''N 44°48'26''W	3430	~120	~400	Horseshoe shape and steep with ravines	Inactive

2.2.2. Mir zone

The second inactive area of about 1 km in diameter, is the Mir zone. It is located 2 km ENE of the TAG active mound and lies between two pillow lava domes at a depth of 3430-3525

m. It consists of three distinct zones of hydrothermal deposits (Rona *et al.*, 1993b), small standing and fallen chimneys, highly weathered sulphide material, red metalliferous sediments, and low-temperature hydrothermal precipitates such as Fe-Mn oxide crusts (Rona *et al.*, 1993a; White *et al.*, 1998). Heat flow values of up to 13.3W/m^2 were reported, indicating local hydrothermal activity (Rona *et al.*, 1993b; Rona *et al.*, 1996) but ongoing low-temperature hydrothermal activity has not been observed in pore water or near-bottom seawater geochemistry.

2.3. Shimmering mound and low-temperature zones

A zone of active low temperature hydrothermal activity of ~6 km^2 (26°07′ to 26°09′N – 44°48 to 44°45′W) has been identified ~ 4 km east of the TAG active mound, and 2 km east of the inactive Alvin zone. It lies at a higher altitude than the other features on the eastern wall. The area consists of low-temperature hydrothermal deposits such as massive layered deposits of nontronite, amorphous Fe-Mn oxides, and Mn oxide birnessite (Rona, 1984; Thompson *et al.*, 1985) and heat flow anomalies. However, no high-temperature hydrothermal venting has been observed directly in this area and no sulphide deposits have been recovered (Rona *et al.*, 1993b; Mills *et al.*, 2001). Humphris *et al.* (2015) suggest that the detachment fault could contribute to the fluid pathways as the fault termination coincides with the deeper areas of the low-temperature zone.

Located at ~ 4 km NNE from the TAG active mound is another area of active low-temperature (22.5°C) diffuse hydrothermal flow called 'Shimmering mound'. The mound is about 50 m in diameter and emits clear fluids (22.5°C) through Fe and Mn oxyhydroxides (Rona *et al.*, 1998). While its relict hydrothermal activity has been confirmed by visual observation of massive sulphides, sampling of sulphidic material, and geophysical models of subsurface massive sulphide deposits (Gehrmann *et al.*, 2019), low-temperature activity has only been reported by one stud (Rona *et al.*, 1998). It is not known whether the active TAG mound and the active Shimmering mound are both supplied with fluids from the same upwelling limb of a convection cell or from different convection cells (Humphris *et al.*, 2015).

2.4. Geochronology

The TAGHF appears to have a complex history involving multiple cycles of active growth of mounds separated by periods of inactivity with anhydrite dissolution and mound

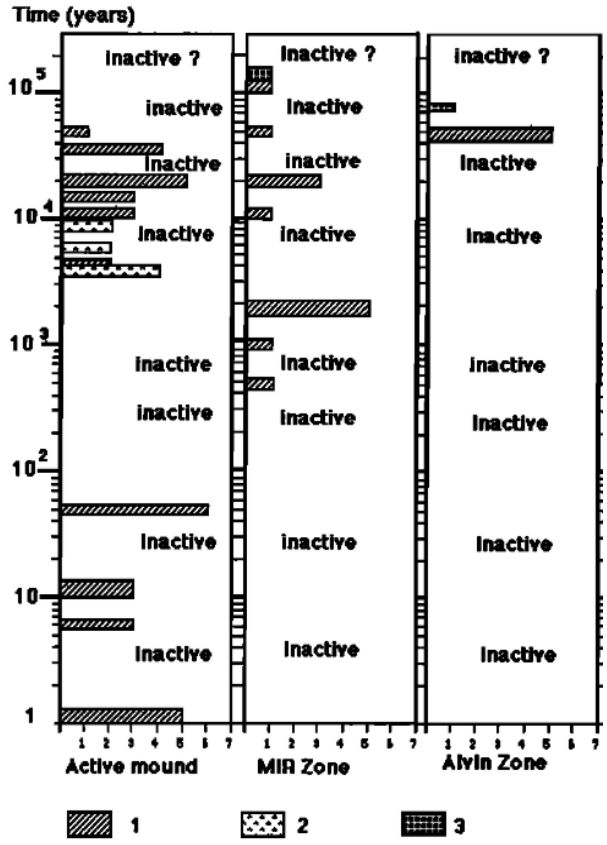

FIGURE 2.5 Summary of the dating of hydrothermal products (1- hydrothermal sulphide; 2 – low-temperature aragonite precipitate, 3 – low-temperature Mn oxide precipitate) provided by Lalou *et al*. (1995). The scale is logarithmic and for each site the horizontal scale gives the number of samples analysed by age group.

collapse (Humphris *et al*., 1995). The active high temperature zone is located on oceanic crust at least 100 ka old. U-series radiogenic dating of sulphide samples from the surface, and from drilled sub-seafloor core indicates that venting at this site started at least 50 ka ago with pulsed high temperature activity every 5 to 6 ka over the past 20 ka (Lalou *et al*., 1993; Lalou *et al*., 1998b; You and Bickle, 1998). Within the structure, the oldest material forms a layer (11 to 37 ka old) in the centre of the deposit surrounded by youngest material (2,3 to 7,8 ka old) both above and below (You and Bickle, 1998).

Precipitation of sulphides (*i.e.* high-temperature hydrothermal activity) in the Alvin zone started at a similar time (50 ka) while the Mir zone shows an older age of sulphide formation with at least 100 ka (Lalou *et al*., 1990; Lalou *et al*., 1993; Lalou *et al*., 1995). Nonetheless, hydrothermal activity likely started earlier as the oldest dating was obtained on low-temperature manganese crusts showing 140 to 125 ka at the Mir zone and 74 ka years at the Alvin zone (FIGURE 2.5) (Lalou *et al*., 1995). Regarding the end of the hydrothermal activity, Metz *et al*., (1988) suggest this finished around 6-8.5 ka in the Alvin zone and Lalou *et al*.

(1995) dated the youngest sulphide deposit at 600 years ago at the Mir zone. Regarding the active TAG mound, the activity was restarted only 60 years ago, after a quiescence of about 4000 years (Lalou *et al.*, 1998b).

2.5. The TAGHF sediments

The TAGHF metalliferous sediments were first described as sediments rich in Fe, Cu, Zn and Mn-rich deposits, probably originating from fine sulphide precipitates that had been oxidized and dispersed by hydrothermal plumes or formed by primary precipitates of Mn-oxide. These sediments are capped by a biogenic calcareous ooze consisting of pale-brown to yellow accumulation of foraminifera, and nanoplankton tests, rich in Fe (Scott *et al.*, 1978; Shearme *et al.*, 1983). Thompson *et al.* (1985) determined the presence of nontronite (Fe-rich clay), birnessite (Mn-oxide) and Fe-oxide originating from low-temperature hydrothermal fluids. In 1988, Metz *et al.* highlight the variation of the hydrothermal input from hydrothermal plumes as a result of episodic pulses of hydrothermal activity. German *et al.* (1990) studied this hydrothermal plume fall-out in the pelagic sediments and demonstrated that the rare-earth elements are scavenged from seawater onto the suspended oxide particles. Atacamite and paratacamite, which are supergene alteration Cu chloride minerals, are identified (Hannington, 1993), as well as native Cu and Cu-Zn grains (Dekov *et al.*, 1999). Different types of sediment deposits were identified: *i.e.* collapse and weathering of chimney material (German *et al.*, 1993), filling of channels by turbidite-like mass wasting, particulate fallout from the plumes (Mills *et al.*, 1993; Mills *et al.*, 1994) and authigenic mineralisation of Mn-oxide (Goulding *et al.*, 1998) and nontronite (Severmann *et al.*, 2004). Geochemical characterization of pore waters confirmed the presence of a low-temperature fluid flow through sulphidic sediments in the south of the active TAG mound (Mills *et al.*, 1996). Severmann *et al.* (2006) investigated the role of pore waters as a transport agent for redox-sensitive metals (Mn, Fe) close to the Southern mound and suggested that metal reduction by microbial prokaryotic activity occurs. The enrichment of prokaryotic communities also plays a role in the distribution of supergene alteration of sulphidic sediments and secondary mineral phases (Glynn *et al.*, 2006).

2.6. Outstanding questions

The TAGHF is one of the best known hydrothermal fields and is considered as a classic example of a modern, volcanogenic massive sulphide deposits. It is therefore an excellent location to investigate the geological fate of the inactive seafloor massive sulphides.

Understanding the fate of hydrothermal deposits after cessation of venting is in turn essential to assess the impact of hydrothermal activity on the ocean system, and the preservation of the deposits in the geological record.

As developed in SECTION 1.1.1, there are three main aims explored in this thesis through the study of the processes recorded and preserved in the metalliferous sediments at the TAGHF. These reveal how the deposits were formed over time, their preservation and dissolution and the fate of the metals over geological time.

To address the question of how hydrothermal activity varies over time and what are the main influencing factors (CHAPTER 4), I use the sediments as a record of the discontinuous hydrothermal activity and identify the systems initiation, formation and decline.

To answer the question of how efficient the subsurface metal trapping mechanism is in sediments surrounding a hydrothermal site (CHAPTER 5), I compare metalliferous sediments from different seafloor environments to identify processes of accumulation, identify how metalliferous sediments evolution in terms of diagenesis and whether metalliferous sediments can be considered as potential mineral resources.

The third question addressed is how hydrothermal sites evolve after the high-temperature hydrothermal flow has ceased (CHAPTER 6). This is approached by studying the uppermost layer of sediments on the top of inactive mounds to define if the sediments participate in the preservation of the sub-seafloor massive sulphides and compare those sediments to analogue terrestrial records to extrapolate diagenetic processes.

Chapter 3 Materials and methods

The samples analysed for this study were collected during two oceanographic expeditions: on the *RV Meteor* (M127) (25th May – 28th June 2016) and on the *RRS James Cook* (JC138) (29th June – 08th August 2016). I participated in both expeditions to the TAG hydrothermal field (Mid-Atlantic Ridge, 26°N), as part of the EU funded (FP7) Blue Mining project, and was integral to the coring programme. On the M127 I was part of the gravity coring team, led by the University of Lisbon (responsible: Prof. Fernando Barriga), and was also responsible for the pore water collection. On JC138 I was responsible for the collection and sub-sampling of sediments and pore waters and the on-board pore water analyses. Back on shore I conducted the analyses of pore water cations with inductively coupled plasma-optical emission spectrometry (ICP-OES) and inductively coupled plasma-mass spectrometry (ICP-MS), hydrogen sulphide by photospectrometry, anions by ion chromatography, and alkalinity by colorimetric titration at the National Oceanography Centre of Southampton (NOCS) and the University of Southampton. In addition, I conducted sediment digests and analyses of cations with ICP-OES and ICP-MS, analyses of mineralogy by optical microscopy and scanning electron microscopy and analyses of sediment granulometry. Additional geochemical analyses that are included in this thesis are X-ray diffraction quantitative mineralogy (Richard Pearce and Ross Williams), nutrient analyses (Dr. Anna Lichtschlag), high resolution X-ray fluorescence core-scanning (performed at the British Ocean Sediment Core Research Facility), carbonate coulometry and oxygen isotopes analyses (performed at the SEAPORT laboratories), and magnetometry measurements (Dr. Chuang Xuan and Dr. Yuxi Jin). For each analysis I conducted the sample preparation and participated in the data processing. Radiocarbon dates were obtained from the NERC Radiocarbon Facility in East Kilbride through a grant (allocation n° 2142.1018) and directed by Dr. Steve Moreton. In addition qualitative mineralogy was conducted by Dr. Jelena Milinovic at the University of Lisbon.

The data acquired during the M127 expedition is used here to approach three specific objectives: (i) Firstly, high-resolution automated underwater vehicle (AUV)-based bathymetry mapping and backscatter mapping helped in the selection of coring stations based on the identification of sediment ponds within a rough terrain topography typical in a hydrothermal field. Bathymetric mapping of hydrothermal mounds is discussed in Chapter 5 and used to address the ageing and decay of hydrothermal deposits. (ii) Secondly, of the 23 sediment cores retrieved, one was taken as a reference about 15 km east

of TAG (26°05.485N - 44°38.770W). In this work, I exclusively refer to the pore water study at the reference coring station. (iii) Thirdly, an assessment of the geochemical vectors for deep-sea hydrothermal mineral exploration were determined from the sediments, in collaboration with the University of Lisbon and GEOMAR, and the results were published in the Blue Mining project deliverables to which I contributed.

All data obtained for this thesis is either available in tables in the chapters, in appendices or in the electronic appendices (.zip files). Finally, data will also be available on the online PANGAEA archive and directly linked to the published articles that can be found under the label JC138.

3.1 Sample collection and on-board processing

Sediment samples were collected during the two cruises using a gravity corer, a mega corer and the Rock Drill 2 (RD2) owned by the British Geological Survey. The gravity corer is an instrument penetrating into the seabed by using its gravity to penetrate into the sediments, while rock drilling uses a diamond rotating annular tool to cut out a cylinder of the sediments or rocks. Finally, mega coring, or multi coring, is achieved through the use of a hydrostatic damping system and usually records undisturbed seabed-water interfaces.

Gravity core planning prior to the M127 cruise was executed based on pre-existing bathymetry and the identification of potential sediment ponds (APPENDIX A.1). On board M127, the strategy was refined through the acquisition of AUV-based high-resolution bathymetry and more suitable coring locations were subsequently identified. During M127, 33 gravity coring stations were conducted and 23 cores were successfully recovered (3 m length, 125 mm-diameter) of which 22 GCs targeted metalliferous sediments and one core was taken as a reference about 15 km east of TAG (M127/711GC; 26°05.485N - 44°38.770W) (APPENDIX A.2). During JC138, 10 gravity cores (2 m-length, 70 mm-diameter, FIGURE 3.1) and 2 mega-cores were retrieved in close proximity to the hydrothermal mounds (TABLE 3.1, FIGURE 3.2). In addition, two ~3 m-long sediment cores were recovered with the BGS rock drill (RD2) (FIGURE 3.1) from above the massive sulphide ore body at the top of Southern mound (TABLE 3.1) after identifying a smooth surface by visual observation with the robotic underwater vehicle (HyBIS). After the rock drill cores were recovered, we encountered lost horizons and cracks (1 to 3 mm-wide) running obliquely in the sediments. Those cracks disturbed the sediments and extended the core lengths, therefore exact penetration depths below the surface were subsequently calculated based on the rock drill

telemetric data (Lehrmann, pers. communication). Further pore waters analyses confirmed that the pore water geochemistry from RD2 cores was not influenced by those cracks and intrusion of seawater. Sampling protocols used during M127 and JC138 are provided in APPENDIX A.3.

TABLE 3.1 Locations and positions of sediment cores rock drilling during JC138, RD = rock drill, GC = gravity core; MC = mega-core; c.c. = core catcher. * Depths are inferred from telemetry data of the rock drill and the length was not fully recovered. Lithostratigraphy logs for the successful retrieving sediments (**) are provided in APPENDIX A.4 and the sampling list are provided in the DIGITAL MATERIAL 1.

Station	Date	Water depth (m)	Positioning		Recovery (cm)	Location
			Lat. °N	Long. °W		
15GC	18/07/2016	3553	26°09.333′	44°48.994′	< 50	Southern mound
16GC**	18/07/2016	3553	26°09.338′	44°48.974′	133	Southern mound
22RD**	23/07/2016	3535	26°09.331′	44°48.959′	190-320 *	Southern mound
23GC	22/07/2016	3537	26°09.392′	44°49.004′	c.c.	Southern mound
27GC**	23/07/2016	3524	26°09.375′	44°48.820′	41	Rona mound
28GC**	23/07/2016	3400	26°08.558′	44°48.416′	194	Mir zone
29GC**	23/07/2016	3430	26°10.339′	44°48.888′	132	Shimmering mound
31RD**	26/07/2016	3536	26°09.334′	44°48.965′	17-168 223-273 *	Southern mound
37MC	27/07/2016	3482	26°09.555′	44°48.453′	17-25	Double mound
38GC**	27/07/2016	3608	26°09.126′	44°48.814′	98	Depositional channel in Alvin zone
39GC**	27/07/2016	3490	26°08.619′	44°48.550′	39	Mir zone fan
49GC**	31/07/2016	3490	26°09.237′	44°48.902′	230	Depositional channel in Alvin zone
51GC**	02/08/2016	3570	26°09.477′	44°49.306′	130	Shinkai mound talus
52GC**	02/08/2016	3397	26°10.283′	44°48.806′	190	Depositional basin W of shimmering mound
54GC	02/08/2016	3600	26°09.873′	44°49.251′	c.c.	North of Shinkai mound
59MC	05/08/2016	35280	26°09.117′	44°48.820′	10	Depositional channel in Alvin zone
62GC**	06/08/2016	3535	26°09.247′	44°48.947′	188	Depositional channel in Alvin zone

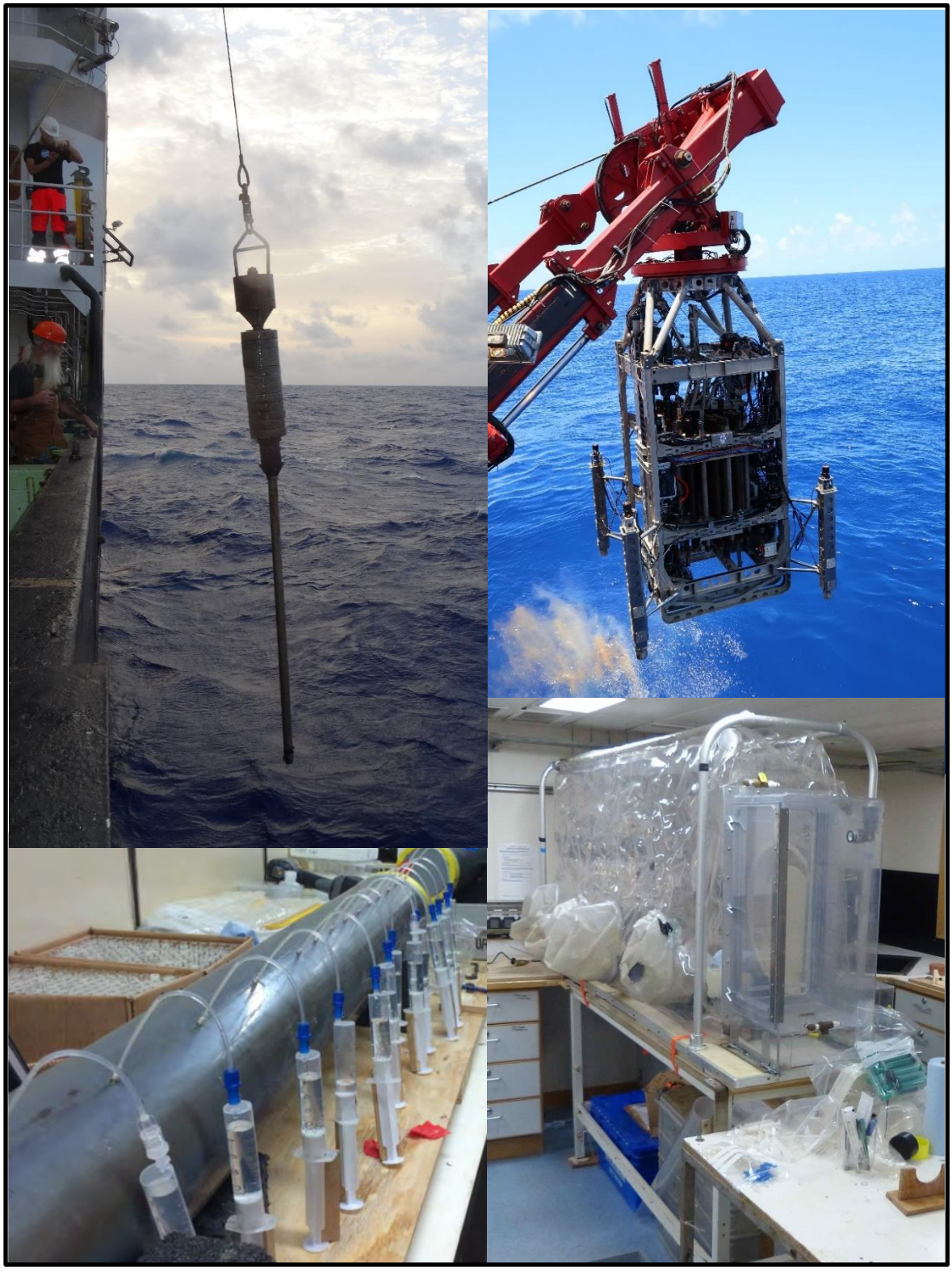

FIGURE 3.1 Sampling techniques. (upper left) Gravity corer and (upper right) BGS Rock drill 2 deployed during the *RRS James Cook* expedition JC138. (bottom left) Pore water sampling using Rhizon soil moisture samplers on the *RV Meteor* M127 expedition (photo © Florian Besson). (bottom right) Glove bag (polythene tent) filled with nitrogen to preserve an oxygen-free environment during the pore water extraction.

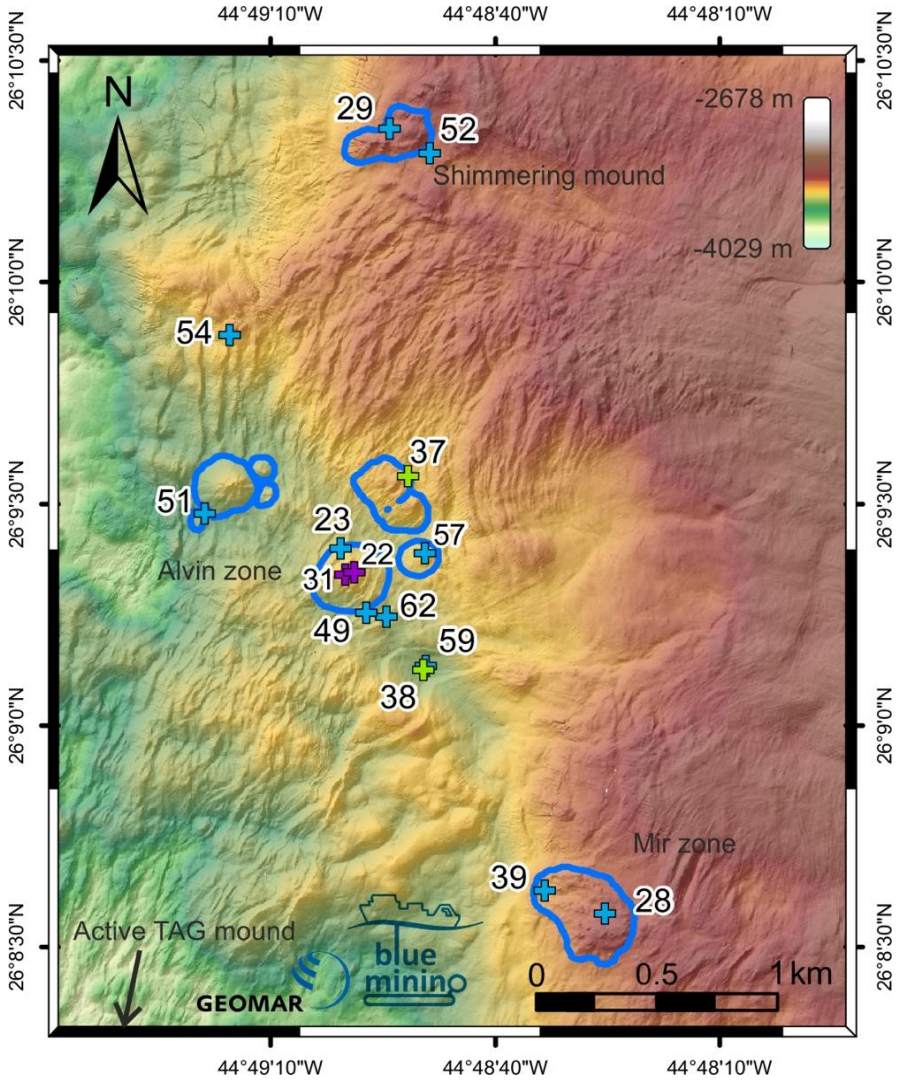

FIGURE 3.2 Coring locations during the *RSS James Cook* expedition JC138 using gravity coring (blue), rock drilling (purple) and megacoring (green). Numbers depict the station numbers. Base map provided by GEOMAR and surveyed by the AUV Abyss during expedition M127.

3.1.1 Pore water sampling

After retrieval, the gravity and rock drill cores were cut into 0.5 or 1 m long sections, capped at both ends and transported to a controlled temperature room set to *in situ* temperature (4°C). At selected intervals (usually every 5 cm for the first 0.5 m, 10 cm from 0.5 to 1.5 m, and every 20 cm intervals below 1.5 m), holes were drilled into the liners and water was extracted with Rhizon Soil Moisture samplers (Rhizon CSS: length 5 cm, pore diameter 0.2 µm; Rhizosphere Research Products, Wageningen, Netherlands; FIGURE 3.1). These Rhizon samplers consist of a small microporous polymer tube (approximately 0.2 µm pore size) that is supported by a stabilizing glass fibre wire and connected to a PVC tube (Seeberg-

Elverfeldt *et al*., 2005). The pore water was extracted using under pressure produced by the attached 10 mL syringes (Luer-Lock connection). Rhizon samplers extract pore waters from a cylindrical volume of about 3 to 4 cm^3 of affected sediments, with a vertical depth resolution of 1 cm (Seeberg-Elverfeldt *et al*., 2005). Therefore the depth range on the pore waters analyses induced by sampling is ± 0.5 cm.

The applied method permitted extraction of the pore water with minimal disturbance of the sediments. To minimize it furthermore, the Rhizon was inserted along the splitting line. The first 0.5 mL of the pore water samples were discarded to reduce the contamination with oxygen and the Rhizon was cleaned before use. Oxidation of the redox-sensitive components in the pore water and sediments by oxygen was minimized by (1) sampling the pore waters prior to the splitting and opening of the core sections; (2) covering drilled holes with oxygen impermeable tapes while no Rhizon was inserted and (3) carrying out the extraction inside a nitrogen filled polythene tent (also called glove bag, FIGURE 3.1). About 10 mL of pore water was collected for every interval and subsequently was distributed in the following aliquots: (i) 2 mL for cations in acid cleaned 7 mL plastic vials; (ii) 1.5 mL for anions and dissolved sulphide in Eppendorf cups prefilled with 0.5 mL of 2% Zinc acetate (iv) 2.2 mL for total alkalinity (TA) filled without headspace in glass vials and (v) approximately 2 mL frozen in plastic vials frozen at -20°C for nutrient analyses. After sampling, the aliquots for cations analysis were acidified with 5 µL suprapur concentrated nitric acid to prevent metal precipitation. TA aliquots were poisoned with 5 µL saturated mercury chloride solution (10 % w/v) to prevent microbial turnover. Overall 232 pore waters samples were collected during JC138.

To analyse the seawater chemistry close to the seafloor, the near-bottom seawater was collected in the overlying water of a multicorer core (59MC) that was deployed at the same station as 38GC, in the depositional channel.

3.1.2 Sediment sub-sampling

After pore water sampling, the gravity core sections were split horizontally and opened into two halves. Both halves were photographed in a portable photography studio (DIGITAL MATERIAL 2). The lithology and stratigraphy were described and included in the digitalized logs (APPENDIX A.4 and DIGITAL MATERIAL 3). Sediment subsamples were taken to match approximately the pore water sample depths (about 1 cm offset) and used for analyses of grain size, porosity, bulk density, mineralogy and bulk rock geochemistry. Further cm^3 of sediments were collected and frozen at -20°C for future microbial analyses. After sub-

sampling, both core halves were wrapped in cling film and packed in resistant polythene plastic sleeves. The working and archive halves are currently stored in a 4°C temperature room at British Ocean Sediment Core Research Facility (BOSCORF, National Oceanography Centre of Southampton), where they were later examined using the ITRAX system.

Depth precision is 1 cm induced by the sub-sampling procedure and therefore depth range is ± 0.5 cm.

3.2 Solid phase analysis

3.2.1 Physical parameters

Grain size was measured on 5 carbonate ooze samples and 18 hydrothermal sediment samples with the Malvern Masterize Particle Size Analyser at the National Oceanography Centre. The instrument measured 5 replicates of the same sample and data are represented as the average of the five measurements (DIGITAL MATERIAL 4).

Porosity and bulk density were calculated from known volume and weight of sediments before and after drying at 50°C or freeze-drying. Large imprecision of the porosity and density measurements results from an imprecise volume sampling (± 0.5 cm^3) with a head-cut syringe. As a result, depth profiles of porosity and density show no visible trend (an example is given in APPENDIX A.5). Results must be carefully interpreted and some outlier values were discarded (DIGITAL MATERIAL 5).

3.2.2 Mineralogy

3.2.2.1 Optical Microscopy

Mineralogy and textural analyses of the bulk sediments were carried out on specific horizons (sulphide layers and Fe oxyhydroxides layers) after impregnation of the sediments in epoxy resin at the National Oceanography Centre/University of Southampton. Polished blocks were subsequently made and analysed under reflected light on a polarizing optical microscope and photographs were taken (DIGITAL MATERIAL 6).

The impregnation was undertaken by displacive fluid impregnation following the method of Kemp *et al*. (1998). To slowly replace the seawater by acetone, the wet samples were placed in a close-fitting, well-perforated cotton foil and immersed in high-purity acetone

for five days, with acetone replacement twice a day. After the final soaking, a "spurr" resin mixture was added in the following proportions:

- vinylcyclohexene dioxide (VCD) 10.0 g
- diglycidol ether of polypropyleneglycol (DER 736) 6.0 g
- nonenyl succinic anhydride (NSA) 26.6 g
- dimethylaminoethanol (DMAE) 0.2 g

The replacement was undertaken twice a day and left to soak for up to four weeks after the last addition of resin. The samples were cured for 72 hours at 30°C, then 24 hours at 45°C and finally 24 hours at 60°C. The blocks were subsequently cut and polished in thin sections.

3.2.2.2 X-ray diffraction (XRD)

Quantitative XRD analyses were carried out on bulk, ground and dried Fe oxyhydroxide sediments after powdering and mixing with a known amount of corundum (25% by weight) with a Philips X'Pert pro with a Cu tube (Kα λ = 1.541) coupled to Siroquant XRD software, at the University of Southampton (National Oceanography Centre). Minerals were identified by comparison with the International Centre for Diffraction Data database, PDF-2 at the University of Southampton. Detection limit of unknown crystalline minerals is *c.* 1 wt%. Example XRD spectra can be found in APPENDIX A.6 and the comprehensive dataset is provided in the DIGITAL MATERIAL 7. Additional qualitative mineralogical results are also provided by the University of Lisbon on a Panalytical X´PERT Pro, a MiniFlex II and X'pert high Score Plus software.

3.2.2.3 Scanning electron microscopy – Energy dispersive X-Ray spectroscopy (SEM-EDS)

Individual mineral grains and 5-10 milligrams of powder were investigated for mineralogy with SEM (Carl Zeiss Leo 1450VP SEM), and characterized by semi-quantitative energy dispersive X-ray (EDS) detector (Oxford Instruments X-Act 10mm^2 area SDD EDS Detector, at the University of Southampton (National Oceanography Centre)) with a carbon coating. Minerals that did not dissolve during the acid digestion were also analysed with a Hitachi TM1000 SEM at BOSCORF, which is more suitable for gaining results quickly as it does not require carbon coating, although it reduces the resolution. Two horizons of Fe oxyhydroxide sediment samples (from Southern mound) were investigated for chemical

mapping, textural morphology and mineralogy using EDS. The data are available in the DIGITAL MATERIAL 8.

3.2.3 Geochemical composition

3.2.3.1 ITRAX-scan chemostratigraphy

The chemostratigraphy of the sediment cores was analysed with the ITRAX core-scanning X-ray fluorescence system (Cox Analytical Systems) (Croudace *et al.*, 2006) at BOSCORF (National Oceanography Centre). The archive halves of the sediment cores were covered in ultra-thin, X-ray transmissive cling film. The vertical resolution is 1 mm. The ITRAX produced a digital X-radiograph for each core, and then underwent XRF analyses for the elements in the range of molar weight from Si to U (DIGITAL MATERIAL 9). The instrument was operated at a voltage of 30 kV, a current of 30 mA, a count time of 30 s with a 3kW Mo X-ray tube. The data were cleaned and processed in the following way:

- Any rows (= depth step of 1 mm) with low total kilo-counts per second (kcps) under 10 000 were deleted as it is identified as a crack or depth without sediment.
- Any rows with high mean standard error (MSE > 10) were considered and either deleted or treated with caution. The MSE depends largely on the grain size. Although occasionally the MSE was above 10 in sandy layers, in particularly in layers consisting of sulphides such as in 39GC, 52GC, 38GC and 52GC, I have decided to not discard the element abundances. Moreover, each sulphide layer has quantitative ICP geochemical composition to constrain the chemostratigraphy. The MSE for each core is reported in the TABLE 3.2.
- Elements which consistently showed a kcps under 300 were marked as unreliable and discarded. Exceptions were made for specific layers that were of high interest for the study (*e.g.* Si in 52GC and S in cores containing sulphides) and I considered values as qualitative to describe the element content fluctuation.
- Element kcps were normalized against total kcps (MacLachlan, pers. comm. 2017)
- A running average of 3 mm was applied to smooth the results and remove any possible individual spikes.

TABLE 3.2 ITRAX maximal MSE and mean MSE for each core analysed in the following chapters. MSE is dimensionless.

Core	Maximal MSE	Mean MSE
22RD	5.89	4.32
29GC	5.19	2.82
31RD	4.93	3.14
16GC	4.69	3.22
27GC	5.80	4.20
28GC	12.72	6.47
38GC	10.81	5.18
39GC	25.85	9.68
52GC	14.94	5.71
49GC	14.89	5.11

In order to obtain high-resolution down-core quantitative results, ITRAX data were calibrated against whole rock geochemistry data (by ICP-OES) from specific intervals for Fe and Ca in 27GC, 28GC, 29GC, 38GC, 49GC and 52GC and for Mn in cores 38GC. Conversion of the ITRAX counts into quantitative results was achieved by determining the best-fit (*i.e.* a correlation coefficient close to 1) regression line between the ITRAX measurements and the bulk rock ICP-OES data (calibration plots, correlation coefficient (R^2)) and regression line equations are available in APPENDIX A.7. This calibration resulted in different slopes and intercepts for each element in each core. For instance, Fe is present in high concentration (*e.g.* > 50 wt%) in my sediments and a decrease in ITRAX Fe sensitivity with increasing content was observed. Therefore, in the case of high Fe content an exponential regression provided a better correlation coefficient. Other reasons for a non-constant relationship between the ICP and ITRAX data can be *i.e.* the different lithological environments with different water content, differences in grain size and matrix effects (MacLachlan *et al*., 2015).

3.2.3.2 Whole rock geochemical analyses

Whole-rock analyses were performed on acid-digested dried material. About 100 mg of dried sediments and sediment standards were accurately weighed in acid-cleaned Savillex Teflon digestion vessels. Acid digestion was undertaken following the in-house lab procedure by William Homoky (2011) (available in the DIGITAL MATERIAL 10) at the University of Southampton (National Oceanography Centre). First, sulphides and

carbonates were oxidized in Aqua Regia (3:1, HCl:HNO_3), afterwards the mixture was evaporated and further digested using a mixture of concentrated HF and $HClO_4$ to dissolve any remaining silicates. Finally, an additional $HClO_4$ volume was added to ensure HF was entirely removed from the previous step. The fully digested samples were then diluted to a 1:400 ratio using 3 M HCl and further to a 1:4000 ratio using a 3% HNO_3 matrix containing an internal spike of Be, Re and In. The samples were analysed with ICP-OES (Thermo Scientific ICAP 6500 Duo) for major elements (Al, Ca, Cu, Fe, K, Mg, Mn, Na, Ni, Sr, Ti, V and Zn) together with 3 matrix-matched rock standards diluted at different ratios (JB1A, JB-3 and BIR1) and with ICP-MS (ThermoScientific X-Series 2) for minor elements and trace elements (Ba, Cd, Co, Cr, Cs, Li, Pb, Rb, Sc, Sn, Th, U, Zr and Au), including rare earth elements (REE). An additional 6 standard solutions were prepared from single element standard solutions to cover the range of concentrations for Mn (55 to 5500 ppb), Zn (20 to 2000 ppb), Cu (1 to 40 ppm), Ag (1 to 20 ppb) and Au (0.5 to 10 ppb). All reported values were corrected for drift and blanks. Drift on the ICP-OES was assessed by a repeat of one standard every 10 measurements while drift on the ICP-MS was assessed with the internal spikes of Be, In and Re derivations between samples. Blanks were measured every 10 samples. The data are available in the DIGITAL MATERIAL 10.

Precision (% relative standard deviation, %RSD) and accuracy (% relative error, %RE) were determined for each analytical run by repeated analysis (n = 3) of two certified reference materials (CRM): (i) marine sediments MESS-1 (National Research Council of Canada), and (ii) sulphide ore mill tailings RTS-1 (National Research Council of Canada). The precisions and accuracies reported in the TABLE 3.3 are a mean of the values obtained for each dataset (APPENDIX A.8). Precision, representing the agreement between a set of results, is calculated using the following formula:

%Relative standard deviation=100(absolute standard deviation/average of CRM values)*

And accuracy, representing the agreement between the result and the true value, is calculated using the following formula:

% relative error= 100(absolute error/CRM real value)*

Rare earth element (REE) and Y (Y-REE) data have been normalised to the Y-REE concentration for chondrites C1 (Evensen *et al*., 1978 or Palme, 1988). Deviations of Y-REE patterns are expressed as anomalies: the Ce anomaly, the Eu anomaly and the heavy- to light-REE fractionation. Eu and Ce anomalies can be expressed either arithmetically or geometrically. Equations used throughout thesis are:

$$Eu\ anomaly = Eu/Eu^* = Eu_n/\sqrt{Sm_n * Gd_n} \quad \text{(Eq. 3.1)}$$

$$Ce\ anomaly = Ce/Ce^* = Ce_n/\sqrt{La_n * Pr_n} \quad \text{(Eq. 3.2)}$$

Where n refers to chondrite normalised values. The normalised La/Gd ratio is used to quantify the fractionation of HREEs (Gd to Lu) from LREEs (La to Eu). The Y-REE precision and accuracy were both within 5% of the CRM MESS-1.

TABLE 3.3 Average of accuracies and precisions of the solid phase geochemical elements as from the APPENDIX A.8. The used CRM for calculating the accuracy is reported. [a] ICP-OES; [b] ICP-MS. NA = the CRM concentration is not available.

Element	Precision (%RSD)	Accuracy (%RE)	CRM
Ag	1.3	NA	
Al [a]	1	2.5	RTS1
Ba [b]	0.5	15.1	RTS1
Ca [a]	0.9	2	RTS1
Cd [b]	1.7	20.1	MESS1
Co [b]	3.5	4.7	MESS1
Cr [b]	2.1	19.9	MESS1
Cs [b]	1.1	NA	
Cu [a]	0.6	2.1	RTS1
Fe [a]	2.3	1.8	RTS1
K [a,]	0.8	6	RTS1
Li [b]	1.1	NA	
Mg [a]	0.8	2.1	RTS1
Mn [a]	2.4	4.1	MESS1
Na [a]	4.2	2.6	RTS1
Ni [a]	1.1	2.6	MESS1
Pb [b]	0.7	1.4	RTS1
Rb [b]	2	NA	
Sc [b]	2.5	NA	
Sn [b]	0.4	35.3	MESS1
Sr [a]	0.7	0.6	MESS1
Th [b]	2.5	NA	
Ti [a]	1.6	4.4	RTS1
U [b]	2.6	NA	
V [a]	1.9	2.4	MESS1
Zn [a]	1.1	11.3	RTS1
Zr [b]	4.2	5.5	RTS1
Au [b]	1.8	20.5	RTS1

Calcium carbonate concentration was measured with a CM5015 coulometer at the SEAPORT laboratories (University of Southampton). For this about 15 mg of the ground sample was placed into 12 ml screw top vials with septa tops (Labco, UK). After acidification in the AutoMate Prep Device (AutoMate FX, Inc., Bushnell, Florida, USA) with 10% phosphoric acid, the evolved CO_2 was measured with an UIC CM5015 CO2 Coulometer (UIC Inc., Joliet, Illinois, USA). Employing the principles of Faraday's Law, the coulometer automatically measures the absolute mass of carbon dioxide evolved from sample acidification. Solid inorganic carbon values have been determined using a pure calcium carbonate standard (CAS #471-34-1), where weight percent $CaCO_3$ = percent C_{inorg} × 8.334. This method of calculation assumes that all of the CO_2 is liberated from $CaCO_3$. Long-term instrument precision is 1.22%. The data are available in the DIGITAL MATERIAL 11.

3.2.3.3 Stable oxygen isotopes ($\delta^{18}O$)

For stable oxygen isotope analysis, 0.06 to 0.40 mg of bulk sediment sample was weighed out into borosilicate glass vials according to their $CaCO_3$ concentration in order to give ~50 µg of pure $CaCO_3$. For the subsequent analysis with a Kiel IV Carbonate device coupled to a MAT253 isotope ratio mass spectrometer (both Thermo Fisher Scientific) at the SEAPORT laboratories (University of Southampton), samples were reacted with suprapur phosphoric acid at 70°C for 420 seconds. After cryogenic removal of water vapour and other gases the resulting CO_2 was measured multiple times against a reference gas. Following data reduction and correction, data were normalised using a two-point calibration with NBS 18 ($\delta^{18}O$=1.93±0.05‰) and NBS 19 ($\delta^{18}O$=-22.99±0.04‰) (IAEA, Vienna, Austria) and reported relative to VPDB (Vienna Pee-Dee Belemnite). In-house reference material (GS1) was used for quality assurance purposes and to report instrument precision. Long-term instrument precision was 0.06‰ for $\delta^{18}O$.

To construct the age-depth model the obtained results were compared to a well-dated signal as a reference signal, the LR04 stack marine oxygen isotope stages (Lisiecki and Raymo, 2005). The approach was to use the software 'AnalySeries' which provide an interface to wiggle match corresponding remarkable features (tie-points) of both signals. The software then mathematically measures similarities and provides correlation coefficients, and linear sedimentation rates (Paillard *et al.*, 1996). Four replicate samples for a single sediment horizon were run and their comparison gave a precision better than 10%RSD. Because 99.9% of foraminifera population in the sediments are composed of planktonic foraminifera and there was a good correlation coefficient (0.80) between the $\delta^{18}O$

values with the reference signal, I concluded that data generated from bulk carbonate analysis were sufficiently reliable. I therefore did not conduct further oxygen isotopes analyses on specific planktonic or benthic foraminifera. The uncertainty of the correlation of the $\delta^{18}O$ signal is estimated to be < 5 kyr, with a clear identification of all glacial and interglacial periods in the longest record from 52GC (145 ka). Further age controls are provided by radiocarbon analyses and reduce the age uncertainty in all the cores (27GC, 38GC, 49GC, 28GC. 29GC, 52GC), except after 70 cm depth in 52GC (where radiocarbon dating could not be applied). The data are available in the DIGITAL MATERIAL 12.

3.2.4 Radiocarbon dating

Radiocarbon dating was carried out on an accelerator mass spectrometry at the NERC-SUERC Radiocarbon Facility in East Kilbride. Sixteen sediment horizons (~ 0.5 cm) were sieved and washed to obtain an even distribution of clean grains. Then, a 8- 10 mg fraction of 300 to 710 µm-wide, clean and intact planktonic foraminiferal tests (*i.e.* Globigerinoides, Orbulina, Truncorotalia, Trilobatus sps) were separated by hand picking under a binocular microscope from the rest of the material (mainly Fe-Mn oxyhydroxides, silica spicules and volcanic material) to provide sufficient material for radiocarbon dating (FIGURE 3.3).

The outer 20 wt% of tests from each sample were removed by controlled hydrolysis with diluted HCl to further reduce any residual diagenetic contamination. The samples were then rinsed with deionised water, dried and homogenised. A known weight of the pre-treated sample was hydrolysed to CO_2 using 85% orthophosphoric acid at room temperature. The CO_2 was converted to graphite by Fe/Zn reduction. A background correction calculated from one sample known to be older than 80 ka was applied to the data (sample SUERC-86749). Reference and monitor materials consisted of ^{14}C-free Icelandic spar calcite. Radiocarbon ages are reported in TABLE 3.4 and the DIGITAL MATERIAL 13, as conventional radiocarbon years BP (relative to AD 1950) and were corrected with the latest versions of OxCal (currently OxCal 4.3; Bronk Ramsey, 2009) and the Marine 13 calibration curve (Reimer *et al.*, 2013) to take into account the marine reservoir effect. The marine reservoir effect (MRE; ranging from -200 to 700 years; by default, 405 yrs in OxCal) is the delayed response to changes in atmospheric ^{14}C between the ocean mixed layer and the atmosphere. The magnitude of this effect depends on the geological time, the location, the water depth, and other parameters such as upwelling waters, currents and different water masses. A Delta R correction is therefore additionally applied to take into account the variation of the global marine reservoir effect varying over oceanic regions. Unfortunately,

Delta R in deep-sea sediments is not yet well constrained, therefore, to be able to compare my results with other published data from the same research area using the same parameters on the radiocarbon dating (*e.g.* Middleton *et al*. 2016), I also assumed the Delta R to be zero. In low sedimentation rate environments, such as at the TAGHF, bioturbation may introduce an age error of several thousand years for individual control points.

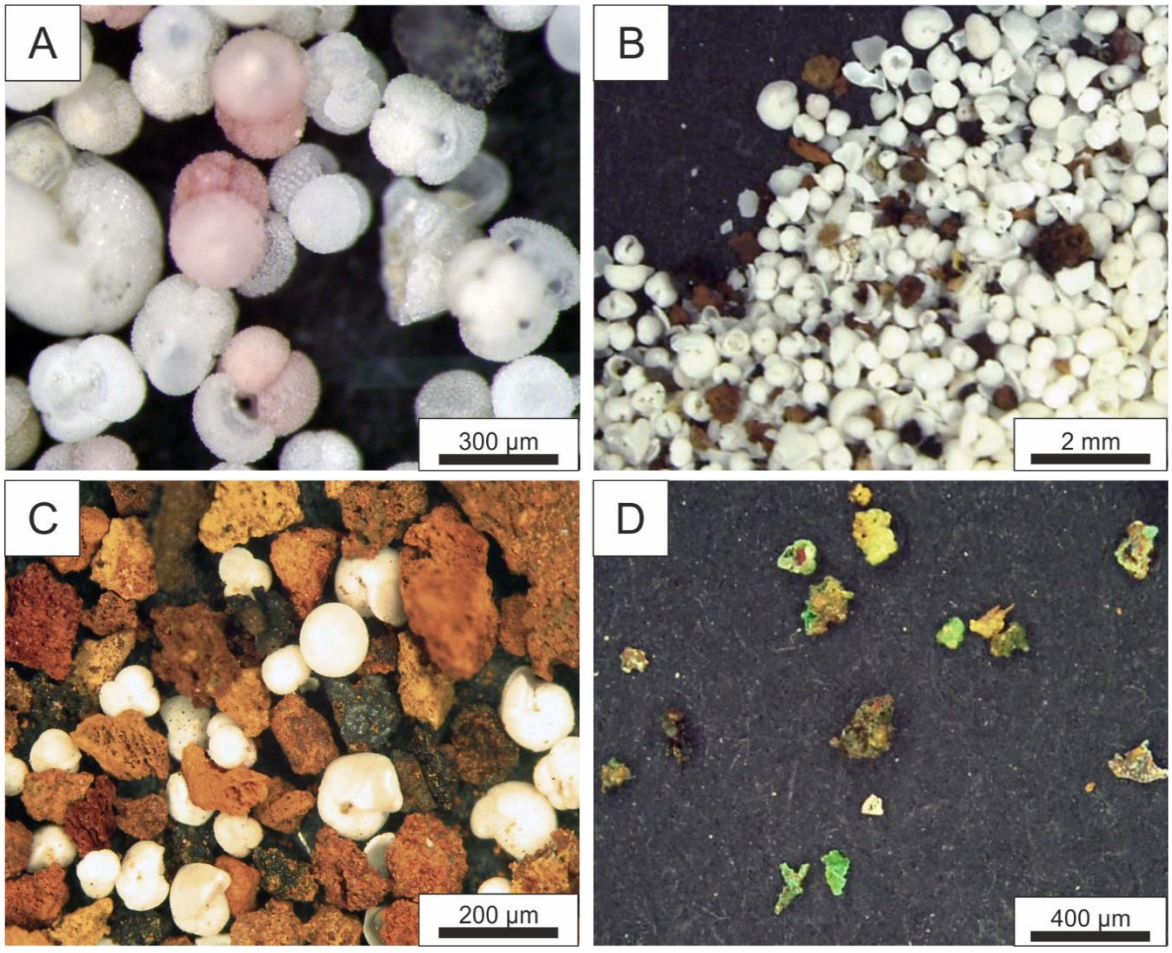

FIGURE 3.3 250-710 µm sieved sediments. (A) Foraminifera sp. Globigerinoides, including pink tests (removed for the analyses), Truncorotalia and Trilobatus. Sampled from JC138/38GC at 18.5cm. (B) Example of a 'fragile' sediment horizon showing numerous debris of foraminifera tests. Sampled from JC138/38GC at 37 cm. (C) Foraminifera sp. Orbulina and Truncorotalia, amongst Mn oxides (dark grains), Fe oxyhydroxides (yellow, orange or red grains). Sampled from JC138/27GC at 15 cm. (D) Example of non-foraminifera material, *i.e.* paratacamite and atacamite minerals.

TABLE 3.4 Radiocarbon raw data and initial processing on the results provided by the NERC radiocarbon facility. Results are reported as conventional radiocarbon years before present (BP; where 0 BP = AD 1950) and % modern ^{14}C, both expressed at the ±1σ level for overall analytical confidence. Where ^{14}C values are distinguishable from NRCF process background, results have been background corrected. ^{14}C results have been normalised to δ^{13}CVPDB‰ = -25 using the ^{13}C values. *Estimated δ^{13}CVPDB‰. One result is close to background and according to the conventions set out in Stuiver and Polach (1977) that result is reported as a minimum age that the sample will be greater than.

Publi-cation code	Sample identified	^{14}C Enrich-ment (% modern)	+/- 1σ (% modern)	Conven-tional ^{14}C Age (yrs BP)	+/- 1σ (^{14}C yrs BP)	%Carbon Content	$\delta^{13}C_{VPDB}$‰ (± 0.1)	
SUERC-86734	JC138_38GC_10	60.28	0.28	4066	37	11.3	1.8	
SUERC-86735	JC138_38GC_18.5	36.31	0.17	8139	38	10.8	1.0	
SUERC-86736	JC138_38GC_29	26.40	0.13	10698	39	11.1	0.6	
SUERC-86737	JC138_38GC_37	21.78	0.11	12243	41	10.6	1.0	
SUERC-86738	JC138_38GC_75	12.21	0.08	16895	53	10.1	1.3	
SUERC-86739	JC138_49GC_6	39.72	0.18	7416	37	10.9	1.3	*
SUERC-86740	JC138_49GC_21	23.43	0.11	11657	39	8.9	1.3	*
SUERC-86744	JC138_49GC_36	12.78	0.08	16524	52	9.5	1.3	*
SUERC-86745	JC138_52GC_30	9.10	0.07	19255	66	10.8	1.3	*
SUERC-86746	JC138_52GC_40	2.09	0.06	31057	240	9.6	1.3	*
SUERC-86747	JC138_52GC_84	0.47	0.06	43108	1036	10.0	1.3	*
SUERC-86748	JC138_52GC_92	0.36	0.06	45292	1364	9.9	1.3	*
SUERC-86749	JC138_52GC_149	0.12	0.06	>48464		939	1.3	*
SUERC-86750	JC138_27GC_15	24.98	0.12	11142	37	9.8	1.4	
SUERC-86754	JC138_28GC_10	50.13	0.22	5548	36	10.3	2.3	
SUERC-86755	JC138_29GC_20	24.45	0.13	11315	42	10.0	2.2	

3.2.5 Paleomagnetism

To constrain the age-depth model based on $\delta^{18}O$ analyses beyond 50 ka (when radiocarbon dating cannot be applied), relative paleomagnetic intensity (RPI) was acquired on the 52GC core on the depositional basin close to Shimmering Mound. The core was continuously subsampled using plastic u-channels of 1.8 x 1.9 cm^2 cross-section over the length of the core section (~50 cm). The natural remanent magnetization (NRM) and the anhysteretic remanent magnetization (ARM) were measured on a 2G Enterprises Superconducting Rock Magnetometer in the shielded room at the University of Southampton. Measurements for each U-channel were made at 1 cm intervals with an additional 5 cm measured beyond both ends of the samples. First, NRM was measured before and after stepwise alternating field demagnetization of peak of 50mT or 100 mT to reach a demagnetization of 700 mT. After completion of NRM measurements, ARM was imparted along the long-axis of the u-channels. The acquired ARM was measured prior to demagnetization and after stepwise alternative field demagnetization at the same peak fields used for NRM. Down-core paleomagnetic records (NRM and ARM intensities) are provided in APPENDIX A.9 and DIGITAL MATERIAL 14. To restore the high-resolution paleomagnetic signal, deconvolution optimization was applied with the UDECON software (Xuan and Oda, 2015). Finally, deconvolved relative paleomagnetic intensity, as NRM_{mean}/ARM_{mean} ratio) was compared to the literature stacks PISO-1500 (Channell *et al*., 2009), HINAPIS (Xuan *et al*., 2016) and SINT-2000 (Valet *et al*., 2005).

3.3 Pore waters

3.3.1 Cations

Concentrations of major cations (B, Ca, K, Mg, Na, Si, Sr) were measured with ICP–OES (Thermo Scientific ICAP 6500 Duo) and concentrations of minor cations (Ba, Co, Cu, Fe, Li, Mn, Mo, Ni, Rb, U, V, Zn) were measured with ICP-MS (ThermoScientific X-Series 2, at the National Oceanography Centre). Both analyses were done on aliquots previously acidified to prevent any metal precipitation, and diluted 50-fold with 3% thermally distilled HNO_3 containing an internal spike of Be, Re and In. All reported values were corrected for drift and blanks. Drift on the ICP-OES was assessed by a repeat of one standard every 10 measurements while drift on the ICP-MS was assessed with the internal spikes of Be, In and Re derivations between samples. Blanks were also measured every 10 measurements.

Precision and accuracy were determined for each analytical run by repeat analysis (minimum 3) of two certified reference materials of similar range in composition as the samples: (i) CRM-SW (Seawater Greyhound) and (ii) SLEW-2 (National Research Council Canada) spiked with Fe, Mn, Cu, Zn, V and Co. Formulae are given in SECTION 3.2.3.2) External reproducibility between ICP-OES and ICP-MS was about 1%RSD for elements in common (*e.g.* Sr), determined by replicate samples. The precisions and accuracies reported in TABLE 3.5 are a mean of the values obtained for each dataset (APPENDIX A.10). I noticed that for elements measured both on ICP-MS and ICP-OES, the element accuracy was better on the ICP-OES while precision was better on ICP-MS. In those cases, I have decided to choose the instrument with the best precision to the detriment of a lower accuracy (for example, Ba in APPENDIX A.10).

TABLE 3.5 Average of accuracies and precisions of the pore waters geochemical elements as from the APPENDIX A.10. The used CRM for calculating the accuracy is reported. [a] ICP-OES; [b] ICP-MS. NA = the CRM concentration is not available. Sp = spiked SLEW.

Elements	Precision (%RSD)	Accuracy (%RE)	CRM
B [a]	0.74	2.91	CRM-SW
Ba [b]	0.96	5.30	CRM-SW
Ca [a]	1.28	5.70	CRM-SW
Co [b]	2.93	10.16	Sp. SLEW
Cu [b]	2.36	6.11	Sp. SLEW
Fe [b]	2.57	4.97	CRM-SW
K [a]	0.69	4.00	CRM-SW
Li [b]	1.21	4.53	CRM-SW
Mg [a]	0.51	6.35	CRM-SW
Mn [b]	1.65	2.71	Sp. SLEW
Mo [b]	2.61	10.29	Sp. SLEW
Na [a]	1.02	2.33	CRM-SW
Rb [b]	1.00	3.13	CRM-SW
Si [a]	2.05	2.81	CRM-SW
Sr [a]	0.59	1.62	CRM-SW
U [b]	1.39	9.49	Sp. SLEW
V [b]	2.67	NA	
Zn [b]	2.69	14.33	Sp. SLEW

3.3.2 Dissolved hydrogen sulphide

The total dissolved hydrogen sulphide (H_2S + HS^- + S^{2-}) concentration was determined by photospectrometry at absorbance of 670 nm following the Fonselius' method described in Cline (1969) in the pore waters of cores 38GC, 39GC, 49GC. The standards were titrated against 0.0125 M sodium thiosulphate solution. Concentrations were below the detection limit in all measured samples, *i.e.* <2 µM.

3.3.3 Anions

Chloride and sulphate were analysed by ion exchange chromatography using a Dionex ICS2500 with 9 mM Na_2CO_3 as eluent on 100-fold diluted samples. The reproducibility of the results was determined by replicates of certified reference material of International Association for the Physical Sciences of the Oceans (IAPSO) seawater standard. Precision was better than 1%RSD and accuracy was better than 3.5%RE.

3.3.4 Nutrients

NO_X (NO_2+NO_3) and NH_4 concentrations were measured with a AA3 Seal Analytics Autoanalyzer after a 13-fold dilution following the method described in Grasshoff *et al*. (1983). The accuracy and precision of NO_X calculated from the seawater nutrients CRM Lot.CA (/www.kanso.co.jp/) was 8%.

3.3.5 Total alkalinity

Total alkalinity (TA) was determined by titration against 0.01M HCl using a mixture of methyl red and methylene blue as an indicator. Analyses were calibrated against the IAPSO seawater standards. Precision and accuracy were better than 8%RSD and 1.7%RE, respectively.

Chapter 4 Synchronised post-glacial suppression of hydrothermal activity across the TAG hydrothermal field, Mid-Atlantic Ridge

As described earlier in this thesis, the main findings of my research are presented in separate chapters that are in the format of stand-alone scientific papers. As a result, there is a minor amount of repletion of the scene setting and methodology chapters. This is an inevitable consequence in the format of the paper/chapters. However, the advantage is that they are virtually ready for submission to the journals as my first-authored publications. For this paper/chapter, the intention is to submit it as a scientific paper to the journal *Geology*. Co-authors will include Anna Lichtschlag (NERC-NOCS, discussion), Steve Moreton (SUERC, radiocarbon dating), Chuang Xuan (University of Southampton, paleomagnetism) and Bramley Murton (NERC-NOC, discussion).

4.1 Abstract

Hydrothermal activity at mid-oceanic ridges plays an essential role in the composition of seawater, cooling of the interior of the Earth and the formation of mineral deposits. A key component missing in the understanding geological processes controlling the hydrothermal circulation are is the variability of the hydrothermal fluxes over geological time. Recent evidence points to changes influenced by external forcing such as climatic forces driving sea-level changes arising from cycles of global glaciation. Here, we show that high-temperature activity from a number of individual sites across the TAG hydrothermal field on the Mid-Atlantic Ridge was synchronously suppressed at the same time as sea-level rose during the last glacial termination. The evidence for this is provided by radiocarbon, paleomagnetic and oxygen isotope dating of hydrothermally-influenced sediments, recovered from the top of inactive hydrothermal mounds and in surrounding depositional basins. In addition to synchronous cessation, at least three vent sites (the active TAG mound, Mir zone and Shinkai mound) show signs of synchronous hydrothermal rejuvenation during the approach to the current sea-level high-stand, between 4 to 8 ka. We find that hydrothermal activity was not fully inhibited during high sea-level periods, and

that hydrothermal activity remained episodic leading to a multistage formation of hydrothermal mounds. The synchronous suppression of hydrothermal activity at the sites across the TAG hydrothermal field supports a hypothesis in which a unique heat source simultaneously feeds several venting sites and that this, and/or the hydrothermal pathways, are influenced by sea-level changes. Records of hydrothermal activity from other locations around the globe are examined to assess whether a synchronous suppression is a coincidence and characteristic only of the TAG hydrothermal system, or whether it is representative of all deep-ocean hydrothermal systems worldwide.

4.2 Introduction

Hydrothermal activity at mid-oceanic ridges (MORs) plays an essential role in the global biogeochemical cycles, supplying metals and other substances to the ocean (Resing *et al*., 2015) and creating hotspots of biodiversity by providing chemical energy for chemosynthetic communities (Jørgensen and Boetius, 2007). It is an equally important contributor for the energy flux from the deep oceanic crust and the formation of large mineral deposits. Calculating the energy flux of the heat sources that power hydrothermal circulation, and its chemical exchange, are critical for understanding the complexity of the driving processes (magmatism and tectonism). Despite numerous studies (*e.g.* Lowell *et al*., 2013; Germanovich *et al*., 2015), a key component missing from the equation is the temporal variability. Knowing the duration of the hydrothermal activity at an individual system is essential to calculate the energy of the underlying source over geological time-scales. Dating primary high-temperature sulphide deposits (*e.g.* Lalou et al., 1990; Jamieson et al., 2013; Cherkashov et al., 2017) brings the first hint of an answer on the active timespan of different hydrothermal fields, however, dating individual samples collected on the seafloor does not provide a continuous record of the hydrothermal activity. Actually, a hiatus between ages obtained from sulphide dating could be induced by a period of hydrothermal inactivity, but could also result from a bias of selected samples. In contrast, a continuous record of the temporal development of vent fields can be found in the proximal and distal pelagic sediments that contain distinct, metal-rich layers reflecting episodes of hydrothermal activity, especially where those sediments provide uninterrupted age records and the oceanic currents transporting the hydrothermal plumes do not change directions. Numerous dating methods can be applied to the sediments, such as radiocarbon dating of the pelagic component (*e.g.* Metz *et al*., 1988; Lalou *et al*., 1990), ^{234}U ingrowth and

^{210}Pb decay (*e.g.* Lalou *et al.*, 1990; Lalou *et al.*, 1993), $^{230}Th_{excess}$ method on the hydrothermal component (*e.g.* Frank *et al.*, 1994; Kuznetsov *et al.*, 2002) and stable oxygen isotopes to reconstruct glacial and interglacial cycles.

In addition to aiding understanding of the variability of heat and mass fluxes over time, these dating methods allow the investigation of the factors causing the change in hydrothermal activity. For example, it has been recently suggested that an increase in hydrothermal activity might be related to glacial-interglacial cycles (Lund *et al.*, 2016; Middleton *et al.*, 2016; Costa *et al.*, 2017). According to this concept, melt production at MORs, driving hydrothermal activity, is related to glacial-interglacial changes with falling sea level during glacial maxima leading to increased rates of decompression melting of the upper mantle (FIGURE 4.1) (Lund and Asimow, 2011; Lund *et al.*, 2018). As a result, melt supply and hydrothermal activity is enhanced during the onset of glacial periods and falling sea level, whereas abrupt rises of sea level during glacial terminations increase pressure on the upper mantle and inhibit melt production and hydrothermal activity.

In this study, ages of sediments from the well-studied TAG hydrothermal field (TAGHF, Mid-Atlantic Ridge, 26°N) were determined by radiocarbon dating, palaeomagnetism and oxygen isotopes. The dating results are coupled with the analyses of sediment lithology and

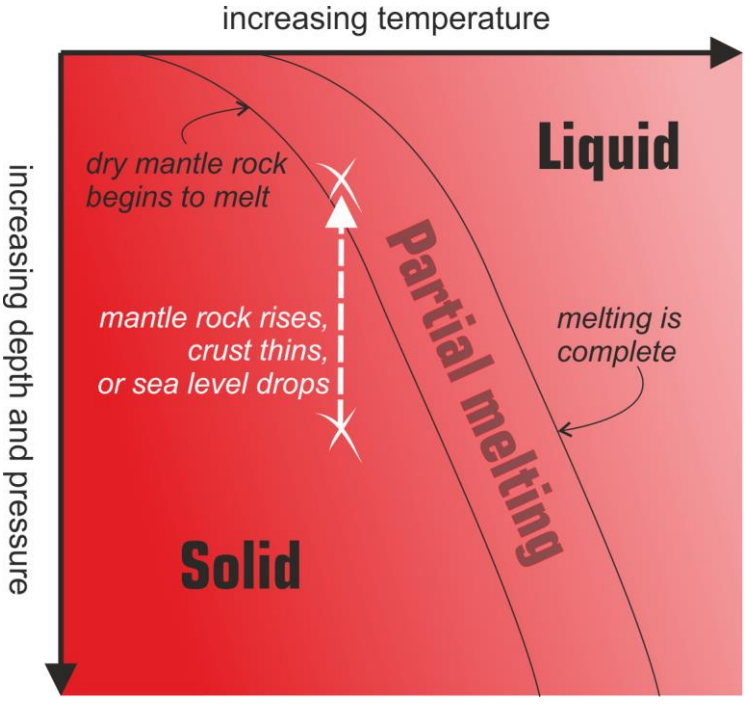

Figure 4.1 Schematic representation of a decompression melting in the mantle rock. When pressure drops (white arrow), the rock will undergo partial melting. If the pressure keeps decreasing, the rock will completely transform into magma.

geochemical composition to: i) determine the history of the hydrothermal activity over the last 180 ka, ii) understand the relative timing of hydrothermal activity across the different sites in the TAGHF and, finally, iii) test whether the activity relates to known external events (*e.g.* volcanism or sea-level changes).

4.3 Geological setting

The Trans-Atlantic Geotraverse hydrothermal field (TAGHF) covers an area of at least 10 by 5 km on the eastern wall of the central axial valley and at a depth of 3600 m (Rona, 1980) The field is located on the hanging wall of a west-dipping active detachment fault at 26°N (26°09.4'N, 44°49.0'W) (Humphris *et al.*, 2015) (FIGURE 4.2). It comprises: i) the hydrothermally active high-temperature TAG mound, ii) a zone of low temperature diffuse flow and iii) two major areas of hydrothermally inactive sulphide mounds (Alvin and Mir zones). The Alvin zone is located 4 km NNE of the active TAG mound and contains several 100-300 m in diameter, 30-60 m high, sulphide mounds. These are dome-shaped, with a thin (<2 m) cover of pelagic carbonate (consisting of foraminifera and nanoplankton tests) and metalliferous sediment (Rona *et al.*, 1993a; Rona *et al.*, 1993b). The mounds identified in the Alvin zone include the Shinkai mound, Southern mound, Double mound, Rona mound (Rona *et al.*, 1993a; Rona *et al.*, 1993b; White *et al.*, 1998; Tivey and Humphris, 2000; Humphris *et al.*, 2015; Petersen and Scientific Party, 2016). The second inactive area, Mir zone, is located 2 km ENE of the active TAG mound. It consists of small, standing and fallen chimneys, highly weathered sulphide material, red metalliferous sediments, and low-temperature hydrothermal precipitates such as Fe-Mn oxide crusts (Rona *et al.*, 1993a; White *et al.*, 1998). Further north of the Alvin zone is an area of active low-temperature

(22.5°C) diffuse hydrothermal flow called Shimmering mound (Fujioka *et al.*, 1999), which was a former high-temperature active mound.

The earliest hydrothermal activity at the TAGHF is represented by Mn oxide crusts recovered from the surface of the Mir zone, that have a minimum age of 140 ka (Lalou *et al.*,

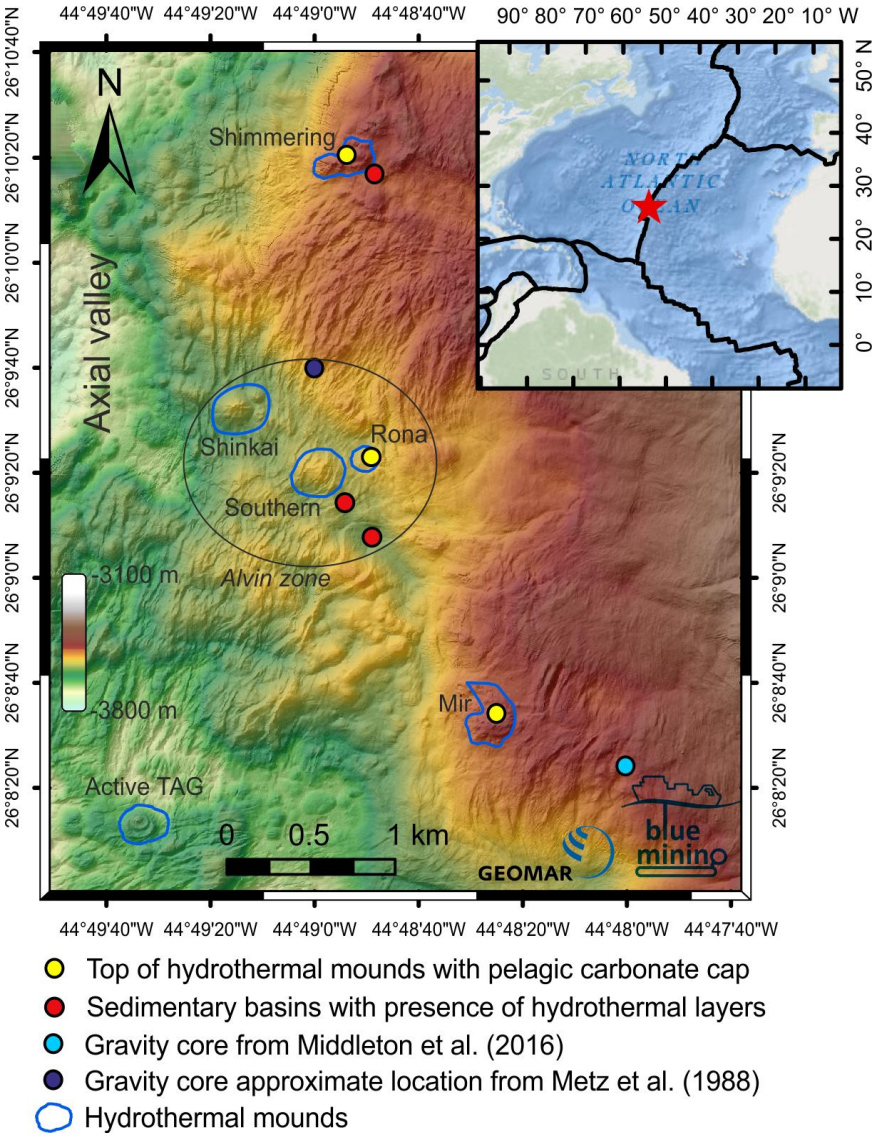

FIGURE 4.2 Shaded bathymetry map of the TAGHF, located on the western ridge flank of the Mid-Atlantic Ridge (insert). Main hydrothermal sites are labelled: the active mound, the Alvin zone, the Mir zone and the Shimmering mound. Coring locations of the sediments are shown by yellow dots (on top of hydrothermal inactive vents) and red dots (in basins with hydrothermal deposits such as debris-flow and hydrothermal plume fall-out). The light blue dot indicates a gravity core close to the Mir zone detailed in Middleton *et al.* (2016), while the purple dot indicates an approximate location for a gravity core detailed in Metz *et al.* (1988). High-resolution bathymetry was acquired by AUV Abyss during M127 cruise (modified from data provided by GEOMAR).

1995). High-temperature hydrothermal activity and sulphide formation began about 100 ka, also in the Mir zone, and 40-50 ka in the Alvin zone and the active TAG mound (Lalou *et al*., 1995). Sub-bottom sulphides recovered from ODP Leg 158 at the active TAG mound suggest hydrothermal activity has occurred since 20 ka with sporadic pulses every 5 ka (Lalou *et al*., 1998b). The latest activity was reactivated about 70 years ago. Previous ages were obtained from discrete individual samples collected on the seafloor, hence none of the previous studies provide a continuous record of the hydrothermal activity within the field. In contrast, pelagic sediments from across the TAGHF provide a continuous record of the hydrothermal activity. Radiocarbon dating of these indicates a later hydrothermal episode and deposition of hydrothermal products between 4 and 8.5 ka (Metz *et al*., 1988[1]; Cherkashov, 1995). FIGURE 4.7 and APPENDIX B.10 report all previously dates as well as our new data.

4.4 Methods

Two lithostratigraphic features in the sediments were investigated. First, found in the sediments on the top of extinct hydrothermal mounds, is the lithological boundary between hydrothermal products and overlying biogenic carbonate pelagic sediments that records the cessation of hydrothermal activity. The second feature is found in sediments deposited in small basins adjacent to extinct hydrothermal mounds and that incorporates hydrothermal particles originating from hydrothermal plumes as well as biogenic carbonate material. The resulting metalliferous horizons record the time-span of the hydrothermal activity. The setting of this study, *i.e.* within the field rather than at few kilometres-distant from the field, prevents the influence of changes in plume direction caused by secular variation in bottom currents. This plume trajectory is a strong parameter in other spatial studies where sediment cores have been recovered at several tens to hundreds of kilometres away from the ridge axis (*e.g.* Costa *et al*., 2017).

[1] Metz *et al*. (1988) report a gravity core taken at the coordinates 26°09.4'N and 44°49.0'W, however the authors describes the location as follows: "The core site was located in a sediment pond at a junction between the east wall of the MAR and the rift valley floor, -0.5-l km NNW of a mound of inactive chimneys (as known as Southern mound; not in the text). One field of known active black smokers was situated about 2 km SSW of the core site". Locating this coring station on the high-resolution bathymetry map (FIGURE 4.1) highlights the lack of precision and therefore only an approximate location is indicated.

4.4.1 Sampling

Six sediment cores were collected with a gravity corer during the RRS *James Cook* expedition JC138 in 2016 (TABLE 4.1) from the top of the Rona mound (27GC) in the Alvin zone, the top of Mir zone (28GC) and Shimmering zone (29GC) and from two depositional basins: i) a channel located to the south of the Alvin zone (38GC, 49GC) and another channel on the east edge of the Shimmering zone (52GC). Details of the collection and preservation procedure can be found in Dutrieux *et al*. (*subm*., this thesis, CHAPTER 6). Photographs of the sediment cores are provided in the APPENDIX B.1.

TABLE 4.1 Gravity coring sites with geographic position and water depth.

Core reference	Location	Core depth (cm)	Water depth (m)	Coordinates
Top of hydrothermal mounds				
27GC	Rona mound	41	3524	26°09.375′N 44°48.820′W
28GC	Mir mound	194	3400	26°08.558′N 44°48.416′W
29GC	Shimmering mound	132	3430	26°10.339′N 44°48.888′W
Depositional basins				
49GC	200 m SE of Southern mound	230	3490	26°09.237′N 44°48.902′W
38GC	500 m SE of Southern mound	98	3608	26°09.126′N 44°48.814′W
52GC	250 m SE of Shimmering mound	190	3450	26°10.283′N 44°48.806′W

4.4.2 Chemostratigraphy

The chemostratigraphy of the sediment cores was analysed at a 1 mm vertical resolution with an ITRAX™ (Cox Analytical Systems) core-scanning X-ray fluorescence system (Croudace *et al*., 2006) at the British Ocean Sediment Core Research Facility (BOSCORF) in Southampton, UK. The instrument was operated at a voltage of 30 kV, a current of 30 mA, a count time of 30 s with a 3 kW Mo X-ray tube. Fe and Ca abundances were normalized to kilo-counts per second (kcps) and a running average of 5 mm was applied to the results. ITRAX data were subsequently calibrated against whole rock geochemistry data for Fe and Ca (APPENDIX B.2) in order to give quantitative results. Whole-rock analyses for major elements (Ca, Fe) and rare earth elements were performed with ICP-OES (Thermo Scientific ICAP 6500 Duo) and ICP-MS (ThermoScientific X-Series 2), respectively, and following the method provided in Dutrieux *et al*. (*subm*.; this thesis, CHAPTER 6). Precision (% relative

standard deviation, %RSD) and accuracy (% relative error, %RE) were respectively 0.9%RSD and 2%RE for Ca, and, 2.3%RSD and 1.8%RE for Fe (*Cf.* section 3.2.3 for a detailed methodology). Rare earth element (REE) data were normalised to the REE content of the chondrite C1 (Evensen *et al.*, 1978). Deviations of REE patterns are expressed as anomalies. The Eu anomaly is expressed geometrically as:

$$Eu\ anomaly\ = Eu_n/\sqrt{Sm_n * Gd_n} \qquad \text{(Eq. 4.1)}$$

(where n refers to chondrite-normalised values).

4.4.3 Age model construction

4.4.3.1 Radiocarbon dating

To provide age control on hydrothermal activity, samples were prepared for radiocarbon dating at the NERC Radiocarbon Facility (NCRF), East Kilbride, UK. Sixteen pelagic sediment horizons were selected to bracket hydrothermal layers (*i.e.* period of hydrothermal activity), sieved and washed with deionised water and 8 to 10 mg of clean and intact planktonic foraminiferal tests (*i.e. Globigerinoides, Orbulina, Truncorotalia, Trilobatus sps*) were handpicked. The outer 20 wt% of the shells were etched by controlled hydrolysis with dilute HCl to remove surface contaminants. The samples were then rinsed in deionised water, dried and homogenised. A known weight of the pre-treated sample was hydrolysed to CO_2 using 85% orthophosphoric acid at room temperature. The CO_2 was converted to graphite by Fe/Zn reduction. The graphite targets were passed to the SUERC AMS Laboratory, East Kilbride, UK for ^{14}C analysis. Reference and monitor materials consisted of ^{14}C-free Icelandic spar calcite. The results are reported as conventional radiocarbon years before present (BP; where 0 BP = AD 1950) and % modern ^{14}C, both expressed at the ±1σ level for overall analytical confidence. Where ^{14}C values are distinguishable from NRCF process background, data were background corrected. ^{14}C results are normalised to $\delta^{13}C_{VPDB}$‰ = -25 using the ^{13}C values (APPENDIX B.3). Those $\delta^{13}C$ values were measured on a dual inlet stable isotope mass spectrometer (Thermo Fisher Delta V) and are representative of the pre-treated sample material. Where there was insufficient sample material to obtain a separate $\delta^{13}C$ value as well as a graphite target an estimated $\delta^{13}C$ value was used. One ^{14}C result was close to background and according to the conventions set out in (Stuiver and Polach, 1977), that result is reported as a minimum age that the sample are older than.

Hydrothermal fluids contain carbon in different forms: CO_2, CH_4 (for instance, up 2000 µmol/kg compared to < 5 nmol/kg in seawater), dissolved inorganic molecules (German and Seyfried, 2014) and dissolved organic compounds (Longnecker *et al*., 2018). Due to a short half-life of ^{14}C, hydrothermal fluids are depleted in this isotope. For example, fluids containing dissolved organic carbon at the Juan de Fuca Ridge, are characterized by $\Delta^{14}C$ as low as -830‰ (McCarthy *et al*., 2011). Therefore, to prevent any contribution from hydrothermal-sourced C, radiocarbon analyses were run on planktonic foraminifera originally living in the upper-portion of the water column.

Radiocarbon ages were processed with the latest versions of OxCal and the marine radiocarbon calibration curve (currently OxCal 4.3; Bronk Ramsey, 2009) and the Marine 13 calibration curve (Reimer *et al*., 2013). The ocean mixed layer has a delayed response to changes in atmospheric ^{14}C. This delayed response is referred to as a marine reservoir age and an average open ocean marine reservoir age of 405 years is applied on all conventional radiocarbon ages.

4.4.3.2 Oxygen isotopes

To complement and extend the age-depth model from radiocarbon ages, stable oxygen isotopes ($\delta^{18}O$) were measured on bulk carbonate sediments on a Thermo Scientific Kiel IV Carbonate coupled with a MAT253 isotope ratio mass spectrometer at the SEAPORT laboratories (University of Southampton). 99.9% of the foraminifera population in the TAGHF sediments were planktonic, therefore we expect similar oxygen isotope results between foraminiferal material and bulk carbonate sediment material. Hence, we considered that our oxygen isotope data from bulk sediments is sufficient to obtain an age-depth model without separating out the planktonic foraminifera. Replicate samples from one horizon agree with a precision better than 8%. To construct the age-depth model, we compared the obtained results to the LR04 stack of marine oxygen isotope stages, which is well-dated (Lisiecki and Raymo, 2005), using the AnalySeries software (Paillard *et al*., 1996). The uncertainty of the correlation is estimated to be < 5 ka, and we were able to identify all glacial and interglacial periods (marine isotope stages, MIS) in the longest record.

4.4.3.3 Relative paleomagnetic intensity

The core, 52GC, from the sedimentary basin in Shimmering zone, close to Shimmering mound, is the only core with sediments older than 50 ka and, therefore, could not be constrained by combining the $\delta^{18}O$ dating with radiocarbon dating. Instead, to constrain

the age of the lower section of the core, variation in relative paleomagnetic intensity (RPI) were measured to identify the Laschamp and Blake event, a well-known geomagnetic excursion at ~115-120 ka BP (Laj and Channell, 2007). For this, the core was subsampled continuously using plastic u-channels of ~1.8 x 1.9 cm^2 cross-section. The natural remanent magnetization (NRM) and the anhysteretic remanent magnetization (ARM) were measured on a 2G Enterprises Superconducting Rock Magnetometer in a shielded room at the University of Southampton. Stepwise in-line alternating-field demagnetization was used with an average of 10 steps. To restore the high-resolution paleomagnetic signal, deconvolution optimization was applied with the UDECON software (Xuan and Oda, 2015). Finally, a deconvolved relative paleomagnetic intensity curve was compared to the literature stacks PISO-1500 (Channell *et al*., 2009), HINAPIS (Xuan *et al*., 2016) and SINT-2000 (Valet *et al*., 2005) (APPENDIX B.5).

4.5 Results

4.5.1 Stratigraphy integrity

The hydrothermal contribution to the sediments is identified by using the Fe and Ca content, the Eu anomaly (FIGURE 4.3) and visual stratigraphic observations (APPENDIX B.1). High concentration of Fe is released from high-temperature hydrothermal-venting chimneys (Resing *et al*., 2015), hence the Fe content is enriched in the hydrothermal-influenced sediments. Hydrothermal material also has a strong positive Eu anomaly, inherited from hydrothermal vent fluids (German *et al*., 1990) and hence Eu anomaly is positively correlated with the Fe content (APPENDIX B.6). The visual stratigraphic observations consist of colour variation, grain size, and presence/absence of layering. With the help of these four variables, we distinguished between four types of lithological units, referred to as i) *pelagic*, ii) *plume-fall out*, iii) *collapsed* and iv) *debris-flow* sediment classes (FIGURE 4.3, *cf.* also APPENDICES B.1 and B.2).

(i) *Pelagic* sediments are beige and are dominated by calcium carbonate (> 20 wt% Ca) and minor amounts of Fe (<10 wt%); this class is expected to have low hydrothermal influence and is found in all cores, either covering inactive hydrothermal mounds or in layers alternating with the following unit type (ii). (ii) *Plume fall-out* sediments have a Fe content between 10 and 30 wt%, and inversely proportional to Ca content ranging from 5 to 25 wt%, suggesting that hydrothermal *plume* particles are settling within a background of pelagic

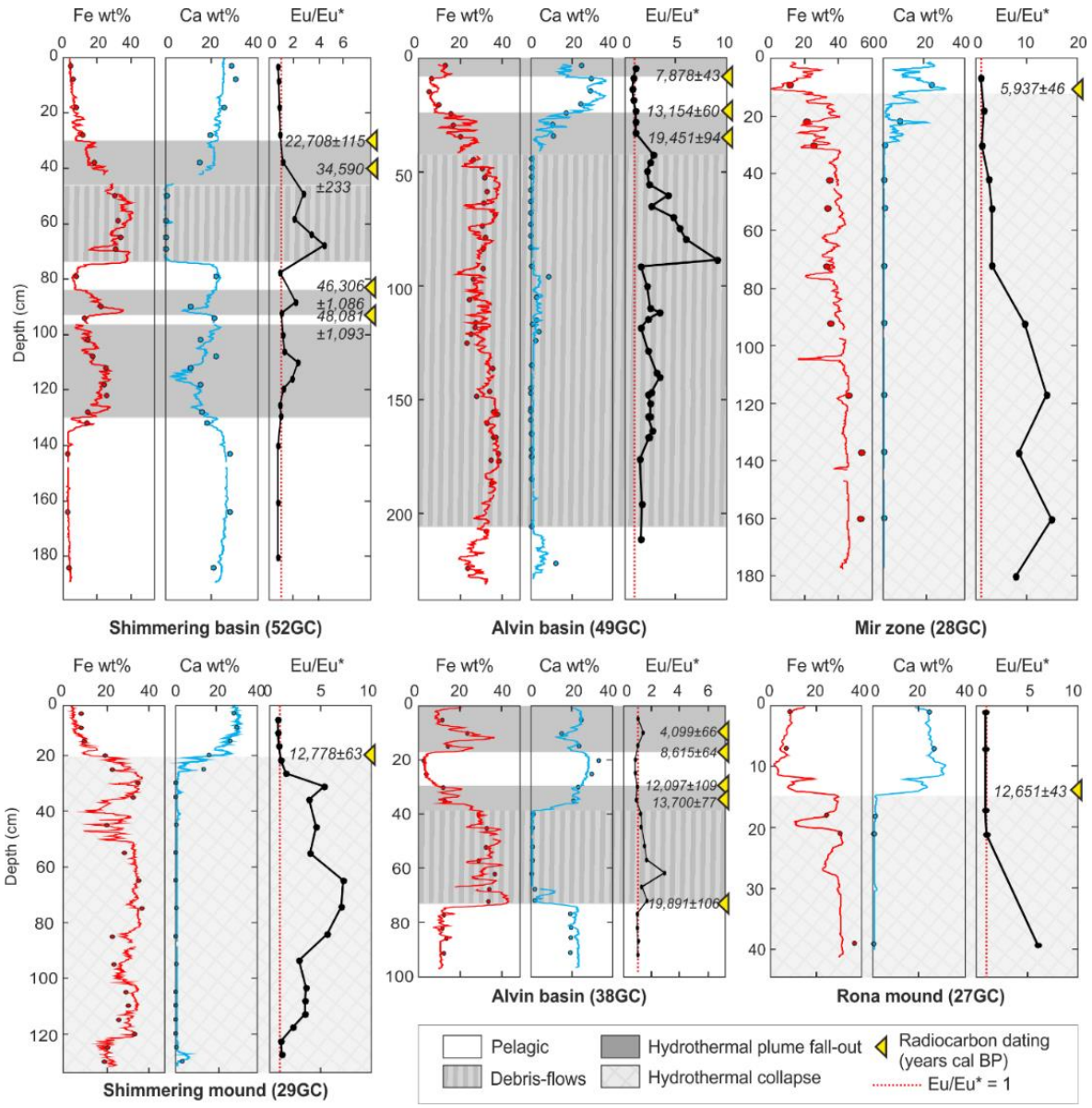

FIGURE 4.3 Down-core profiles of Fe, Ca and Eu/Eu* in different locations at the TAGHF. Data for Fe and Ca are ITRAX chemostratigraphy (solid lines) calibrated by ICP-OES bulk geochemistry (circles) (*cf.* APPENDIX B.2). In the Eu/Eu* profiles, the red dashed line represents a ratio of 1 and the scale is adapted in the different profiles to better represent the value variation. Values above 1 are positive anomalies and indicate a hydrothermal influence of the sediments. Radiocarbon dating horizons are shown as yellow triangles. Pelagic-dominated depths are white and hydrothermal layers are grey with differentiation between hydrothermal plume fall-out layers (plain grey), hydrothermal debris-flow deposits (striped grey) and collapsed hydrothermal material (cross-hatched grey).

sedimentation. The REE distribution of pelagic sediments is overprinted by a hydrothermal REE signature resulting in a low positive Eu anomaly (*e.g.* <2). Sediments are reddish and

grain sizes range from fine silt to mud. This class is present in depositional basins, such as the Shimmering basin (52GC) and in the Alvin basin (38GC and 49GC). (iii) "*Collapsed*" sediments entirely consist of bright red Fe-oxyhydroxide minerals, with a very poorly-sorted grain-size distribution and are exclusively derived from hydrothermal mound material and accumulated by disintegration, collapse and weathering of hydrothermal edifices. These sediments have a strong negative Eu anomaly, Ca is absent or low, and often black Mn oxides are present. We find this class on the surface of the inactive hydrothermal mounds: Mir zone (28GC), Rona mound (27GC), and Shimmering mound (29GC). (iv) *Debris-flow* sediments are rich in Fe (> 20 wt%), depleted in Ca (often absent), presenting layering and have a strong negative Eu anomaly (indicative of a hydrothermal source such as weathered sulphides. The layers show a rapid vertical geochemical and mineralogical variation (admixture of sulphides and oxides) and often a fining upward grain-size distribution. These deposits are present at several hundreds of meters away from the mounds and in basins such as the Shimmering basin (52GC) and Alvin basin (38GC and 49GC).

The lower part (>160 cm) of 52GC, at the Shimmering basin, contains basaltic fragments (APPENDIX B.7) and shows an increase in Si, K, Ti, Ni and Zr and a decrease in Ca content with depth (APPENDIX B.8), indicative of close proximity of the bottom of the core to the volcanic basement.

4.5.2 Temporal reconstruction of hydrothermal activity

The radiocarbon dating shows no time-reversal (*i.e.* younger ages at deeper depths) within single cores, and fits with glacial-interglacial $\delta^{18}O$ reconstructions, where available, and therefore allow us to treat the plume fall-out sediments as reliable records of hydrothermal activity. All radiocarbon dates are provided in a table in the APPENDIX B.3. At the most northern hydrothermal zone, the Shimmering zone, chronology was done on the longest sedimentary record (52GC, FIGURE 4.4) collected from a sedimentary basin located 100 m south of the hydrothermal mound (FIGURE 4.2). The age-depth model (FIGURE 4.4 and APPENDIX B.9) shows that increased Fe input, indicative of increased hydrothermal activity, spans from 72 ka (130 cm) to 22.7 ka (30 cm) with input variation over time. The model indicates that two periods of reduced hydrothermal activity occurred in the MIS 3 between 39-46 ka and 48-56 ka. The appearance of unsorted, hydrothermally-derived material

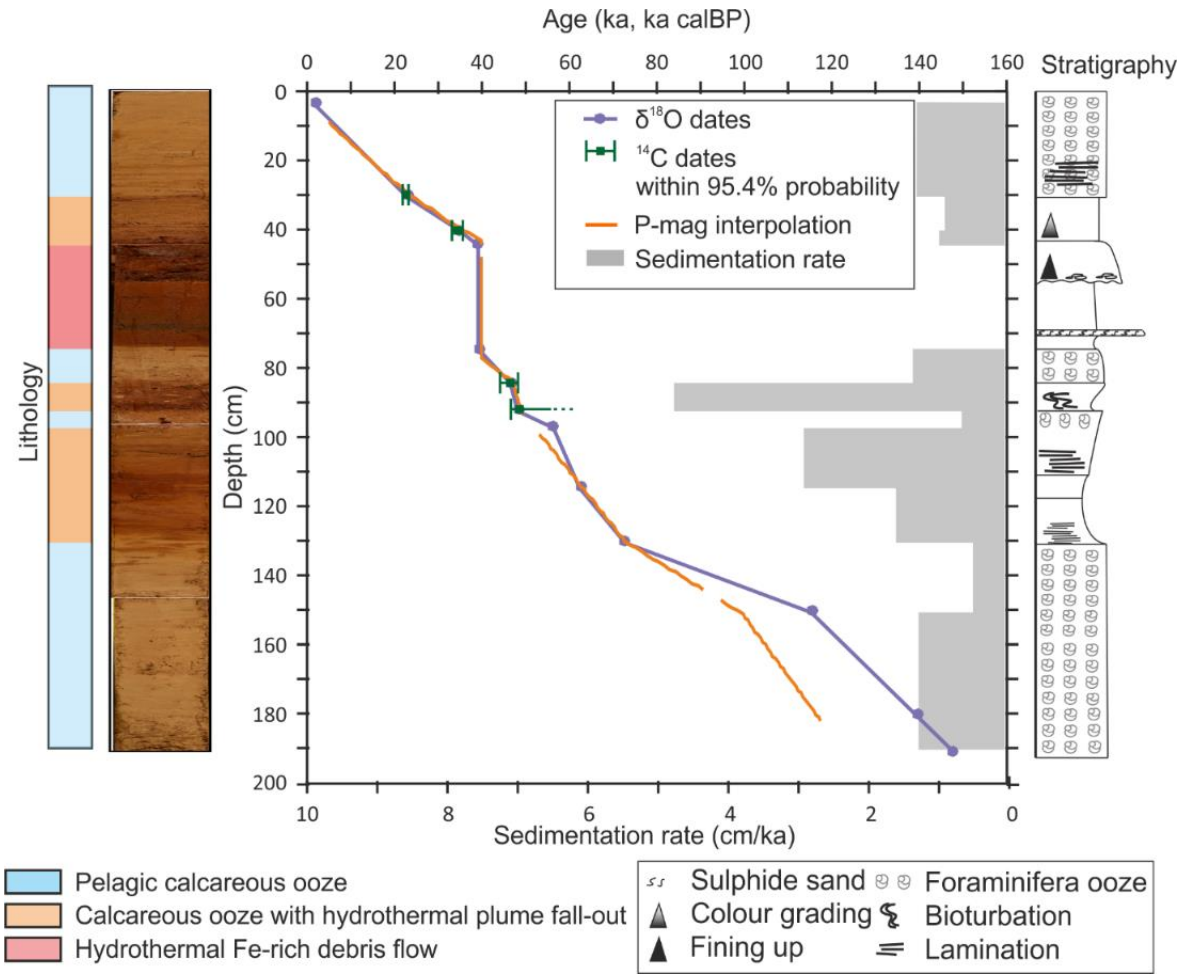

FIGURE 4.4 Age-depth model for 52GC (Shimmering basin) together with the lithology, core photography and stratigraphy. The three constrains are δ18O dating, radiocarbon dating and mean RPI interpolation. The sedimentation rate is presented as a function of depth. Tie-point data and sedimentation rates are provided in APPENDIX B.9.

indicates a debris-flow event at around 39 ka. Additional absolute dating of the Shimmering zone is provided by radiocarbon dating of sediments from the top of Shimmering inactive hydrothermal mound (29GC, FIGURE 4.2), that are directly overlying hydrothermal sediments (20 cm, FIGURE 4.3). Results from here confirm that hydrothermal activity ceased around 12.8 ka cal BP (FIGURE 4.5A).

At the Alvin zone, radiocarbon dating on the top of Rona mound (28GC) confirms that its hydrothermal activity ceased around 12.6-12.7 ka cal BP (FIGURE 4.5B). This age is in accordance with ages recorded in the Alvin basin, *i.e.* 12.1 ka cal BP at 29 cm from core 38GC, and 13.1 ka cal BP at 21 cm from 49GC (FIGURE 4.3). Therefore, the main hydrothermal activity spans the duration of MIS2 (FIGURE 4.5B). During the hydrothermal activity period, successive debris-flow events in the sedimentary basin at 39-75 cm-depth from 38GC, occurred between 13.7 and 19.9 ka. Another debris-flow occurred in the same

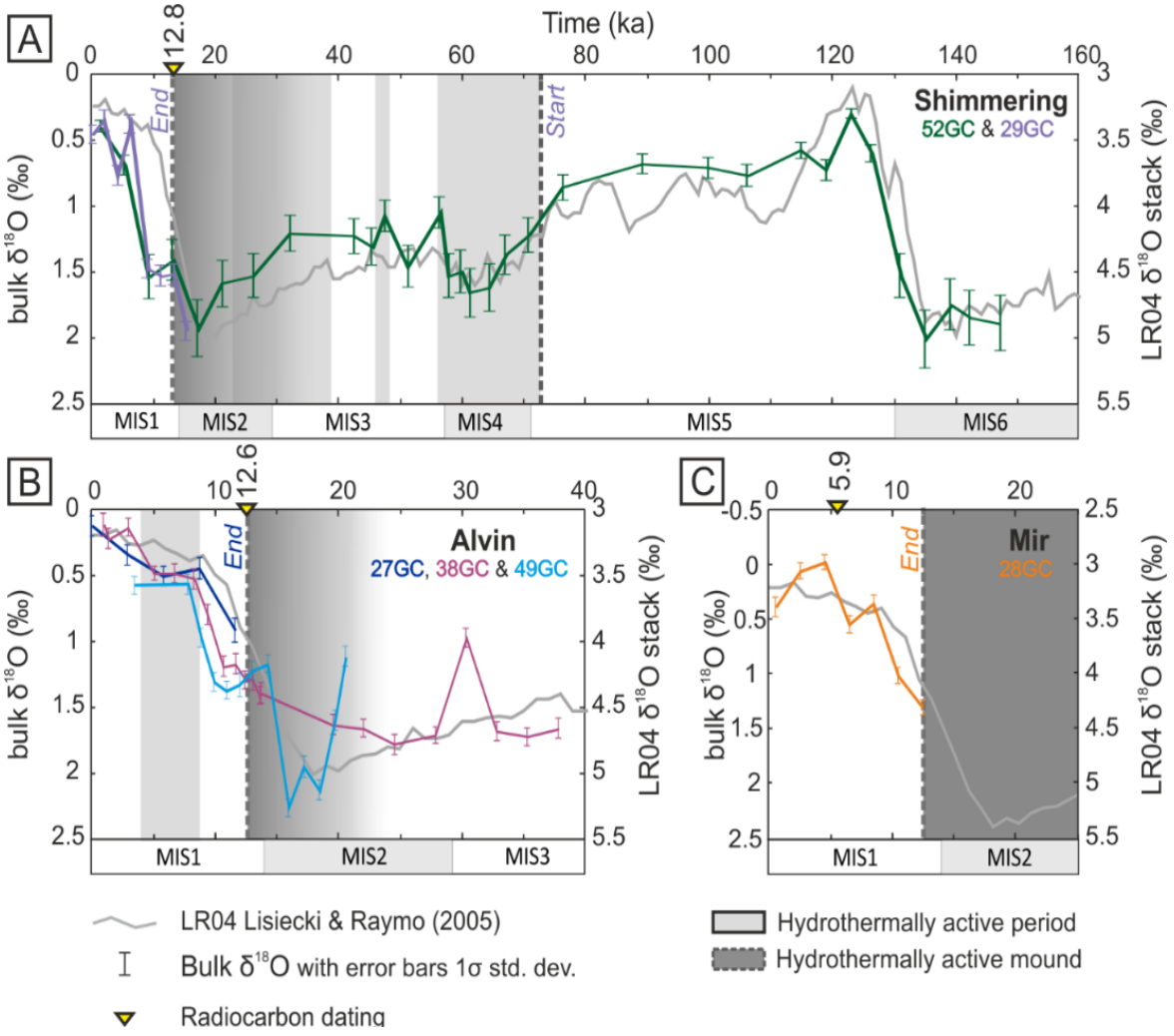

FIGURE 4.5 Bulk carbonate $\delta^{18}O$ as a function of age for (A) Shimmering zone (green and purple lines), (B) Alvin zone (blue and magenta lines) and (C) Mir zone (orange line), compared to the global benthic $\delta^{18}O$ LR04 stack of Lisiecki and Raymo (2005) (grey line). We estimate age confidence better than 5 ka for Shimmering zone, and confidence decreases for Alvin and Mir due to the lack of tie-points. Periods of hydrothermal activity are shown in grey boxes.

environment (49GC, 40 cm) and is older than 19.5 ka. Radiocarbon dating from this depositional basin (cores 38GC and 49GC) indicates an additional increase of activity between 4 ka calBP and 8.6 ka cal BP. This later episode of activity is recorded between 10 to 18.5 cm in core 38GC and in the first 6 cm in core 49GC. It is very likely that the uppermost part of core 49GC was lost during its recovery due to over-penetration of the gravity corer, hence explaining why the upper part of the core 49GC is relatively older, and chemically different from the upper part of core 38GC.

At Mir zone, the single radiocarbon date from the upper interface between the hydrothermal horizon and the pelagic one indicates that hydrothermal activity had ceased

before 5.9 ka cal BP. Assuming a constant sedimentation rate over the first 20 cm of pelagic sediments, the oxygen isotope data dates the cessation of the hydrothermal activity in the Mir zone at 12.5 ka (FIGURE 4.5C).

4.6 Discussion

Before interpreting the processes driving hydrothermal activity at the TAGHF, we first address the reliability of the lithology and the sediment geochemistry as proxies for contribution of hydrothermal output from the surrounding hydrothermal venting. We then discuss in detail the synchrony of the hydrothermal activity across the field and discuss which and how external factors control the hydrothermal flux. Next, we discuss the magmatic and tectonic controls at the TAGHF, and finally, we discuss the implications of those results for MOR systems in general.

4.6.1 Primary hydrothermal input *versus* post-depositional remobilisation

The lithological and geochemical variations in the sediments can be considered as a record of the contribution of hydrothermal output from the surrounding hydrothermal vents. However, after deposition and burial of hydrothermal and pelagic components, diagenetic remobilisation could alter the character of the primary hydrothermal signals (Mills *et al.*, 2010; Costa *et al.*, 2017). Our previous studies of the sediments from the TAG area have identified diagenetic processes, such as ongoing weathering of sulphides, development of oxic and suboxic zones, and mobilisation and re-precipitation of Mn, Cu and Co (Dutrieux *et al.*, *subm.*; this thesis, CHAPTER 6). However, in our sediments these processes are found to be negligible compared to the original hydrothermal Fe signal due to the close proximity to the vents providing extremely high input (up to 40%) of hydrothermal Fe to the sediments. As a result, we can use Fe/Ca ratios as reliable proxy for periods of hydrothermal activity.

4.6.2 Synchrony of the hydrothermal activity

The chronology provided in this study suggests a relationship between glacial cycles (and therefore sea level changes) and hydrothermal activity (FIGURE 4.6). We present new evidences consistent with the hypothesis that the TAG hydrothermal activity responds to

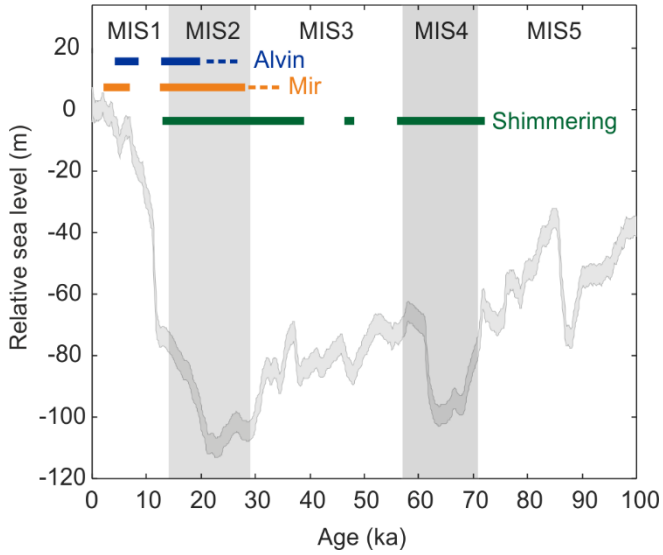

FIGURE 4.6 Timeline of the three investigated mounds plotted with the relative sea level curve. The sea level curve is from Grant *et al*. (2014) (upper and lower bound of the 95% probability interval for the probability maximum). The shaded areas highlight the glacial periods and the dashed lines express the uncertainties on the active period length and start of the hydrothermal activity at Alvin and Mir zones. Data include this paper and sedimentary records from Metz *et al*. (1988) and Middleton *et al*. (2016).

rates of sea level change, and that the global hydrothermal flux may have been significantly higher during the onset of glaciation periods than observed today.

In all of the studied hydrothermally inactive mounds (Rona mound, Mir mound and Shimmering mound), our dating shows a hiatus in hydrothermal input marked by a return to pelagic-dominant biogenic carbonate sedimentation at 12.6, 12.8 and 12.5 ka, respectively. Because the samples used to determine those ages are from directly above sulphide deposits, this hiatus most likely represent a marked decrease or cessation of hydrothermal activity. These dates are synchronous between the three inactive mounds across the mounds and align with dates published by Middleton *et al*. (2016) for the Mir zone (FIGURE 4.7). Sulphide dating by Lalou *et al*. (1995) indicates that the TAG active mound was active, starting from around 50 to 40 ka until 14 to 16 ka at least on the lower terrace *(i.e.* 'the first mound'). Later on, the initiation of the currently active complex is dated at around 11 ka, which strengthens the hypothesis of synchrony (Lalou *et al*., 1995). This onset of suppression of hydrothermal activity coincides with the period known as the Younger Dryas (11.7 to 12.9 ka) and glacial termination I, which is the period of maximum rate of sea-level change (rise) from fully glacial (low sea level stand) to interglacial (high sea level), as indicated by the highest $\delta^{18}O$ values (FIGURE 4.5). This synchrony strongly

suggests that the different mounds are fed by a single heat supply and hydrothermal source. This is understandable in a slow-spreading ridge environment where magma chambers reside deep at the base of the crust or upper mantle (Rona *et al.*, 2010) and a single magma chamber (*i.e.* the heat source) provides heat energy for hydrothermal fluids via branching pathways (e.g. such as through long-duration, deeply penetrating axial valley and detachment faults) to feed several distinct mounds over a broad area. In contrast, at fast-spreading ridges such as the East Pacific Rise, heat sources are shallower and faults are smaller making smaller hydrothermal fields and with possibly shorter duration. A single

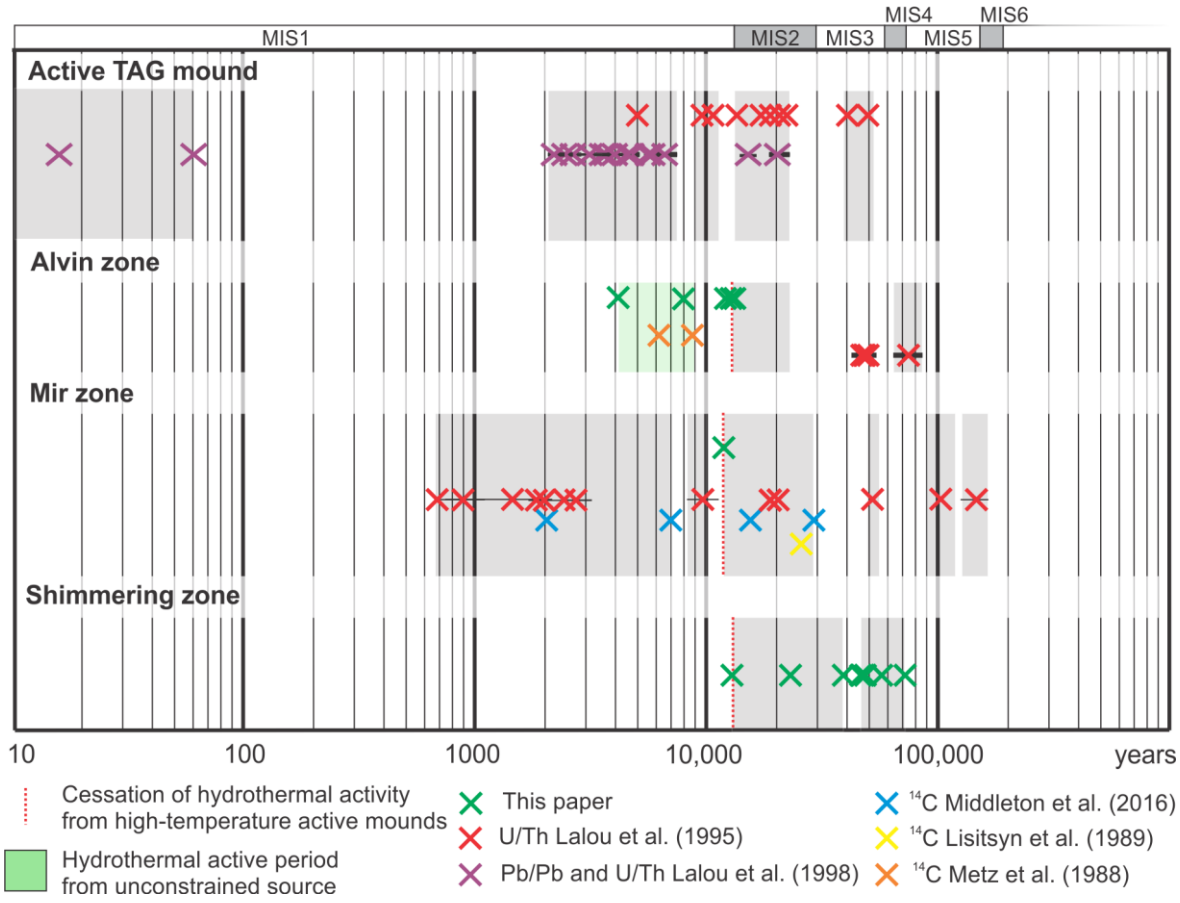

FIGURE 4.7 Geochronological summary of the four hydrothermal zones at the TAGHF compiling published dating on a logarithmic scale from this and previous studies (*cf.* legend and APPENDIX B.10). MISs are indicated on the upper part and shaded areas are the glaciation periods (MIS2, MIS4 and MIS6). Shaded areas in the graph indicate confirmed hydrothermal active periods and dashed red lines indicate the suggested cessation time of the hydrothermal activity. The active mound and Mir zone are the two active zones during the last 10 ka with a re-juvenescence. The hydrothermal active periods younger than 10 ka and recorded at the Alvin zone (green shaded area) are most likely related to the TAG active mound, the Mir zone or Shinkai mound. The error bars are within the cross width if not represented.

heat source driving venting across the TAGHF mounds should produce the same geochemistry, especially magmatic signatures for the hydrothermal fluids. To test this hypothesis further geochemical analyses of fluid inclusions from sulphides at the different eSMS deposits could be investigated, but are beyond the scope of this study.

Our results also show that synchrony is also apparent for much older periods of hydrothermal activity at the TAGHF. The start of high-temperature hydrothermal activity at the Shimmering mound, at 72 ka (FIGURE 4.5A), is synchronous with the oldest manganese crusts (*i.e.* 74 ka) sampled in the Alvin zone (Lalou *et al*., 1995) and could suggest a similar timespan for both zones. This age range coincides with a rapid rate of fall of sea level (Grant *et al*., 2014) during the onset of the MIS4 (57 to 71 ka) glaciation period. During MIS4, hydrothermal activity at Shimmering mound and Alvin zone was continuous. This observation is similar to findings from the Mir zone during MIS2 (14 to 29 ka), which includes the period when a pulse of hydrothermal activity started at 28 ka (Middleton *et al*., 2016). In an active vent field debris-flow events are more likely as instability is induced by the steep topography, the active tectonism (seismicity) and uninterrupted growth of the vents (Shanmugam, 2018). This could explain the debris-flow dated between 13.7 and 19.9 ka, transporting mass-wasted hydrothermal material from surroundings hydrothermal mounds into the Alvin zone sedimentary basin.

The sediments recording the 59 ka-long activity in the Shimmering basin also present a decreased input of hydrothermal particles between 39 and 46 ka, during the MIS3 (29 to 57 ka). This confirms the sporadic character of Shimmering mound activity, similar to the Alvin, Mir and active mounds (Lalou *et al*., 1995). Therefore, although a return to pelagic sedimentation conditions occurred during interglacial intervals (MIS1 and MIS3; FIGURE 4.6), hydrothermal activity did not entirely ceased and was sporadic. The compiled dating available across the TAGHF (FIGURE 4.7) supports the hypothesis that Mir zone and Alvin zone also significantly decreased their hydrothermal activity during the MIS3 (29 to 57 ka) and could indicate that hydrothermal activity was lower during the onset of interglacial periods due sea-level rises inhibiting melt production.

4.6.3 Partial rejuvenation in the last 10,000 years

In the Alvin zone depositional basin (cores 38GC and 49GC; FIGURE 4.2), a younger episode of hydrothermal activity was recorded between 4 and 8 ka. These dates are similar to those published by Metz *et al*. (1988) for the same location, and Middleton *et al*. (2016) in the Mir

zone. We discuss here the processes responsible for this rejuvenation. The onset of this rejuvenation is broadly coincident with the 8.2 ka event, which is marked by continued sea level rise. The rapid sea-level rise is attributed to both meltwater pulses (MWP) (at least the MWP-1C around 7.6-8.2 ka) and the abrupt collapse of Laurentide Ice Sheets linked to an outflow from glacial lakes to the oceans (Blanchon, 2011).

The absence of hydrothermal input and dominance of pelagic sedimentation observed in the sediments from Shimmering mound (29GC) and Rona mound (27GC) in the period 4 to 8 ka indicates that these mounds were not the source of hydrothermal input. Based on the observed Fe content higher in 38GC (23 wt%) compared to 49GC (12 wt%) (FIGURE 4.3), we assume the potential source must be closer to 38GC than 49GC. Their respective core locations (FIGURE 4.2) therefore suggest that the active TAG mound or the Mir zone are the potential source for the hydrothermal contribution in the depositional basin located south of the Alvin zone. Furthermore, it has been shown that the Mir zone and the active TAG mound were reactivated in the last 10 ka (Lalou *et al*. 1995). Unfortunately, this hypothesis does not explain why Metz *et al*. (1988) observed a hydrothermal event between 3.6 and 6.3 ka with >90% of hydrothermal contribution in sediments recovered from 0.5 to 1 km NNW of Southern mound because this core is more distal from the Mir zone or the active mound than 38GC or 49GC in the Alvin basin. We suggest the hydrothermal material to this location was sourced directly from Shinkai mound, located to the west and potentially closer to the Metz *et al*. (1988) coring location than Southern mound. This suggestion concurs with the evidence that Shinkai mound is younger, based on the morphology of the mound with fewer faults, the presence of relatively unaltered inactive chimneys and an the absence of pelagic sediment cover (Murton *et al*., 2019). Due to the close proximity between Shinkai mound and the neighbouring mounds in the Alvin zone, it is not possible to constrain the source of hydrothermal particles recovered in the Alvin zone. The best approach to confirm the younger activity at Shinkai would be to date some sulphides collected directly from Shinkai mound.

4.6.4 Implications for magmatic and tectonic controls on hydrothermal activity

A synchronous cessation of hydrothermal activity, 12.5 ka ago, strongly suggests that a common heat source was feeding several mounds simultaneously. It is only later that hydrothermal activity would occur only at vent sites closer to the axial valley, as suggested

by the rejuvenation at the TAG active mound and, most likely, the Shinkai mound. However, while Shinkai and the TAG active mound share the same proximity to the ridge axis, and therefore possibly the same magmatic source, the Mir zone is the furthest away yet shows evidence of recent and younger activity. MIR zone also shows evidence of the longest time-span of hydrothermal activity across the TAGHF, with the earliest form of hydrothermal precipitation present as of Mn crusts dated at 140 ka (Lalou *et al.*, 1995). We suggest that MIR mound was synchronised with the rest of the field before 12.5 ka, and shared a common heat source on-axis but, once off-axis, the location implies a tectonic control that would provide a structural pathway for hydrothermal fluids to reach the seafloor. The role that active detachment faults exert on the hydrothermal circulation at the TAGHF is strongly established (Humphris *et al.*, 2015), but its influence is still poorly understood. Additionally, the position of the fault termination that could host focused hydrothermal venting remains unknown and most of the hanging wall, including the entire northern half comprising the Shimmering zone, has yet to be characterised geophysically.

Shimmering and Mir mounds are furthest from the axial valley, and it is therefore logical that they are the oldest zones showing earliest signs of high-temperature hydrothermal activity. Similarly, both sites are located at shallower depths (FIGURE 4.8) and could be potentially related to the concept that seafloor bathymetry fabric responded to climate-driven fluctuation (Olive *et al.*, 2015). This concept suggests that sea level changes modulate melt production in the underlying mantle and that abyssal hills (bathymetric highs and lows with a characteristic spacing of 1 to 10 km) recorded fluctuation in the MOR magma supply following the Milankovitch cycles (Olive *et al.*, 2015). However, it was also suggested that the northern part of the TAGHF may be on a young oceanic core complex, which then inhibits this concept of bathymetry fabric (Petersen and Scientific Party, 2016). Furthermore, an increase in lithophile elements at the end of the core from Shimmering basin (*i.e.* 190 cm, in 52GC) is most likely due to weathering of the oceanic crust and suggests the gravity core reached the basaltic basement. The age of the bottom horizon, *i.e.* 145 ka, is within the predicted range of 115 to 150 ka for the seafloor at this location, assuming a simple asymmetric half spreading rate of 1.3 cm/a during the last Ma (McGregor *et al.*, 1977) and a distance of 1.5 to 2 km away from the zone of volcanic accretion at the plate boundary. The same calculation predict of minimum 300 ka for the crustal age beneath the Mir zone. In conclusion, from the calculations and the shallower depths of the two inactive zones, both range of ages coincide with a glacial period (145 ka in MIS6 for Shimmering zone and 300 ka in MIS8 for Mir zone).

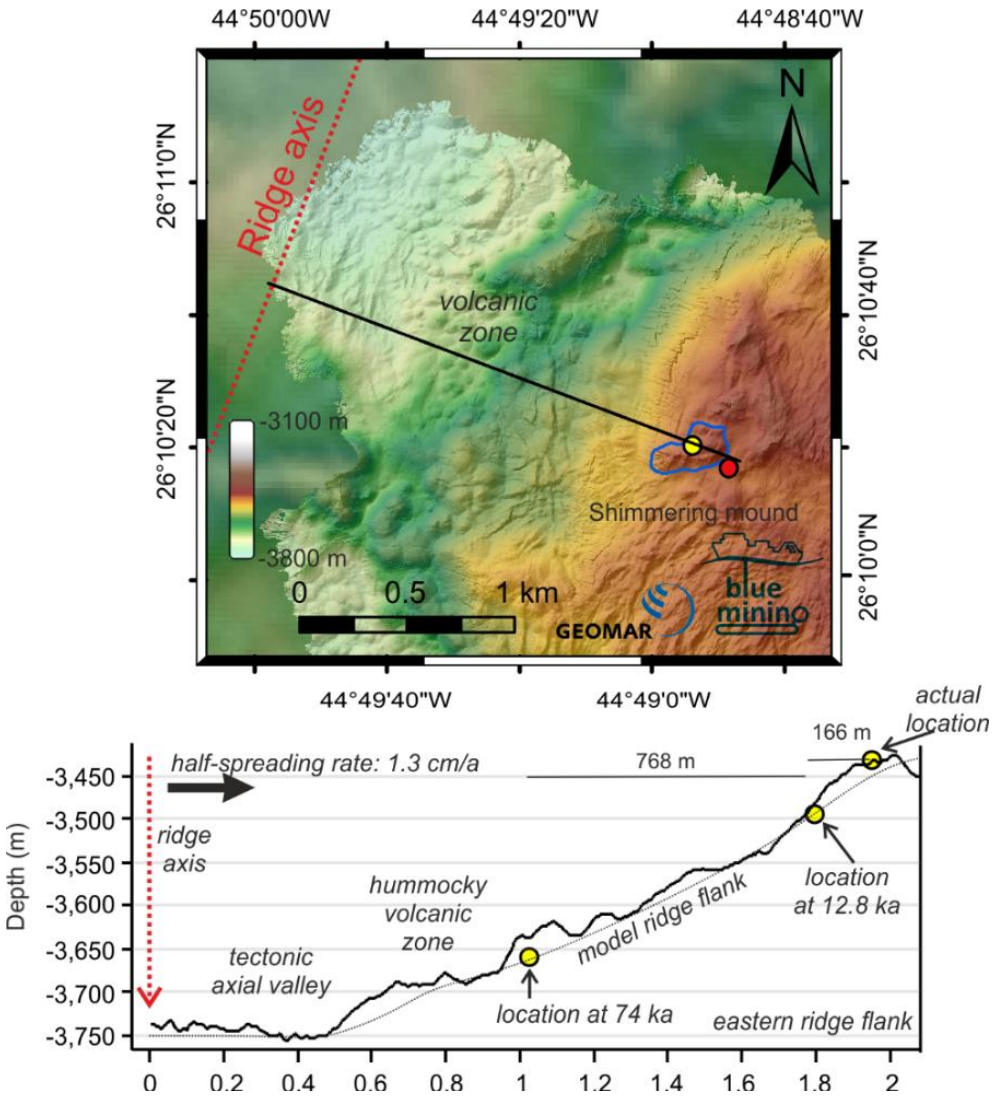

FIGURE 4.8 Bathymetry map of the northern segment of the TAGHF with Shimmering zone and depth profile of the eastern ridge flank from the ridge axis. Location of the Shimmering mound at the start of hydrothermal activity (72 ka) and at the cessation of hydrothermal activity (12.8 ka) on the idealised ridge flank. During 59 ka of hydrothermal activity, the mound drifted for about 800 m to the east.

4.6.5 Age of other hydrothermal systems at MOR

The high-resolution bathymetry studies of the TAGHF have identified numerous extinct hydrothermal mounds within the field. This is perhaps not surprising given that the slow-spreading rate of the MAR helps to concentrate the number of inactive vents within the study area. It is interesting to ask whether other hydrothermal fields show a similar synchrony in activity between vent sites, and whether they are synchronised with the TAGHF. Unfortunately, not many vent fields have been mapped in the same high-

resolution as the TAGHF. Furthermore, these vent fields lack continuous geochronological data of the type presented here. However, there are other possible contenders: the Semenov field located at 13°30'N on the Northern Equatorial MAR (consisting of one active vent and at least four known inactive vent sites; Cherkashov *et al*., 2017). Sulphides have been dated older than 12 ka, or younger than 10 ka, and could potentially indicate a similar post-glacial suppression at the same glacial termination (about 11 ka) (Cherkashov *et al*., 2017). However, a lack of continuous dating between 10 and 12 ka and the sampling resolution do not allow us to confirm the inactivity during this period. Furthermore, dating from hydrothermal fields along the Northern Equatorial MAR demonstrate that maximum activity occurred at 38-35 and 30-20 ka (Cherkashov *et al*., 2017), which coincides with the hydrothermal activity observed at the Shimmering mound (FIGURE 4.4). A younger period of activity between 2-8 ka (Cherkashov *et al*., 2017) also endorses the assumption of a partial rejuvenation of hydrothermal activity during the current interglacial.

Compilation of more than 500 dating points for individual samples across the world ocean (FIGURE 4.9) shows that the oldest dates are found in slow and ultra-slow spreading ridges (*i.e.* MAR and Indian Ridge) (*i.e.* Cherkashov *et al*., 2017; Yang *et al*., 2017). On the other hand, sample ages from intermediate (Juan de Fuca Ridge) (*e.g.* Jamieson *et al*., 2013) and fast-spreading ridges (East Pacific Rise) are on average younger (< 60 ka) and can be explained by sampling bias. Hydrothermal systems exploration is focused on the axial valleys, where active hydrothermal sites are located. Older sulphides from inactive vents would be considerably further off-axis, on ridge flanks, and most likely buried and hence harder to locate. On first sight, it is not clear whether the compilation shows a direct correlation between hydrothermal events and interglacial-glacial cycles. The reasons could be that hydrothermal activity during interglacial periods is not completely prevented but simply reduced and more intermittent. To compare variations of hydrothermal fluxes with time, geochronological studies of hydrothermal-overprinted sediments are also plotted alongside in FIGURE 9. Hydrothermal sedimentation records along the East Pacific Rise show maximum metal inputs coinciding with the last deglaciation (termination I, around 15 ka) and the penultimate deglaciation (termination II, around 130 ka) (Lund *et al*., 2016). However, at the Juan de Fuca Ridge, 500 ka-long records of Fe, Mn and Cu fluxes suggest periods of high hydrothermal activity could also span interglacial periods (FIGURE 4.9) (Costa *et al*., 2017). This compilation and the low dating resolution enhance the need for further studies on hydrothermal sediments at a maximum of different vent sites to confirm

whether the causal relationship with the glacial terminations or a coincidence of synchrony at the TAGHF.

4.7 Conclusion

This study demonstrates a remarkable synchronisation in activity between a number of discrete hydrothermal sites across the TAGHF, Mid-Atlantic Ridge. By dating hydrothermal events from their record in the sediments deposited in the vicinity of the sites, we show a synchronous suppression of high-temperature activity at 12-13 ka at three major sites: Shimmering mound, Mir mound and Rona mound. This suppression coincided with a rapid rate of rise in sea level following the last glacial termination at the end of MIS2. During the glacial and interglacial periods (MIS2 and MIS4), hydrothermal activity appears to have been continuous across the TAG field, with hydrothermal fluxes having been significantly higher during glacial periods compared with today. A partial rejuvenation of the field occurred in the last 10 ka with activity ongoing at the TAG active mound and recently ceased at the Mir zone and Shinkai mound. Our results are evidence for a common heat source, driving the hydrothermal activity at the TAG field, which also responds to rapid rates of climate-forced sea-level changes. Our data also supports the hypothesis that rapidly rising sea-level suppresses decompression melting in the upper mantle resulting in a short hiatus in melt supply to the heat source powering the TAGHF. The evidence for recent rejuvenation of hydrothermal activity at the off-axis MIR zone requires either a separate off-axis heat supply, or an open pathway for fluids to tap into the hydrothermal mounds from the axial heat source. We consider that the presence of active detachment tectonics beneath the MIR zone is the most likely process that maintains this open pathway for hydrothermal circulation. The data presented here demonstrate that hydrothermal activity across the TAGHF ceased after the last glacial maximum, implying a common heat source feeding several vents simultaneously, and a sensitivity to rapid sea-level fluctuations.

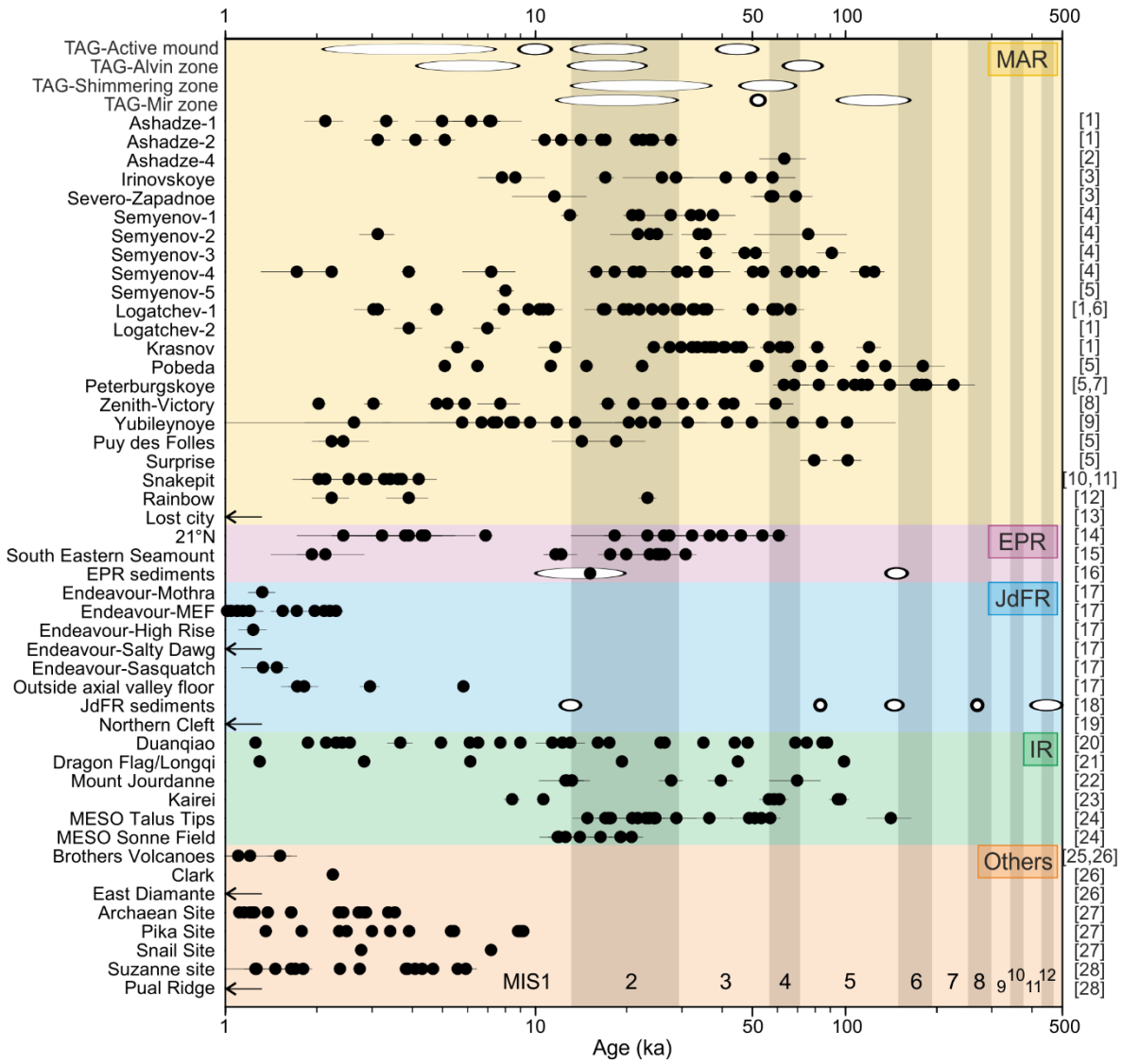

FIGURE 4.8 Geochronological compilation of hydrothermal activity (*cf.* previous page for caption).

FIGURE 4.9 (previous page) Geochronological compilation of hydrothermal activity from worldwide hydrothermal fields and categorised by geological settings in different oceanic basins (coloured horizontal areas). The time axis is expressed in logarithmic values and hydrothermal fields exclusively younger than 1,000 years-old are indicated by an arrow. Vertical grey bars highlight the glacial-interglacial periods with the shaded areas being the glacial periods. Dots indicate dating of individual hydrothermal samples (Mn-rich crust, clay, sulphide or barite) with displayed error bars (1σ variability), and elongated white ovals indicate the timespan of activity recorded in sediments (at TAGHF, this study; at the EPR; and at the JdFR). MAR = Mid-Atlantic Ridge, EPR = East Pacific Rise, JdFR = Juan de Fuca Ridge, IR = Indian Ridge and 'others' include Kermadec and Mariana intra-oceanic arcs and troughs, and Manus back-arc basin. References in brackets: 1 - Kuznetsov and Maksimov (2012); 2 - Cherkashev *et al*. (2013); 3 - Kuznetsov *et al*. (2018a); 4 - Kuznetsov *et al*. (2011); 5 - Cherkashov *et al*. (2017); 6 - (Lalou *et al*., 1996); 7 - Kuznetsov *et al*. (2015); 8 - Kuznetsov *et al*. (2013); 9- Kuznetsov *et al*. (2018b); 10 - Lalou *et al*. (1990); 11 - Lalou *et al*. (1993); 12 - (Kuznetsov *et al*., 2006); 13 - (Ludwig *et al*., (2011); 14 - Lalou and Brichet (1982); 15 - (Lalou *et al*., (1985); 16 - Lund *et al*. (2016); 17 - Jamieson *et al*. (2013); 18 - Costa *et al*. (2017); 19 - Koski *et al*. (1994); 20 - Yang *et al*. (2017); 21 - Liang *et al*. (2018); 22 - Münch *et al*. (2001); 23 - Wang *et al*. 2012); 24 - Lalou *et al*. (1998a); 25 - de Ronde *et al*. (2005); 26 - Ditchburn *et al*. (2012); 27 - Ishibashi *et al*. (2015); 28 - Johns *et al*. (2014).

4.8 Acknowledgements

The authors acknowledge support from the European Union Seventh Framework Programme Grant No. 604500 (EU-FP7) 'Blue Mining: breakthrough solutions for the sustainable deep-sea mining value chain" under grant agreement 604500. They would like also to gratefully acknowledge the JC138 shipboard party for its assistance in data collection and sample acquisition and Geomar Abyss AUV team for the provided high-resolution bathymetry maps during M127. AMD thanks Matt Cooper, SEAPORT laboratories and palaeomagnetism and environmental magnetism laboratories for their help with geochemical, isotopic and paleomagnetic analyses, respectively. The British Ocean Sediment Core Research Facility (BOSCORF) is thanked for using their facilities. The radiocarbon dating work was supported by the NERC Radiocarbon Facility NRCF010001 (allocation number 2142.1018 awarded to AL). AMD wish to thank John Jamieson for sharing the worldwide dating database and thoughtful comments on the interpretation. This work was supported by a PhD studentship to AMD from the Graduate School of the National Oceanography Centre, Southampton.

Synchronised post-glacial suppression of hydrothermal activity across the TAG hydrothermal field, Mid-Atlantic Ridge

Chapter 5 Metal preservation in hydrothermal sediments from the TAG hydrothermal field, Mid-Atlantic Ridge

This chapter was submitted as a scientific manuscript to publication in *Geochimica et Cosmochimica Acta* on the 2nd of August 2019, and submitted after review on the 08th of February 2020. Contributions from the co-authors consists in the discussion of the results (Lichtschlag, Murton and Barriga), sampling (Martins) and provision of mineralogy results (Milinovic). The author list is:

Dutrieux A M, Lichtschlag A, Barriga F J A S, Martins S, Milinovic J and Murton B J.

5.1 Abstract

The Trans-Atlantic Geotraverse hydrothermal field (TAGHF) on the Mid-Atlantic Ridge at 26°N contains sediments characterized by high metal content that may be of similar economic value to the seafloor massive sulphide deposits themselves. Here, we report morphological, mineralogical and geochemical data that reveal the origin, preservation and mobilisation of metals within these hydrothermal sediments. These sediments were recovered by gravity coring and rock drilling from three distinct seafloor environments: (a) (a) On the top of extinct hydrothermal mounds, metalliferous sediments are predominantly composed of Fe oxyhydroxides (goethite, hematite and ferrihydrite) with low concentrations of base metals Cu, Co and Zn. These are mainly derived from oxidative seafloor weathering of massive sulphides. (b) On the flanks and at the base of extinct hydrothermal mounds, sediments containing cm-thick layers of unsorted sulphide sands have high base metal contents (*e.g.* up to 28% Cu). These sediments were deposited by mass transport of hydrothermal precipitates (chimneys). On burial, sulphides reacted with ingressing seawater resulting in dissolution and mobilization of metals into pore waters leading to partial release into the ocean. (c) In depositional basins, up to a few hundreds of meters distal from the mounds, recurrent turbiditic flows rapidly deposit several meters of metalliferous sediments. These include fining-upwards sequences of thin sulphide sand layers, mixed with Fe-oxyhydroxides. Later diagenetic processes generated reduced conditions that dissolved Cu, Co and Mn, which were mobilized upwards, reprecipitated

at the oxic/sub-oxic boundary, near the seafloor, as oxides and transient chlorides; before Co and Cu were eventually adsorbed on precipitated particles of Fe-Mn oxyhydroxide. Together, these processes determine the metal tenor of the sediments surrounding seafloor massive sulphide deposits, control the extent of metal release into the ocean and impact the composition of the subducted ocean sediment with implications for the global metal cycle.

5.2 Introduction

Hydrothermal systems along mid-oceanic ridges and back-arc spreading centres host seafloor massive sulphides (SMS) rich in elements such as Cu, Zn, Pb, Au and Ag. These deposits are regarded as having the potential to complement to mineral resources on land, where metal grades are in decline (Petersen *et al*., 2016). Hydrothermal SMS deposits are often associated with metalliferous sediments, which are characterized by a high Fe and Mn contents (Gurvich, 2006), and which may present a resource potential in their own right. For example, the Atlantis II Deep in the Red Sea is estimated to contain ~90 Mt of metalliferous sediments (Bertram *et al*., 2011).

On the seafloor, metalliferous sediments result from a combination of processes such as settling of hydrothermal plume fall-out, physical and chemical degradation of SMS deposits, and mass transport and deposition into surrounding channels and basins (German *et al*., 1993; Goulding *et al*., 1998; Webber *et al*., 2015). After deposition, they can be modified by *in situ* diagenesis and authigenic mineralization. Together, SMS deposits and their associated seafloor metalliferous sediments are widely distributed around the globe (Gurvich, 2006; Hannington *et al*., 2011). The sediments provide excellent records of the history of hydrothermal activity (Gurvich, 2006), act as potential vectors to the presence of hidden ore bodies (Liao *et al*., 2018), and constitute a significant, but hitherto unaccounted for, reservoir of base and ferrous metals in the ocean crust that are ultimately supplied to subduction zones. To date, however, little is known about the spatial distribution of hydrothermal metalliferous sediments, or how their specific environments of deposition, origin and diagenesis affect the preservation of their metal contents.

Here, we address the question of what controls the deposition and preservation of metals in hydrothermal sediments at the TAG Hydrothermal Field (TAGHF) on the Mid-Atlantic Ridge. In particular, we attempt to show how their formation and preservation varies in different environments, *i.e*. at the top of extinct hydrothermal SMS mounds, the slope and

base of these mounds, and in more distal depositional channels and basins. Using a series of gravity cores, we compare metalliferous sediments from these different environments, focusing on their metal contents, mineralogy and modes of deposition, metal mobilisation, and preservation. The TAGHF is one of the best-known hydrothermal fields and is considered a classic example of a modern, volcanogenic massive sulphide deposit (VMS) (*i.e*. a typical surficial lens of massive sulphides and a deeper stockwork) (Hannington *et al*., 1998).

5.3 Geological setting

The TAGHF, discovered in 1972 (Scott *et al*., 1974; Rona, 1980), is located on the hanging wall of a west-dipping active detachment fault on the eastern flank of the Mid-Atlantic Ridge (26°09.4'N, 44°49.0'W) at a water depth of 3600 m (Rona, 1980; Humphris *et al*., 2015) (FIGURE 5.1). It comprises: i) the hydrothermally active high-temperature TAG mound, ii) a zone of low temperature diffuse flow, and iii) two major areas of hydrothermally extinct sulphide mounds (Alvin and Mir zones) (also called inactive, or relict mounds). The active TAG mound is a ~200 m diameter, 60 m high, black smoker complex with chimneys at the summit and a cover of sulphide talus and manganese crusts. The highest temperature 'black smoker' chimneys are composed of anhydrite, pyrite and chalcopyrite, while the lower temperature 'white smoker' chimneys are enriched in sphalerite and cluster to the southeast of the mound (Thompson *et al*., 1988). The Alvin zone, located 2.5 km NNE of the active TAG mound, contains several 100-300 m diameter, 30-60 m high, sulphide mounds. These are dome shaped, with discontinuous sulphide outcrops, standing and toppled chimneys, and a thin (<0.5 m) cover of pelagic carbonate sediments (Rona *et al*., 1993a; Rona *et al*., 1993b). The mounds identified in the Alvin zone include the Shinkai mound, Southern mound, Double mound and Rona mound (Rona *et al*., 1993b; Rona *et al*., 1993a; White *et al*., 1998; Tivey and Humphris, 2000; Humphris *et al*., 2015; Petersen and Scientific Party, 2016). The second inactive area, Mir zone, is located 2 km ENE of the active TAG mound. It consists of small standing and fallen chimneys, highly weathered sulphide material, red metalliferous sediments, and low-temperature hydrothermal precipitates such as Fe-Mn oxide crusts (Rona *et al*., 1993a; White *et al*., 1998).

Dating of TAGHF sulphides shows that the Mir zone and the Alvin zone have ages of formation of 140,000 and 74,000 years, respectively (Lalou *et al*., 1995). The high-

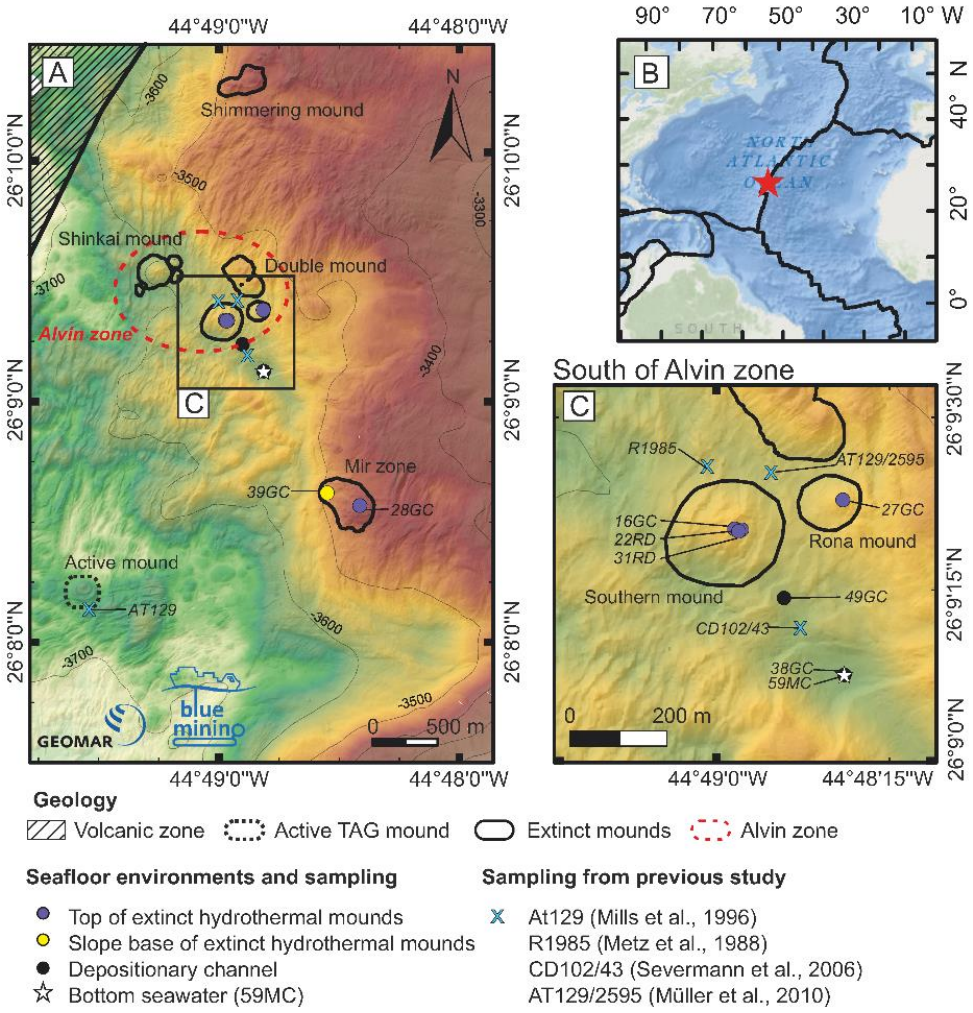

FIGURE 5.1 TAGHF bathymetry maps. (A) Shaded bathymetry map with main hydrothermal sites of the TAGHF, located on the western ridge flank of the Mid-Atlantic Ridge. The active mound, the four extinct mounds (Shinkai, Double, Rona and Southern mounds) grouped into the Alvin zone, the Mir zone and the low-temperature active Shimmering mound are highlighted in blue on the map. The shaded area is the volcanic zone; (B) Location of the TAGHF on the Mid-Atlantic Ridge (basemap provided by GEBCO-ESRI); (C) Zoom-in on the south of Alvin zone with Southern and Rona mounds and the depositional channel intercut by long faults. The bathymetry map was generated during the M127 cruise (Petersen and Scientific Party, 2016; Petersen, 2019a). Coring and drilling locations of the sediments are shown as purple, yellow or black dots. The multicore (59MC) location for near-bottom seawater sampling is indicated by the white star. Sediment sampling locations from previous studies are also shown on the map (cross), including Mills *et al*. (1996), Metz *et al*. (1998), Severmann *et al*. (2006) and Müller *et al*. (2010).

temperature hydrothermal activity at the Alvin zone finished around 6,000-8,500 years ago (Metz *et al*., 1988) and continued to about 600 years ago at the Mir zone (Lalou *et al*., 1995).

The currently active TAG mound initiated about 40,000-50,000 years ago, with sporadic pulses of high-temperature sulphide formation since then, the latest having started 70 years ago (Lalou *et al.*, 1995).

Sediments rich in metals such as Fe, Cu, Zn and Mn occur at the TAGHF (Scott *et al.*, 1978). These are capped by a pale-brown biogenic calcareous ooze, also rich in Fe, and consisting of foraminifera and nanoplankton tests (Shearme *et al.*, 1983). Different types of sediment deposits are identified, *e.g.* particulate fallout from the plumes, oxidized sulphide precipitates, filling of channels by turbiditic mass wasting, and authigenic low-temperature mineralization. Fe- and Mn-oxyhydroxides and some sulphides, derived from hydrothermal plume fall-out, are incorporated within the pelagic carbonate background (German *et al.*, 1993; Mills *et al.*, 1993).

In the following sections, I present evidence for the processes forming the sediments and how chemical conditions following burial have contrived to generate reducing conditions in some depositional environments that have led to diagenetic processes of metal mobilisation and enrichment.

5.4 Methods

5.4.1 Sampling

Sediment cores were collected with a gravity corer (GC) during the RRS *James Cook* cruise JC138 in summer 2016 (Table 1). Coring locations were identified with the help of high-resolution bathymetry acquired by autonomous underwater vehicle (Petersen and Scientific Party, 2016) and visually with the robotic underwater vehicle (HyBIS) (Murton and Scientific Party, 2018). Cores were collected from three different geomorphological environments (FIGURE 5.1): i) the tops of the extinct hydrothermal mounds (Southern mound (core 16GC), Rona mound (core 27GC) and Mir zone (core 28GC), ii) a sedimentary fan at the lower slope of Mir zone (core 39GC) and iii) from a depositional channel located in the south of the Alvin zone (core 38GC & core 49GC) (FIGURE 5.1C). In addition, ~3 m-long sediment cores were recovered with the BGS rock drill (RD2) from above the massive sulphide ore body at the top of Southern mound (core 22RD & core 31RD). In this paper, we present and discuss geochemical analyses of the solid phase and the pore water chemistry from three representative cores (one for each environment: core 16GC, core 39GC

and core 38GC). The full data are available in APPENDICES C.1.6 and C.1.8. Additional data, *i.e.* for cores 22RD, 31RD, 27GC, 28GC and 49GC are available in APPENDICES C.2. Near-bottom seawater was collected from water overlying the sediment in a mega core at the same site as 38GC in the depositional channel (59MC).

Pore waters were extracted from the sediment cores through holes drilled in the plastic core liners of the GC and the RD immediately after retrieval at 5 cm-intervals in the first 50 cm, and 10 cm-intervals thereafter, using Rhizon fluid samplers connected to air-tight syringes (Seeberg-Elverfeldt *et al.*, 2005; Lichtschlag *et al.*, 2015). If changes in lithology were visible in lower resolution than 10 cm, pore water was extracted every 5 cm (*e.g.*, 38GC and 49GC). The pore waters were sub-sampled and preserved for analyses of cations (acidified with 5 µL of suprapur concentrated nitric acid), anions and dissolved hydrogen sulphide (in 0.5 mL of 2% zinc acetate), total alkalinity (stored headspace-free in glass vials and poisoned with saturated $HgCl_2$) and nutrients (frozen at -20°C). After pore water extraction, the sediment cores were split horizontally, described and logged for lithology and structure. Sediment subsamples were taken in the undisturbed sediments adjacent to the pore water samples and used for analyses of porosity, grain size, mineralogy and bulk rock geochemistry.

TABLE 5.1 Locations and station positions of gravity cores, the mega core and the rock drill cores at the TAGHF. *Depths are inferred from telemetry data of the rock drill and the length was not fully recovered.

Core reference	Location	Core depth (cm)	Water depth (m)	Coordinates
Top of extinct hydrothermal mounds				
16GC	Southern mound	133	3510	26°09.338N 44°48.974W
22RD	Southern mound	190-320*	3535	26°09.331N 44°48.959W
31RD	Southern mound	17-168 223-273*	3536	26°09.334N 44°48.965W
27GC	Rona mound	41	3524	26°09.375N 44°48.820W
28GC	Mir zone	194	3400	26°08.558N 44°48.416W
Slope base at extinct hydrothermal mounds				
39GC	Mir zone fan	39	3490	26°08.619N 44°48.550W
Depositional channel				
49GC	200 m SE of Southern mound	230	3490	26°09.237N 44°48.802W
38GC	500 m SE of Southern mound	98	3608	26°09.126N 44°48.814W
59MC	500 m SE of Southern mound	15	3528	26°09.540N 44°48.820W

5.4.2 Solid phase analysis

5.4.2.1 Physical parameters

Grain size was measured on 5 carbonate ooze samples and 18 hydrothermal sediment samples with the Malvern Masterize Particle Size Analyser at the National Oceanography Centre (Appendix C.1.1). Mean porosity and bulk density of carbonate and hydrothermal sediments for flux calculations for cores 16GC, 27GC, 38GC and 49GC were calculated from known volume and weight of sediments before and after drying at 50°C or freeze-drying overnight.

5.4.2.2 Mineralogy

A few milligrams of powder from selected samples were analysed, as grain mounts, by scanning electron microscopy (Leo 1450VP SEM), and characterized by semi-quantitative energy dispersive X-ray (EDS) analyses with a carbon coating (APPENDIX C.1.2). Minerals that did not dissolve during the acid digestion have also been analysed with a tabletop microscope (Hitachi TM1000). X-ray diffraction qualitative analyses were carried out on sediments after powdering with a Philips X'Pert pro with a Cu tube (Kα1 λ = 1.541 Å) and Siroquant XRD software at the University of Southampton, and on a PANalytical X´PERT Pro, a MiniFlex II, Rigaku and X'Pert High Score Plus software at the University of Lisbon (Milinovic *et al*., 2017) (APPENDIX C.1.3).

5.4.2.3 Geochemical composition

The chemostratigraphy of the sediments was analysed in a 1 mm vertical resolution with the ITRAX core-scanning X-ray fluorescence system (Cox Analytical Systems) (Croudace *et al*., 2006) at the British Ocean Sediment Core Research Facility (BOSCORF) in Southampton, UK. The instrument was operated at a voltage of 30 kV, a current of 30 mA, a count time of 30 s with a 3kW Mo X-ray tube. Element abundances were normalized to kilo-counts per second (kcps) and a running average of 5 mm was applied to the results (APPENDIX C.1.4). ITRAX data were calibrated against whole rock geochemistry data for Mn in order to get more quantitative results. Correlation coefficients were better than 0.96 (APPENDIX C.1.5).

Whole-rock analyses were performed by inductively coupled plasma mass-spectrometry (ICP-MS; ThermoScientific X-Series 2) and inductively coupled plasma optical emission spectrometry (ICP–OES; Thermo Scientific ICAP 6500 Duo) on approximately 100 mg of dried, acid-digested material. After oxidation of sulphides and carbonates in *aqua regia* (3:1, HCl:HNO_3), the mixture was evaporated and further digested using a mixture of HF and $HClO_4$ to dissolve any remaining silicates. The samples were then diluted to a 1:400 ratio using 3 mol/L HCl and further to a 1:4000 ratio using a 3% HNO_3 matrix containing an internal spike of Be, Re and In. The samples were analysed with ICP-OES for major elements (Ca, Cu, Fe, Mn and Zn) together with 6 rock standards and with ICP-MS for minor elements and trace elements, including rare earth elements (REEs) and Yttrium (Y-REEs) (APPENDICES C.1.6, C.1.7 and C.2.1). Precision and accuracy were determined for each analytical run by repeated analysis (n = 3) of two CRMs: (i) marine sediments MESS-1 (National Research Council of Canada), and (ii) sulphide ore mill tailings RTS-1 (National

Research Council of Canada) and averages for each run were found to be less than 4% (precision) and 3% (accuracy), except for Co and Zn which had an accuracy of 7%. The REE precision and accuracy were both within 5% of the CRM MESS-1. Rare earth elements (REEs) data have been normalized to C1 chondrites (Evensen *et al.*, 1978). Deviations of REE patterns are expressed as anomalies; *i.e.* Ce anomaly and Eu anomaly. Eu and Ce anomalies are expressed by following equations (5.1) and (5.2), respectively:

$$Eu\ anomaly\ = Eu_n/\sqrt{(Sm_n * Gd_n)} \qquad \text{(Eq. 5.1)}$$

$$Ce\ anomaly = 3Ce_n/2(La_n + Nd_n) \qquad \text{(Eq. 5.2)}$$

where n refers to chondrite normalized values.

5.4.3 Pore water analysis

Concentrations of major cations (B, K, Mg, Na, Rb, Si, and Sr) were measured with ICP-OES and concentrations of minor cations (Ba, Co, Cu, Fe, Mn, U, V, and Zn) were measured with ICP-MS at the National Oceanography Centre and the University of Southampton, respectively. Both analyses were done on aliquots, diluted 50-fold with 3% thermally distilled HNO_3 containing an internal spike of Be, Re and In. Precision and accuracy were determined for each analytical run by repeat analysis (n = 3) of two certified reference materials of similar range in composition as the samples: (i) CRM-SW (Seawater Greyhound) and (ii) SLEW-2 (National Research Council Canada) spiked with Fe, Mn, Cu, Zn, V and Co. Precision was better than 5% for Mg, Cu, Fe, Mn and Zn, and 10% for Co. External reproducibility between ICP-OES and ICP-MS analyses was about 1% RSD for elements in common (*e.g.* Sr), determined by replicate samples. We provide the data for elements that are not discussed in this paper (i.e. B, Ba, Ca, K, Li, Na, Rb, Si, Sr, U and V) in APPENDICES C.2.2 and C.2.3, and DIGITAL MATERIAL 15).

Chloride and sulphate were analysed by ion exchange chromatography using a Dionex ICS2500 with 9 mmol/L Na_2CO_3 as eluent on 100-fold diluted samples. The reproducibility of the results was determined by replicates of certified reference material of International Association for the Physical Sciences of the Oceans (IAPSO) seawater standard. Precision was better than 1% and accuracy was better than 3.5%.

Total dissolved hydrogen sulphide ($H_2S + HS^- + S^{2-}$) was determined by photospectrometry at absorbance of 670 nm following the method of Cline (1969).

Total alkalinity (TA) was determined by titration against 0.01 mol/L HCl using a mixture of methyl red and methylene blue as an indicator. Analyses were calibrated against the IAPSO seawater standard. Precision and accuracy were better than 8% and 2%, respectively.

NO_X (NO_2 + NO_3) and NH_4 were measured with a AA3 Seal Analytics Autoanalyzer after a 13-fold dilution following the method described in Grasshoff *et al.* (1983). The accuracy and precision of NO_X calculated from the seawater nutrients CRM Lot.CA (/www.kanso.co.jp/) was 8%.

5.4.4 Calculations of Mn fluxes

To understand if precipitation of Mn is realistic in the hydrothermal sediments of the TAGHF, the fluxes of dissolved Mn were calculated at three sites: Southern mound (16GC) and in the depositional channel (38GC and 49GC) (TABLE 5.2) using Fick's first law of diffusion:

$$J_{Mn} = - D_{Mn} * \phi * (\delta C_{Mn}/\delta x), \quad \text{(Eq. 5.3)}$$

where J_{Mn} = the diffusive flux (mol/cm² y), D_{Mn} = Mn diffusion coefficient in the sediment at 5 °C corrected for tortuosity using equation 4; ϕ = porosity; $\delta C_{Mn}/\delta x$ = concentration gradient. A negative flux indicates the element diffuses out of the sediment. Porosity values were calculated from an average of measurements obtained on hydrothermal sediments from the top of the mounds (0.82) and from sediments from the depositional channel (0.75). D_{Mn} is calculated using the equation Eq. 5.4. All calculations and the Mn pore water profile in 49GC are provided in APPENDIX C.1.9.

$$D_{Mn} = D^0_{Mn} / (1 - ln (\phi^2)), \quad \text{(Eq. 5.4)}$$

Where D^0_{Mn} = Mn diffusion coefficient in seawater, 3.5 x 10^{10} cm²/s (Schulz, 2006).

The higher vertical sampling frequency of 5 cm and a linear gradient (*e.g.* a R^2 of 0.99 in 38GC) over the specific sampling interval (60 to 90 cm in depth) indicate a constant diffusion of Mn from below at the time of sampling, and therefore the maximal Mn supply that is currently present has been calculated from this gradient.

To understand whether dissolved Mn diffusion could be responsible for precipitation of Mn oxides, the Mn fluxes are compared to the total solid Mn contents (in g) per surface

area, which were calculated by integrating the ITRAX calibrated data expressed in g/cm^2 on a sediment thickness corresponding to the horizons bearing the Mn oxides. The horizons are 21 cm at the Southern mound (*e.g.* the first 21 cm below the sediment surface in 16GC), 22 cm in the depositional channel at 38GC (*e.g.* the interval in between 38-60 cm) and finally 40 cm at 49GC (i.e. between 20 and 60 cm).

TABLE 5.2 Modelling parameters. (a) Calculated with Eq. 4 from Schulz (2006) and (b) from Lalou *et al*. (1995).

Core	**16GC**	**38GC**	**49GC**
Environment	Top of Southern mound	Depositional channel	Depositional channel
Porosity	0.82	0.75	0.75
Mn horizon depths in sediments	0-21cm	38-60 cm	20-60 cm
Mn diffusion coefficient in sediments (cm²/s)[a]	2.68 x 10^{-6}	2.38 x 10^{-6}	2.38 x 10^{-6}
ITRAX Mn calibration equation R²	0.95	0.97	0.98
Solid Mn mass per surface area (mol/cm²)	~ 0.25	~ 0.004	~ 0.01
Flux J_{Mn} (mol/cm² y)	~ -3.3 x 10^{-6}	~ -6 x 10^{-8}	-2.74 x 10^{-8}
Pore water concentration gradient (µmol/L.cm)	(minimal, as calculated on a 74,000 years period) ~ 39	(calculated from pore water concentrations) ~ 1.1	0.48
Time/age (years)	At Alvin Zone[b]: 74,000 (oldest Mn oxide crusts) 45,000 (youngest sulphide rocks)	90,000 (this study)	385,000

5.5 Results

5.5.1 Sediment spatial distribution and stratigraphy

Our results show that the lithology, stratigraphy and thickness of the sediment cover vary between the different seafloor environments. The tops of the extinct hydrothermal mounds

were sampled in the Alvin zone (FIGURE 5.2A) and the Mir zone. Sediments from the Alvin zone (Southern and Rona mound) contain five different lithologies; none of them contained sulphide grains. The upper layer comprises a widespread 20-40 cm thick cover of beige carbonate ooze consisting of pelagic material (FIGURE 5.3A), referred to in this paper as unit M1 (M = mound). Visual observation, however, identified some relict sulphide chimneys and boulders, and dark patches of ferromanganese crusts. The rocks are generally encrusted with secondary minerals, *i.e.* red iron oxyhydroxides, yellow jarosite, or green atacamite/paratacamite (Murton *et al.*, 2019). At both, Southern mound and Rona mound, the weathered surface geology transitions into a ~10 cm thick, heterogeneous, coarse and unsorted, dark unit (unit M2) followed by 1.7 to 2.8 m thick, red to orange coloured, iron-rich, and poorly sorted sediments (units M3 and M4, FIGURE 5.3B). Unit M3 contains a few larger grains up to 2 mm and the grain texture shows millimetre-size to centimetre-size agglomerates and clasts. Below these sediment units is a silicified "jasper" layer (Unit M5, FIGURE 5.3C) that transitions rapidly into a massive sulphide body. Rock drill and gravity cores from the Mir zone were, overall, stratigraphically identical to those described from the Alvin zone (*e.g.* unit M1 followed by M2 and a mixed M3/M4). The major difference was that the mound had a thinner sediment cover (~0.7 m) in some locations than at the Alvin zone.

At the base of the extinct mounds, the sediment cover became thinner (< 0.5 m), with frequent boulders of chimney material or massive sulphides (FIGURE 5.2B). The rocks are similar to those found on the top of extinct mounds, also generally encrusted with secondary minerals, *e.g.* red iron oxyhydroxides, yellow jarosite, and green atacamite/paratacamite. The core described in detail, 39GC, was recovered from the Mir zone fan, at the west edge of Mir zone, and is composed of up to 39 cm of sandy metalliferous sediments with no carbonate material (FIGURE 5.3D).

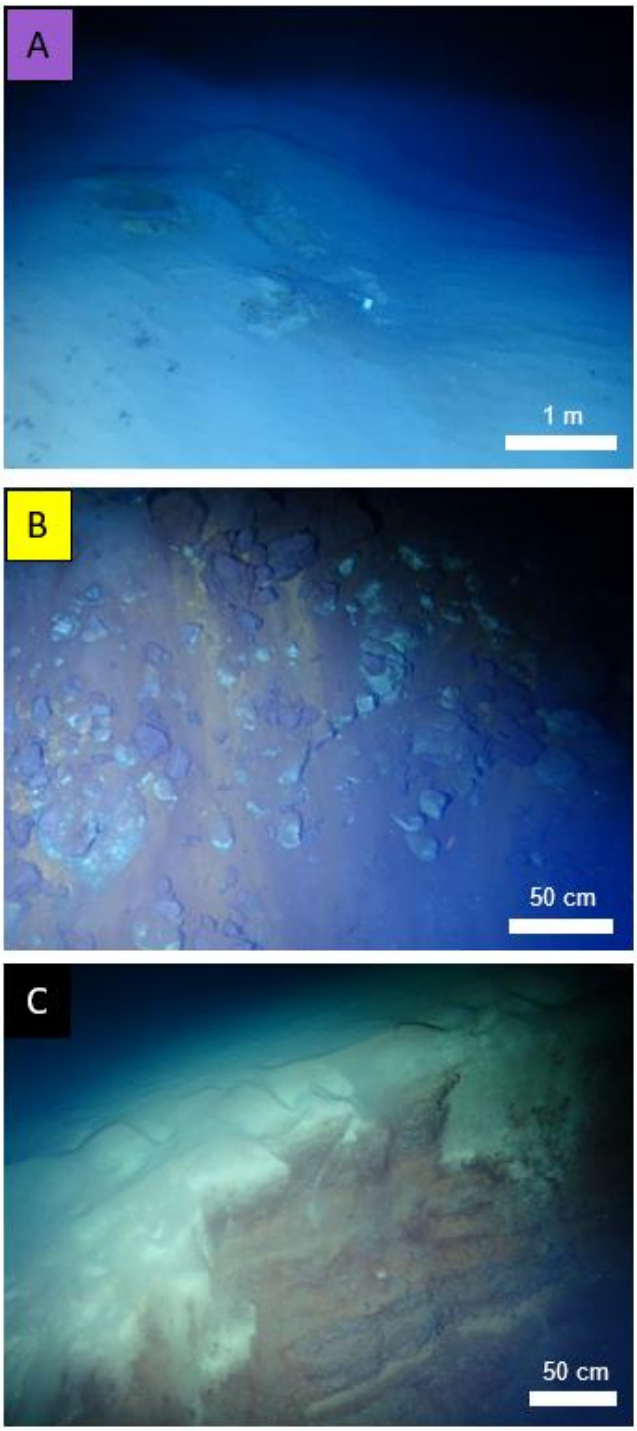

FIGURE 5.2 HyBIS video footage. (A) Flat carbonate ooze cover on top of the extinct Southern mound (Alvin zone); the green beacon indicates the sampling station for the RD2; (B) Numerous boulders made of Fe oxides and sulphides on the slope of an extinct mound within a hydrothermal sediment cover. The green coating on rocks is due to atacamite and paratacamite minerals which are formed by secondary Cu weathering; (C) fault scarp in the depositional channel showing the thick accumulation and bedding of metal-rich sediments overlain by beige pelagic calcareous sediments.

FIGURE 5.3 (next page) Schematic stratigraphy logs (upper panel) and photographs (lower panel) of selected sections from split metalliferous sediment cores from the top of a hydrothermally extinct mound, from the slope base of mound and in a depositional channel. Depths and lengths of the different lithological units are variable, however a range of depths is indicated in the upper panel. The selected sections for the photographs are indicated by the letters. (A) Carbonate ooze cap at Rona mound (27GC), followed by dark Mn oxide crusts in Unit M2. (B) Transition between Unit M3 and M4 on the top of Southern mound (station 22RD). (C) Sample of silicified Fe-rich "jasper" recovered by the rock drill at the station 22RD directly underneath the sediment cover, and above the sulphide ore body. (D) Full core in the Mir zone fan showing numerous sulphide grains and pebbles mixed with Fe oxyhydroxides (39GC). (E) Graded bedding due to the settling of plume fall-out particles within the pelagic carbonate ooze overprinted by bioturbation (38GC) (F) Turbidity flow layers showing a Bouma sequence: sulphide grains mixed with sand size oxide fragments (Ta) and finer dark brown mud-size grains at the top (Tb, Tc, Td) and fine clay cap (Te).

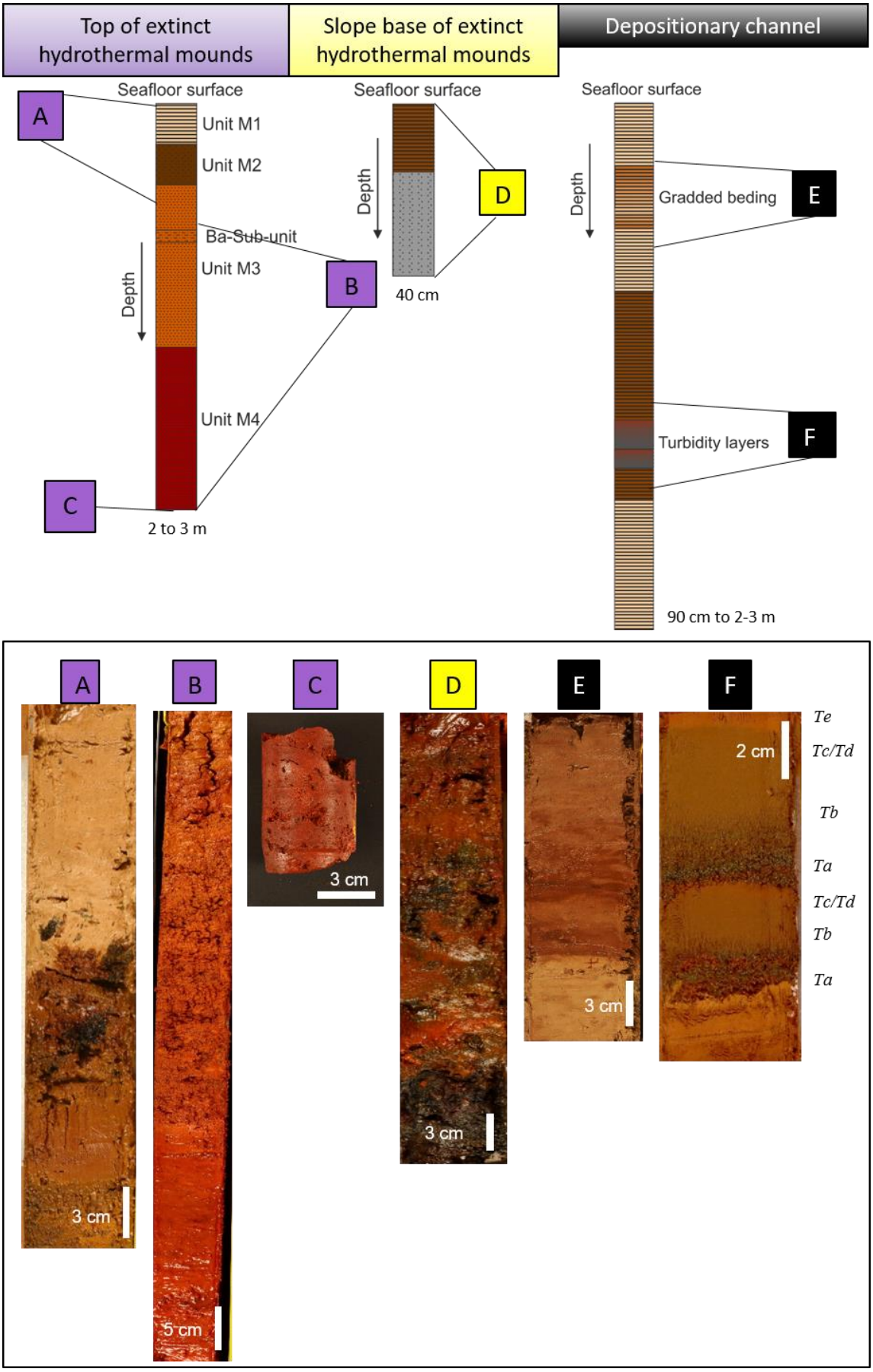

FIGURE 5.3 Schematic stratigraphy logs (*cf.* caption on the previous page).

In adjacent basins and depositional channels (FIGURE 5.1C), up to few hundred meters further away from the hydrothermally extinct SMS mounds, visual observations showed large fault scarps exposing a thickness of more than 10 m of layered metalliferous sediments (FIGURE 5.2C). The stratigraphy shows differences in the graded bedding (FIGURE 5.3E, F), typical of turbidite Bouma sequences (Bouma, 1962). Here, the eroded base is composed of coarse sulphidic sand (*Ta*), indicating a high energy flow, with grain-size fining upward, followed by the sequences *Tb*, *Tc* and *Td* with fine sand and silt grains. The uppermost sequence (*Te*) is composed of clay. In core 49GC, also taken from the depositional channel, turbidity sequences are less distinctive with more repetitive turbidity flows of sulphidic sands and oxyhydroxide silty sands in fine laminar layers. The upper Bouma sequences (*Td, Te*) are often eroded and show a return to a pelagic sedimentation conditions that are not always preserved between subsequent turbidity flows. The details of the grain size analyses can be found in APPENDIX C.1.1).

5.5.2 **Mineralogy**

On the tops of all the extinct hydrothermal mounds, unit M1 comprises a pelagic cover that consists of calcareous foraminifera and other nanoplankton with iron oxide particles, including goethite and amorphous ferrihydrite (details of the mineralogy can be found in APPENDIX C.1.3). The underlying unit, M2, is composed of heterogeneous brecciated material of Fe and Mn oxides (todorokite, birnessite). Beneath this is the orange to red coloured unit M3 and M4, composed mainly of goethite, hematite, nontronite, montmorillonite, quartz and amorphous Fe oxyhydroxides. On Southern mound, unit M3 also contains depth intervals with coarse grained barite crystals with slightly eroded, delicate rosette shapes (FIGURE 5.4A) with a diameter of 0.3 and 1 mm, *e.g.* core 22RD at ~220 cm, core 31RD at ~150 cm, and core 16GC at ~50 cm. These crystal morphologies are typically of primary hydrothermal barite that has precipitated from Ba-enriched hydrothermal fluids reacting with sulphate from seawater in high-temperature hydrothermal chimneys (Griffith and Paytan, 2012). Hence, the presence of primary high-temperature hydrothermal barite crystals in the sediments indicates an origin from hydrothermal chimneys, with the primary sulphides having been completely weathered.

Sediments forming the base of the extinct mounds (Mir zone fan) consist of Fe-oxyhydroxides (goethite and ferrihydrite) and sulphides (mainly pyrite and chalcopyrite), co-occurring with Fe-oxyhydroxides without calcite or detrital Al-bearing minerals.

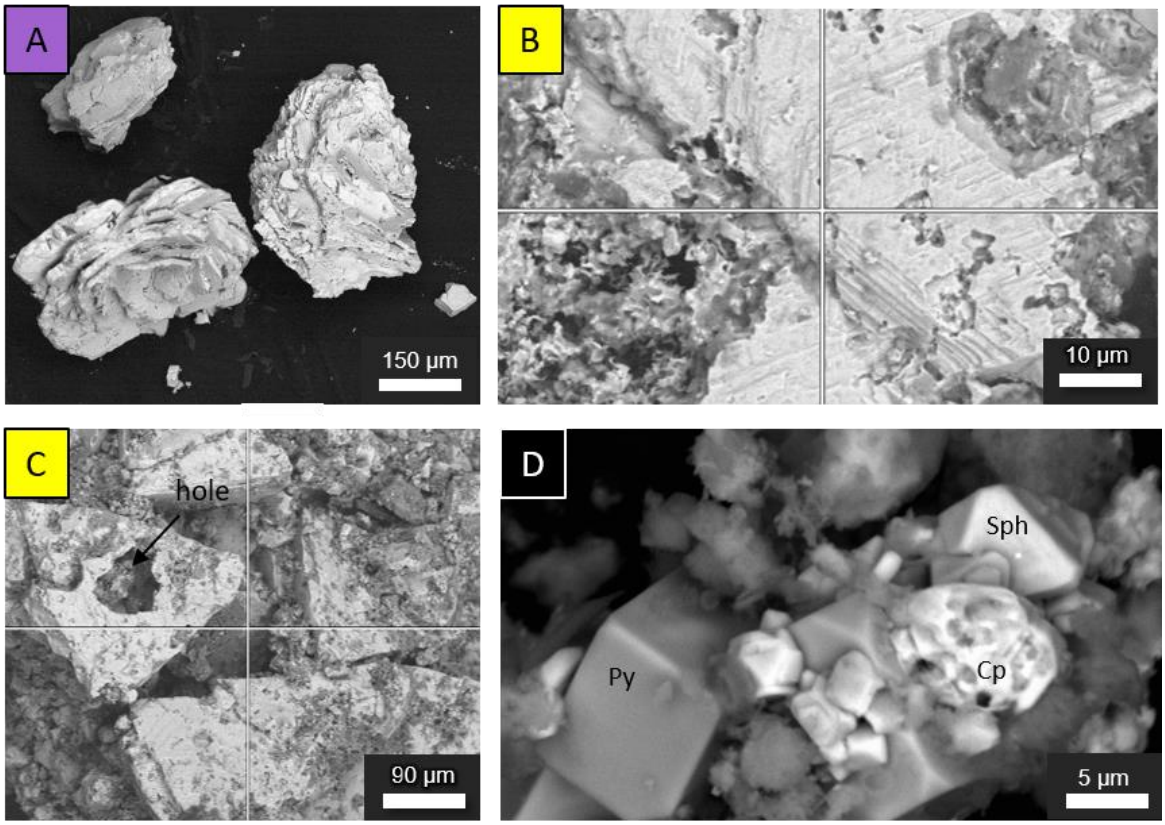

FIGURE 5.4 SEM microphotography. (A) Barite grain from unit M3 of Southern mound (22RD at 150 cm depth); (B) Zoom-in in the chalcopyrite dissolution pitting; (C) large (*i.e.* few hundred µm long) chalcopyrite grains with indications of partial dissolution pitting from the Mir Zone fan (D) Aggregate of fine grains (*i.e.* few ten of µm long) cubic pyrite (Py), partially dissolved chalcopyrite (Cp) and Cu-rich sphalerite (Sph) presenting octahedral faces and likely chalcopyrite disease (Barton and Bethke, 1987) from a thin sulphide layer in the depositional channel. Semi-quantitative EDS geochemical analyses of the three minerals are provided in the Supplementary Information D.

According to the three-component model described by Metz *et al.* (1988), these components are of hydrothermal origin. While pyrite shows intact crystal faces, chalcopyrite has a vuggy texture associated with partial dissolution (FIGURE 5.4B, C).

In the core from the depositional channel (38GC), graded bedding, expressed by the darkening coloration from the addition of hydrothermal Fe-oxyhydroxides, is present in the pelagic calcareous nanofossil ooze (FIGURE 5.3E). Deeper in the core, fining-upwards sequences of metalliferous sediments, typical of deposition by turbidity currents, mainly comprise Fe-oxyhydroxides (hematite, nontronite, goethite, ferrihydrite) with truncated cubic pyrite, sphalerite with chalcopyrite disease and chalcopyrite in the base of the turbidity sequence *Ta* (FIGURE 5.4D). Chalcopyrite disease (Barton and Bethke, 1987;

Bortnikov et al., 1991) is present as fine chalcopyrite intergrowths or disseminations in sphalerite that may result from replacement or co-precipitation in the presence of high-temperature Cu-rich fluids and is typical for seafloor and VMS deposits.

5.5.3 Geochemistry

Combined XRF chemostratigraphy (APPENDICES C.1.4) and bulk analyses (APPENDICES C.1.4 and C.2.1) show that the sedimentary cover of carbonate ooze in all environments contains an average of 25 wt% Ca, with up to 23 wt% of Fe and the two elements show a strong negative correlation (R^2 = -0.92). Other metals that are present in the ooze are Mn (mean 0.19 wt%), Cu (mean 0.66 wt%), Zn (mean 0.08 wt%), Co (mean 26 ppm) (APPENDICES C.1.6 and C.2.1). Statistical analyses of correlation of the ITRAX data (APPENDIX C.1.10.) show that Cu and Zn are preferentially related to Fe (R^2 = 0.71 and 0.88, respectively), while Co is correlated to Cu (R^2 = 0.67).

On the top of the mounds, horizons with a maximum enrichment in Mn are found in unit M2 (FIGURE 5.5A, APPENDICES C.1.6 and C.2.1), *e.g.* with 15 wt% Mn at Southern mound (16GC), and 20 wt% Mn at Rona mound (27GC). Unit M2 also shows the highest and most variable content in trace metals (TMs), for example sediments at Rona mound are enriched in Cu (1.3 wt%), Zn (0.3 wt%) and Co (270 ppm). At those sites Cu and Co strongly correlate with Mn-phases in unit M2 (R^2 = 0.89 and 0.8, respectively, for the core 16GC, (APPENDIX C.1.4). The deeper units, M3/M4, have low to negligible contents of TMs (Cu 0.11 wt%, Zn 0.1 wt% Zn, Co < 1 ppm and Mn 0.16 wt%). Zn ranges from 250 to 3000 ppm and its behaviour is complex as its content in the M2 unit varies compared to the other units. For example, at Rona mound, Zn concentrations are higher in unit M2 (0.3 wt% Zn), but not at Southern mound.

In the sediments from the base of the slope of the SMS mounds (i.e. from the Mir zone fan, core 39GC, FIGURE 5.5B and APPENDIX C.1.6) the metal content is variable: e.g. Fe (25 to 35 wt%), Zn (0.10 to 0.40 wt%), Cu (6 to 28 wt%), and Co (up to 100 ppm), while Mn and Ca contents are in general low (< 0.05 wt% and < 0.7 wt%, respectively). At 30 cm, close to the bottom of core 39GC, the Cu, Co, Zn and S contents increase, confirming the presence of sulphide minerals (*e.g.* pyrite and chalcopyrite) found in the mineralogical analyses. Statistical analyses show that Cu, Co and Zn are preferentially found in sulphide minerals (R^2 = 0.75, 0.80 and 0.52, respectively), rather than Fe phases (R^2 = -0.88, -0.78 and -0.62, respectively) (APPENDIX C.1.4).

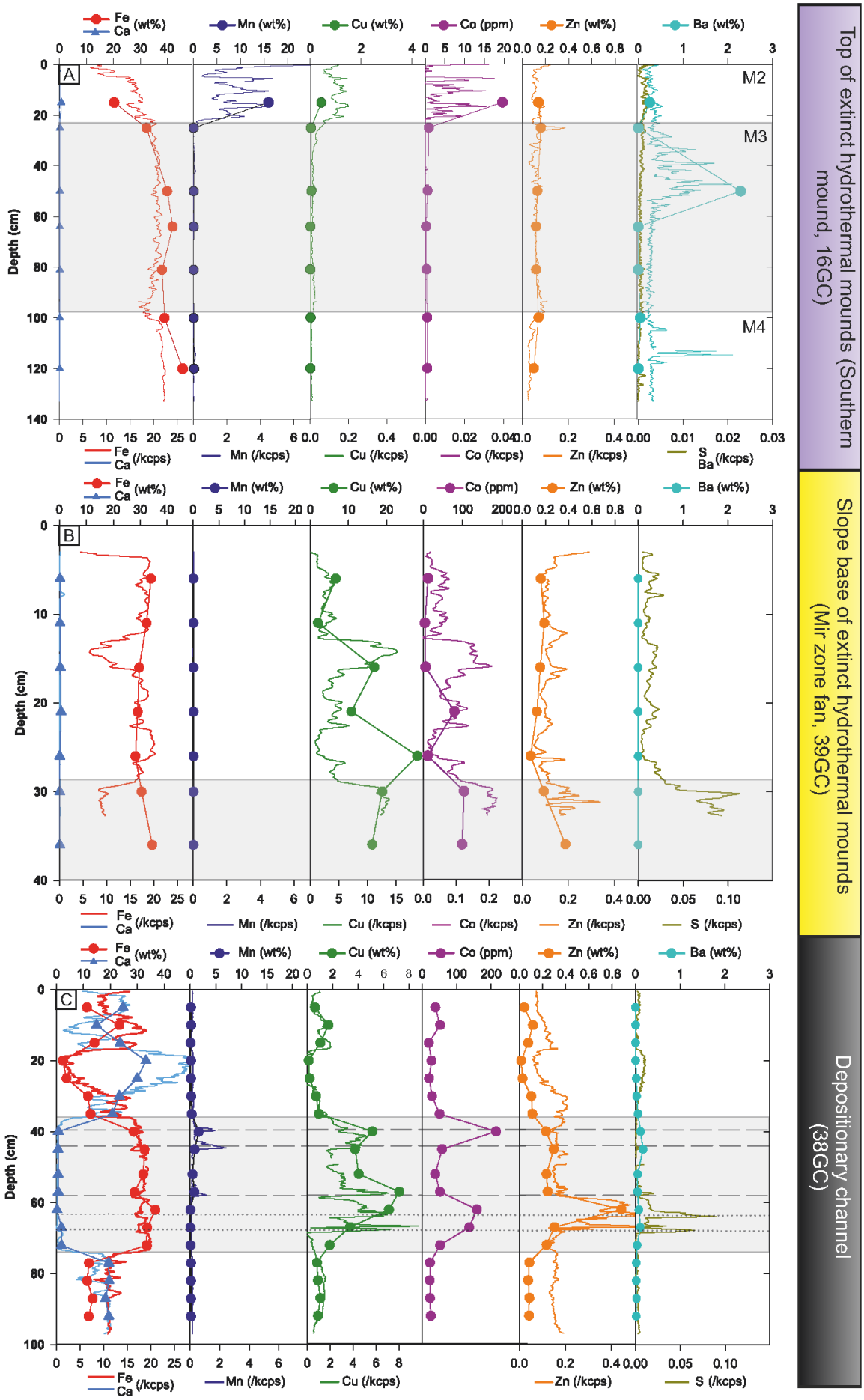
Top of extinct hydrothermal mounds (Southern mound, 16GC)
Slope base of extinct hydrothermal mounds (Mir zone fan, 39GC)
Depositionary channel (38GC)
A
B
C
M2
M3
M4
Depth (cm)
Fe (wt%)
Ca (wt%)
Mn (wt%)
Cu (wt%)
Co (ppm)
Zn (wt%)
Ba (wt%)
Fe (/kcps)
Ca (/kcps)
Mn (/kcps)
Cu (/kcps)
Co (/kcps)
Zn (/kcps)
S (/kcps)
Ba (/kcps)

FIGURE 5.5 (previous page) Geochemistry down-core profiles. ITRAX chemostratigraphy (solid lines) and ICP-OES and ICP-MS sediment geochemistry from selected samples (dots) profiles from the three different environments: (A) On the top of an extinct mound (Southern mound, 16GC), (B) at the base of a slope (Mir Zone fan, 39GC), (C) in the depositional channel (38GC). Note the different scales of Cu and of Co in the different panels. Shaded depths correspond to the lithology units in the text for (A) and FIGURE 5.3. Dashed lines in (C) correspond to Mn-rich layers and the dotted lines correspond to sulphide layers. Unit M1 was not recovered at the 16GC coring station in (A).

In the depositional channel (core 38GC, FIGURE 5.5C, APPENDICES C.1.4 and C.1.6), the Fe content in the shallow pelagic unit is variable (up to 25 wt%), and directly related to the presence of various iron-oxyhydroxide phases and inversely proportional to the Ca (carbonate) content (R^2 = -0.99) (APPENDIX C.1.4). Cu, Co and Zn contents are also directly proportional to the Fe content (R^2 = 0.91, 0.72 and 0.55, respectively). In the turbidite layers, numerous peaks in S content correlate with sulphide mineral-rich horizons (58 cm, 64 cm and 68 cm, FIGURE 5.4D) that also contain enrichments in Cu and Zn (up to 7.23 wt% and 0.88 wt%, R^2 = 0.57 and 0.68, respectively) (APPENDIX C.1.4). Mn is also enriched in the sediments from the depositional channel, but limited to three horizons, *e.g.*: at 40 cm (1.66 wt%), 45 cm (0.85 wt%), and 58 cm (0.83 wt%) in which Cu and Co contents also increase up to 7 wt% and 200 ppm, respectively. In a second core (core 49GC), collected 250 m away from core 38GC, metal contents and distribution were similar with up to 10 wt% Cu in the sulphide and Mn-rich horizons. The concentrations of Cu, Zn and Co in these different sedimentary environments are comparable with that of massive sulphides collected from the Alvin zone and the Mir zone (TABLE 5.3).

To understand the contribution from different sources of metals to the depositional channel, the geochemistry of cores 38GC, 39GC and 49GC, is plotted in a ternary Cu-Zn-Fe plot (FIGURE 5.6 Ternary Cu-Zn-Fe diagram.) together with that of mound-top material and typical black and white smokers (TABLE 5.4). The plot illustrates that (i) mound-top material is almost entirely made of Fe, (ii) black smokers are made of Fe and Cu and (iii) white smokers are the only source providing Zn into the system.

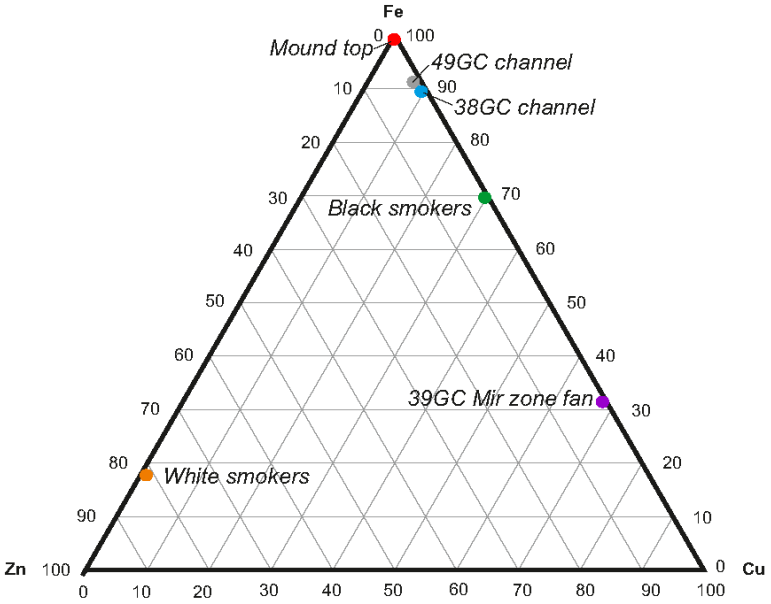

FIGURE 5.6 Ternary Cu-Zn-Fe diagram. Average concentration from black smokers, white smokers (data are provided in APPENDIX C.3), mound-top material (from top of the extinct mound, this study) and the depositionary channel 49GC core are plotted.

TABLE 5.3 Composition of the massive sulphides from Rona mound, Southern mound, Mir zone and the sediments from the depositional channel and the Mir zone fan (detailed data in APPENDIX 223C.3). We regard the SMS samples as representative for the total range of geochemical compositions found at the mounds. N is the number of samples. Source: [1]Blue Mining geochemical analyses provided in APPENDIX 223C.3 (Murton *et al.*, 2019) , [2](Rona *et al.*, 1993b; Krasnov *et al.*, 1995; Petersen, 2000; Hannington *et al.*, 2004); [3]this study.

TAGHF	**Alvin zone massive sulphides (Rona mound)[1]**		**Alvin zone massive sulphides (Southern mound)[2]**		**Depositional channel (38GC, 49GC)[3] Sediments**		**Mir zone massive sulphides [2]**		**Mir zone fan[3] sediments**	
Element	range (min-max)	avg.	range	avg.	range	avg.	range	avg.	range	avg.
Cu (wt%)	0-10.9	1.75	0.1-5.7	2	0.1-10.3	2.3	0-26.8	12.25	2-28	14.2
Zn (wt%)	0-8.4	0.66	0.1-0.5	0.3	0-1.9	0.3	0-22	3.76	0-0.4	0.2
Co (ppm)	2-348	145	10-1610	552	15-214	57	2.5-1100	113	4-104	45
N	17		19		56		30		7	

TABLE 5.4 Average concentrations of Fe, Cu and Zn for the depositional channel and the Mir zone fan (this study), active TAG black smokers and active TAG white smokers (for the compilation data, refer to APPENDIX 223C.3). We consider the Ca concentration to be zero in chimney material, assuming anhydrite is quickly dissolved before deposited in the sediments. Ca concentration in the pelagic sediments (assuming it consists of 100% calcium carbonate) at TAG is around 40 wt%. The three columns on the right-hand side indicate the ratio of each element on a base of Fe, Cu and Zn, and as represented in the ternary diagram Fe-Cu-Zn (FIGURE 5.6). Source: Krasnov *et al*. (1995); Tivey *et al*. (1995); Petersen (2000), and Geological Survey of Canada.

Source/ sample	N	Fe wt%	Cu wt%	Zn wt%	Ca wt%	$\frac{Fe}{Cu+Zn+Fe}$	$\frac{Cu}{Cu+Zn+Fe}$	$\frac{Zn}{Cu+Zn+Fe}$
Depositional channel (49GC)	16	28	2.3	0.4	5	91.15	7.49	1.37
Depositional channel (38GC)	18	19.66	2.23	0.18	14.07	89.07	10.11	0.82
Mir zone fan (39GC)	7	14.19	31.16	0.18	0.25	31..17	68.44	0.40
Black smokers	21	24.6	10.6	0.2	/	69.57	29.86	0.57
White smokers	42	9.9	0.6	45.3	/	17.74	1.00	81.26
Mound-top sediment	7	35.1	0.1	0.1	/	99.32	0.34	0.34
Pelagic sediment	/	/	/	/	40			

The solution from three simultaneous linear equations (Eq. 5.5, 5.6 and 5.7) is used to determine the relative contributions from different sources to the sediments sampled by the gravity cores 38GC and 49GC and indicates that for both ~21% of sediments are originally from black smokers material and less than 1% (respectively 0.20 and 0.69%) from white smokers material. However ~41% is derived from mound-top material for core 38GC and 65% for core 49GC (APPENDIX C.3.1).

Fe wt% in the core = 24.6 [BS] + 9.9 [WS] + 35.1 [MD] (Eq. 5.5)

Cu wt% in the core = 10.6 [BS] + 0.6 [WS] + 0.1 [MD] (Eq. 5.6)

Zn wt% in the core = 0.2 [BS] + 45.3 [WS] + 0.1 [MD] (Eq. 5.7)

Where BS is the percentage of black smokers as a source, WS is the percentage of white smokers as a source, MD is the percentage of mound-top sediments as a source.

The non-resolving equation system for sediments in 39GC Mir zone fan (as it stands outside of the triangle formed by mound top - white smokers - black smokers in FIGURE 5.6) requires

a different composition of one of the sources (massive sulphide) with a material that was initially richer in Cu (APPENDIX C.3.1).

5.5.4 Rare earth elements and Yttrium

REE patterns of marine sediments are useful to test for the effects of hydrothermal input and sediment-seawater interaction; positive Eu anomalies are inherited from hydrothermal fluids whereas negative Ce anomalies are inherited from seawater. Yttrium was also considered as indicator for seawater influence as it has geochemical behaviour similar to that of other REEs and is placed between Dy and Ho in the REE distribution plots. Positive Y anomalies are indicators for mixing of hydrothermal fluids with seawater during upflow because iron oxyhydroxides preferentially scavenge REE by which does not include Y (Bau and Dulski, 1999). Together, Y-REEs are plotted against fluids and other sediments from the TAGHF in FIGURE 5.7 (APPENDIX C.1.7). Pelagic sediments with elevated iron contents, such as in the graded bedding of the depositional channel (FIGURE 5.3E), have a positive Eu anomaly (FIGURE 5.7A). The Y-REE pattern for the Mn-oxide rich unit, M2, shows both a positive Eu, a negative Ce anomaly (FIGURE 5.7B) and a positive Y anomaly. Units M3 and M4, that are exclusively composed of Fe oxyhydroxides, have similar REE patterns, with concentrations that range over an order of magnitude, but are lower than those in the pelagic sediment of M1, and exhibit a weak negative Ce anomaly, a weak positive Y anomaly and a strong positive Eu anomaly (FIGURE 5.7C). The lowest Y-REE concentrations are found in sulphide clasts in sediments from the slope base of the mound (Mir zone fan) and have a positive Eu anomaly, but do not show any Ce or Y anomalies (FIGURE 5.7C).

5.5.5 Pore water geochemistry

To test for the presence of hydrothermal fluids within the sediment, dissolved Mg, Cl and SO_4 concentrations were measured in pore waters (dissolved Ca was not used as it can be influenced by pelagic carbonates). Pore waters in the sediments from all three studied environments, exhibit constant concentrations of these components with depth and are similar to the composition of seawater collected from immediately above the seafloor (57 mmol/L Mg, 594 mmol/L Cl and 29.4 mmol/L SO_4) (FIGURE 5.8, APPENDICES C.1.8 and C.2.2).

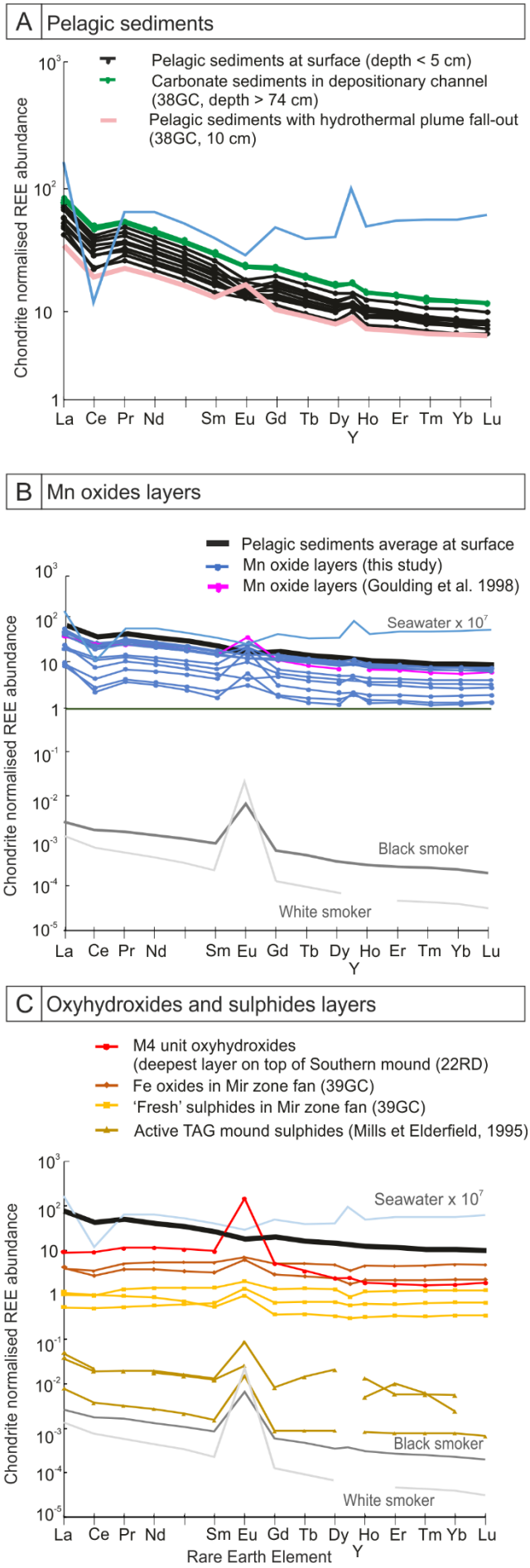

FIGURE 5.7 Y-REE distribution.

(A) Chondrite normalised Y-REE data for TAGHF carbonate sediments at the surface (negative Ce/Ce* and Eu/Eu*), at depth (negative Ce/Ce*) and containing hydrothermal plume fall-out (positive Eu/Eu*). (B) Chondrite normalised Y-REE data for TAGHF Mn-rich layers (positive Eu/Eu* and negative Ce/Ce*) (blue circles), and background sedimentation (black line). (C) Chondrite normalised Y-REE data for TAGHF sediments for oxides and sulphides. Y-REE abundance increases from TAG mound 'fresh' sulphides (triangle dots), followed by 'fresh' sulphides recovered in the 39GC (see FIGURE 5.4D) in the Mir zone fan (positive Eu/Eu*, no Ce/Ce*) (yellow square) towards oxides collected with the sulphides (positive Eu/Eu*, negative Ce/Ce*) (brown diamond) and finally oxyhydroxide layers collected from M4 (positive Eu/Eu*, negative Ce/Ce*) (red circle). The highest Eu/Eu* (=29.35) was found in the deepest M4 unit next to the Fe-rich silicified layer at Southern mound. Reference data for seawater (North-Atlantic Deep waters) scaled by 10^7 is provided by German *et al.* (1990) and Mitra *et al.* (1994); black smokers by Douville *et al.* (1999); White smokers by Mitra *et al.* (1994); Mn oxides by Goulding *et al.* (1998); TAG mound sulphides (white smoker chalcopyrite, black smoker chalcopyrite and massive pyrite average) from (Mills and Elderfield, 1995b).

To test for microbial or diagenetic changes (*e.g.* carbonate dissolution), the total alkalinity (TA) of the sediments was also measured. Sediments from the top of the mounds have a TA similar to seawater (2.4 mmol/L, FIGURE 5.8A). In contrast, in the sediments at the slope base (*e.g.* Mir zone fan) TA decreases from 2 mmol/L towards 0 at 30 cm (FIGURE 5.8B) and in the depositional channel, TA almost doubled with depth from bottom seawater values (2.4 mmol/L) at the surface to 4 mM at a depth of 70 cm (FIGURE 5.8C).

Dissolved TMs (Fe, Mn, Zn, Co and Cu) were analysed to test for dissolution and mobilisation of metals from the host sediments. Throughout the cores on the top of the mounds, TMs were found to have low concentrations with no distinctive trends (FIGURE 5.8A). In contrast, sediments from the slope base of the mound (Mir zone fan) have between one and three orders of magnitude higher concentrations of dissolved TMs than in the environments from the top of the mounds or in the depositional channels. In general, Mn and Co decrease with depth, while Zn and Cu increase, and Fe remains constant (FIGURE 5.8B). Maximal concentrations found are: Fe (3052 µmol/L), Mn (21.1 µmol/L), Zn (39 µmol/L), Cu (49.2 µmol/L), and Co (274 nmol/L). In the depositional channel (38GC, FIGURE 5.8C), Fe is low (mean of 2 µmol/L), and Zn variable with a maximum of 4.2 µmol/L. Below 60 cm depth, Mn and Cu concentrations increase with depth from <1 µmol/L up to 38.5 and 27.9 µmol/L respectively, and Co increases from <0.1 nmol/L up to 32 nmol/L.

FIGURE 5.8 (next page) Pore water geochemistry down-core profiles for Mg, Fe, Mn, Cu, Co, Zn (dots), Cl (crosses), TA (crosses) in the three different environments: (A) On the top of an extinct mound (Southern mound, 16GC), (B) At the base of a slope (Mir Zone Fan, 39GC). (C) In the depositionary channel (38GC). Note the change of content scale for Cu and Co to maximise the variation visibility. Sediment chemostratigraphy (solid lines) are plotted to highlight the relationship between the pore water and solid phases. Shaded depths correspond to the lithology units in the text for (A) and FIGURE. 5.3. Dashed lines in (C) correspond to Mn-rich layers and the dotted lines correspond to sulphide layers.

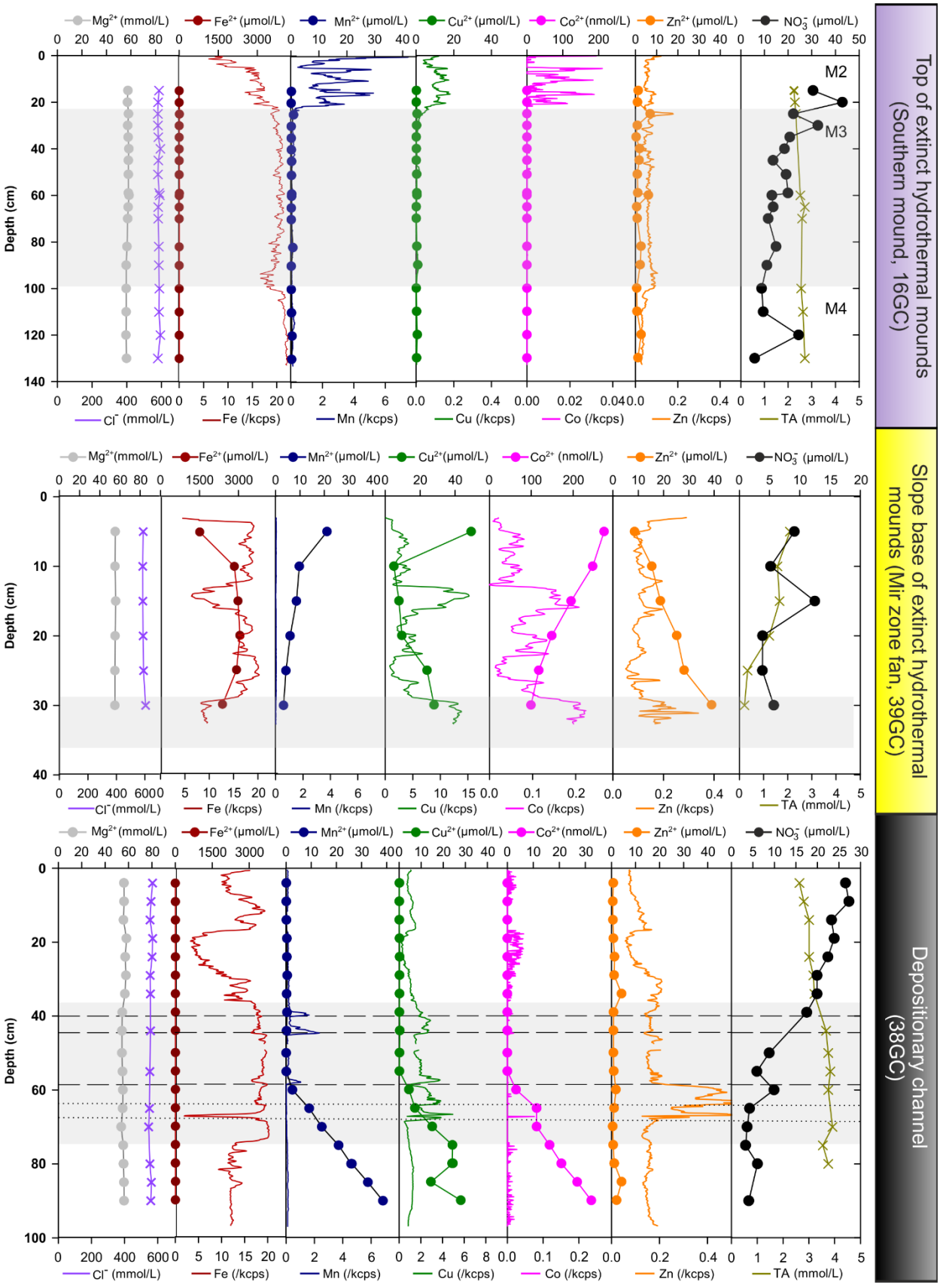

FIGURE 5.8 Pore water geochemistry down-core profiles.

In the depositional channel (38GC), NO_3, which when decreasing can be used as an indicator for microbial activity (i.e. denitrification or nitrate reduction), was found to have concentrations typical of the North Atlantic Deep Waters (Hansell and Follows, 2008) at the sediment surface, but was nearly absent (3 µmol/L) at 120 cm depth (FIGURE 5.8C). In the same core (38GC), NH_4 concentrations show a peak of 38 µmol/L at 25 cm (APPENDIX C.1.8) indicating decomposition of organic matter by denitrification. At Southern mound (16GC) and the Mir zone (28GC), the NOx concentrations also decrease from 43 µmol/L to 6 µmol/L (at 130 in cm depth) and 25 µmol/L to 3 µmol/L (at 178 cm in depth), respectively (FIGURE 5.8A) (Pore water species concentrations are given in APPENDICES C.1.8, C.2.2 and C.2.3). In all cores analysed, the dissolved sulphide concentration was below 2 µmol/L, which is close to the detection limit (LOD = 1 µmol/L) and hence the data are not shown.

5.6 Discussion

At the TAGHF, metalliferous sediments are present at the tops of hydrothermal mounds, their slopes and beyond their bases where they are found to be accumulated in distal channels. Despite a common source, *i.e*. hydrothermal activity, we find distinct differences in the contents and distribution of metals in the sediments occupying the different depositional environments. These differences indicate distinct mechanisms for metal preservation and re-mobilisation, related to transport and later diagenetic processes. Ultimately, these mechanisms will determine if the deposits could present a potential resources for these base metals.

5.6.1 Origin and controls on the distribution of the metalliferous sediments

At the TAGHF, the lowest contents of non-ferrous metals, including Cu, Zn or Co, are found in the hydrothermal sediments on top of the mounds. For example, the average Cu content (0.11%) is 2 orders of magnitude lower than at the base of the mounds (14.2 wt%), and one order of magnitude lower than in the depositional channel (2.2 wt%). Sulphide minerals were not detected in sediments from the tops of the mounds, but in the more distal environments Cu is associated with sulphide phases present in coarse sandy layers. Although Fe oxyhydroxides may also precipitate from low-temperature hydrothermal fluids (*e.g*. Hein *et al*., 2008; Laurila *et al*., 2014), and despite the low abundance of non-

ferrous metals in the mound top sediments, a hydrothermal origin is demonstrated by both a positive Eu anomaly of the Fe-oxyhydroxide layers (FIGURE 5.7C), inherited from high-temperature hydrothermal fluids (Klinkhammer *et al*., 1994; Mills and Elderfield, 1995b), and by the presence of detrital barite crystals that originated from high-temperature hydrothermal chimneys (Griffith and Paytan, 2012) (FIGURE 5.4A). Hence, the evidence points to the metalliferous sediments on top of the mounds originating from the weathering of the sulphides that in turn were derived from the collapse of high-temperature hydrothermal sulphide chimneys. During weathering and oxidation, Cu and Zn have been lost by dissolution and iron sulphides were replaced by insoluble iron-oxyhydroxides leading to an overall depletion of non-ferrous metals compared to hydrothermal sediments preserved in the other environments across the TAGHF (FIGURE 5.9A).

In contrast, the presence of sulphide grains in the coarse grain sand layers at the base of the slopes suggests that part of the hydrothermal material was transported downslope and buried before it could be fully weathered (FIGURE 5.9B). We suggest such physical mass wasting resulted from the disintegration of chimney material. It has been suggested for other hydrothermal systems that the degree of physical disintegration of sulphide minerals, and the thickness of depositional beds, and the degree of grain-size sorting, is directly proportional to the distance the material has been transported (Webber *et al.*, 2017). For example, in the Mir zone fan, centimetre-thick layers of unsorted sulphides sands intermixed with fine-grained Fe oxyhydroxides were observed. This indicates a proximal type of sedimentary facies typical of rapid deposition. The absence of biogenic or detrital (non-hydrothermal) components further implies rapid deposition compared with the background pelagic sedimentation rate (*i.e*., ~8 cm/ka for a sedimentation enriched in vent-derived particles) (Metz *et al*., 1988). The triggering mechanism of such mass wasting, rapid transport, and deposition was most likely slope instability, induced by steep topography (e.g. growth of hydrothermal chimneys), active tectonism (mid-ocean ridge seismicity), and/or high sedimentation rates (Shanmugam, 2018). These processes are common close to active hydrothermal mounds. For example, unsorted sulphide-rich horizons are often present in sediments recovered from around the active TAG mound (push-core AT129; FIGURE 5.1) (Mills *et al*., 1996; Petersen, 2000). Similarly, at the Beebe Vent, at the Mid-Cayman Spreading Centre, sediments rich in coarse grained sulphides and fine grained iron oxides have been recovered from seafloor depressions located within a 100 m of the active hydrothermal sulphide mounds (Webber *et al.*, 2015). Hence, the base of slope of SMS mounds form environments that lead to more rapid accumulations of sulphides and metals

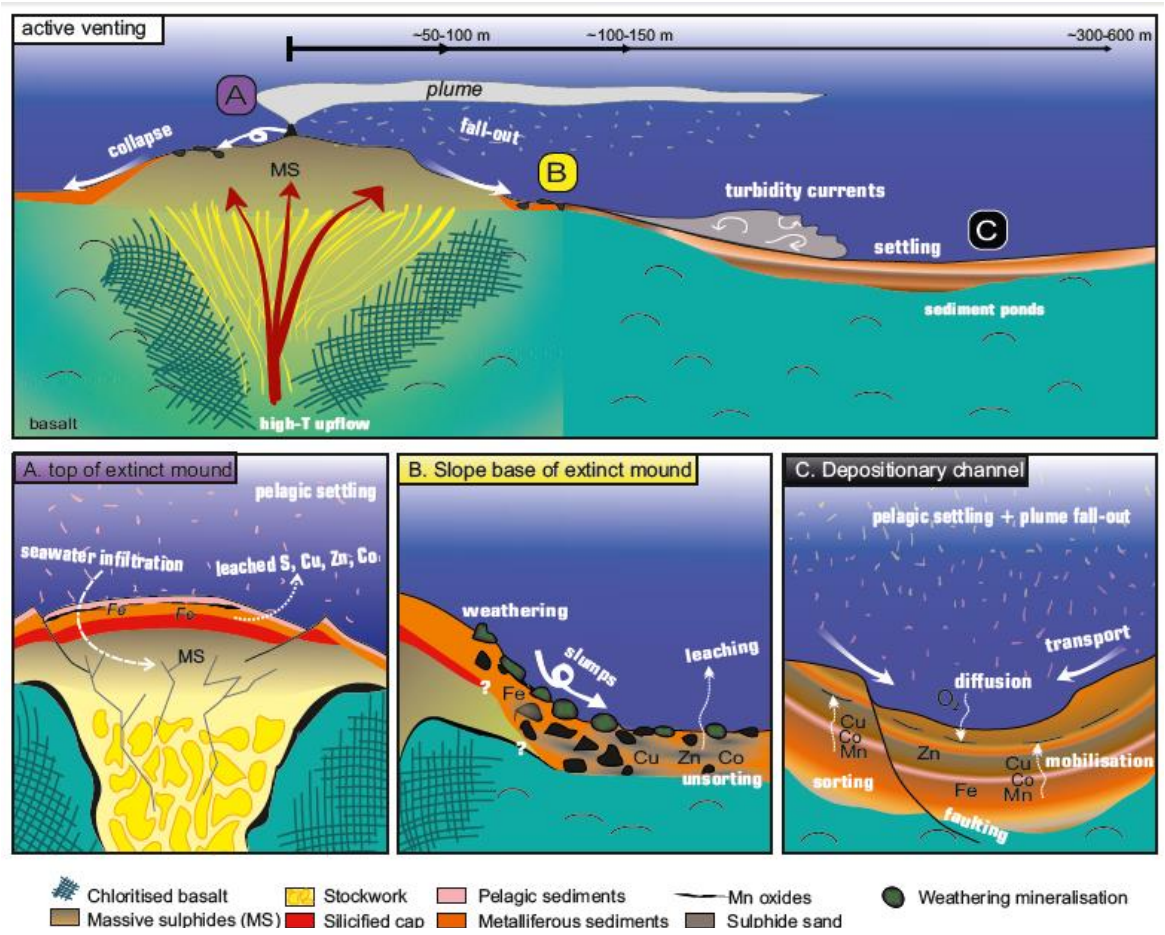

FIGURE 5.9 Conceptual illustration for three distinct seafloor environments found at the TAGHF. A) At extinct hydrothermal mounds, the sediment cover is exclusively composed of Fe oxyhydroxides, originating from sulphide oxidation. Low-temperature venting is responsible for the formation of Mn-oxide crusts within the sediments, while seawater infiltration is responsible for metal leaching; B) At the base of extinct hydrothermal mounds, the sediment cover is thin and composed of unsorted Fe-oxyhydroxides mixed with sulphides and secondary weathering minerals (*e.g.* atacamite, jarosite) provided by constant collapse or slumps due to the steep topography. Sulphidic sediments are dominant and metals are mobilized and can be released to the water column. The boundaries between the sediments, the silica cap, the massive sulphides and the basaltic crust in (A) and (B) are inferred ; C) At further distance, in distal depositionary channels, repetitive mass wasting during turbidity events has brought material into depressions where sulphide, oxides and pelagic sediments are accumulated in thin, sorted layers. After rapid burial, early diagenesis takes place, oxygen diffuses in the sediments and an oxic/suboxic boundary develops where Mn, Co, Cu, that diffuse upward from a deeper source, precipitate. A range of distances where we find the different environments at the TAGHF are expressed in meters.

contents are ~100 times greater compared to the tops of the mounds, where the metals were largely lost due to weathering and leaching.

Beyond the base of slope of the SMS mounds, metalliferous material is transported in turbidity currents that eventually deposit sediments in distal (over 100's - 1000's m) ponds and channels. For example, in core 49GC from the TAGHF depositional channel (located 100's m from the SMS mounds), the sediments are sorted in fining-upward sequences, with heavy sulphide sands originating from hydrothermal chimneys forming the basal layers and finer clays and oxyhydroxide particles at the tops, indicative of turbidity current transport and deposition (FIGURE 5.3F). The presence of some eroded basal layers and the absence of interbedded, background pelagic (carbonate) sediments indicates the rapid deposition and accumulation of these metalliferous sediments, which are comparable to those described in stratiform VMS deposits at the Tharsis, Iberian Pyrite Belt (Barriga and Carvalho, 1983). At even greater distances ($\geq$ 500 m from the SMS mounds, e.g. core 38GC) the proportion of pelagic sediment increases, where it often forms distinct calcareous layers in between thin metalliferous ones. In summary, the presence of consecutive turbidite layers and metal contents in the depositional channel up to 20 times higher than that on top of the mounds highlights the important role of mass wasting and sedimentary transport processes in enriching metalliferous sediments that are moderately distal to hydrothermal SMS mounds.

To test if the metalliferous sediment layers are derived from the nearby SMS mounds, their compositions are compared to massive sulphide and Fe oxyhydroxide samples collected from the tops of adjacent SMS mounds (TABLE 5.3, the calculations based on Eqs. 5.5, 5.6 and 5.7, and FIGURE 5.6). In seafloor massive sulphide hydrothermal systems, compared with the massive sulphide within the mound, high-temperature 'black smoker' chimneys are richer in chalcopyrite and are the primary source for Cu, while lower-temperature 'white smoker' chimneys are richer in sphalerite and the primary source of Zn (Webber *et al.*, 2015). At the TAGHF, we have shown that when weathered and completely oxidized, these sulphides effectively become barren and composed almost entirely of Fe oxyhydroxide.

In the TAGHF depositional channel, Cu, Zn, and Co contents are significantly higher (TABLE 5.2) than in sulphides recovered from the nearby Southern mound (FIGURE 5.6). This may be explained by the sulphides recovered from Southern mound not being representative of the metalliferous sediments in the depositional channel (i.e. the primary chimney material has been lost). Alternatively, the sediments are composite and derived

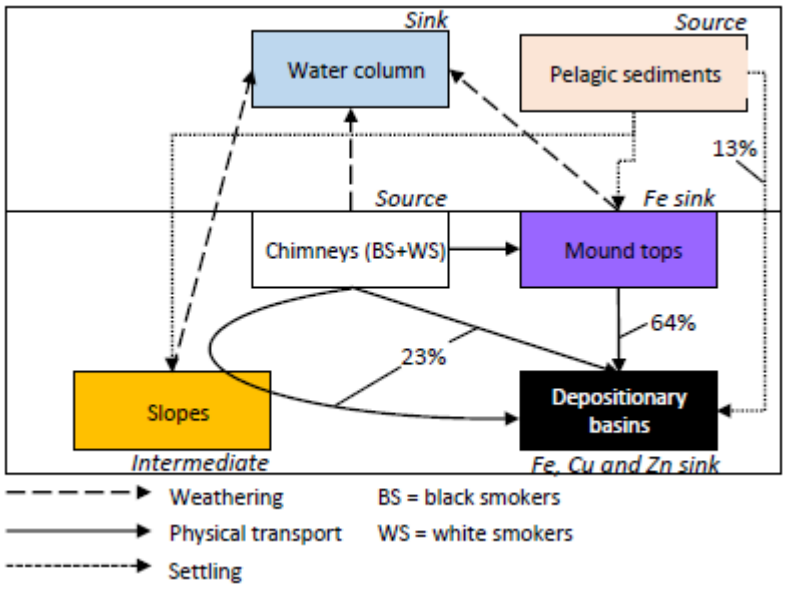

FIGURE 5.10 Simplified box model representing the different processes occurring in a hydrothermal system. Percentages describe the proportion of material from each source (chimney material, mound-top material and pelagic sediments) for metals (Cu, Zn and Fe) to form the sediments of the gravity core 49GC in in the depositionary channel. Those numbers will fluctuate with distance from the hydrothermal source. BS and WS refers to black and white smokers respectively.

from several sources, for example incorporating material from neighbouring SMS deposits such as the Rona mound apparently richer in Zn and Cu (TABLE 5.3).

Contributions from different sources in the depositional channel (FIGURE 5.6, TABLE 5.4 and APPENDIX C.3.1) show that 49GC and 38GC are similar with a greater proportion in Fe (between 40 and 65% as fine-grained oxide/hydroxides), about 20% are sediments rich in Cu and less than 1% of sediments are rich in Zn. We interpret that they originated mainly from the weathered mound-top material rather than from sulphide chimneys (FIGURE 5.10). At the Mir zone fan, the metalliferous sediments have a similar composition to the massive sulphides exposed and preserved on the top of the Mir zone mound, indicating this as their likely provenance (TABLE 5.3).

My results point to four main processes contributing to the metalliferous sediments at the TAGHF: (i) the mixed assemblage of coarse sulphide sands and fine-grained iron-oxyhydroxide in the depositional channel indicates that these sediments were derived from mound tops where hydrothermal sulphide structures were being actively eroded and the sulphides had already formed a significant proportion of gossan material. (ii) The supply of weathered material (gossan) into the depositional channel varied, indicate sources in

different stages of weathering and hydrothermal activity. (iii) The MIR zone delta sediments reflect a source that had little weathering and was comprised mainly of primary sulphide. (iv) 13% to 38% of the material in the sediments is not of hydrothermal sulphide origin and probably derived from pelagic sediments and detrital material (*e.g.* volcanoclastic). As an example (APPENDIX C.3.1), if we include pelagic sediments as an end-member in our calculations, which contain about 40 wt% Ca, we can explain the observed 5.2 wt% Ca in the depositional channel sediments by the addition of 13% of pelagite (TABLE 5.4).

In addition to downslope transport, fine-grained, particulate hydrothermal plume fallout may add to the metal content in all the sediments in the TAGHF. Plume-derived input is differentiated from sediments derived from weathered and oxidized sulphide deposits by their sorted, clay-size particles (APPENDIX C.1.1). Plume fallout is particularly visible in pelagic sediments, with up to 10 times increase in Fe concentration (FIGURE 5.3E), compared with background pelagic carbonate, and accompanied by an Eu anomaly (FIGURE 5.7A) typical for plume fall out (German *et al.*, 1993; Mills and Elderfield, 1995a). While the distribution of plume-derived fallout depends on the distance from the hydrothermal source and velocity and variability of deep oceanic currents, its vertical distribution in the sediment column is attributed to changes in the intensity and episodic nature of hydrothermal activity in the area (FIGURE 5.1C) (Metz *et al.*, 1988).

5.6.2 Diagenetic impacts on metal mobilisation

5.6.2.1 Sulphide weathering and metal release to the water column

To determine the ultimate fate of the metals in these deposits, it is important to understand the degree of diagenesis affecting metalliferous sediments shortly after deposition. During burial, these can undergo diagenetic alteration resulting in a re-dissolution of metals and their release into the water column. These processes can be driven by the penetration of oxic seawater into the sulphide-rich sediments resulting in diagenetic alteration by oxygenation. Reducing and acidic conditions can occur at depth in the sediments where seawater penetration is limited. Microbial activity can also generate conditions for sulphide dissolution. The distribution of metals in the sediment requires additional processes such as diffusion (slow) or advection (fast). All of these processes can be assessed from vertical profiles of pore water composition and comparing their metal concentrations with co-

existing solid phases. Indications of biotic processes can be derived from analysis of total alkalinity (TA) and nitrate (NO_3).

All of these processes are indicated for the Mir zone fan, where the thickest accumulation of sulphide-rich sediments is found. Here, metals (Fe, Mn, Cu, Co and Zn) are dissolved in pore waters in high concentrations, compared with seawater, and their concentrations vary independently of the solid phase (FIGURE 5.8B). Two different behaviours of dissolved metal cations in pore waters are observed below the surface, and occur regardless of changes in concentrations in the solid phase. Over a depth interval of 30 cm, Zn and Cu increase with depth while Co and Mn decrease monotonically. Co, Cu and Mn are redox sensitive elements that behave in a similar way, hence their contrasting trends cannot be attributed solely to changes in oxidation state. Instead, we interpret the increasing concentration of Zn and Cu to non-equilibrium processes affecting the host sulphide minerals. For example, the increase in dissolved Zn is consistent with ongoing dissolution of sphalerite at depth, as well as decreasing pH. In experiments, it was found that the rate of sphalerite dissolution is reduced by the presence of a protective oxidative layer on the mineral surfaces (most likely Fe oxides) (Knight *et al.*, 2017). We suggest that rapid oxidation of sphalerite nearer the seafloor (immediately following deposition) results in decreased rates of current dissolution, compared to greater depths in the sediment column where seawater ingress was less and pH is allowed to increase. A similar process, involving mineral stability, affects dissolved Cu concentrations. Further evidence for acid attack is found in pitting and tarnishing of the chalcopyrite crystals in the sulphide sands at the base of the Mir zone fan sediment core (FIGURE 5.4B and FIGURE 5.4C). We suggest these low pH conditions are maintained by the continuous release of acidic fluids from sulphide oxidation and dissolution in the sediments caused by the partial and limited ingress of seawater into the sediments (Ridley, 2012). Furthermore, the REE-Y signatures of the sulphides at the Mir zone delta (FIGURE 5.7C) do not show a negative Ce anomaly or a positive Y anomaly, suggesting that they had little opportunity to equilibrate with seawater and hence are relatively 'fresh' primary hydrothermal precipitates.

In contrast to the Mir zone fan sediments, those in the upper 60 cm of the depositional channel have low concentrations of Co, Cu Mn and Zn in their pore waters, despite having these elements in the solid phase, especially Zn (*e.g.* in sphalerite) (FIGURE 5.8C). The absence of these dissolved metals in the pore waters indicates oxygen penetration down to 60 cm below the seafloor. Below this depth, the redox elements increase in concentration,

indicating reducing conditions. However, concentrations of dissolved Zn remain low, suggesting that pH conditions are not sufficiently low to support Zn in solution, even in the lower part of the sediment pile where anoxic conditions prevail. Alternatively, the sphalerite deep in the sediments are reworked and already protected from further dissolution by the formation and growth of an oxidative coating (Knight *et al*., 2017), as well as being predominately low-Fe sphalerite that is more resistant to oxidation (Weisener *et al*., 2004; Knight *et al*., 2017).

In a system that is continuously open to seawater circulation, the resulting acidity would be neutralised and the resulting dissolved metals would be removed and lost to the larger reservoir of ocean water (Ridley, 2012). We suggest these conditions pertain to the mound-top sediments due to the absence of sulphides. In those sediments, sulphide weathering is completed and pore waters no longer contain any dissolved TM, indicating a stable, oxic environment. This is further demonstrated by the seawater-like composition of major ions (*i.e*. Cl, Mg, SO_4) in pore waters indicating complete seawater ingression into the sediments and equilibrium between pore waters and ocean bottom waters.

To explain the dissolution of supergene sulphides, we suggest weathering processes in the mound-top sediments were once similar to those affecting the sulphides on the mound slopes and bases. In these environments, trace metals are leached into the water column, leading to a metal depleted deposit that is typically referred to as a gossan (Herzig *et al*., 1991). Initially, gossans have a high porosity and permeability due to the agglomeration of coarse particles (Goulding *et al*., 1998), such that seawater circulates through the sediments resulting in oxidative weathering. Not all the mobilized metals are lost and some (*e.g.* Cu and Co) are re-adsorbed on Mn oxides in the upper layers of the gossan (*e.g*. Murray, 1975; Balistrieri and Murray, 1986). However, degree of element exchanges between sulphide weathering, Mn oxide scavenging and the water column release is still largely unknown.

Elsewhere, the presence of a pelagic carbonate sedimentary unit (M1) can act as a buffer for both TA and pH and would trigger precipitation of metals from the pore fluids (*i.e.* acting as a pH barrier) (Ridley, 2012). However, carbonate sediments are largely absent from the mound slopes. As a result, the sulphidic sediments in these environments are unprotected from seawater oxidation and the resulting dissolved metals are free to diffuse upward in the water column. Together, these conditions release Fe, Mn, Cu, Zn and Co into pore waters until, or unless, the deposit is isolated from further seawater interaction by burial.

5.6.2.2 Redox zonation and metal re-distribution

Redox processes within the TAGHF metalliferous sediments can determine the state of dissolution or precipitation of Cu, Co and Mn and advection and diffusion can decouple the concentration of these cations from the surrounding solid phases. Mn-oxide rich layers are common in deep-sea sediments, where redox fronts (boundaries between oxygenated and reduced conditions) prevail. These occur in places where oxygen penetrates increasingly deeper into the sediment column and meets upward diffusing dissolved Mn mobilized under sub-oxic conditions (Froelich *et al.*, 1979; Burdige, 1993; Thomson *et al.*, 1993).

In the TAGHF sediments, Mn-oxide rich horizons are interpreted as indications for the presence of past, stalled, redox fronts. Several of these are preserved in the depositional channel sediments (FIGURE 5.5C and FIGURE 5.8C), below which the increase of dissolved Mn, Cu and Co in pore waters indicates sub-oxic conditions. For example, the low concentrations of dissolved O_2 and H_2S and lack of Fe mobilisation is evidence that the metalliferous sediments in the depositional channel (core 38GC) are sub-oxic rather than fully anoxic. Elsewhere dissolved Mn, Cu and Co concentrations reach their maximum concentrations near the top of the Mir zone fan sediment column, where sulphide clasts and solid Mn-oxides are undetected (FIGURE 5.8B). This concentration in pore fluids of these dissolved elements is evidence that the sedimentary column is anoxic in the upper few centimetres. To maintain anoxic conditions in the upper sediment column requires consumption of oxygen and restricted ingress of fresh seawater. We suggest the oxygen was initially consumed by rapid weathering of the uppermost sediments soon after deposition, during exposure to shallow-penetrating oxygenated seawater, resulting in an anoxic environment that maintained high concentrations of dissolved Mn, Cu and Co in the pore waters.

In non-metalliferous marine sediments, redox conditions are generally maintained by the degradation of organic matter by microorganisms, resulting in an increase of TA (Aquilina *et al.*, 2013), and consumption of NO_3 with depth indicative of microbial respiration (Froelich *et al.*, 1979). Evidence for microbial prokaryotic metabolism and degradation of organic matter has been reported for sediments elsewhere in the TAGHF (FIGURE 5.1) (Glynn *et al.*, 2006; Severmann *et al.*, 2006; Müller *et al.*, 2010). However, the relatively low organic carbon content in TAGHF sediments (0.14-0.45 wt.%; Severmann *et al.*, 2006), the only slight decrease in TA with depth in analysed cores, and the presence of NO_3 (FIGURE

5.8C) in the upper 60 cm of the metalliferous sediments suggest that organic carbon degradation may not be sufficient to maintain sub-oxic or anoxic conditions alone. An alternative mechanism is the partial oxidation of the sulphides. In this scenario, the redox boundary continuously migrates downwards due to the oxygen diffusing from the water column into the sediments (Thomson *et al.*, 1993), resulting in progressively deeper sulphide oxidation leading to precipitation of solid phases in the shallow section, and acidic and sub-oxic conditions at depth.

Microbially catalysed reactions might add to the sub-oxic conditions, enhancing the abundance of redox sensitive trace metals at the redox boundary (Glynn *et al.*, 2006; Severmann *et al.*, 2006; Müller *et al.*, 2010). However, at the depositional channel (core 38CG), the continuous and linear increases in concentrations of dissolved Mn, Cu, and Co with depth in pore waters below the redox front (60 cm in depth) indicate upwards diffusion of these elements from more deeply buried horizons (FIGURE 5.8C). The source could be sulphide-rich sands and Mn-oxides from which metals can be released and leached under anoxic conditions from sulphide-rich sands and Mn-oxides into the pore waters.

Therefore, even though redox processes are responsible for metal mobilisation within the sediments, they are also responsible for metal preservation. Once sulphides are buried within the deeper sub-oxic layers, they are likely to be preserved from further oxidation as they are stable under low Eh conditions. Hence, metals are either contained in the sulphides or in oxides and chlorides or as adsorption on pre-existing oxides, in response to encountering the redox boundary (FIGURE 5.9C). The ultimate fate of these rapidly buried metals depends on the competition between the rate at which sulphides are oxidize, the speed of burial of the sediments and the diffusion of oxygen from the overlying seawater. Conditions of preservation will be favoured in geographic locations with increased inputs of detrital components (*e.g.* close to continents) and enhanced marine biological productivity resulting in increased rates of organic matter input, controlling the development of anoxic environments. For example, hydrothermal deposits close to volcanoes will be preserved by burial under low permeability accumulations of tephra or lava.

The TABLE 5.5 is a comparative summary from the three environments on the processes explained above in the context of metal mobilisation and metal preservation.

TABLE 5.5 Comparative summary for three different environments: top of the mounds, talus and fans and distal depositionary basins. This table complements FIGURE 5.9.

Characteristic	Top of extinct hydrothermal mounds	Slope and base of extinct hydrothermal mounds	Distal depositional basins and channels
Sulphides	Absent	Thick (cm) and unsorted layers	Thin (mm) and sorted into turbidity *Ta* layer.
Fe	Highest concentration as oxyhydroxides	Present	Present in turbidity layers and in plume fall-out layers
Mn	enrichment in discrete horizons as MnO_2 crust fragments	Absent	Enrichment in discrete horizons
Cu, Zn, Co	Depletion except in Mn oxide horizons	Enrichment associated with sulphides	Enrichment associated with sulphides and Mn oxides
Origin	Collapse of chimney material and authigenic mineralization	Slumps	Turbidity currents and plume fall-out
Metal mobilisation (except Fe)	Mobilisation completed	Ongoing (sulphide leaching)	Ongoing (microbial diagenesis)
Metal preservation	Fe only	No preservation	Yes, in turbidity layers and by Mn oxides adsorption
Fate	Source to water column	Sink by mass transport and source by weathering	Sink in the sediments

5.6.2.3 Sources of Mn in Mn-oxide rich horizons

We have argued that, in the depositional channels, Mn-rich layers (core 38GC between 38 and 60 cm) are the consequence of a diffusive mobilisation under sub-oxic conditions and precipitation of Mn oxides under oxic conditions. What it is not entirely certain, however, is the primary source of this Mn or how long it took to form.

To test how long it took to form the Mn layers in the sediments under processes of redox mobilisation and metal re-precipitation, and to constrain the magnitude of the Mn gradient required for this, the Mn fluxes were calculated for three different locations, *i.e.* the depositional channel (based on two different cores) and on the top of the mounds (Southern mound). At the depositional channel (38GC), and with a calculated maximal diffusive Mn flux upward through the sediments of -6.10^{-8} µM/cm².yr (TABLE 5.2 and APPENDIX C.1.9), the time required to accumulate 0.004 mol/cm² Mn (equivalent to 0.25g/cm², TABLE 5.2) in the Mn-rich interval (between 38 and 60 cm depth) would be around 70,000 yrs. Similar calculations at the 49GC core highlight the variability in the fluxes and time required as a

flux of -2.7 $.10^{-8}$ μM/cm².yr leads to at least 385,000 yrs. It is thought that hydrothermal activity began at TAGHF ~140 ka ago (Lalou *et al.*, 1995), suffices to accumulate the Mn-rich horizons. Therefore, the primary Mn source could be fall-out from distal hydrothermal plumes (Shearme *et al.*, 1983) that thereafter underwent burial, reduction and diffusion, without requiring an additional source of Mn below. However, in the depositional channel, at few hundred meters apart (core 49GC), the time required to form the Mn oxide horizons under current Mn flux conditions would be $\geq$ 380 ka. This indicates that either the plume-derived Mn flux was highly variable in time or space, and/or an additional source of Mn has been added from some other source.

Higher contents of Mn (two orders of magnitude higher than in the depositional channel, 13.5 g/cm² equivalent to 0.25 mol/cm² over the first 22 cm) (TABLE 5.2) are found on top of Southern mound. Currently, no dissolved Mn is present in the pore water, hence only a minimal Mn flux required to form this layer can be calculated (APPENDIX C.1.9). The absence indicates the layer is oxic and that there is no current Mn mobilisation. The minimal average flux required to precipitate this concentration of solid phase Mn at the redox boundary is calculated to have been $3.32\ 10^{6}$ mol/cm².y, assuming it accumulated steadily over the 74 ka that has elapsed since high-temperature hydrothermal activity and sulphide mineralization ceased at Southern mound (Lalou *et al.*, 1995). This indicates that for Mn precipitation from the advected pore waters a concentration gradient of ~ 50 μmol / L.cm would be required. One explanation for the discrepancy between required and measured gradients by almost two orders of magnitude can be an additional source of Mn, such as an advective flux of Mn-rich hydrothermal fluids upwards through the sediments overlying the top of the SMS mound. Such a high advective flux at the mound tops also explains why the Mn-rich layers are found at the interface between the top of the metalliferous sediments (unit M2) and the base of the calcareous pelagic ooze (unit M1). This implies the upward advection of the Mn was fast enough to fully overcome the downward diffusion of seawater oxygen into the sediments. Ferromanganese crusts have been found in large proportions on the surface of the TAGHF (Scott *et al.*, 1974; Petersen and Scientific Party, 2016) and are thought to be formed by ascending, reduced hydrothermal fluids in low-temperature venting environments (Thompson *et al.*, 1985; Mills *et al.*, 1996). In our case, the Mn-rich layers are now buried below a pelagic cap and Mn pore water concentrations are similar to ocean bottom seawater, demonstrating the cessation of upward advecting fluids that once formed the Mn precipitates.

5.6.3 Metalliferous sediments and the global metal budget

In the context of the global geochemical budget, the contribution and role of metals contained in seafloor hydrothermal sediments remains uncertain. A simple calculation suggests that hydrothermal systems are ten to twenty times more abundant on the mid-ocean ridge axes than suggested by the frequency of active hydrothermal systems (Murton *et al*., 2019). Extrapolated to the ridge flanks and abyssal plains, this implies a significant amount of metalliferous sediment is buried beneath the pelagic sediments that accumulate as the ocean plate ages and moves away from its spreading axis. While this metalliferous material may have an impact on our understanding of global subducting sediment (GLOSS) (Plank, 2014), much depends on whether it is preserved. It is already known that low-temperature hydrothermal fluid flow and hydrothermal mineralization is common within the ridge flanks, presumably inducing a redistribution of the metals (*e.g*. Mottl and Wheat, 1994; Bodeï *et al*., 2008; Fisher and Wheat, 2011). We also find metalliferous sedimentary rocks associated with VMS deposits (*e.g*. Cann and Gillis, 2004; Prichard and Maliotis, 2007; Robertson and Degnan, 2008; Revan *et al*., 2019) on land, demonstrating some seafloor metalliferous sediments can be preserved. Our work on the TAGHF metalliferous sediments demonstrates that preservation of the metal grades requires rapid burial and effective isolation from seawater dilution. There is a balance between the dissolution of sulphides under redox and acidic conditions, resulting from partial penetration of seawater into the sediments, and stabilization of mobilized metals within pore waters by precipitation under fully oxygenated conditions. Where there is no protection from seawater alteration, sulphides become fully oxidized and the non-ferrous metals like Cu, Co and Zn are lost to the ocean leaving a residual gossan composed of Fe oxyhydroxides.

5.6.4 Sediments as potential mineral resources

The Cu and Au geochemical results (see SECTION 6.6.2.3 and DIGITAL MATERIAL 10) in the sediments obtained for this study have been compiled with geochemical analyses of additional gravity cores collected during M127 and JC138 (APPENDIX C.4, and described in Lusty *et al*., 2017). With an average concentration between 2 to 5 wt% Cu, the sediments in the depositional channel of the Alvin zone can be considered as potential mineral resources in the same way as eSMS deposits (FIGURE 5.11A). Similarly, Au contents (Lusty *et al*., 2017)

are correlated with Cu concentrations and are also the highest in depositional basins or at the flanks and base of the Mir zone (FIGURE 5.11B).

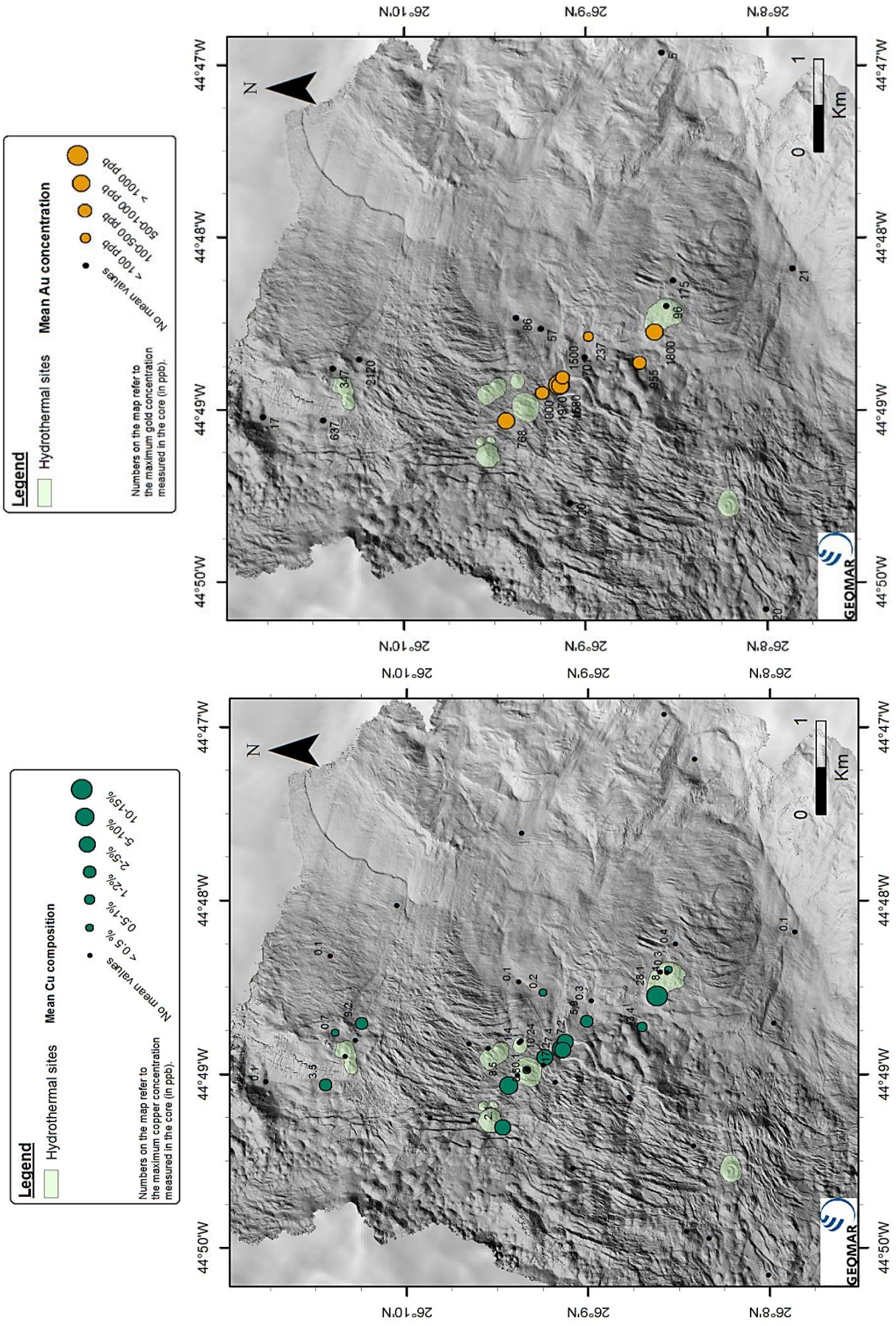

FIGURE 5.11 (previous page) Average gold and copper concentration distribution across the TAGHF. The highest concentrations occur around the mounds (typically at the flank bases) and in depositional basins. 'No mean values' indicates insufficient data is available to calculate a mean concentration (*cf.* APPENDIX C.4 for the dataset summary).

Spatial analyses of the bathymetry (APPENDIX C.5) highlights the sediment accumulation and debris-flow direction, driven by gravity. This 'drainage network' can be visualised, based on the current seafloor bathymetry, using drainage analysis routines in GIS applications (FIGURE 5.12). This analysis assumes the slopes are not significantly modified since deposition (*e.g.* by tectonic movements) and facilitates identification of the source regions and depositional basins with potential to hold the greatest volume of metalliferous sediment accumulations. Tonnage of metalliferous sediments for the depositional basins within the Alvin zone was estimated using this approach (TABLE 5.6 Example of tonnage estimates at the depositional basins within the Alvin zone. Av = average; Conc. = concentration.TABLE 5.6). The area contains several sedimentary ponds within the zone, and is estimated to be about 200,000 m^2. An average sediment thickness was determined (5 m), based on visual observation of seafloor exposures, although the thickness is highly variable

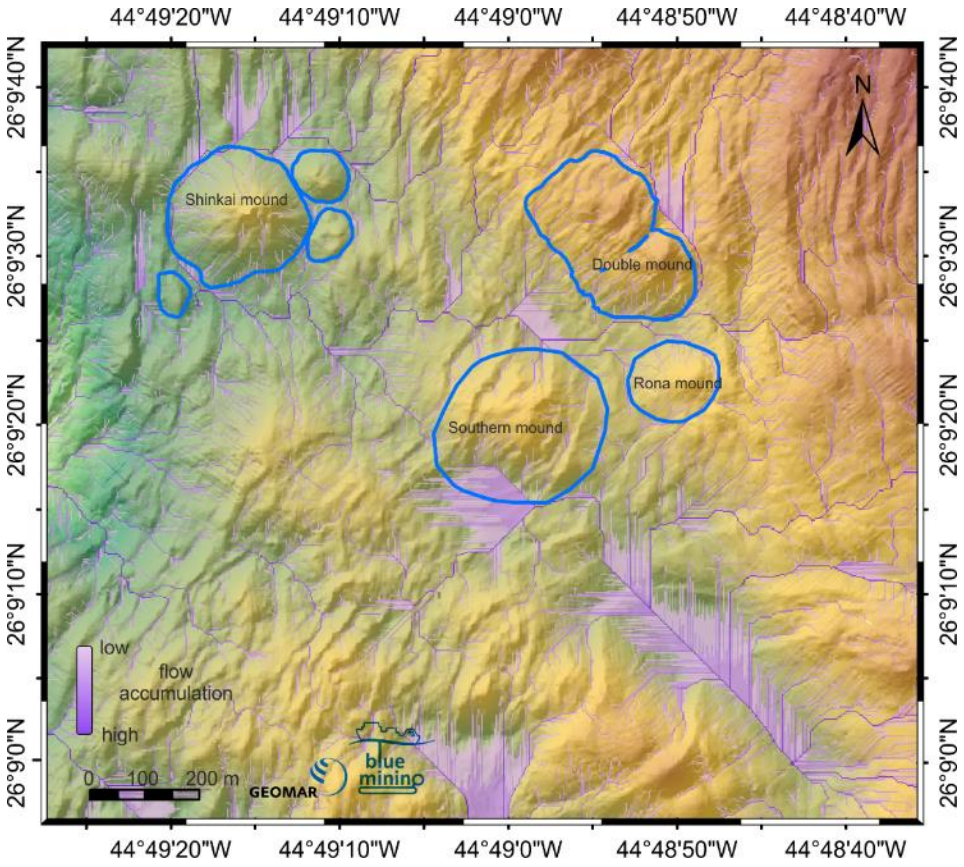

FIGURE 5.12 Flow accumulation network over the Alvin zone (*cf.* APPENDIX C.5 for the methodology).

and could reach up to 10 meters. A density of 2.5 t/m^3 was chosen as this was calculated from direct measurements of the sediments recovered from this location and furthermore, it represents a value between the average sediment density (1.7 t/m^3) taken at 716 DSDP drill sites and the ocean bedrock density (2.9 t/m^3) (Tenzer and Gladkikh, 2014). This represents 2.5 Mt of sediments containing 2.3wt% of Cu. The final Cu tonnage of the basin is therefore about 57,500 tonnes (TABLE 5.6). Comparing this tonnage to tonnage estimates of the mound-stockwork complex of the active TAG mound (2.7 Mt of massive and semi-massive sulphides at 2 wt% Cu; Hannington *et al*., 1998), our calculated tonnage is significant in terms of resource potential. Indeed, on its own, the tonnage of the sedimentary deposits exceeds the estimated tonnage for active TAG mound and would not sufficient to attract exploration companies, however they could be considered within the exploitation of inactive hydrothermal SMS mounds. Furthermore, any future exploration of sediment-hosted mineral deposits should also consider the degree and conditions of preservation. Indeed, a higher input of detrital components (such as biogenic ooze or volcanic material) will help preserve the metal tenor, although it will also lead to a grade decrease by rapid dilution.

TABLE 5.6 Example of tonnage estimates at the depositional basins within the Alvin zone. Av = average; Conc. = concentration.

Area (m^2)	**Thickness (m)**	**Volume (m^3)**	**Density (t/m^3)**	**Tonnage (Mt)**	**Av. grade Cu conc. (Wt%)**	**Cu tonnage (t)**
200,000	5	1,000,000	2.5	2.5	2.3	~57500

5.7 Conclusions

Metalliferous sediments in the TAGHF located at the top of extinct mounds, at the base of the mounds and in distal depositional basins and channels display discrete geochemical, morphological and mineralogical characteristics reflecting the origin of the metals, their depositional and the diagenetic processes that proceeded after their deposition. Processes trapping metals are found to be most effective in depositional channels where metals are rapidly deposited and buried, while metals are almost completely depleted from the mound-top sediments where exposure to seawater has extensively weathered the hydrothermal edifices and depleted the metal tenor. The concentration of metals in the sediments also depends on their distance of transport and the morphology of the seafloor,

with the highest metal concentrations found in sediments flanking the mounds and their proximal depository fans.

These data show that SMS collapse, mass wasting and transport by turbidity events transport, redistributes and rapidly deposits hydrothermal materials away from their sources. Sediments remaining on mound-tops are exposed to seawater where they release their metals retained in chlorides (transiently) and oxides. Sediment proximal to their source, such as in talus and fans, on the slopes of hydrothermal mounds, are coarser and more resistant to alteration and preserve the highest metal concentration in thick beds. More distal deposits accumulate metals in depositional basins by repetitive turbidity events. Those processes rapidly bury and compact both primary sulphides and secondary oxides.

Early diagenesis takes place in each of these three environments. Sulphide oxidation and organic carbon degradation control the redox zonation. When the resulting redox boundary is restricted to deep horizons, dissolved non-ferrous metals diffuse to shallower depths, however, are not released into the water column, but are contained in oxides, chlorides and by adsorption on Fe-Mn-oxyhydroxides. Redox sensitive metals, such as Cu and Co, are therefore enriched and preserved in these environments and found in primary sulphides and secondary Mn oxides. Zn enrichment is exclusive to primary sulphides and is not influenced by later redox conditions. Where a carbonate sediment cap is missing, oxygen rapidly diffuses into the sediments and metals are leached into the water column. Where deposits are recent, high metal contents are retained within thick layers of unsorted sulphides; for example, in the sediments on slopes. However, sulphides exposed to seawater penetration for a longer time tend to fragment and, with increased surface area, the metals dissolve into pore waters and are eventually lost to the ocean. Ultimately, these reactions leave barren Mn oxides and Fe oxyhydroxides behind. This study demonstrates that sediments in distal depositional channels are likely of greater economic value to the SMS deposits themselves. Although, any future exploration of sediment-hosted mineral deposits should consider the conditions of preservation along with the contribution from the sources. Indeed, a higher input of detrital components will help retain the metal tenor, although it will also lead to a grade decrease by rapid dilution.

5.8 Acknowledgments

The authors acknowledge support from the European Union Seventh Framework Programme Grant No. 604500 (EU-FP7) 'Blue Mining: breakthrough solutions for the sustainable deep-sea mining value chain" under grant agreement 604500. The authors would like also to gratefully acknowledge the JC138 shipboard party for its assistance in data collection and sample acquisition, the HyBIS and BGS RD2 rock drill technical support team. The authors acknowledge Geomar Abyss AUV team, Sven Petersen and Sebastian Graber for the provided ship-based bathymetric data of cruise M127 available from Petersen (2019a, 2019b). AMD thanks Matt Cooper, Kate Peel and Richard Pearce for their help with geochemical analyses. The British Ocean Sediment Core Research Facility (BOSCORF) is thanked for using their facilities. FB, SM and JM would like to acknowledge the financial support FCT through project UIDB/50019/2020 - IDL. This work was supported by a PhD studentship to AMD from the Graduate School of the National Oceanography Centre Southampton. We thank Academic Editor and two anonymous reviewers for their constructive and helpful comments, which improved the quality of this paper.

Metal preservation in hydrothermal sediments from the TAG hydrothermal field, Mid-Atlantic Ridge

Chapter 6 Evolution of seafloor hydrothermal deposits: role of the surficial sediments

This chapter complements the preceding chapter (CHAPTER 5) by providing additional results and discussion on formation of Fe-oxyhydroxide sediments collected from the top of extinct hydrothermal mounds. It is intended to be converted to a scientific paper, addressing the preservation of hydrothermal sulphide deposits, for submission to an international journal (potential journals are *Chemical Geology, Minerals* and *Marine Geology)*. In addition to my results presented here, the journal paper will be in collaboration with my fellow Blue Mining PhD student, Iain Stobbs, who focuses on the formation of a Si-Cap lithology that occurs widely throughout the TAGHF and the implication of the cap and gossan sediments for preservation of sub-seafloor ore deposits). Nevertheless the data and results presented in this chapter pertain entirely to my own work

6.1 Abstract

Seafloor massive sulphides (SMS) are the modern-day analogues of volcanogenic massive sulphide deposits found on land. The SMSs form via high-temperature hydrothermal fluids and once high-temperature hydrothermal fluid flow has ceased, the extinct SMS (eSMS) experience oxidative weathering and are slow burial by sediments. Sediments overlying eSMS are commonly compared to terrestrial gossans (*i.e.* secondary deposit typically with a red colour, largely consisting of Fe-oxides and occurring above a terrestrial deposit). The role of seafloor gossans in eSMS evolution and preservation is largely unknown. Here we report the results of analyses on sediments recovered from the top of three inactive hydrothermal mounds in the TAG hydrothermal field (Mid-Atlantic Ridge, 26°N). These mounds are covered by an up to 3.5 m-thick sediment layer of hydrothermal origin that overlies the silicified Fe-rich layer and the eSMS ore body. In the shallow part of the sediments (variable depth), goethite, nontronite, amorphous Fe oxides (ferrihydrite), and Mn oxides are dominating, and the sediments consist of poorly sorted mud to gravel-size, angular clasts. In contrast, in the deeper horizons close to the silicified layer (about 3 m depth), hematite and quartz are dominating with an average fine mud grain size and partially recrystallized hematite. In both parts, sulphide minerals are absent and the Fe-oxyhydroxide (FeOx) sediments have a low transition metal content (except Fe). Pore water analyses show an increase of dissolved Ca and Si with depth that may be linked to the anhydrite dissolution and jasper formation respectively. Down-core changes in the lithology suggest that

there are two principal types of post-depositional modification of the mound-top sediments: first, an alteration by the penetrating oxygenated seawater resulting in recrystallization of the hydrated FeOx, complete weathering of sulphidic minerals and complete mobilisation of trace metals; secondly, low to moderate temperature (>60°C) hydrothermal precipitation of ferrihydrite, goethite and hematite. In addition, upward diffusion of dissolved silica may play a role in the production of silica gels leading to the formation of the silicified layer. This study also finds that metal enrichment, commonly observed in terrestrial gossans, is not occurring during the first stages of alteration of the eSMS, but most likely at a later stage of metamorphism or weathering.

6.2 Introduction

As demand for raw metals increases, mining companies exploit lower-grade ores and deeper deposits. Seafloor massive sulphides (SMS) are rich in Cu, Zn, Pb, Ag and Au, and their resource potentials are frequently compared to the volcanogenic massive sulphides (VMS) mined on land (Cathles, 2011; Hannington *et al*., 2011). It has been suggested that metal accumulations that are associated with inactive mounds (*i.e.* extinct, former venting) are larger than that at active deposits because they have undergone a complete formation cycle (German *et al*., 2016b). In addition, inactive mounds have a lower proportion of endemic fauna than actively venting complexes , where abundant fauna is observed (Van Dover *et al*., 2018). Therefore, inactive deposits may be at least of equivalent economic interest for mining as active ones, but with a reduced environmental impact. However, the weathering processes and geochemical evolution of the inactive mounds are poorly constrained.

Thick sediment layers covering inactive mounds are the interface between the ore deposits and the world ocean and, like terrestrial gossans, are defined as intensely oxidized material forming the upper part of an ore deposit (Herzig and Hannington, 1995). Yet it is not known what role seafloor gossans play in the preservation or alteration of the ore deposits. In this study, I present the geochemical, textural and mineralogical results of Fe-oxyhydroxide sediments (hereafter referred as FeOx sediments) and pore waters collected from the top of three hydrothermally extinct mounds at the TAG hydrothermal field (TAGHF, 26°N) on the Mid-Atlantic Ridge, which represent a continuous sampling from the drilled sub-SMS rocks detailed in Lehrmann *et al*. (2018).

The results of my study provide new insights on the decay of a hydrothermal system from the decline of its hydrothermal activity, through the incorporation of sulphides in the sedimentary

record and the development of a gossan; they also help to understand the implication of a gossan formation for the resource potential of SMS deposits and the protection for sub-SMS deposits.

6.3 Geological setting

The TAGHF, discovered in 1972 (Scott *et al*., 1974; Rona, 1980), is located on the hanging wall of a west-dipping active detachment fault on the eastern flank of the Mid-Atlantic Ridge at 26°N (26°09.4'N, 44°49.0'W) and at a depth of ~3600 m (Rona, 1980; Humphris *et al*., 2015) (FIGURE 6.1). It is one of the largest hydrothermal systems in the world with currently one active high-temperature venting complex (the active TAG mound), two inactive hydrothermal zones (Mir zone and Alvin zone) and low-temperature zones (Shimmering zone and the East zone) (Rona *et al*., 1993b; White *et al*., 1998). Rock drilling at the active TAG mound by the Ocean Drilling Program in 1994, showed that the upper part of the mound consisted of pyrite breccia that was located above a silicified and pyritised stockwork blended to altered basaltic crust (Petersen *et al*., 2000) with an estimated tonnage to 2.7 million of tons of massive and semi-massive sulphides (Hannington *et al*., 1998). The sediment cover at the active TAG mound is thin (less than 50 cm-thick) and consists of sulphides, oxyhydroxides and clays, through which low-temperature fluid flow was identified (Mills *et al*., 1996). At the Alvin zone (FIGURE 6.1), located ~2.5 km NNE of the active TAG mound, four 100-300 m diameter fairly circular inactive mounds include Shinkai mound (Rona *et al*., 1998; White *et al*., 1998), Southern mound, Double mound (Rona *et al*., 1993b; Rona *et al*., 1993a) and Rona mound (Murton *et al*., 2019). These are dome shaped with discontinuous sulphide outcrops, standing and toppled chimneys, and a thin (< 1 m) cover of pelagic carbonate sediment (Rona *et al*., 1993a; Rona *et al*., 1993b). Radiometric dating indicates the presence of hydrothermal sulphides as young as 6,000 years old and manganese crusts as old as 74,000 years old (Lalou *et al*., 1995; this thesis, CHAPTER 4). A second inactive area, Mir zone, is located 2 km ENE of the active TAG mound. It consists of small standing and fallen chimneys, highly weathered sulphide material, red metalliferous sediments, and low-temperature hydrothermal precipitates such as Fe-Mn oxide crusts (Rona *et al*., 1993a; White *et al*., 1998). Radiometric dating indicates that hydrothermal activity commenced 140,000 years ago, first precipitating a Mn crust; the active episode ceased only 600 years ago (Lalou *et al*., 1993).

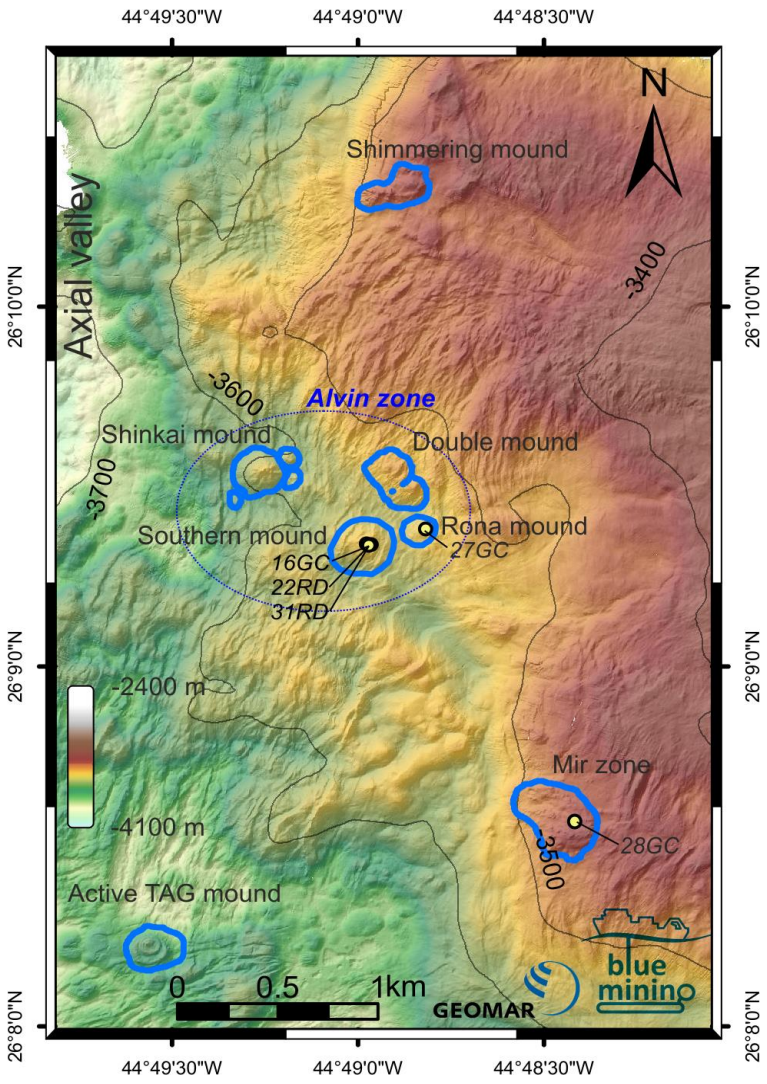

FIGURE 6.1 Shaded bathymetry map with main hydrothermal sites of the TAGHF, located on the western ridge flank of the Mid-Atlantic Ridge. The active mound, the four extinct mounds (Shinkai, Double, Rona and Southern mounds) grouped into the Alvin zone, the Mir zone and the low-temperature active Shimmering mound are highlighted in blue on the map. Bathymetry data are provided by the AUV Abyss at 2 m resolution during M127 cruise (GEOMAR; Petersen and Scientific Party, 2016). Coring and drilling locations of the sediments are shown as circles.

Sediments rich in metals (Fe, Cu, Zn and Mn) occur at TAGHF. These are capped by an ubiquitous pale-brown biogenic calcareous ooze (Scott *et al.*, 1978; Shearme *et al.*, 1983). Different types of sediment deposits are identified (see SECTION 4.5.1 for definitions), *i.e.:* particulate fallout from the plumes (German *et al.*, 1993; Mills *et al.*, 1993), oxidised sulphide precipitates, filling of channels by turbiditic mass wasting, and authigenic low-temperature mineralisation (Goulding *et al.*, 1998; Mills *et al.*, 2001; Severmann *et al.*, 2004). The highest concentrations in economic metals (*e.g.* Cu, Zn) are found at the base of slopes of hydrothermal mounds, while the thickest accumulations of metalliferous sediments are found in distal depositional basins where the detritus has been transported by mass wasting (Dutrieux *et al.*, *subm.*;this thesis, CHAPTER 1).

6.4 Methods

6.4.1 Sediment sampling and preservation

Five sediment cores were collected during JC138 from three different inactive mounds by gravity coring (7 cm diameter) and rock drilling (5 cm diameter) (FIGURE 6.1). Coring locations were determined from high-resolution bathymetry acquired with an autonomous underwater vehicle (AUV Abyss, GEOMAR) during a previous cruise (M127, Petersen and Scientific Party, 2016) and for some of the locations, by visual observation with the robotic underwater vehicle (HyBIS, National Oceanography Centre). Coring instruments were deployed above a smooth surface, expected to correspond to a sediment pond area, directly on the top of inactive mounds. Gravity cores were recovered from the Southern mound (JC 138/16GC), Rona mound (JC138/27GC) and Mir zone (JC138/28CG) (TABLE 6.1), while two additional drill cores were recovered with the BGS rock drill (RD2) at Southern mound, JC138/22RD and JC138/31RD; these two locations were less than 20 meters apart.

Details about the collection of pore water and solid phase samples are provided elsewhere in this thesis (SECTION **3.1**). Briefly, a lithostratigraphic log was produced (APPENDIX A.4), pore water samples were extraction using Rhizons samplers (Seeberg-Elverfeldt *et al*., 2005) and preserved for further analyses, and sediments were sub-sampled for grain size analysis, and mineralogical and geochemical analyses.

TABLE 6.1 Locations and station positions of gravity cores and rock drill cores at the TAGHF. *Depths are inferred from telemetry data of the rock drill and the length was not fully recovered.

Core reference	Location	Core length (cm)	Water depth (m)	Coordinates
711GC	Reference core ~ 18 km from TAGHF	300	2130	26°05.485′N 44°38.770′W
16GC	Southern Mound	133	3510	26°09.338′N 44°48.974′W
22RD	Southern Mound	190-320 *	3535	26°09.331′N 44°48.959′W
31RD	Southern Mound	17-168 223-273 *	3536	26°09.334′N 44°48.965′W
27GC	Rona Mound	41	3524	26°09.375′N 44°48.820′W
28GC	Mir Zone	194	3400	26°08.558′N 44°48.416′W

6.4.2 Pore water analysis

Concentrations of dissolved Ca and Si in pore waters were measured with inductively coupled plasma optical emission spectrometry (ICP–OES; Thermo Scientific ICAP 6500 Duo). The analyses were run on acidified samples, diluted 50-fold with 3% thermally distilled HNO_3. Precision and accuracy were determined for each analytical run by repeat analysis (n=3) of the certified reference material CRM-SW (Seawater Greyhound) (with a similar range in content as my samples). The measured value was accurate to ± 2.8%RE for Si and 5.7%RE for Ca. Precision was better than ± 2%RSD. Pore water concentrations were compared to a reference core, collected ~18 km away from TAGHF during cruise M127 (Petersen and Scientific Party, 2016). This reference core consisted entirely of calcareous shell fragments.

6.4.3 Solid phase analysis

Grain size analyses for 12 samples of FeOx sediments were run on a Malvern Masterize Particle Size Analyser. Each sample was measured four times. The chemostratigraphy of the five cores was obtained with ITRAX X-ray core scanning, while additional bulk rock geochemical analyses were performed with an inductively coupled plasma-mass spectrometer (ICP-MS, ThermoScientific X-Series 2) and ICP-OES after dissolving the sediments. Down-core profiles for 16GC are provided in CHAPTER 5 of this thesis and the down-core profiles for 27GC, 28GC, 22RD and 31RD can be found in the APPENDIX D.1. The Au content of the sediments was analysed by ICP-MS in all 5 cores with 5 in-house standards diluted from single elements standards to cover a range of 0 to 40 ppm. Precision between replicates of the certified reference material RTS-1 (Natural Resources Canada) is 1.8%RSD. Accuracy was calculated from the same reference material and is 20.5%Rel. Error. Rare earth elements were measured with ICP-MS, normalised against C1 chondrite (Evensen *et al*., 1978) and the Eu anomaly and Ce anomaly were calculated using Eq. 3.1 and Eq. 3.2. (This thesis, CHAPTER 3).

To interpret the microfabric and chemical mapping, FeOx sediment samples from Southern mound were sub-sampled, resin impregnated cut and polished prior to being observed in thin section by transmission and reflective microscopy. The impregnation was undertaken by a displacive fluid impregnation method following the method of Kemp *et al*. (1998). This involved sediment soaking in acetone, maintained in a well perforated cotton and aluminium foil wrapping in a close-fitting case. Two of these samples were prepared for SEM study with a carbon coating. EDS chemical mapping was obtained on selected areas.

XRD analyses were carried out on FeOx sediments after powdering and mixing with a known amount of corundum with a Philips X'Pert pro with a Cu tube (Kα λ = 1.541) at the University of Southampton for quantitative mineralogical analyses.

A fully detailed description of the geochemical and mineralogical analyses can be found in this thesis, CHAPTER 3.

6.5 Previous studies

The geology and geochemistry of the TAGHF and, in particularly the eSMS deposits, and the metalliferous sediment distribution and geochemistry were already discussed in previous studies by Murton *et al*. (2019) and Dutrieux *et al*. (this thesis, CHAPTER 5). The following is a short summary of previous findings relevant to this work.

At the Alvin zone, the surface geology was investigated with HyBIS dives and grab sampling while high-resolution bathymetry mapping provided the relief of the four eSMS mounds (FIGURE 6.2). The summit areas at both Southern and Rona mounds have occasional relict chimneys, and are covered with red hydrothermal sediments and with pelagic sediments. HyBIS-grabbed surface material comprises of massive pyrite breccias, layered massive sulphides and sulphidic chimney materials. These sulphides are commonly coated with Fe oxyhydroxides and green atacamite, indicating secondary mineralisation due to oxidative weathering (Murton *et al*., 2019). Murton (op. cit.) also demonstrate that Southern and Rona mounds are older than their neighbouring Shinkai mound because of their smoother slopes, a dome morphology, the scarcity of chimney structures and a thicker sediment cover.

In sediments collected at the summit of Southern and Rona mounds (FIGURE 6.2) and at the Mir zone five different sulphide-free lithologies (FIGURE 6.3) can be distinguished that are common across the TAGHF. Unit M1 (M for mound) is a pelagic carbonate ooze cap, which is ubiquitously visible across the area although it was only directly recovered at Rona mound (27GC) (APPENDIX D.1.2). This unit M1 is directly followed by Unit M2, which is a heterogeneous brecciated sediment made of Fe and Mn oxides (todorokite and birnessite) with variable grain sizes up to

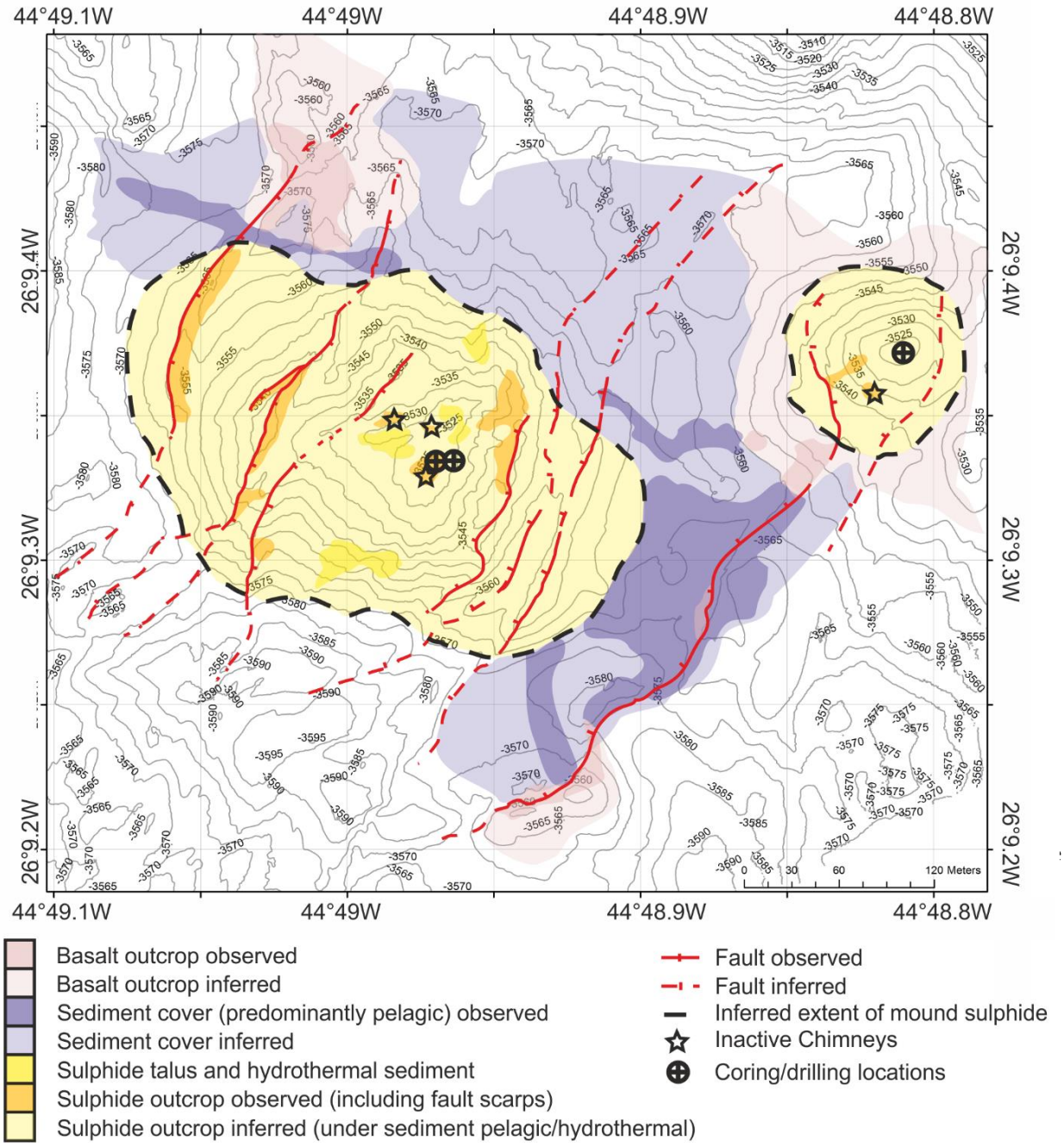

FIGURE 6.2 Geological map of Southern mound and Rona mound, interpreted from the high-resolution bathymetry, surface samples and video surveys. Note, the white areas are unmapped (map from Murton *et al.*, 2019).

several centimetre and forming a crusty, friable material. The two following units are the focus of this paper: Unit M3 and M4. Together they comprise the FeOx unit. In unit M3, the mineralogy is mainly composed of goethite, nontronite, montmorillonite, quartz and other amorphous Fe oxyhydroxides. Below, Unit M4 is similar to M3, although the colour changes from orange to dark red, suggesting a hematite dominance, and it shows the highest Fe content (up to 50 wt%). Units M1 and M2 can be intermingled, as well as unit M3 with unit M4, therefore boundaries are not always discrete or discernible. Below the deepest sediment unit, M4, cores 22RD and 31RD at

Southern mound recovered the transition to the silicified "jasper" layer (Unit M5). At the top of the Mir zone, the same units are present, although units M1 and M2 are intercalated and the boundary between M3 and M4 is gradual, *i.e*. visual observations showed a gradual change of mineralogy and colour with depth (FIGURE 6.3), although the gradual change was only visually observed and not quantified. Non-ferrous trace metals (*e.g*. Cu, Zn, Co) are depleted in the units M3 and M4 compared to the Unit M2, with means of 0.11wt% Cu, 0.1wt% Zn, < 1 ppm Co and 0.16wt% Mn.

6.6 Results

In the following sections, I describe the results of additional surface mapping and FeOx analysis. The aim of this study is to determine the physical and geochemical evolution of the seafloor gossans located above long- extinct hydrothermal mounds (*e.g*. Southern mound) to understand their implication for preservation or alteration of the SMS deposits.

6.6.1 Surface geology and morphology

To investigate physical and geochemical processes within the sediments and the SMS ore body, I first describe the bathymetry of the Mir zone, while Murton *et al*. (2019) provide an extensive surface geological study of the eSMS deposits at the Alvin zone (*cf*. SECTION 6.5).

High-resolution (50 cm) multibeam swath bathymetry mapping of the hitherto almost unexplored Mir zone (SE of the TAGHF) and slope mapping revealed an oval-shaped elevated mound with a surrounding steep slope (> 20° slope angle) and an altitude of about 80 meters. The circumference shows a rough terrain and opens into a slump feature, indicative of a deposit fan in the NW corner. Small circular standing structures, which could be sulphidic chimneys are arranged on the circumference and the highest points of the mounds. Depressions are a common feature in the flatter central area (FIGURE 6.4).

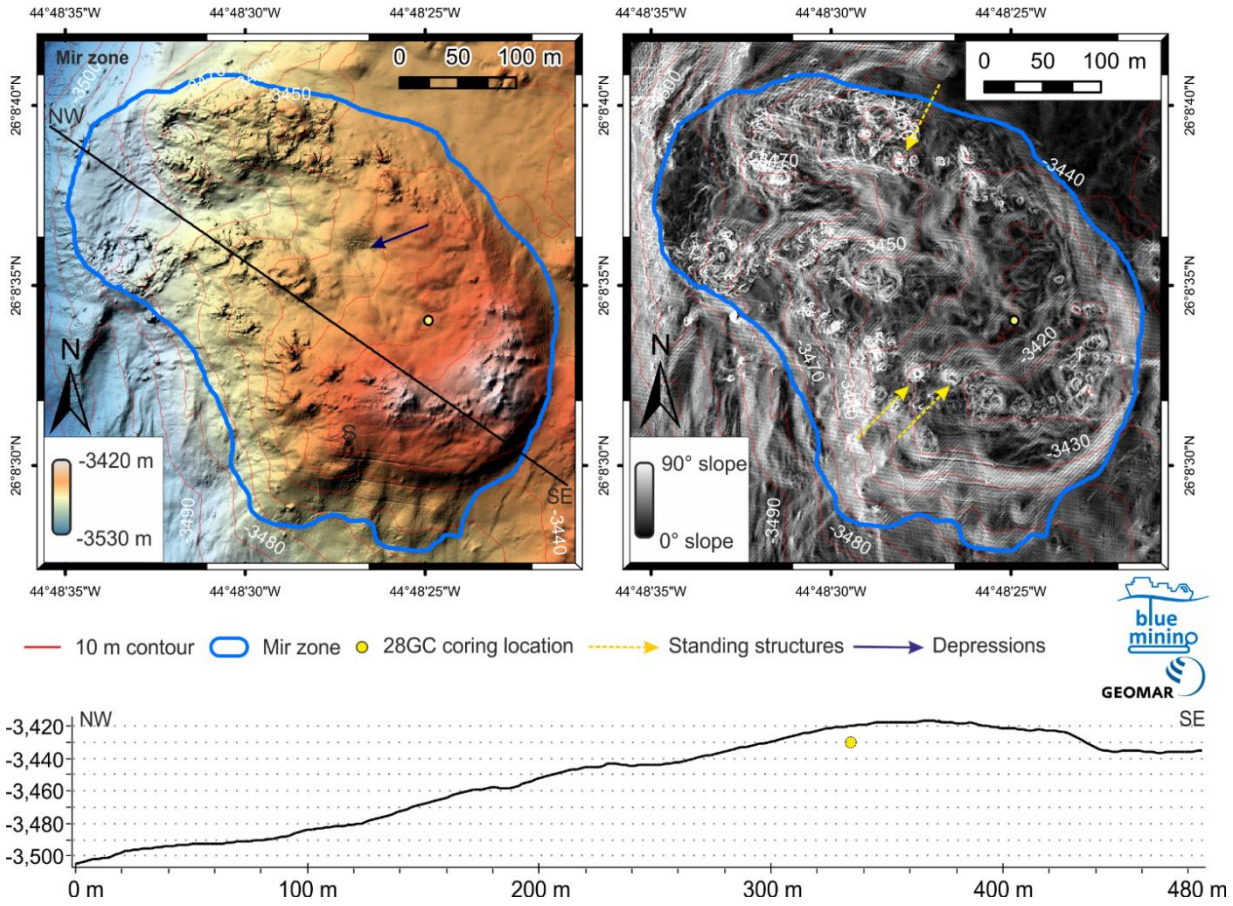

FIGURE 6.4 Mir zone bathymetry. (Left) Colour-shaded bathymetry maps (0.5 m resolution) of the Mir zone and NW-SE topography profile transect revealing a few pits (pockmarks). (Right) Slope map of the Mir zone, showing the circular standing structures that could be hydrothermal chimneys. The centre is relatively flat and weakly dip towards the NE corner of the mound where a slump is indicated by a higher slope. Bathymetry data are provided by the AUV Abyss during M127 cruise (GEOMAR; Petersen and Scientific Party, 2016). (Bottom) Topography profile of the transect NW-SE with the Mir zone heights and a slump fan in the

6.6.2 Solid phase

To understand how the lithology chemically evolved after the high-temperature hydrothermal fluid flow ceased, FeOx sediments from Units M3 and M4 were further investigated at the extinct mounds (Southern mound, Mir zone and Rona mound) for quantitative mineralogy and grain size distribution.

6.6.2.1 Stratigraphy

Grain size analyses at eSMS mounds in the FeOx units show that the sediments are very poorly sorted, with a polymodal grain size distribution (FIGURE 6.5). Unit M3 contains up to 1.5% gravel-sized grains in a matrix of clay, coarse silt and fine sand (at a variable %). Particle morphology was determined by SEM mapping in a sample from unit M3 from Southern mound (126 cm, 31RD, FIGURE 6.7). Additional microphotographs were taken under an optical microscope in transmitted and reflected light, with and without the crossed polarisation, and are available in the APPENDIX D.3 and D.4 respectively for units M3 and M4, respectively. For M3 sediments, microphotography shows a large variation in the grain sizes between <0.1 mm to several mm. An angular euhedral clastic morphology is dominant. Some clasts present a longitudinal or concentric layering texture, while some show a uniform plain texture (FIGURE 6.7A). Clasts also show a variety of mineralogy, some with a higher crystallinity as shown by a higher reflectivity on the SEM. Contrary to M3, M4 sediments are restricted to a smaller grain size range (FIGURE 6.5) between clay (a minimum of 35% and up to 87%) and silt and with less than 10% sand. Remnants of pelagic sediment (foraminifera tests) are still present (APPENDIX D.4A). SEM mapping in a M4 unit sample from Southern mound (292-293 cm, 31RD, FIGURE 6.8) confirms a fine clastic grain size with a matrix made of a clay grain size fraction. The clasts are between 50 and 400 µm (FIGURE 6.8A) and show dissolution and mechanical disintegration (FIGURE 6.8C). Some regions (up to 5 mm) exclusively consist of botryoidal layered hematite with a higher crystallinity (FIGURE 6.8B, Appendix D.3B).

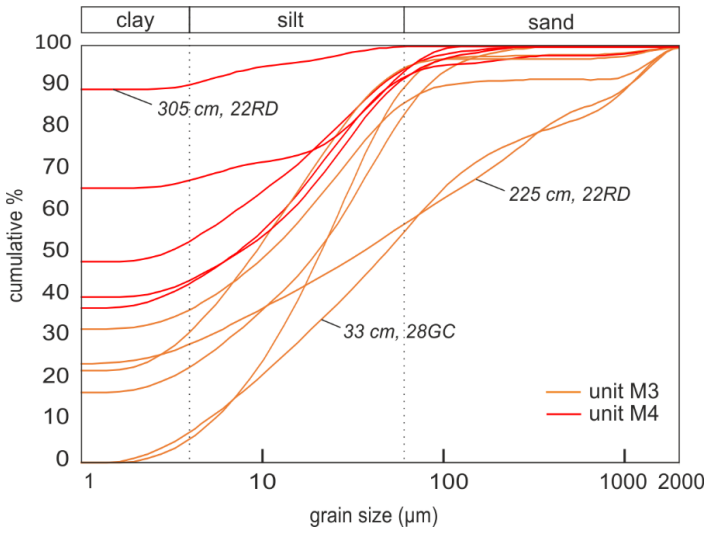

FIGURE 6.5 Grain size distribution for sediments in units M3 and M4. Note the sediments in M4 are more fine-grained than sediments in M3.

6.6.2.2 Mineralogy

At the eSMS mounds, goethite, hematite and amorphous iron oxides are the three most abundant minerals in units M3 and M4 (FIGURE 6.6). At depth, the mineral assemblage is composed of hematite (hem) and quartz (qtz), such as at depth 190 cm in core 28GC (hem:qtz 89:11%), 229 cm in 31RD (hem:qtz 94:6%) and 305 cm in 22RD (hem:qtz 91:9%). Amorphous minerals, *i.e.* ferrihydrite, are more concentrated at shallower depths, co-occurring with goethite. XRD quantitative analysis cannot distinguish nontronite (a smectite clay) from todorokite (a Mn-oxide) as spectrum peaks overlap, however, as with geochemical analysis, the presence of Mn was detected in the M2 unit (up to 15 wt% in 31RD at 32 cm-depth), I interpret this as the presence of todorokite in these units. Paratacamite (a Cu chloride mineral) was observed as grains restricted to a horizon at 117-120 cm depth at the Mir zone and accounts for the concentration peak in Cu observed in the chemostratigraphy (APPENDIX D.1.3).

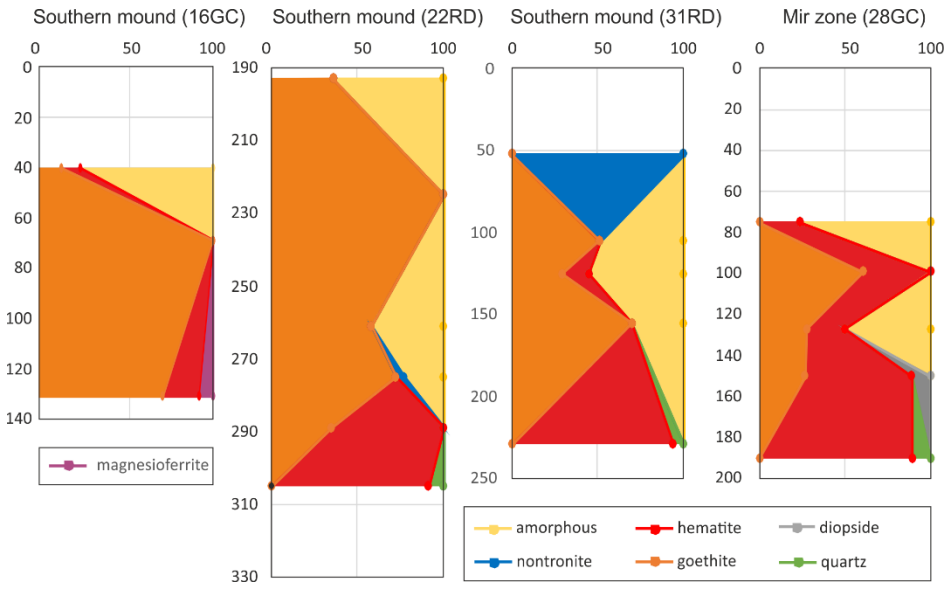

FIGURE 6.6 Cumulative mineralogy depth profiles for Southern mound and Mir zone.

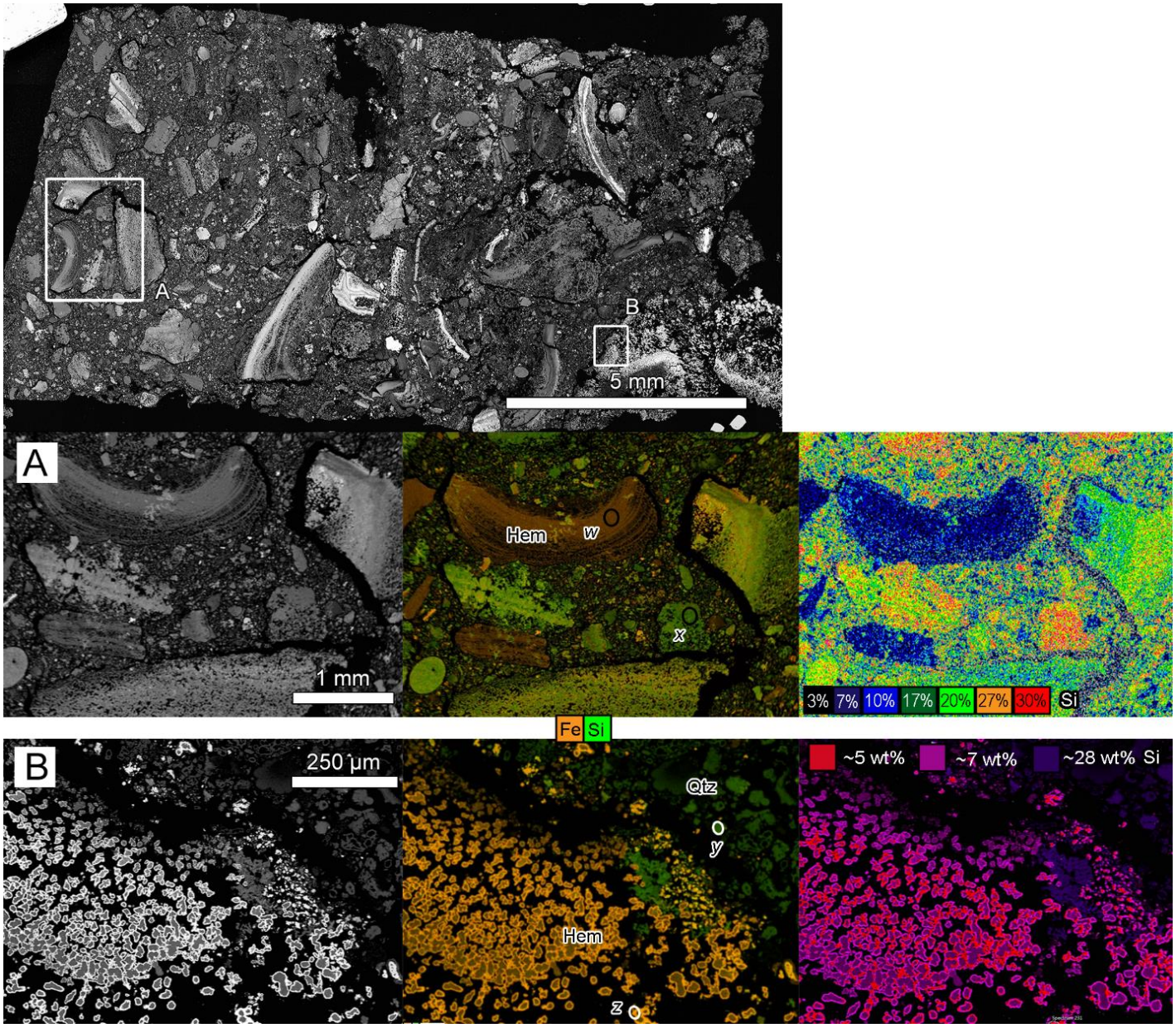

FIGURE 6.7 SEM Microphotography and EDS mapping at 126 cm depth (31RD).

(TOP LEFT) Montage mapping. Boxes A and B correspond to the detailed mapping on the bottom figures. Middle figures are elemental mapping of Fe and Si.

In panel (A), right figure is a Si composition mapping, showing a Si content between 0 and 30 wt% and indicating presence of Si oxides.

Panel (B) shows 25 to 50 µm grains (pink colour on the right figure), coated with a crystallised hematite and therefore are less porous (red on the right figure) and more reflective. Anhedral quartz grains are also present. EDS elemental analyses of the boxes A and B, and the areas *x, y* and *z* are reported in APPENDIX D.3.

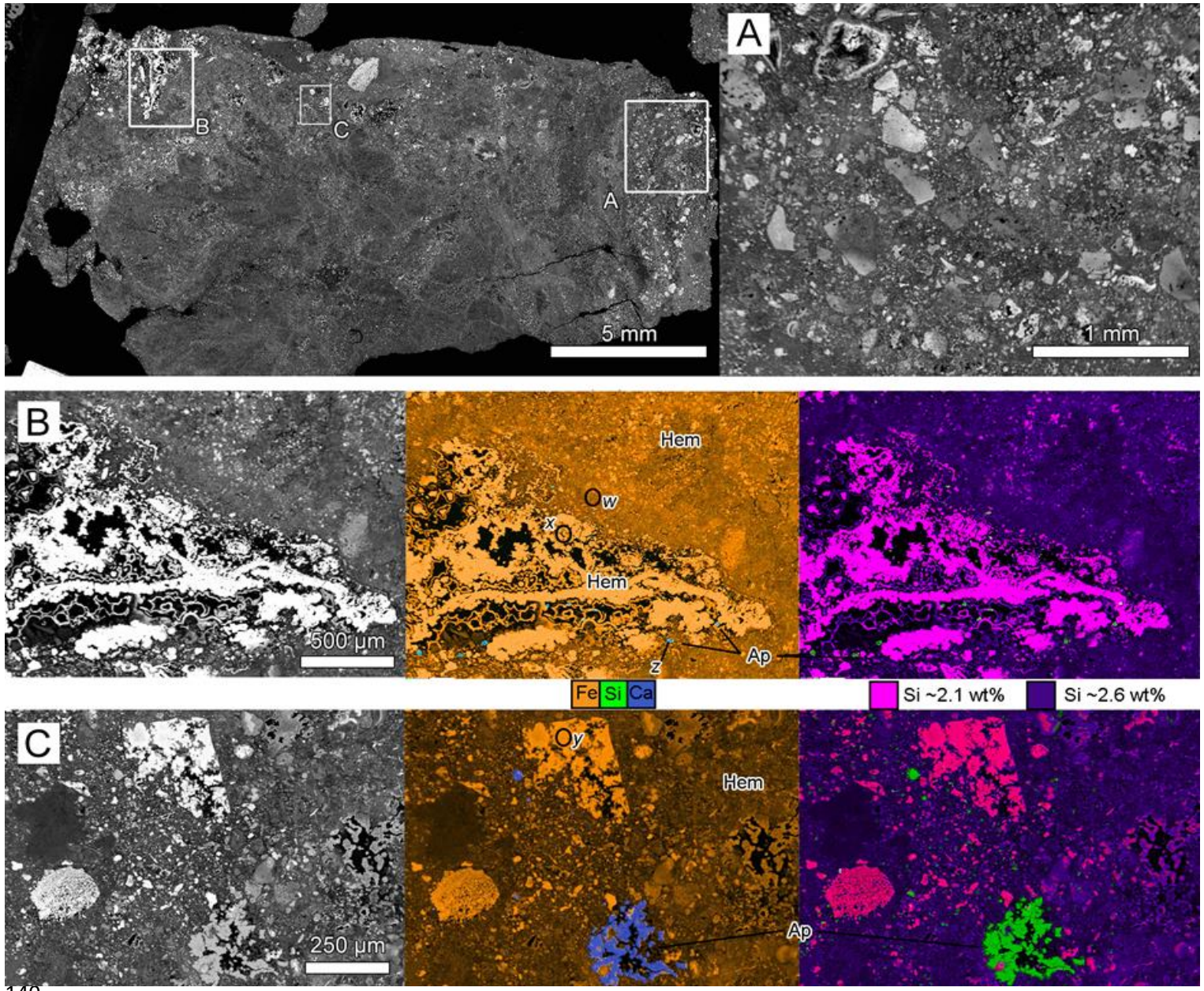

FIGURE 6.8 SEM Microphotography and EDS mapping at 292-293 cm depth (22RD).

(TOP LEFT) montage mapping. Boxes A, B, C correspond to the detailed mapping on the top right and bottom figures. Middle figures are elemental mapping with Fe, Si and Ca (+P). Left figures are phase analyses showing a distinction between crystallised grains of hematite (Hem) with up to 2.2% Si and a finer matrix incorporating up to 2.8% Si. Apatite (Ap) is present in up to 250 µm euhedral grains. EDS elemental analyses of the boxes A, B and C, and the areas w, x, y and z are reported in APPENDIX **D**.7

6.6.2.3 Geochemistry

Gold was suggested to be present in seafloor gossans (Hannington et al., 1995), however, the gold content measured in my sediments are negligible in all cores: 38 out of 42 samples show contents lower than 150 ppb. An exception is a sample from 117 cm at the Mir zone that has 5.5 ppm Au and an extremely high Cu content (8.7 wt%).

Results of SEM-EDS mapping of Fe, Si, O, P, and Ca, carried out on resin impregnated FeOx blocks are reported in FIGURE 6.7, FIGURE 6.8 and APPENDIX D.7. The deepest sediment unit (*i.e.* at 292cm, 22RD, Southern mound) is entirely composed of Fe_2O_3 (93%) and SiO_2 (~5%). The other 2% are composed of traces of K, Na, Mg, Al oxides and Ca phosphates. Phase analysis show that minerals with high reflectance (FIGURE 6.8B) contain up to 2.2% Si compared to the matrix that had up to 2.8% Si, which is most likely due to the crystallised lattice of hematite reducing the incorporation of Si. In comparison, the greyish reflective area corresponds to a matrix of fine-grain hematite, with a botryoidal aspect with Si oxides within its grain boundaries. Apatite grains are present, and can be large (up to 250 μm). For shallower sediments at Southern mound (*e.g.* unit M3 at 126 cm depth in 31RD, Fig 8), geochemical mapping reveals an increase of up to 35% of Si oxides at the expense of Fe, due to a greater proportion of quarzitic clasts. 20 to 50 μm grains of hematite (with 8% Si impurities) are coated with slightly purer hematite (5% Si) (FIGURE 6.7C).

6.6.2.4 Rare earth elements

REE patterns of marine sediments are useful to test for the presence of hydrothermal input and sediment-seawater interaction; positive Eu anomalies are inherited from hydrothermal fluids whereas negative Ce anomalies are inherited from seawater. Across the TAGHF coring sites, Unit M1 consisting of pelagic carbonate sediments, which have a negative Ce anomaly, also show either no (*i.e.* Eu/Eu* = 1) or a weakly negative Eu anomaly. Unit M2, which is Mn-oxide rich, exhibits both negative Ce and positive Eu anomalies. Units M3 and M4 have similar REE patterns, and REE concentrations vary by one order of magnitude (FIGURE 6.9A). However, their REE contents are lower than in the pelagic sediments. They also exhibit a variable negative Ce anomaly (Ce/Ce* ranges from 0.3 to 1) (FIGURE 6.9B) together with a strong positive Eu anomaly (Eu/Eu* ranges from 1.4 to 20.6) (FIGURE 6.9C). The magnitude of the Eu anomaly is highest in the deeper horizons, and the highest value (Eu/Eu* = 20.6) was observed in the deepest (302 cm) layer recovered from the top of Southern mound (22RD), immediately above the silicified jasper layer. In addition, the cores

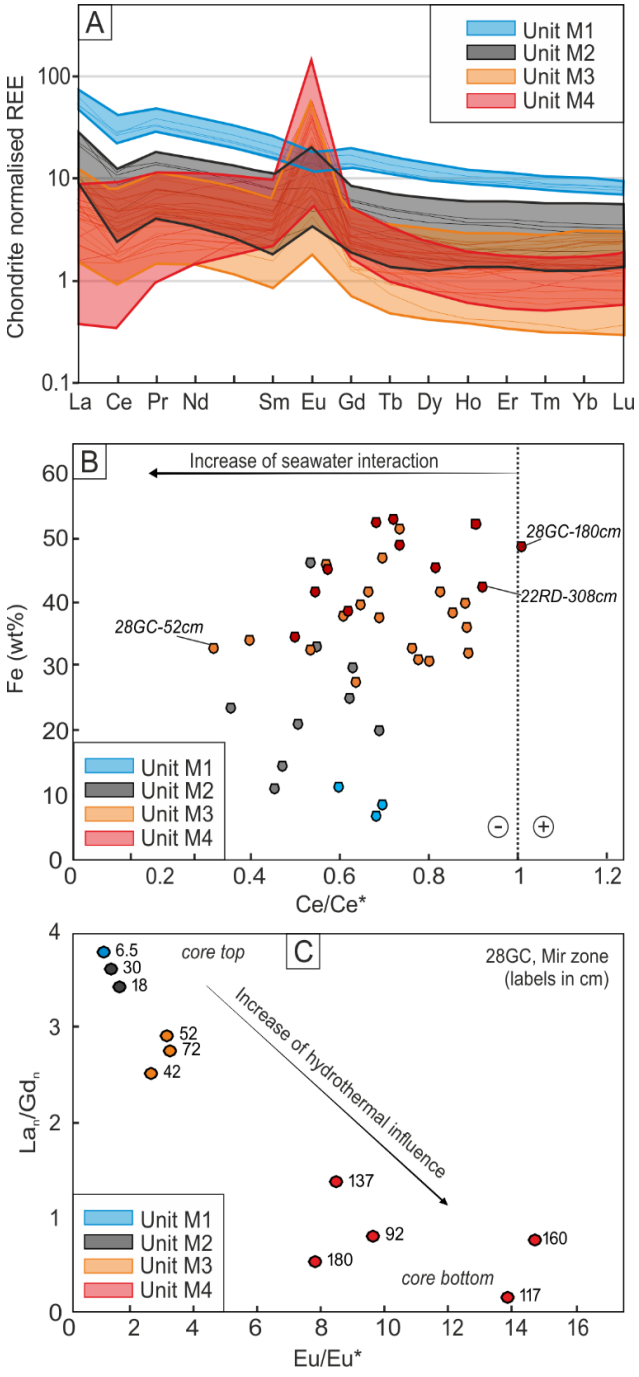

FIGURE 6.9 REE plots.

(A) REE distribution in sediments from the top of the mounds. Unit M1 is the pelagic carbonate ooze, Unit M2 the Mn-oxide rich layers, M3 and M4 the shallow and deep FeOx layers respectively. M2, M3 and M4 show positive Eu anomalies, in contrast to M1. (B) Ce/Ce* as a function of Fe content in the solid phase. All samples show negative Ce anomalies, except one (28GC-180 cm). The plot shows the variability of Ce anomaly with the FeOx units. The arrow represents the increasing influence of seawater. (C) Co-variation in Eu anomaly and La_n/Gd_n in the Mir zone core (28GC). The arrow represents the evolution of REE patterns with progressive hydrothermal influence, corresponding to deeper horizons.

also show La_n/Gd_n ratios that decrease downwards, with unit M4 showing the lowest ratios (*e.g.* at the Mir zone), indicating a low LREE/HREE fractionation (low La_n/Gd_n) that is coincident with increasingly positive Eu/Eu* anomalies (FIGURE 6.9C).

6.6.3 Pore water geochemistry

Dissolved Ca was analysed to test for dissolution of Ca-rich minerals (anhydrite, calcite and apatite). At the sediment surface across the TAGHF, Ca concentrations were about 10.5 to 11 mmol/L, *i.e.* similar to the seawater. At the Southern mound, the Ca concentrations increased with depth to 11 mmol/L at 130 cm (16GC) and 11.5 mmol/L at 300 cm (22RD)

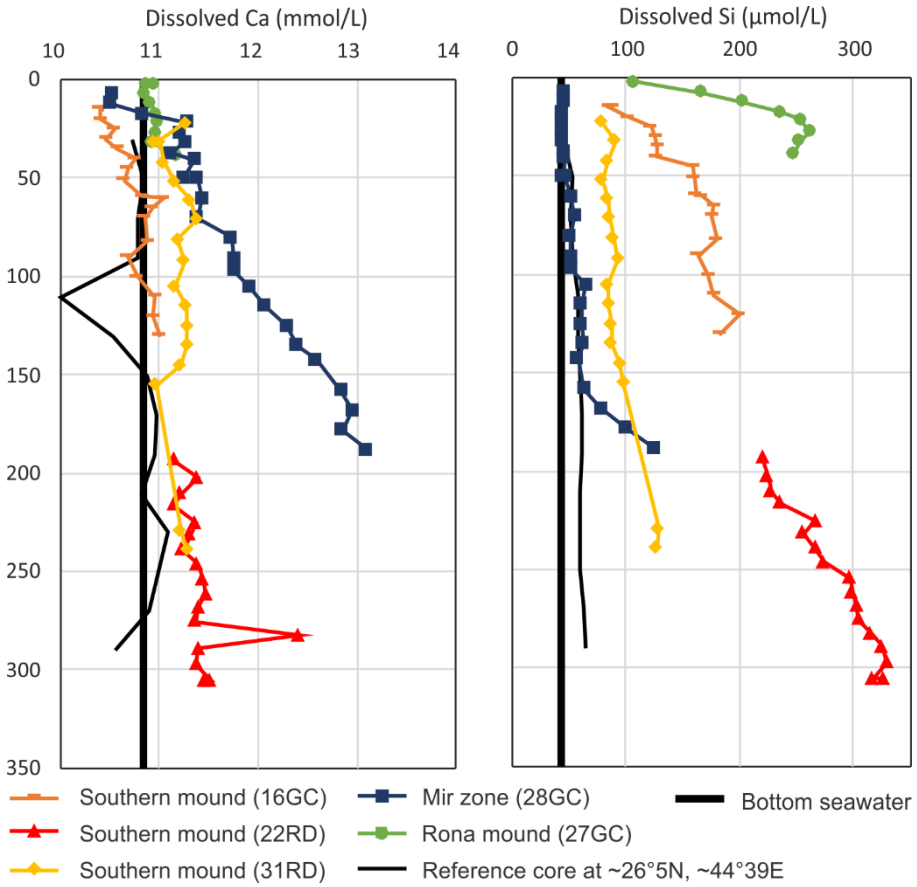

FIGURE 6.10 Dissolved Si and Ca profiles in the five study cores and in a reference core located about 18 km away from the TAGHF (Station M127/711, Petersen and scientific party, 2016). Errors bars are within the width of the markers.

(FIGURE 6.10). Also at the Mir zone, Ca increased from 10.5 mmol/L at the sediment surface to 13.1 mmol/L at 190 cm. At Rona mound, also a Ca concentration increased to 11.2 mmol/L was found at 40 cm.

Similarly, the silica concentration (FIGURE 6.10) at each site increased with depth. The highest concentrations of up to 325 µmol/L were found in the deepest horizons from the 22RD core at the boundary with the silicified jasper (unit M5). The lowest concentration in silica was found at the Mir zone (28GC) and was similar to the seawater concentration, although concentrations started to increase over a 30 cm interval at the bottom of the core from 45 µmol/L to 125 µmol/L. The highest gradient of silica concentration was found at the Rona mound (27GC), where the near seafloor concentration was already 100 µmol/L ppm and rose up to 260 µmol/L at 25 cm depth.

6.7 Discussion

The results highlight lithological changes within depth in the seafloor gossans, as regards to the texture, mineralogy and geochemistry. Those variations could be explained by several tightly intertwined chemical and physical processes occurring in sediment deposits on the top of the mounds after the high-temperature hydrothermal fluid flow ceased. I distinguish several processes in the following discussion. First of all, the well-known oxidative weathering of sulphidic chimney material produces amorphous FeOx deposits, accompanied by the disintegration of sulphide material into increasingly smaller fragments. Secondly, the produced amorphous FeOx minerals undergo a diagenetic transformation into goethite, and possibly hematite. Thirdly, authigenic ferrihydrite precipitates from low-temperature fluids and is afterwards transformed into goethite or hematite depending on the physiochemical conditions (*e.g.* temperature and pH). Finally, lithification of the sediments by precipitation of quartz sturdily cap the ore body and the dissolved silica present in elevated concentration in pore waters may be an essential factor in this process. Ultimately, those processes characterize the seafloor sediments on top of inactive hydrothermal mounds and I compare the produced sediments with analogous terrestrial gossans to highlight the differences and hitherto determine unknown processes that could one, or both of them.

6.7.1 Disintegration and oxidative weathering of sulphides

In the previous CHAPTER 5, the origin of the mound-top sediments was suggested to be an accumulation of intensively weathered chimney material and massive sulphides. The indications for the complete weathering by seawater were the current stable, oxic environment, the absence of trace metals (Mn, Zn, Co and Cu) in sediments and pore waters and the presence of hydrothermal barite (Dutrieux *et al*, subm.; this thesis, CHAPTER 5). Here I provide additional evidence for the accumulation of former chimney material and massive sulphide by looking at the texture and grain size distribution. First of all, the numerous and large angular clasts of FeOx minerals and quartz from Unit M3 (FIGURE 6.7) indicates that brecciation process was responsible for the accumulation. The absence of sorting (FIGURE 6.5) is further evidence for an 'fresh' and 'immature' depositional environment with short-distance transport (m to 10 m), such as *in situ* collapse of hydrothermal chimneys, where disintegration into smaller particles is governed by the long-term exposure to seawater. Foraminifera tests are present in the deeper part of unit M4 (APPENDIX D.4A), showing that sediments were once on the surface of the seafloor and that deposition and burial are partly

responsible for the accumulation. However unit M4 is dominated by better sorting and smaller grain sizes than unit M3, therefore other processes will have occurred in addition to *in situ* collapse and clast disintegration, such as authigenic precipitation.

REE patterns of hydrothermal sediments have characteristic features that can be attributed to their formation and accumulation modes (Mills and Elderfield, 1995b). Hydrothermal fluids usually have a positive Eu anomaly due to the preferential solubility of Eu^{2+} under reducing conditions (Klinkhammer *et al.*, 1994). All hydrothermal mound-top sediments (M2, M3 and M4) show pronounced vent fluid characteristics, a strong enrichment in LREE and a positive (chondrite-normalised) Eu anomaly (FIGURE 6.9A), which confirms that they precipitated from hydrothermal fluids. Yet, the FeOx layers also have negative Ce anomalies (FIGURE 6.9B), characteristic of scavenging of REE from oxic seawater (German *et al.*, 1990; Mitra *et al.*, 1994), *i.e.* indicating their in situ formation under equilibrium with seawater.

The Ce anomaly is present almost throughout the entire FeOx layer, sulphides are absent and transition elements contents (Cu, Zn, Co, *etc.*) are low which is evidence that oxidative weathering of hydrothermal material has progressed to completion. Nonetheless, it is not entirely known if oxidation is strictly limited to the seafloor or whether it also continues within the sediments. In other terms, it is still unknown if sulphide may be found in the sediment pile on the top of extinct hydrothermal mounds due to a deposition rate greater than the sulphide oxidation rate or if the sulphides are exclusively weathered on the seafloor before being buried. This information could inform us on the story and timeline of the weathering. To address this competition between oxidation kinetics and deposition rate, I looked at the secondary products of the sulphide weathering at the TAGHF include jarosite, secondary copper minerals (Hannington, 1993; Murton *et al.*, 2019), and, most abundantly, ferrihydrite.

Ferrihydrite, a poorly crystalline, metastable and fully hydrated Fe-hydroxide ($5Fe_2O_3 \cdot 9H_2O$) is formed from rapidly hydrolysed Fe^{3+} solutions released into pore waters at hot or moderate-temperature. Reduced hydrothermal fluids conduct Fe^{2+} cations and once reacting in a oxidizing environment precipitate ferrihydrite (Alt, 1988; Ridley, 2012). During ageing and suboxic and oxic diagenesis, ferrihydrite will transforms to more crystalline Fe phases, *i.e.* hematite and goethite. At 5°C and pH 8, in laboratory settings, ferrihydrite has a half-life (*i.e.* time required to transform half content of the mineral into another mineral) of approximately 500 days, which is a geologically rapid transformation rate (Schwertmann and Murad, 1983; Schwertmann *et al.*, 2004). However, rates of transformation vary

considerably with temperature, pressure, and the geochemical composition of the environment, and the half-life can reach up the order of ~100 ka under natural conditions (Dunk and Mills, 2006). In TAG mound-top sediments, ferrihydrite is restricted to Unit M3 (*e.g.* up to 160 cm in 28GC, Mir zone), which suggests that sulphides may be buried as deep as in Unit M3 and then consequently altered into ferrihydrite. However, the absence of ferrihydrite in Unit M4 implies either that ferrihydrite has never been present at this depth or that the ferrihydrite has been completely transformed into a further product. If ferrihydrite has never been present up to this depth, this implies that sulphides may never have been buried up to this depth, and therefore that another process is in charge of the sediment formation (such as authigenesis). If ferrihydrite was completely transformed into goethite or hematite, it requires that the physiochemical conditions in M4 favours a rapid transformation of ferrihydrite in sediments significantly older than M3.

Trace metal concentration (Cu, Co, Mn) measured in the eSMS mound sediments do not show variability between the units M3 and M4 and suggests there is no direct correlation between those metals and the mineral assemblage (*e.g.* quartz-hematite or ferrihydrite-goethite). However, ITRAX chemostratigraphy indicates a decrease in some elements (*e.g.* Zn) in Unit M4, *i.e.* the hematite-quartz assemblage but to date no explanation could have been drawn. Furthermore, modelling and experimental studies demonstrated that the sorption of most metals was weaker on goethite than on ferrihydrite (Sajih *et al.*, 2014). This observation supports the findings that ageing and transformation of ferrihydrite into goethite will not help preserving metals but, rather will enhance metal release into the pore waters and eventually to the water column.

6.7.2 Authigenic hydrothermal mineralisation

In the FeOx sediments from Unit M4, the absence of fractures or dissolution features in the botryoidal and layered crystallised hematite, and a finer grain size compared to the FeOx in Unit M3 suggest post-depositional precipitation within the sediments.

REE from Unit M4 show a different pattern than in M3 *i.e.* a strong positive Eu anomaly and a low LREE fractionation (FIGURE 6.9C). During high-temperature hydrothermal activity, anhydrite precipitation within the mounds preferentially scavenges Eu^{2+} resulting in a positive Eu anomaly in the anhydrite, which is stronger than in black smoker fluids (Mills and Elderfield, 1995b; Humphris *et al.*, 2005). When the ambient temperature drops below 150°C, dissolution of anhydrite occurs within the interior of the mounds (Petersen *et al.*, 2000). At the Mir zone, anhydrite was not found in the drill cores, but, based on textural

mineralogy within the mounds, its presence during the active stage is strongly suspected (Lehrmann *et al.*, 2018). Low-temperature hydrothermal fluids seeping through the upper part of the mounds acquire anhydrite REE characteristics with strong positive Eu anomalies and a relatively flat LREE pattern (La_n/Gd_n close to 1) (Mills and Elderfield, 1995b; Petersen, 2000). Therefore, the down-core increase in Eu anomaly and decrease in La_n/Gd_n observed in FeOx sediments (FIGURE 6.9C) indicate a low-temperature formation that was subsequent to the high-temperature hydrothermal activity and most likely involved anhydrite dissolution. This authigenic precipitation was occurring more often in the deepest layers due to their closest proximity to the source of low-temperature fluids.

Anhydrite dissolution from the interior of the mound could be responsible for additional features observed within the sediments. First, depressions at the Mir zone have characteristics similar to fluid expulsion features like pockmarks (FIGURE 6.4). Pockmarks on the seafloor are frequent results caused by sediment collapse into dissolution zones and remobilisation of sediments by fluid flow (Hovland *et al.*, 2002). In this hydrothermal environment, the pockmarks could be the result of subsidence and collapse of the sulphide edifice caused by anhydrite dissolution at depth. Second, the increase of dissolved calcium at depth in the sediments indicates diffusion from a source below. This source could consist of dissolved anhydrite contained in the SMS deposits' interior (Lerhmann *et al.*, 2018). When dissolved, sulphate and calcium are expelled into the pore waters and diffuse towards the seafloor. It is suggested that the source of calcium is anhydrite rather than calcite or apatite, as it unlikely that calcite and apatite are present in sufficient concentration in SMS deposits or the jasper layer to explain the Ca gradient. The gradient towards higher dissolved Ca observed at the Mir zone could also be explained by the fact that Mir zone is a younger mound with anhydrite dissolution ongoing.

It is likely that the processes responsible for the presence of hematite encountered at the TAGHF, occur similarly in other worldwide deposits. For example, hydrothermal hematite-rich deposits have been previously reported to occur on the seafloor at the Blanco Fracture Zone (Hein *et al.*, 2008) where a moderate-temperature, strongly oxidized, silica- and iron-rich, sulphur-poor hydrothermal fluid is suggested to explain the precipitation of hematite and quartz. A minimum temperature of 115°C is required for hydrothermal fluids to precipitate hematite as a stable mineral phase (Bischoff, 1969).

How important the proportion of authigenic precipitation of hematite is over accumulation of oxides derived from weathering of sulphides is not entirely clear. The presence of clasts indicate that accumulation from sulphide collapse is not negligible, while the absence of

goethite in unit M4 can be explained by a preferential precipitation of authigenic hematite when the temperature is moderate. The favoured mineral will depend on the temperature and pH of the original environment. A pH of 8 and a higher temperature (> 30°C) will convert ferrihydrite to hematite via structural arrangement and dehydration (Campbell, 1991; Schwertmann *et al*., 1999; Cudennec and Lecerf, 2006), while a lower pH (*e.g.* 4) and a low temperature (ocean bottom, *i.e.* ~4°C) favours goethite by dissolution-nucleation-precipitation (Schwertmann and Murad, 1983; Dunk and Mills, 2006).

6.7.3 The role of Si in lithification

The presence of a Si-Fe cap (a jasper layer) between the massive sulphide ore and the FeOx sediments at the seafloor and only observed on the top of hydrothermally inactive or active mounds could act as a protection barrier for the massive sulphides from oxidative weathering (Stobbs et al., 2019). I suggest that the origin of this Si-Fe cap comes from the sediments, and therefore the silicification, or lithification, of the sediments does help to the preservation of the economic potential of the massive sulphide deposits.

In seafloor environments, silica is either derived from biological production in the water column and on the seafloor (radiolarians, sponges or diatoms), river input of weathered terrestrial rock or from hydrothermal activity (DeMaster, 1981). Hydrothermal dissolved silica precipitation is commonly attributed to steep temperature gradients during fluid cooling, induced by the mixing of seawater and hydrothermal fluids. The same process can occur in subsurface sediments when hydrothermal fluids mix with entraining seawater resulting in a silica saturated, conductively cooled fluid, promoting silica precipitation (Grenne and Slack, 2003). At low temperature, silica precipitates as metastable hydrous polymorph opal-A silica (Jones and Segnit, 1971; Zhu, 2005) and is thought to form a silica-rich gel before transitioning to the metastable polymorphs of opal-CT and opal-C before transforming into quartz, with dehydration (by heat or pressure) driving the crystallisation and structural re-ordering (Zhu, 2005). These transformation processes occur at a late-stage of hydrothermal activity in the hydrothermal sediments and are thought to be responsible for the Si-Fe caps overlying the massive ore deposits (Fe being provided by Fe sulphides or Fe oxyhydroxides) (Stobbs, 2020). In the hydrothermal sediments at the TAGHF, no information on Si content of the sediments is available as the method used (HNO_3 – HCl - HF acid digestion) volatilises Si. However, mineralogy from XRD and SEM-EDS analyses has indicated the presence of Si minerals, in particularly quartz. This presence of quartz is particularly visible in the deeper layers (up to 10 wt%) in Unit M4 just above the Si-Fe cap

that leads to suggest that quartz is somehow related to the Si-Fe caps. In addition, dissolved Si in pore waters from the sediments show a downward increase in concentration (FIGURE 6.10), which indicates a deeper source. We know that the lithified cap overlying the massive sulphide ore is composed of silica (SiO_2/silica minerals > 50 wt%) and Fe oxides or oxyhydroxides. The proximity of both quartz and a greater concentration of dissolved Si, with the Si-Fe caps could therefore show a relationship between the availability of Si and the silicification forming the jasper cap. Hydrothermal Si products are often associated with hematite in volcanogenic massive sulphide ores (Franklin *et al*., 2005) and in the seafloor hydrothermal deposits (Alt, 1988; Hein *et al*., 2008), similar to that found in Unit M4 at the TAGHF, and hence may indicate a hydrothermal origin for the silicification.

6.7.4 A seafloor gossan in the geological record

Terrestrial FeOx sediments, soils or rocks originated from complete oxidative weathering of massive sulphides are called gossans and are now found in extruded paleo-oceanic ridges. As my sediments are mainly originated from oxidative weathering, although still on the seafloor, I compared my results with terrestrial gossans and seafloor gossans. The results show that the gossans cover directly above the eSMS bodies is depleted in transition metals, and therefore, at least at TAGHF, the mound-top sediments cannot be considered as a potential economic mineral resource. Yet previous studies, including at TAGHF and at VMS deposits, have found a different result (Herzig *et al*., 1991). Hannington *et al*. (1988) presented evidence for supergene enrichment of gold in oxidized sulphide sediments (up to 15 ppm Au), and associated secondary Cu enrichment, and suggested this occurred during seafloor weathering. In addition, the oxidized VMS ores in ancient massive sulphides are commonly enriched in gold in the zone of secondary Cu-sulphides and gossans, for example in Cyprus Skouriotissa orebody (Herzig *et al*., 1991) and the Iberian Pyrite belt (Velasco *et al*., 2013). The FeOx sediments, which represent a relatively-newly formed gossan, over an eSMS ore body, have generally low gold contents (< 150 ppb). Therefore, the gold content discrepancy between the Au-Cu-rich gossans studied by Hannington *et al*. (1988) and those of my study has yet to be explained. Two hypotheses are regarded here. Firstly, the material studied by Hannington *et al*. (1988) could have not yet been completely weathered into FeOx, and would be more comparable to a "fresh", and relatively unweathered material similar to the sediments found at the rim and the lower base of the Mir zone or in small and distal sedimentary basins (*cf.* this thesis, CHAPTER 5, SECTION 5.6.2.1). Oxidative weathering may be responsible for the formation of Au-rich secondary Cu-sulphides, however processes such as rapid burial is required to preserve the

high concentration of metals (this thesis, CHAPTER 5). Secondly, it could be probable than an additional stage responsible for a gold enrichment occurring during the ageing of a seafloor hydrothermal mounds moving odd-axis has not yet occurred at the TAGHF. Otherwise, complete destruction of the exposed sulphides and secondary minerals (such as jarosite, and atacamite) will follow, leaving behind a barren Fe-oxide gossan. This destructive evolution is comparable to the different stages of gossan maturity observed during supergene exhalative weathering at VMS deposits where the final results are the dominance of goethite, quartz and hematite (Velasco *et al*., 2013). Another explanation for the higher concentration of gold and trace metals in terrestrial gossans could be due to recent meteoric weathering and leaching of the underlying or body by acid sulphate ground waters which transport metals from their source into the sediments (*e.g.* Benedetti and Boulëgue, 1991; Andreu *et al*., 2015).

The evolutionary stages of the sediments can be reconstructed as follows (not especially in geochronological order as hydrothermal activity is cycling and some stages could not be recorded, FIGURE 6.11).

- Low-temperature hydrothermal mineralisation across the TAGHF is suggested by numerous indicators: nontronite was found at the Alvin zone mounds (Severmann *et al*., 2004), the active TAG mound (Mills *et al*., 1996) and Mir zone (Rona *et al*., 1993b; Rona *et al*., 1996) and this mineral precipitation requires reduced hydrothermal fluids with temperature of 54-96°C (Severmann *et al*., 2004). Second, Fe-Mn crusts are precipitated by low-temperature hydrothermal fluids. And finally, REE patterns in the sediments indicate a low-temperature fluid seepage.
- A medium-temperature, Fe-rich, S-poor and reduced hydrothermal fluid (> 115°C) precipitates authigenic hematite, identified in our sediments by their high crystallinity, when they start mixing with cool oxidized seawater.
- A Si-rich hydrothermal fluid leads to the formation of Si gels within the sediments, with a temperature varying between 50 and 120°C (Stobbs *et al*. 2020). When the fluid starts mixing with cool oxidized seawater, the precipitation of Si can explain the concentration gradient in dissolved Si in the sediment pore waters. Those Si gels will subsequently transform into a series of silica polymorphs to finally form the Si-Fe caps above the massive sulphide layers.
- Oxic seawater penetrates the sediments and weathers sulphide-derived materials accumulated by sulphide chimney collapse. A circulation of heated seawater may be responsible for the diagenetic ferrihydrite transformation into hematite at depth.

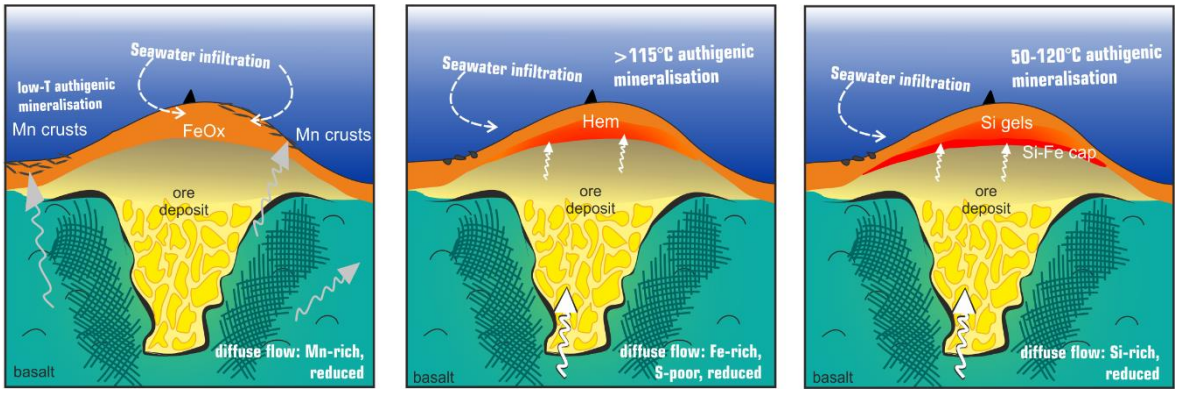

FIGURE 6.11 Evolutionary stages of some processes (oxidative weathering by seawater infiltration, medium-temperature authigenic mineralisation of hematite and quartz, transformation of Si gels into Si-Fe caps, low-temperature hydrothermal mineralisation of Mn crusts).

Fe-Mn crusts associated with low-temperature reduced fluids have been collected at other locations than on the top of inactive mounds (*e.g.* few kilometres away from the active vent sites on the East) (Mills *et al.*, 2001), indicating fluids can be channelled and can diffuse through the sediments at further distance from a hydrothermal mound (Mills *et al.*, 2001). Regarding the medium-temperature, Fe-rich or Si-rich hydrothermal fluids, we cannot yet confirm the presence of a warmer temperature *in situ* (we would need to measure the temperature within the sediments, several meters deep, in a hydrothermal mound that we know at its later waning stage), and also it has not been demonstrated the presence of such fluids in another environment close to seafloor hydrothermal systems in the literature. It is not clear yet at what spatial extent those fluids influence the sediment geochemistry although results obtained in sediments sampled away from a hydrothermal mound (see CHAPTER 5) suggest that advection of warm fluids is likely restricted to the main ore body.

6.8 Conclusions

Sediments recovered from the surface of the TAGHF eSMS mounds primarily consist of Fe oxyhydroxides: goethite, ferrihydrite and hematite, with minor amounts of todorokite (Mn-oxide), quartz and nontronite and have low contents of transition metals apart from Fe and Mn. We could differentiate two post-depositional processes impacting the sediment composition, once the high-temperature hydrothermal fluid flow had ceased: Firstly, sulphide-derived material is converted into ferrihydrite by oxidative weathering; then the ferrihydrite is transformed into goethite. However, increased temperatures at greater depth in the sediments, caused by the proximity of the ore body, can lead to recrystallization of ferrihydrite into hematite, rather than into goethite. On the other hand, advective moderate-

temperature (>115°C) reduced, silica and/or iron-rich hydrothermal fluids can diffuse upwards towards the seafloor and induces the precipitation of silica polymorphs and authigenic hematite, due to a sharp temperature gradient. This process can play a role in the silicification of the sediments to form the Si-Fe cap layer. While the first process (oxidative weathering) induces a considerable loss of metals, from the sediments, the second process (authigenic precipitation of Si) will protect the underlying ore body.

The sediment deposits found at the TAG mound-tops are considered to be close analogues of the gossans identified at VMS deposits, *e.g.* at the Troodos sulphide deposits, however my study demonstrates that no similar supergene enrichment (in particularly gold) is found at the relatively recently formed gossans. Consequently, I suggest that any enrichment must occur at an additional stage, occurring during the ageing of the deposits. For example, it could occur after the drifting of the deposits away from the hydrothermal heat source, during the lithification of the deposits, during a seafloor uplift (and combined with the presence of mineral-rich pore water fluids) or during exhalative supergene weathering.

My findings on the gossanisation process endorse the three evolution stages currently observed in supergene gossans, which are i) the oxidative dissolution of sulphides; 2) the diagenetic evolution of the oxyhydroxides and 3) the physical reworking of the previously formed oxides (collapse of the hydrothermal material, and cementation by low to medium-temperature hydrothermal mineralisation). Nevertheless, due to their unique geology and geochemistry, the gossans remain excellent indicators as a surface exploration guide for buried SMS deposits on land as well as in submarine conditions.

Chapter 7 Conclusions

In this thesis, I have presented evidence for the following: (i) a detailed geochronological study of the hydrothermal activity at the TAGHF (CHAPTER 4), (ii) a comparative study of the metal preservation in three distinctive sedimentary environments (*i.e.* top of inactive hydrothermal mounds, base of mound slopes and depositional basins) (CHAPTER 5) and (iii) an in-depth investigation of post-depositional chemical and physical processes in the metalliferous material overlying the eSMS deposits (CHAPTER 6).

This final chapter provides a synthesis of the findings of these studies, placed in an evolutionary context for the TAGHF and highlighting the post-depositional processes occurring in the sediments. Following this, I summarize the answers to the three questions posed in the introduction of this thesis and the main conclusions drawn from my new results. Finally, I identify potential future areas of research within the context of (i) geochronological evolution of a hydrothermal system, (ii) deep-sea mineral exploration, (iii) mineral deposits, and (iv) global geochemical budgets. The FIGURE 7.1 complements the conclusions chapter to highlight the intertwined connections between processes, evolutionary stages and environments. This figure also provides a summary of the conclusions of this thesis.

7.1 Discussion on the geochronological evolution of the TAGHF

In the last 30 years, numerous authors have contributed to the understanding of the evolution of the TAGHF. These authors include Tivey *et al*. (1995), who showed that mixing of hydrothermal fluids with seawater inside the sulphide mound leads to ongoing remobilisation of metals and a zone refinement at the active TAG mound; Lalou *et al*. (1995) provided the first geochronological dating of the system; one of the most comprehensive studies is provided by (Petersen, 2000; Petersen *et al*., 2000), partly summarised in the section 1.4 of this study. Here, below, I provide an extended history of the rise and fall of the TAGHF, based on my findings from mineralogical, geochemical and geochronological analyses.

7.1.1 Rise

Seafloor age estimates of the TAGHF provided in CHAPTER 4 suggests that the furthest eastern SMS mound that is known, *i.e.* the Mir zone, lies on a > 270 ka-old oceanic crust (according to a spreading half-rate of 1.3 cm per year to the west). This age is the maximum age of initiation of hydrothermal activity at the TAGHF. At this location, the oldest hydrothermal material, a 140 ka old Mn crusts, was dated by Lalou *et al*. (1995) and is thought to have precipitated from diffusing, low-temperature hydrothermal fluids that were precursors to the later high-temperature hydrothermal activity. However, Mn crusts are products originating either from diffuse venting, low-temperature fluids channelled away from high-temperature vent sites or formed by hydrogenous incorporation of Mn particles into the sediments released by hydrothermal vents (Mills *et al*., 2001). Hence, it could be possible that high-temperature hydrothermal venting already occurred at 140 ka east of the current hydrothermal system, i.e. on the ridge flanks, where currently seeping of reduced fluids occurs and where hydrothermal Mn precipitates have been identified.

7.1.1 Apogee

The apogee of a hydrothermal system is reached when high-temperature hydrothermal fluids are focused at vents and both massive sulphides on the seafloor and in the subsurface, form SMS mounds (FIGURE 1.8). Geochronological analyses, detailed in CHAPTER 4, were applied on hydrothermally-influenced sediments consisting of Fe and Mn-oxide plume particles released by black smokers, interbedded with non-hydrothermal, *i.e*. biogenic pelagic carbonate sediments. The resulting layering records the episodic pulses of hydrothermal activity and confirms that high-temperature hydrothermal activity across TAG spanned from at least 100 ka at the Mir zone and from 72 ka at the Shimmering mound to the present day. The results also indicate that a partial rejuvenation occurred between 4 and 8 ka simultaneously across the TAGHF at the Mir zone, Alvin zone (most likely Shinkai mound, which show features of a younger deposits), and the TAG active mound. The recent rejuvenation at the off-axis Mir zone requires either a separate off-axis heat supply, or an open structural pathway for fluids spawned from the axial heat source. A more likely process to maintain this open pathway is the presence of active detachment-fault tectonics (*e.g*. Humphris *et al*., 2015) beneath the Mir zone.

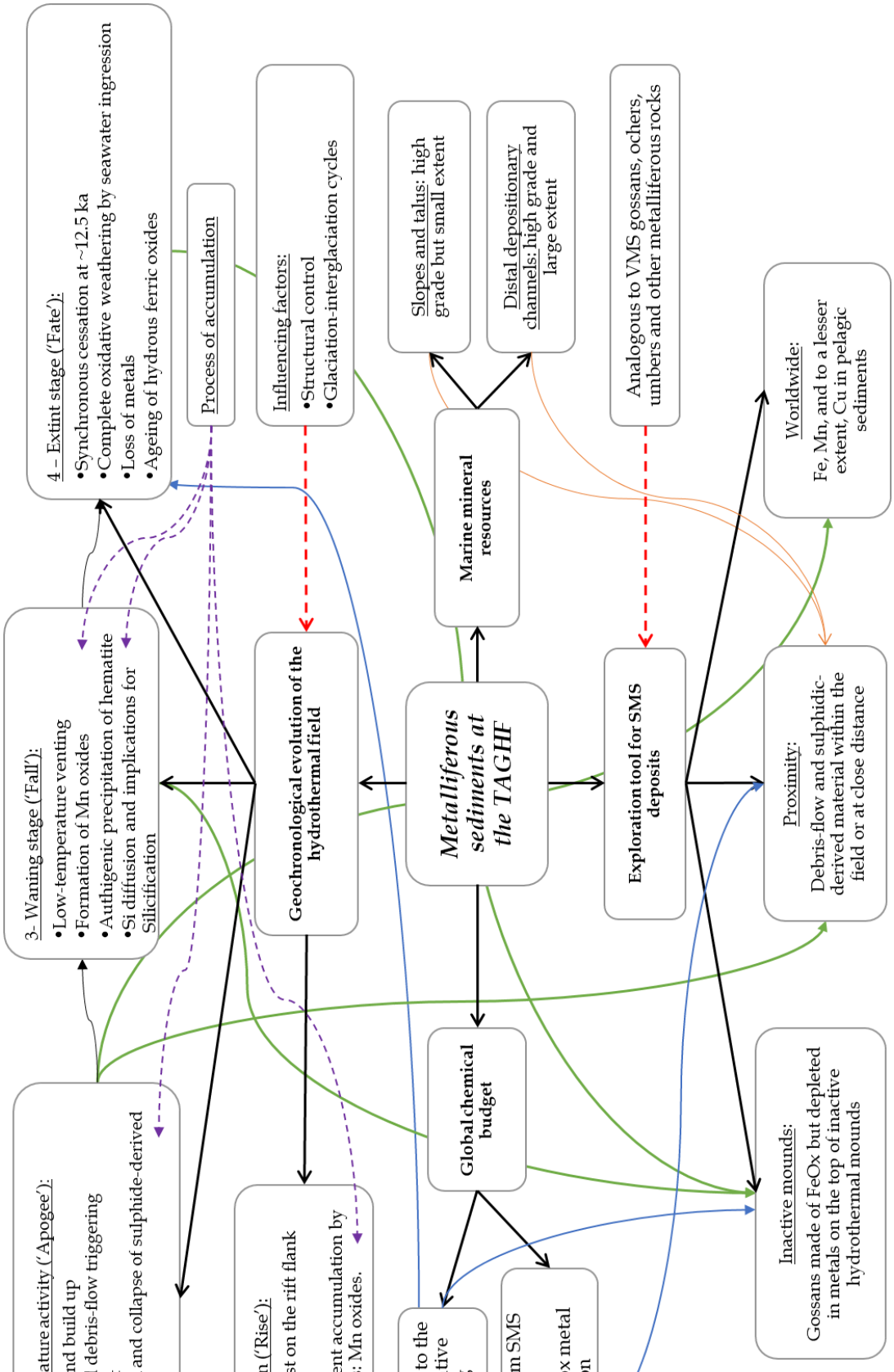
4 – Extint stage ('Fate'):
•Synchronous cessation at ~12.5 ka
•Complete oxidative weathering by seawater ingression
•Loss of metals
•Ageing of hydrous ferric oxides
Process of accumulation
Influencing factors:
•Structural control
•Glaciation-interglaciation cycles
Slopes and talus: high grade but small extent
Distal depositionary channels: high grade and large extent
Analogous to VMS gossans, ochers, umbers and other metalliferous rocks
3- Waning stage ('Fall'):
•Low-temperature venting
•Formation of Mn oxides
•Authigenic precipitation of hematite
•Si diffusion and implications for Silicification
Geochronological evolution of the hydrothermal field
Marine mineral resources
Metalliferous sediments at the TAGHF
Exploration tool for SMS deposits
Worldwide:
Fe, Mn, and to a lesser extent, Cu in pelagic sediments
Proximity:
Debris-flow and sulphidic-derived material within the field or at close distance
2- High-temperature activity ('Apogee'):
•Sulphide mound build up
•Instability and debris-flow triggering
•Plume fall-out
•Accumulation and collapse of sulphide-derived material
Global chemical budget
1- Field settling and formation ('Rise'):
•Within a young basaltic crust on the rift flank
•Oldest Mir zone
•Start of metalliferous sediment accumulation by diffusion on flank sediments: Mn oxides.
Source of metals to the ocean by oxidative weathering
Sink of metals from SMS material
by burial and redox metal redistribution
Inactive mounds:
Gossans made of FeOx but depleted in metals on the top of inactive hydrothermal mounds

FIGURE 7.1 (previous page) Schematic box model showing the processes affecting the metalliferous sediments and the relationships between processes, evolutionary stages and environments. The colour and shape of the arrows categorize the different links (*e.g.* blue lines are related to the geochemical budgets).

When a vent is hydrothermally active, it generates hydrothermal products increasing in volume and accumulating sediments, a process that could lead to structural instability of the seafloor and produce debris-flows. CHAPTER 5 investigates the origin and processes responsible for hydrothermal sediment accumulation. Debris-flows or turbidity currents, observed in distal locations from the hydrothermal mounds, may not only be specific to periods of hydrothermal activity, but their frequency likely increases in active periods. This is the case for the debris-flows dated at the Shimmering mounds and in the Alvin zone, which are contemporaneous with periods of hydrothermal activity (CHAPTER 4). The presence of sulphide in the sediments is a consequence of gravity-driven debris-flows bringing older, high-temperature deposits to the flanks and bases of the mounds, and subsequently depositing them in depositional basins. On the flank and bases, sediments contain thick (cm-scale) unsorted layers of sulphide with high-base metal contents (*e.g.* up to 28 wt% Cu), although the thickness of these sediment layers is less than a meter. In contrast, in the depositional channels and basins, sediments accumulate up to several meters thick and consist of sorted mm-scale layers of sulphides and sulphide-derived material with a high metal grade (*e.g.* up to 10 wt% Cu).

7.1.2 **Fall**

The remarkably synchronous cessation of hydrothermal activity at 12-13 ka at a number of discrete hydrothermal sites across the TAGHF implies a common heat source feeding several venting sites simultaneously. This cessation coincides with a rapid rise in sea-level, following the last glacial termination. If the rapid sea-level rise suppresses decompression in the mantle and results in a short hiatus of melt supply, then this relationship could support the sensitivity of hydrothermal systems to rapid sea-level changes. Alternatively, it might reflect other pressure driven changes to the sub-seafloor with consequences for fluid pathways and substrate permeability.

Weak and remnant hydrothermal activity may still persist in apexes of the TAGHF away from the active mound. For example, shimmering waters were observed at Southern mound (Murton *et al.*, 2019), temperature abnormalities were measured in sediment cores

during M127 expedition (Petersen and Scientific Party, 2016) and heat flow values up to 13.5 W/m^2 (Rona *et al*., 1996) were measured at the Mir zone. It seems reasonable, therefore, to assume that heat flow will eventually decrease to background values only once the hydrothermal field moves well away from the axis of the Mid-Atlantic Ridge.

CHAPTERS 5 and 6 report the processes occurring in the sediments overlying the eSMS deposits after high-temperature hydrothermal fluid flow has ceased. During the waning stage of hydrothermal activity, hydrothermal fluids undergo a decrease in temperature. As a result, most of the base metals, except Fe and Mn, precipitated before reaching the seafloor and the deposits become dominated by the precipitation of Mn oxides in shallow horizons (about 30 cm-depth). Ferromanganese crusts are commonly present underneath the pelagic carbonate cover across the TAGHF and highest Mn concentrations among all the sedimentary environments studied here is found on the top of the extinct mounds. To precipitate these horizons, CHAPTER 5 presents evidence that a strong advective flux was once required, such as low-temperature, Mn-rich, reduced fluid flow in a late-stage of the hydrothermal activity of the system. When these fluids come in contact with a redox zone, Mn precipitates and subsequently dissolved, redox-sensitive metals (*e.g*. Cu and Co) in pore waters absorb onto Mn-oxides, explaining the higher downhole concentration of those elements in the Mn-rich layers.

In CHAPTER 6, the down-core change in lithology in sediments from the top of the inactive mounds was examined. The abundance of highly crystalline hematite, dominating over other Fe-oxyhydroxides, in deep horizons requires Fe-rich, moderate-temperature (>115°C) fluids. In addition, the REE patterns and an elevated dissolved Ca concentration are indicative of diffuse fluid seepage due to hydrothermal anhydrite dissolution within the sulphide mound. Anhydrite dissolution at the TAG active mound was responsible for brecciation and collapse of the top of the mounds, as already suggested by Petersen *et al*. (2000). In addition, upwards diffusion of dissolved Si in pore waters towards the seafloor, may account for the precipitation of quartz and a probable, but not yet confirmed, presence of silica gels. The silica gels would lead to the silicification of oxyhydroxide sediments, and ultimately to the formation of a thick, and most likely impermeable Si-Fe caps or jasper layer, protecting the sulphides from seawater and oxidation (Stobbs, 2020). The multi-stage formation of the hydrothermal mounds (*i.e*. rejuvenation of high-temperature hydrothermal activity, CHAPTER 4; Lalou *et al*., 1998) may be responsible for a combined presence of Mn oxide and hematite precipitation (as each requires a different fluid

composition) and trace metal refinement within the sediments and could also explain the recrystallization of amorphous silica to quartz.

7.1.3 Fate

In CHAPTER 6, the presence of gossans on top of the SMS mounds is evidence that seawater has penetrated and oxidation has completely altered the massive sulphide cover derived from chimney material. As a result, the gossans are depleted in many of the base metals, such as Zn and Cu. Similarly, no gold supergene enrichment is found, and this lack of gold contrasts with the Au-Cu rich gossans and terrestrial VMS deposits. The discrepancy suggests that any gold enrichment must occur after the drifting of the deposits away from its hydrothermal heat source. The transition into the jasper layer below the sediments shows that the silicification processes responsible for the Si-Fe caps formation requires an invasion of the gossan material by silicifying fluids. Hence silicification post-dates the gossan formation, which was presumably on-going during the waning stages of the hydrothermal activity.

Meanwhile, mass-wasting and transport of SMS material from the mounds onto the surrounding seafloor produced thick layers of metalliferous sediment across the TAGHF. The lack of significant oxyhydroxide material and the dominance of sulphide in many of these sediments show that they were accumulated during periods of high-temperature hydrothermal activity when sulphide chimneys and structures were being formed most rapidly. In depositional basins the rapid burial by pelagic sediments initially protects the sulphides and metal-rich sediments, and is the most effective metal-trapping mechanism of all the environments studied so far. In the sediments of those locations, diagenetic processes involve redox remobilisation of some redox sensitive metals (Cu, Mn and Co). However, sulphides exposed to seawater penetration for a longer time tend to fragment and the metals dissolve into pore waters from where they are eventually lost to the ocean, such as observed at the base of the slopes of hydrothermal mounds. Ultimately, pelagic sediments, rich in Fe and Mn released from surrounding younger hydrothermal vents, settle and smooth the topography of the mounds surface, such as at Rona mound.

7.2 Conclusions of the study

7.2.1 How does hydrothermal activity vary over time at a specific hydrothermal field and are there influencing factors?

My study demonstrates that there is a synchronisation in activity between a number of discrete hydrothermal sites across the TAGHF. Firstly, a synchronous suppression of high-temperature activity occurred at 12-13 ka at three major sites: Shimmering mound, Mir mound and Rona mound, implying a common heat source feeding several vents simultaneously. This suppression coincides with a rapid rate of rise in sea level, following the last glacial termination at the end of MIS2. Then, hydrothermal activity appears to have been continuous across the TAG field, with hydrothermal fluxes being significantly higher during glacial periods compared with today. In the last 10 ka, a partial rejuvenation of the field occurred with activity ongoing at the TAG active mound and recently ceased activity at the Mir zone and Shinkai mound.

The results support the hypothesis that rapidly rising sea-level suppresses decompression melting in the upper mantle resulting in a short hiatus in melt supply to the heat source powering the TAGHF. The evidence for recent rejuvenation of hydrothermal activity at the off-axis MIR zone requires either a separate off-axis heat supply, or an open pathway for fluids to tap into the hydrothermal mounds from the axial heat source.

7.2.2 How efficient is the subsurface trapping mechanism for metals in sediments surrounding a hydrothermal site?

The efficiency of the trapping mechanism for metals depends on the location of a hydrothermal site. Metalliferous sediments in the TAGHF, located at the top of extinct mounds, at the base of the mounds, and in distal depositional basins and channels, display discrete geochemical, morphological and mineralogical characteristics reflecting the origin of the metals, their depositional processes and diagenesis. Processes trapping metals are found to be most effective in depositional channels where metals are rapidly deposited and buried, while sediments from the mound-tops, where exposure to seawater has extensively weathered hydrothermal sulphide edifices and their products, have seen their metals almost completely depleted. The concentration of metals in the sediments also depends on their distance of transport and the morphology of the seafloor, with the highest metal

concentrations found in sediments flanking the mounds and their proximal depository fans.

These data show that SMS collapse, mass wasting and transport by turbidity events, redistributes and rapidly deposits hydrothermal materials away from their sources. Sediments remaining on mound-tops are exposed to seawater, where they release their metals retained in chlorides (transiently) and oxides. Sediments proximal to their source, such as in talus and fans, on the slopes of hydrothermal mounds, are coarser and more resistant to alteration and preserve the highest metal concentration in thick beds. More distal deposits accumulate metals in depositional basins by repetitive turbidity events. Those processes rapidly bury and compact both primary sulphides and secondary oxides.

Early diagenesis takes place in each of these three environments. Sulphide oxidation acts together with organic carbon degradation to control the redox zonation. When the resulting redox boundary is restricted to deep horizons, dissolved non-ferrous metals diffuse to shallower depths and are not released to the water column, but contained in oxides, chlorides and by adsorption on Fe-Mn-oxyhydroxides. Redox sensitive metals, such as Cu and Co, are therefore enriched and preserved in these environments and found in primary sulphides and secondary Mn oxides. Zn enrichment is exclusive to primary sulphides and is not influenced by later redox conditions. Where a carbonate sediment cap is missing, oxygen rapidly diffuses into the sediments and metals are leached into the water column. Where deposits are recent, high metal contents are retained within thick layers of unsorted sulphides; for example, in the sediments on slopes. However, sulphides exposed to oxygenated seawater penetration for a longer time tend to fragment and, with increased surface area, the metals dissolve into pore waters and are eventually lost to the ocean. Ultimately, these reactions leave behind barren Mn oxides and Fe oxyhydroxides. This study demonstrates that sediments in distal depositional channels are of similar economic value to the SMS deposits themselves. Although, any future exploration of sediment-hosted mineral deposits should consider the conditions of preservation along with the contribution from the sources. Indeed, a higher input of detrital components will help retain the metal tenor, although it will also lead to a grade decrease by dilution.

7.2.3 How do hydrothermal sites evolve after the high-temperature hydrothermal flow ceased?

Sediments recovered at the surface of the TAGHF eSMS mounds dominantly consist of Fe oxyhydroxides: goethite, ferrihydrite and hematite, with minor todorokite (Mn-oxide), quartz and nontronite and display low contents of transition metals apart from Fe and Mn. Post-depositional processes occurring in the sediments, once the high-temperature hydrothermal fluid ceases, are of two principal types. On one hand, there is an oxidative weathering of sulphide-derived material into ferrihydrite. This ferrihydrite later transforms into goethite. However, if the deeper sediment layers are warmer due to the proximity to the ore deposits, then the increase of temperature in the oxygen-rich water will lead to recrystallization of ferrihydrite into hematite, rather than into goethite. On the other hand, an advective moderate-temperature (>115°C) reduced, silica and/or iron-rich hydrothermal fluid diffuses towards the seafloor and induces the precipitation of silica gel and polymorphs, and authigenic hematite, due to a sharp temperature gradient, and which play a role in the silicification of the sediments to form the Si-Fe cap layer.

While the first type (oxidative weathering) induces a considerable loss of metals, the second type of process (authigenic precipitation) helps to protect the underlying ore body. These sediment deposits are considered to be close analogues of the gossans identified at VMS deposits, *e.g.* at the Troodos sulphide deposits. However, my study demonstrates that no similar supergene enrichment (in particularly gold) is found at the relatively recently formed gossans. Consequently, I suggest that any enrichment must occur after the drifting of the deposits away from the hydrothermal heat source, for example during the lithification of the deposits, seafloor uplift or during exhalative supergene weathering.

My findings on the gossanisation process endorse the three evolution stages currently observed in supergene gossans, which are: i) the oxidative dissolution of sulphides; 2) the diagenetic evolution of the oxyhydroxides and 3) the physical reworking of the previously formed oxides (collapse of the hydrothermal material, and cementation by low to medium-temperature hydrothermal mineralisation). Nevertheless, the gossans remain excellent indicators as a surface exploration guide for buried SMS deposits on land as well as in submarine conditions due to their unique geology and geochemistry.

7.3 Future work

7.3.1 Further research in a geochronological context

CHAPTER 4 reveals that hydrothermal activity was suppressed simultaneously across the TAGHF at the last glacial termination. This finding suggests that external forcing from climate change has an unexpected influence on hydrothermal activity through mechanisms, as yet, unknown. I suggest future research is focused on testing this finding in other hydrothermal systems, preferably in the metalliferous sediments from across the world ocean, and this way, to confirm a causal relationship between global climate and hydrothermal activity. Comparing hydrothermal activity at intermediate to fast-spreading ridges with slow-spreading ridges could also provide distinctions between each type of spreading centres, such as the confirmation of shorter hydrothermal active timespans or a more frequent activity, both suggested to occur at fast spreading ridges. Deep-sea exploration of inactive hydrothermal fields on ridge flanks could be extremely helpful to assess past hydrothermal activity. In this context, IODP expeditions 390 and 393 (2020-2021) targets the South-Atlantic seafloor to quantify the past hydrothermal contributions to global geochemical cycles and investigate the signature of changing ocean chemistry in the hydrothermal record http://iodp.tamu.edu/scienceops/expeditions/south_atlantic_transect.html).

7.3.2 Future research in deep-sea exploration

Modern-day exploration of hydrothermal systems largely depends on distal hydrothermal plume signal sensors (*i.e.* heat, optical, oxidation-reduction potential, methane, Mn, Fe and ^{3}He) deployed on AUVs (German *et al.*, 2008). However, this technique is limited to the detection of active vents, and therefore catalogue of inactive vents, or fields, is currently biased. Additional geophysical techniques, such as seafloor bathymetry, side-scan sonar, seismic reflection and electromagnetics, can be applied in a field-scale resolution to detect inactive mounds (*e.g.* Gehrman *et al.*, 2019). In the future, sediments should also be used in deep-sea exploration and in the following paragraph I provide suggestion how to best use them.

From an exploration point of view, at a oceanic basin-scale, Fe and Mn oxide sediments provide excellent vectors for hydrothermal systems: geochemical proxies/signals are carried over long distances by hydrothermal plumes, are resistant to alteration after

deposition and ratios such as (Fe+Mn+Al)/Al ratio can be used as indicator for the distance to the hydrothermal site, as they increase closer to hydrothermal sites (Boström *et al*., 1969; Feely *et al*., 1992; Feely *et al*., 1994a; Resing *et al*., 2015; Liao *et al*., 2018). However, within a hydrothermal field, the Fe and Mn input from overlying hydrothermal plumes to the sediments will be so high that it will overprint the chemical composition of the sediments, and hence using ratios as vectors will be difficult. However, in this case, as explained in CHAPTER 5, the sediment lithology and geochemistry can be used, as both depend on the sediment accumulation processes and the geological environment, and also depend on the distance to the hydrothermal mounds. Hence, on-board visual inspection of sediments collected with a gravity corer or of surface sediments could be used as a preliminary vector: the proportion of the hydrothermal facies in the sediment core, consisting of Fe oxyhydroxides, sulphides or Mn oxides, will consistently increases towards a hydrothermal mound in FIGURE 7.2. In addition, it is possible to conclude which environment the sediments are coming from by comparing their lithology:

- Sediments deposited in distant depositional basins have thin (mm-scale) sulphidic sand layers and thick accumulation (up to several meters) of Fe and Mn oxyhydroxides, deposited in turbiditic flows.
- Sediments deposited at distances less than 50-100 m to the hydrothermally active mound have thick (cm to dm-scale) sulphide sand layers in very poorly sorted sediments. The pore waters will be acidic and reducing, containing high concentrations (up to ppm values) of transition metals.
- Sediments deposited on top of inactive hydrothermal mounds are dominated by a mineralogical assemblage of red Fe oxyhydroxides (gossans), and are characterized by the absence of trace metals (as described in CHAPTER 6).

The Ocean Technology and Engineering group at the National Oceanography Centre are currently developing a sensor for *in situ* measurements of total alkalinity and dissolved Fe and Mn (Milani *et al*. 2015; Schaap *et al*., 2019) to be deployed from autonomous systems. This type of sensor deployed on an ROV or AUV, as well as direct geochemical analyses of pore waters (by spectrophotometric sensors, Milani *et al*., 2015) and temperature, could speed up the recognition of diffuse hydrothermal fluids and sulphide deposits leading to identification of old or recent, undiscovered hydrothermal sites.

On a second matter, geochemical exploration for vectoring hydrothermal systems should also consider low-cost efficient strategies such as offshore prompt mineralogical and geochemical determination methods (*e.g.* on board XRD analytical instruments) (Milinovic *et al.*, 2017). The results could provide a mineralogical map, in near-real time, of the seabed and identify the potential vectors.

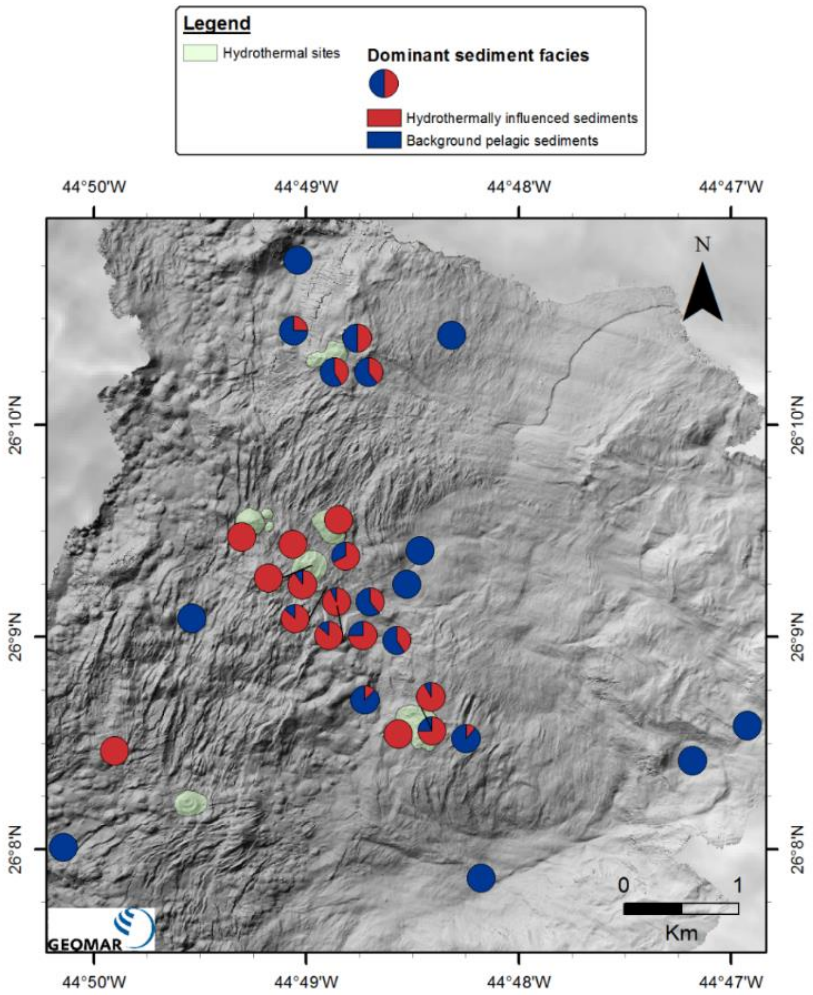

FIGURE 7.2 Sedimentary facies distribution at the TAGHF based on geochemical analyses at 30 gravity coring and rock drilling stations during M127 (data provided by Blue Mining, unpublished) and JC138. Based on stratigraphic logs, the percentage of core length with hydrothermal influence has been calculated as 100*(hydrothermal influenced sediment/full length), where hydrothermal influenced sediments have >10wt% Fe concentration and reddish colour, and are represented by the pie charts for each station. (*cf.* APPENDIX C.4 for the dataset summary).

7.3.3 Future research in mineral resource assessment

Following the results of this thesis, many uncertainties remain about the resource potential of metalliferous sediments at the TAGHF (see SECTION 5.6.4). While there is an agreement

on the metal tenor as an interest to economic resources, the volume of the ore deposit is largely unconstrained. In order to characterise the feasibility of such an exploitation, lateral extension and depth penetration of the deposit must be assessed. These parameters could be addressed by geological mapping and geophysical surveys (*e.g*. seismic surveys and sub-bottom profilers).

Given the relationship between metalliferous sediments and SMS deposits, there is a clear requirement for extended and comprehensive descriptions of the metalliferous subsurface around the world to fully assess the potential of metalliferous sediments as mineral resources. There is a particular interest to study hydrothermal systems lying within exclusive economic zones as those systems will have an important socio-economic and political impact. Ultimately, to determine the ecological impact of such mining, it is elemental to fully understand the complex interaction of geological and biological communities and establish a legal frame for the protection of the benthic communities.

7.3.4 Future research in the global metal budget assessment

From a wider context of the Earth system and the global geochemical budget, the fate of the metals contained in the hydrothermal sediments is uncertain. Their preservation cannot be assured through geological time during their passive transport away from the ridge. Indeed, low-temperature hydrothermal fluid flow and hydrothermal mineralisation are common within the ridge flanks, presumably inducing a redistribution of the metals. Nevertheless, metalliferous sedimentary rocks associated with VMS deposits are commonly found on land, thus indicating that a certain proportion of those metals can be preserved through sediment lithification and uplift.

The compositional data that is available for hydrothermal sediments is exceedingly limited, in comparison to that of hydrothermal vent fluids, chimney sulphates and sulphides and buoyant plume particles. Future research and modelling of metal fluxes requires quantification of fluxes from a series of different sources and sinks: from weathering of sediments in the ocean, riverine inputs, or scavenging by sediments. The opportunity to apply the metal budget calculations of sediments at a greater distance from their source could provide a stronger and more reliable model, defining what percentage of hydrothermal sulphides are weathered into Fe oxyhydroxides (the gossans) and what percentage of sulphidic material is transported away and preserved into the sediments as a sink which will then be in the long term recycled in the subduction zones.

Appendix A **Supplementary material to the methods and analyses**

A.1 **M127 Gravity coring strategy**

Gravity core planning prior to the *RV Meteor* expedition M127 cruise based on pre-existing bathymetry and with identification of the potential sediment ponds.

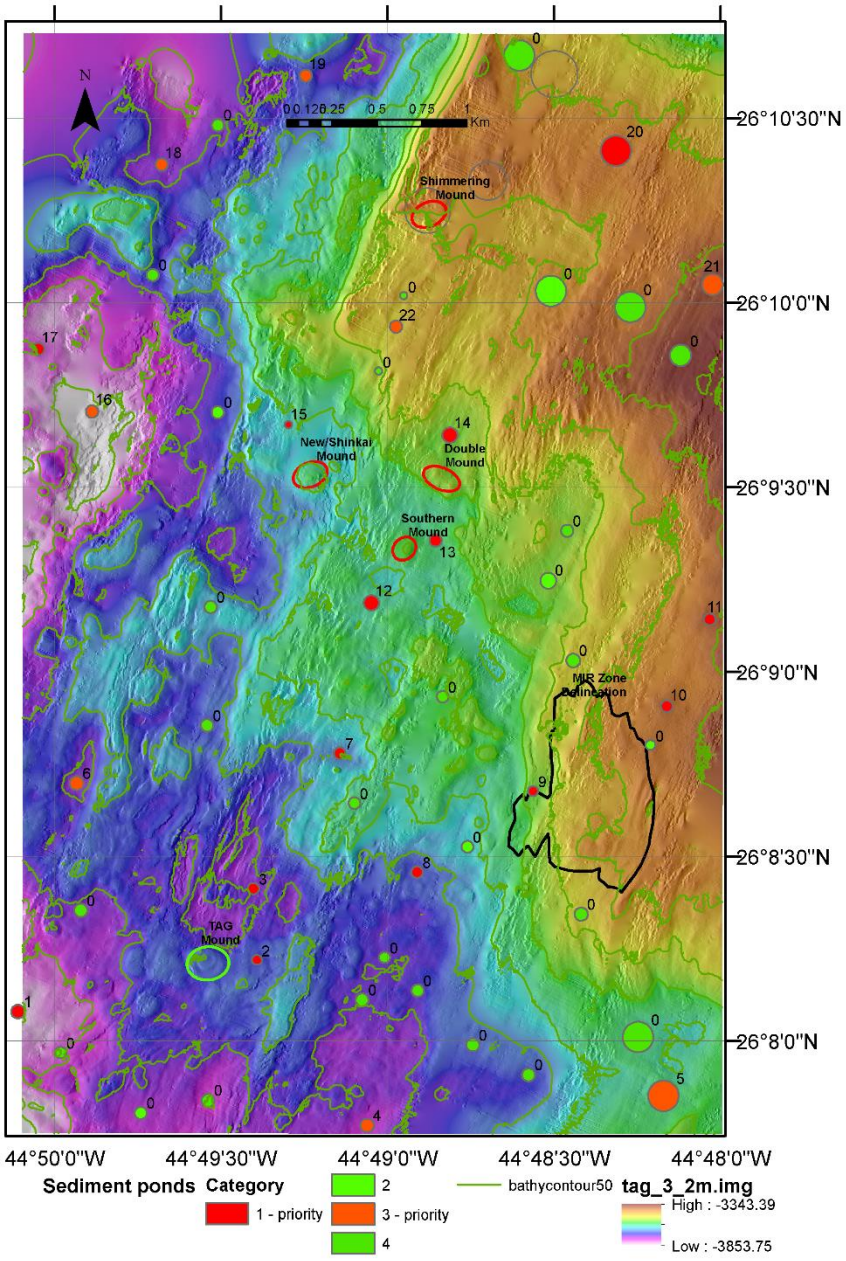

A.2 Coring location during M127 expedition

Coring location map during the M127 expedition on board the *RV Meteor*. Insert indicates the reference core location (M127/711). Location of the TAGHF is on the west of the insert. M127/710 was an unsuccessful attempt to recover a reference core. From Petersen and Scientific Party (2016).

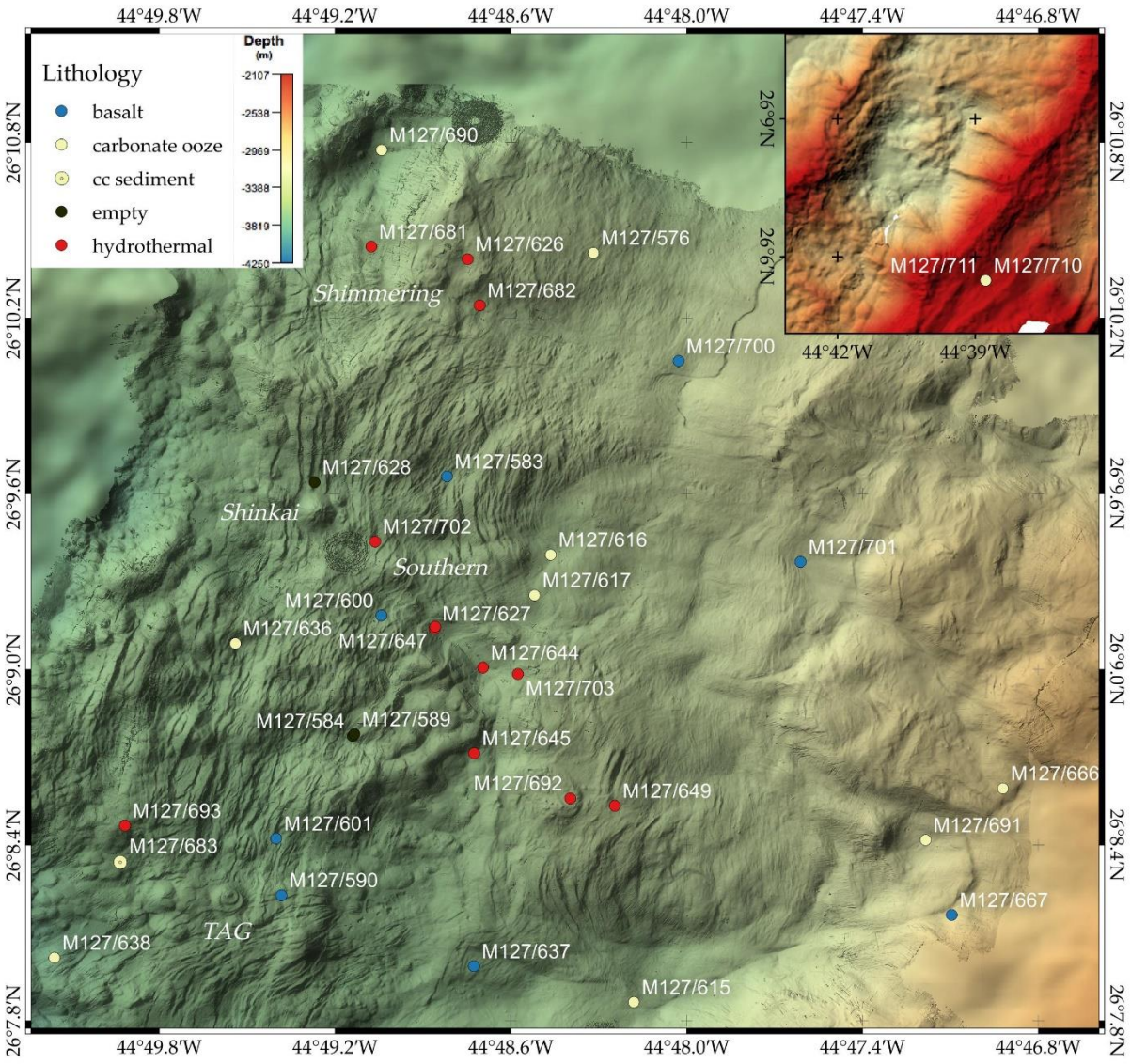

A.3 Workflow followed during the cruise M127 and JC138

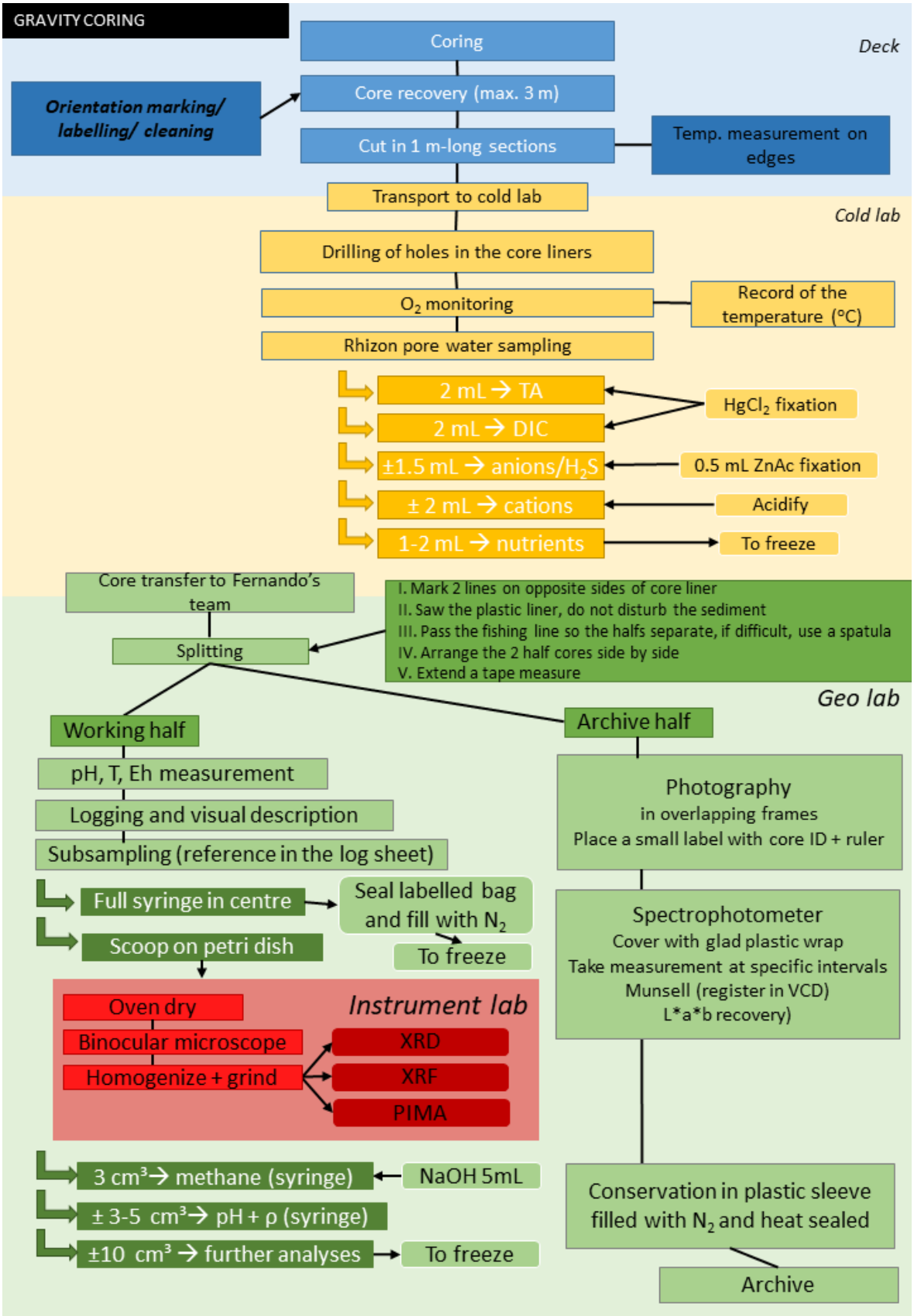

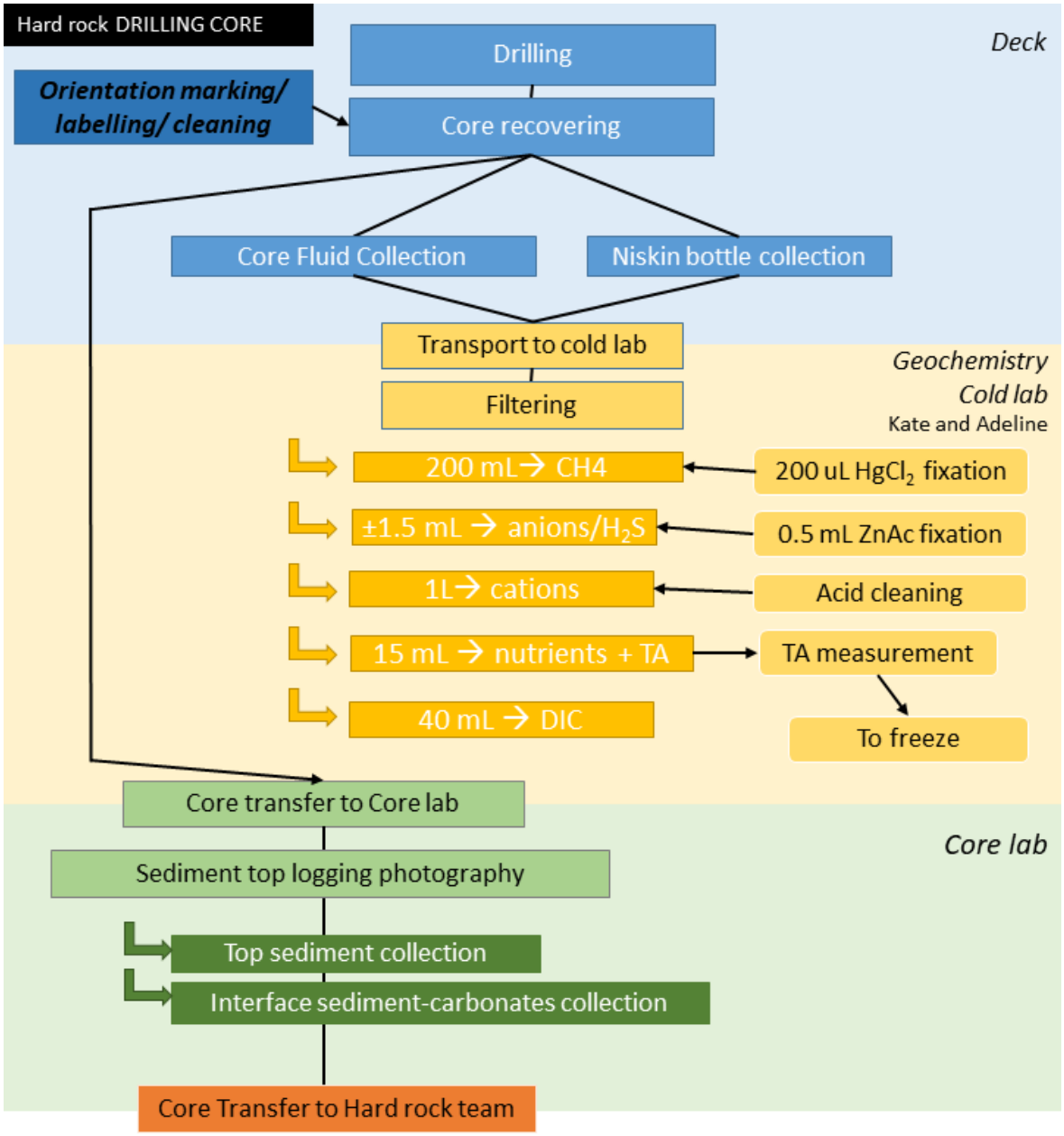
Hard rock DRILLING CORE
Deck
Drilling
Orientation marking/ labelling/ cleaning
Core recovering
Core Fluid Collection
Niskin bottle collection
Transport to cold lab
Filtering
Geochemistry
Cold lab
Kate and Adeline
200 mL → CH4
200 uL HgCl2 fixation
±1.5 mL → anions/H2S
0.5 mL ZnAc fixation
1L → cations
Acid cleaning
15 mL → nutrients + TA
TA measurement
40 mL → DIC
To freeze
Core transfer to Core lab
Core lab
Sediment top logging photography
Top sediment collection
Interface sediment-carbonates collection
Core Transfer to Hard rock team

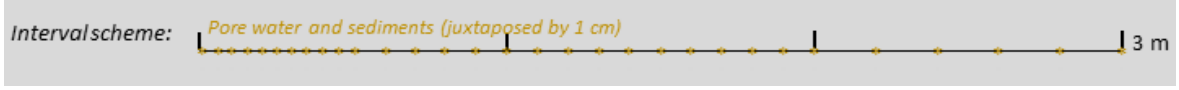
Interval scheme:
Pore water and sediments (juxtaposed by 1 cm)
3 m

A.4 Stratigraphy logs of JC138 cores (Digital)

Logs of the 12 cores recovering non-disturbed sediments are provided in the DIGITAL MATERIAL 2 and 3), from the sediment coring chapter from JC138 cruise report (Murton and Scientific Party, 2018), written by A. Dutrieux, S. Martins, K. Peel, I. Stobbs. The sample symbol o indicate pore water samples, + for sediment samples and X for sediment samples for the University of Lisbon. a*, b*, and L* are three reflectance parameters measured with a hand-held colorimeter (Spectrophotometry - CM - Konica Minolta 700d) in order to identify the colour. This study has been carried by the University of Lisbon.

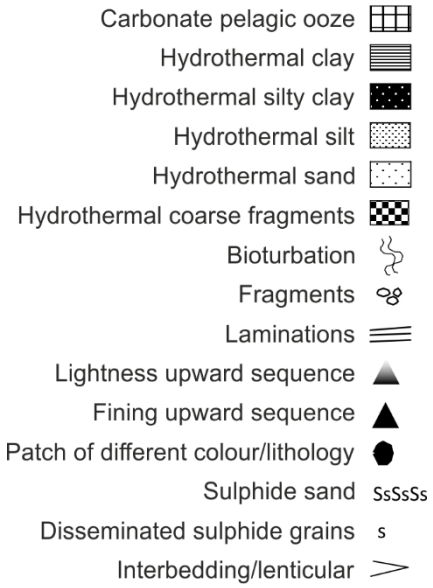

A.5 Porosity and density depth profile

Example of porosity and density depth profiles in 38GC alongside with the photography of the core. The data are available in the DIGITAL MATERIAL 5).

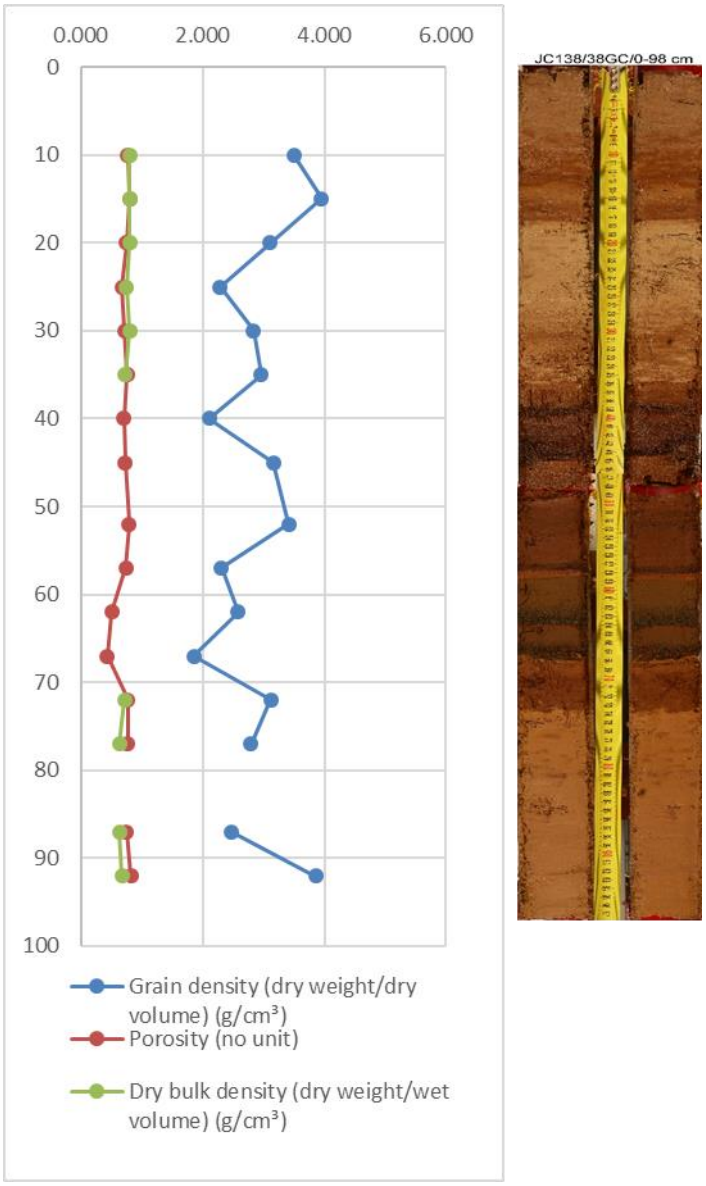

A.6 Examples of XRD analytical spectra

All the spectrum and results are available in the DIGITAL MATERIAL 7.

Below: Quantitative analyses in 22RD (289 cm) indicating halite, hematite, goethite (and spiked corundum).

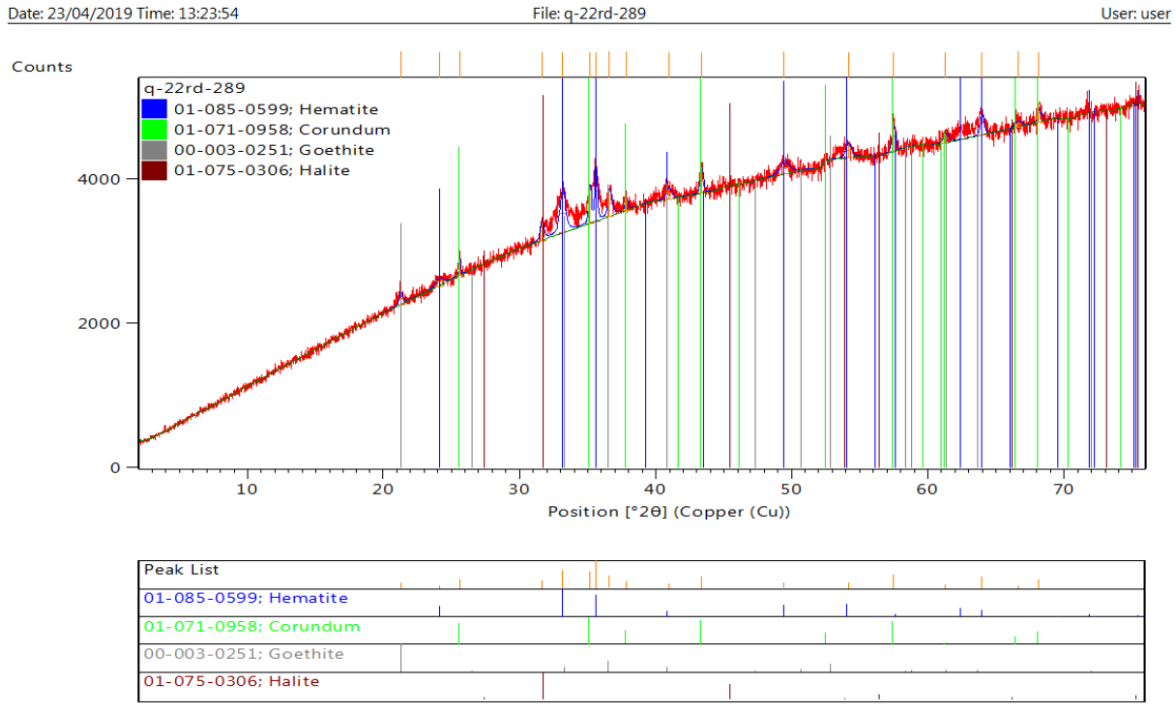

Below: Quantitative analyses in 28GC (130 cm) indicating halite, hematite and quartz (130 cm) (and spiked corundum).

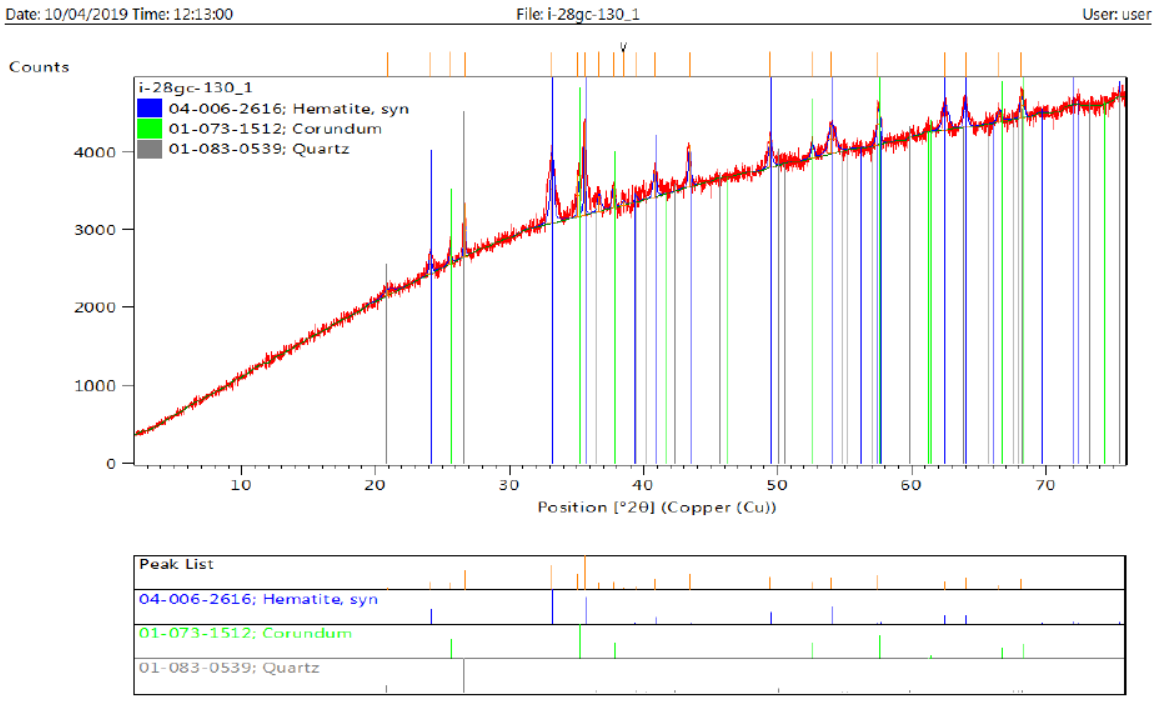

Below: Qualitative analyses in 38GC (67 cm) indicating pyrite, chalcopyrite and goethite.

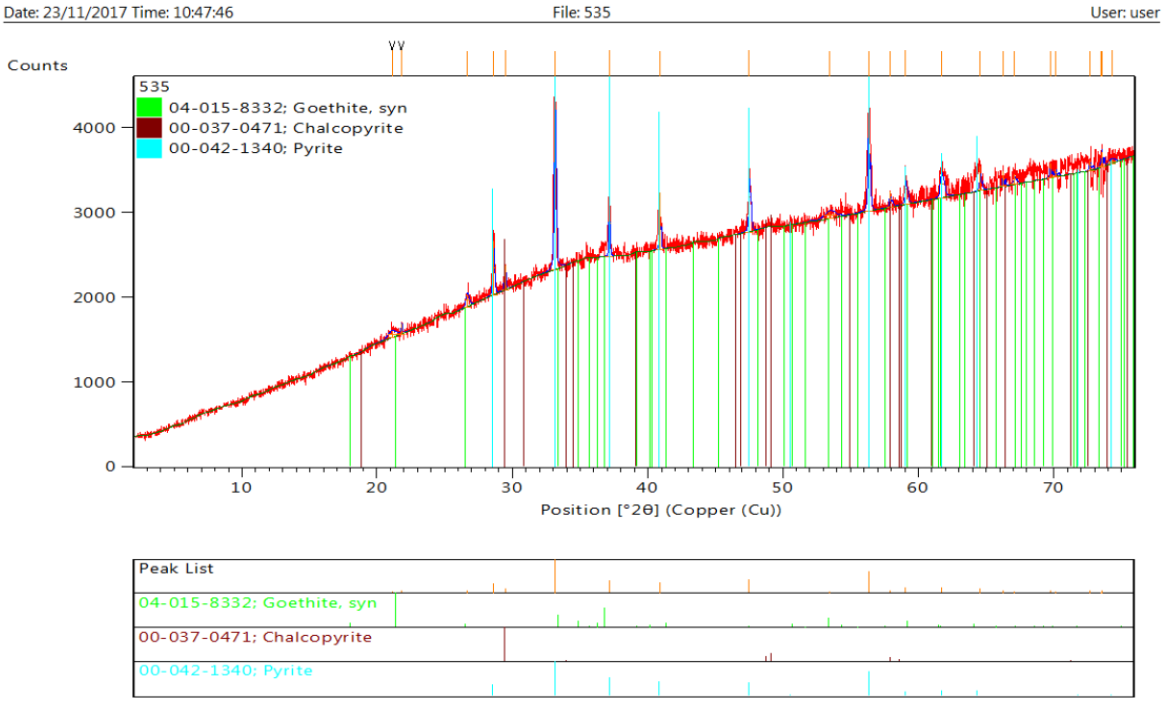

A.7 ITRAX calibrations

Fe and Ca calibration plots of ITRAX measurements against bulk rock geochemistry data, correlation equations and correlation coefficients R^2 for 6 cores 27GC, 28GC, 29GC, 38GC, 49GC and 52GC, and additional calibration plots for Mn in core 38GC. ICP analyses were performed on a 1 cm diameter sample; therefore, wiggle matching of some values vs. depth gives a better correlation. This is acceptable to consider a unique calibration for each core dataset.

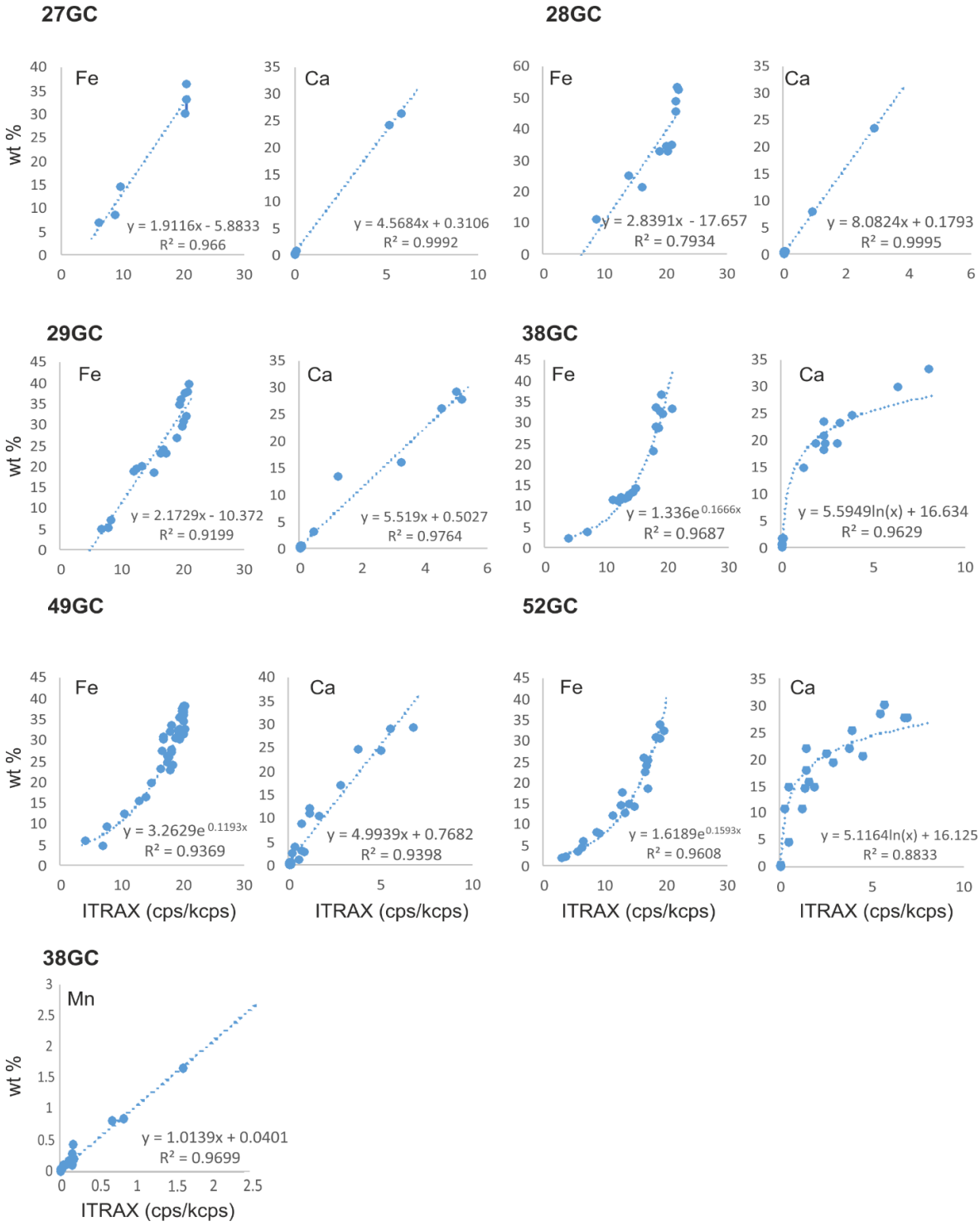

A.8 Precision and accuracy of cations in the solid phase

Quality control of the data was done by comparing accuracies of two CRMs: MESS1 (marine sediment collected in the Miramichi River estuary), and RTS1 (sulphide ore mill tailings) with their literature values, and by comparing the precisions for those two CRMs. Due to the large number of samples, the samples were divided in three batches. Analytical parameters and measured element lists differ between the batches. Therefore, precisions and accuracies were calculated for each element, in each batch and for each instrument and are reported and are reported below and in a bar chart. The average precisions are expressed as %RSD in TABLE 3.3. I also averaged accuracies for MESS1 and RTS1 and chose the best value as reported in TABLE 3.3 and in a bar chart below. Each bar represents one batch.

Samples were distributed following this way:

- Batch 1 consists of 39GC, 49GC and 38GC sediment samples
- Batch 2 consists of 16GC, 22RD, 27GC, 28GC and 31RD sediment samples
- Batch 3 consists of 29GC and 52GC sediment samples

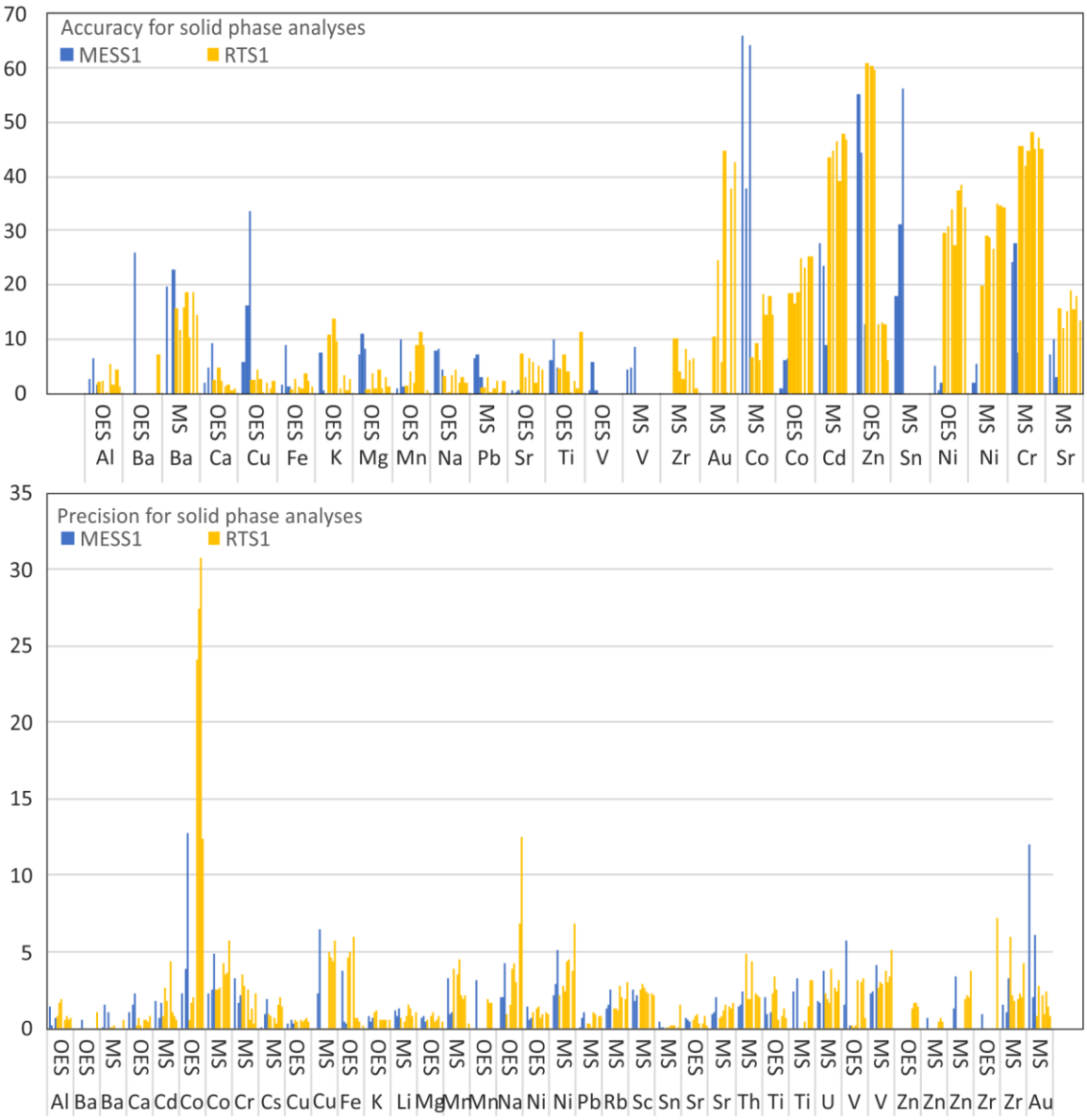

(above) Graphic representation of the accuracies and precisions for the solid phase analyses. Example: Al element was only measured on ICP-OES, in the three batches, with 1 MESS1 and 2 RTS1 samples in each batch. Therefore, for each batch, I've obtained 1 accuracy and precision value for MESS1, and 2 accuracy and precision values for RTS1. In total, the three blue lines represents each a MESS1 value of a batch (3 for three batches), and the six yellow lines represents each a RTS1 value of a batch (2 samples * three batches). All accuracy values are less than 10 and all precisions values are less than 2.

(next page) Solid phase precisions for each element, in each batch and on each instrument. Green numbers are values between 0 and 5, yellow for between 5 and 10 and red for higher than 10%RSD. In the batch 2, additional in-house standards were added for Cu, Mn and Zn and are indicated with an *. Av. is for average value, Instr. for instrument and El. for element. If no data is presented, then the CRM concentration was not available.

El.	Inst. (down)	MESS	MESS	MESS	RTS1	RTS1	RTS1	RTS1	RTS1	RTS1	RTS1	Av.
	Batch (right)	1	2	3	1	1	1	2	2	2	3	
Ag	MS							1.48	1.74	1.01		1.3
Al	OES	1.51	0.31	0.73	0.82	1.72	1.94	0.60	0.89	0.66	0.80	1.0
Ba	OES			0.59							1.08	0.8
Ba	MS	0.04	1.64	1.15	0.12	0.04	0.21				0.61	0.5
Ca	OES	1.06	1.59	2.30	0.26	0.77	0.32	0.58	0.62	0.54	0.92	0.9
Cd	MS	1.87	0.71	1.68	0.85	2.77	1.86	4.47	1.14	0.94	0.63	1.7
Co	OES	2.36	3.90	12.78	0.61	1.80	2.06	24.12	27.54	30.80	12.45	11.8
Co	MS	2.34	2.60	4.94	2.54	2.62	2.75	4.38	3.64	3.71	5.83	3.5
Cr	MS	3.39	1.75	2.18	3.57	2.91	2.61	0.66	1.38	0.32	2.37	2.1
Cs	MS	0.18	1.02	1.94	0.95	0.82	0.73	0.34	1.63	2.14	1.53	1.1
Cu	OES	0.35	0.65	0.44	0.63	0.47	0.69	0.55	0.61	0.78	0.53	0.6
Cu	MS		2.34	6.53				5.09	4.67	4.42	5.84	4.8
Fe	OES	3.80	0.52	0.38	4.68	5.06	6.10	0.76	0.77	0.45	0.28	2.3
K	OES	0.91	0.50	0.73	1.07	1.21	0.68	0.66	0.66	0.68	0.63	0.8
Li	MS	1.24	0.91	1.37	0.79	0.49	0.90	1.66	1.36	0.90	1.06	1.1
Mg	OES	0.81	0.92	0.55	0.69	0.87	1.17	0.55	0.60	0.87	0.50	0.8
Mn	OES	3.30	0.94	1.13	3.91	3.56	4.60	2.20	1.94	2.25	0.43	
Mn*	OES		3.27					2.04	1.72	1.73		2.4
Na	OES	2.15	2.08	4.28	1.03	1.61	3.98	4.28	3.07	6.93	12.64	4.2
Ni	OES	1.47	0.66	0.81	1.14	1.35	1.47	0.76	0.97	1.07	0.94	1.1
Ni	MS	2.26	2.98	5.21	2.27	2.79	2.51	4.44	4.54	3.86	6.92	3.8
Pb	MS	0.13	0.74	1.13	0.34	0.37	0.16	1.15	0.97	0.86	0.83	0.7
Rb	MS	1.33	1.59	2.63	1.41	1.42	1.28	2.84	2.15	1.97	3.08	2.0
Sc	MS	2.59	1.90	2.27	2.59	3.01	2.72	2.43	2.41	2.38	2.25	2.5
Sn	MS	0.52	0.11	0.18	0.14	0.17	0.21	0.26	0.23	0.06	1.67	0.4
Sr	OES	0.80	0.68	0.52	0.67	0.91	1.03	0.40	0.44	0.85	0.24	0.7

El.	Inst. (down)	MESS	MESS	MESS	RTS1	RTS1	RTS1	RTS1	RTS1	RTS1	RTS1	Av.
Sr	MS	0.97	1.18	2.07	0.80	0.89	1.20	1.63	1.53	1.43	1.76	1.3
Th	MS	1.45	1.62	2.46	4.92	1.96	1.95	4.40	2.30	2.23	2.08	2.5
Ti	OES	2.06	0.98	1.09	2.38	3.43	2.62	0.61	0.87	1.33	0.75	1.6
Ti	MS		2.48	3.30				0.53	1.53	3.24	3.21	2.4
U	MS	1.86	1.69	3.83	2.32	2.03	1.74	3.94	2.75	2.52	3.16	2.6
V	OES	1.63	5.75	0.25	0.26	0.14	0.25	3.24	3.11	3.39	0.71	1.9
V	MS	2.38	2.49	4.15	2.78	3.06	2.91	3.87	3.13	3.46	5.20	3.3
Zn	OES							1.40	1.68	1.72	1.48	1.1
Zn*	OES		0.73					0.48	0.75	0.53		
Zn	MS		1.39	3.43				2.03	2.23	2.12	3.81	2.5
Zr	OES			0.99							7.34	4.2
Zr	MS	1.58	1.06	3.38	6.07	2.21	1.85	2.00	2.38	2.09	4.32	2.7
Au	OES				0.82	2.84	2.18	1.12	2.43	1.57		1.8

(Next page) Solid phase accuracies. No data refers to the unavailability of a CRM concentration. Green numbers are values between 0 and 5, yellow for between 5 and 10 and red for higher than 10%RSD.

El.	Inst. (down)	MESS1	MESS2	MESS3	RTS1	RTS1	RTS1	RTS1	RTS1	RTS1	RTS1	Av. MESS1	Av. RTS1
	Batch	1	2	3	1	1	1	2	2	2	3		
Al	OES	2.87	6.65	1.85	1.85	2.28	0.39	5.51	1.73	4.37	1.26	3.8	2.5
Ba	OES			26.22							7.21	26.2	7.2
Ba	MS	19.96	88.00	23.02	15.47	11.65	16.10	18.70	10.57	18.70	14.74	43.7	15.1
Ca	OES	1.91	4.84	9.43	2.04	4.94	2.39	1.23	1.72	0.66	1.14	5.4	2.0
Cd	MS	27.65	23.72	8.95	43.42	44.97	46.68	39.18	47.95	46.93	87.53	20.1	50.9
Co	OES	66.19	37.99	64.49	6.50	9.24	6.20	18.49	14.69	18.02	14.68	56.2	12.5
Co	MS	1.07	6.30	6.63	18.23	16.61	18.86	24.97	23.28	25.30	25.46	4.7	21.8
Cr	MS	24.31	27.85	7.47	45.39	42.08	45.03	48.22	45.22	47.43	45.26	19.9	45.5
Cu	OES	5.80	16.16	33.87	2.30	4.44	2.68	0.25	1.92	1.13	2.22	18.6	2.1
Fe	OES	1.74	9.17	1.33	0.19	2.85	1.21	0.84	3.74	2.28	1.23	4.1	1.8
K	OES	7.73	0.78	135.07	10.54	13.77	9.79	1.08	3.34	0.51	2.71	47.9	6.0
Mg	OES	7.18	11.22	8.37	0.26	3.73	0.91	4.60	0.81	2.96	1.35	8.9	2.1
Mn	OES	0.88	9.91	1.40	1.16	4.08	1.96	8.85	11.53	9.02	0.60	4.1	5.3
Na	OES	7.87	8.38	4.57	2.98	0.30	3.42	4.51	1.92	3.07	2.11	6.9	2.6
Ni	OES	5.20	0.81	1.91	29.34	30.95	34.03	27.58	37.72	38.59	34.31	2.6	33.2
Ni	MS	2.13	5.65	0.00	19.62	29.26	29.02	26.80	35.30	34.70	34.55	2.6	29.9
Pb	MS	6.45	7.13	3.09	0.67	2.92	0.25	0.86	2.33	0.19	2.35	5.6	1.4
Sn	MS	18.17	31.31	56.47								35.3	
Sr	OES	0.78	0.45	0.52	6.96	2.93	6.54	5.77	2.09	5.06	4.52	0.6	4.8
Sr	MS	7.20	10.16	3.15	15.42	12.07	15.24	19.05	15.79	18.17	13.56	6.8	15.6
Ti	OES	6.20	10.21	4.81	4.32	7.21	4.24	0.44	2.54	1.04	11.32	7.1	4.4
V	OES	0.69	5.89	0.52								2.4	
V	MS	4.41	4.68	8.81								6.0	
Zn	OES	55.29	44.49	12.86	60.67	60.52	59.94	12.98	13.29	12.97	6.15	37.5	11.3
Zr	MS				9.88	4.09	2.58	8.29	6.14	6.68	1.03		5.5
Au	MS				10.25	24.53	5.88	43.98	1.62	36.84			20.5

A.9 Down-core paleomagnetic records

NRM intensity and progressively demagnetized ARM intensity for the core 52GC.

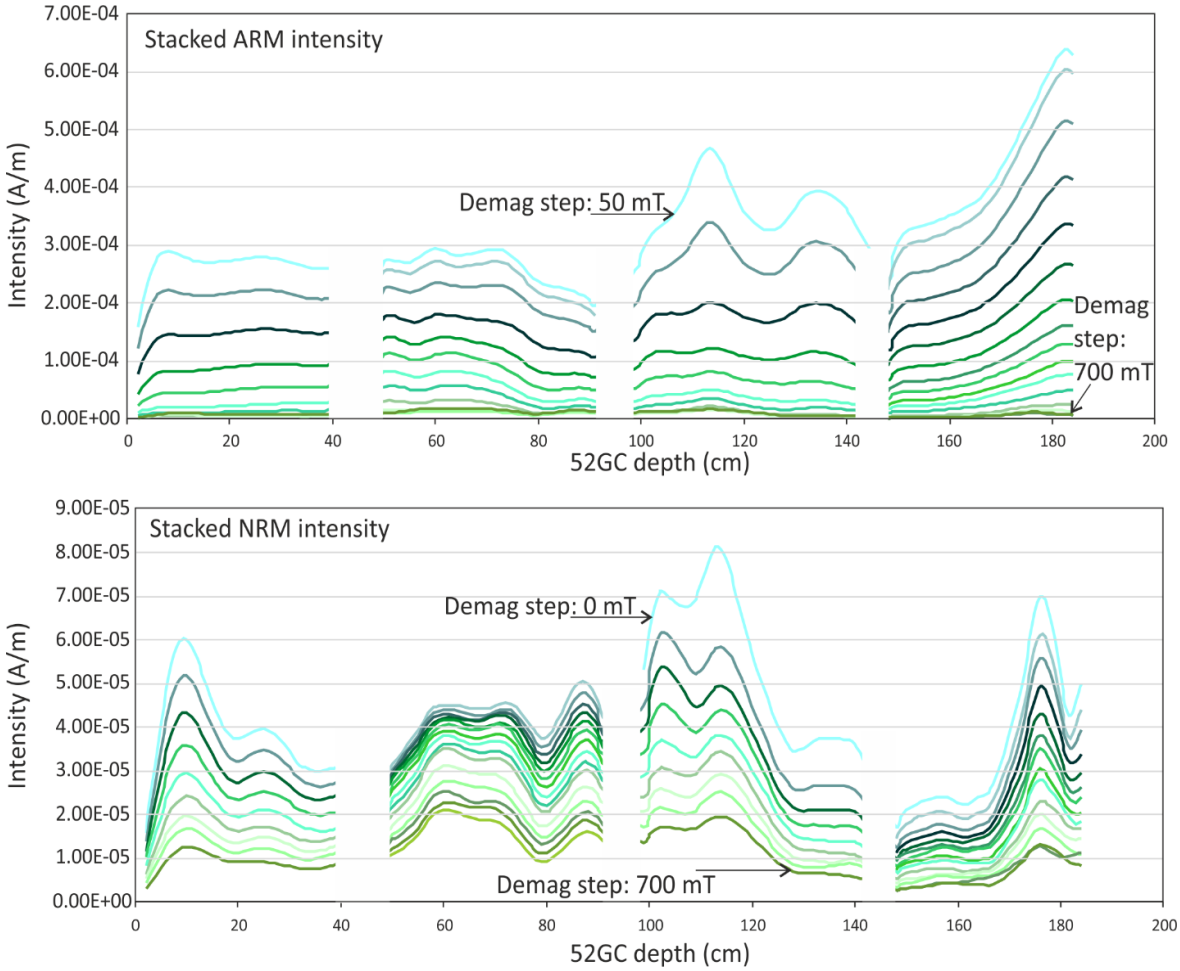

A.10 **Precision and accuracy of cations in pore waters**

Quality control of the data were run by comparing accuracies of two CRMs: *SLEW* and *CRM-SW* values with their literature values, and by comparing precision for those two CRMs. Due to the large number of samples, samples were divided into seven batches. Analytical parameters and measured elements differ between the batches. Therefore, precisions and accuracies were calculated for each element, in each batch and on each instrument and are reported in the Table below, together with a bar chart. In the bar chart, each bar represents one batch. The average precisions expressed as %RSD is reported in TABLE 3.5 together with the averaged accuracies for the CRMs Spiked SLEW or *CRM-SW*.

Samples were distributed following this way:

- Batch 1 consists of 711GC (the reference core) and 682GC
- Batch 2 consists of 644GC
- Batch 3 consists of 645GC, 692GC, 576GC
- Batch 4 consists of 16GC and 49GC
- Batch 5 consists of 27GC, 29GC and 38GC
- Batch 6 consists of 39GC, 22RD, 31RD and 59GC
- Batch 7 consists of 28GC and 52GC

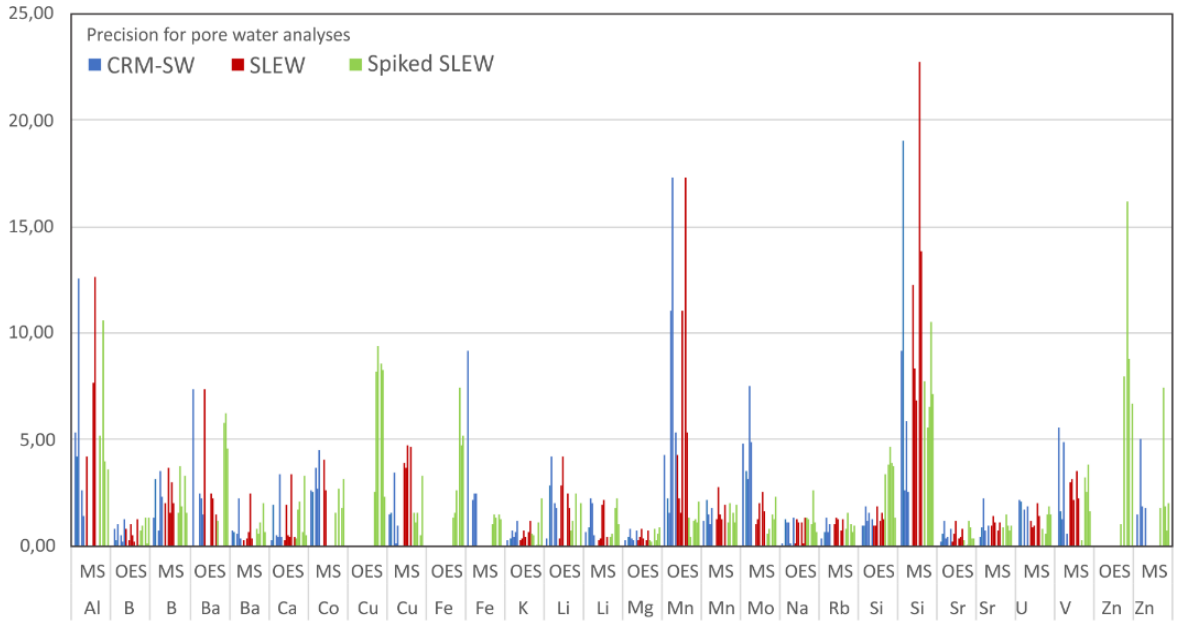

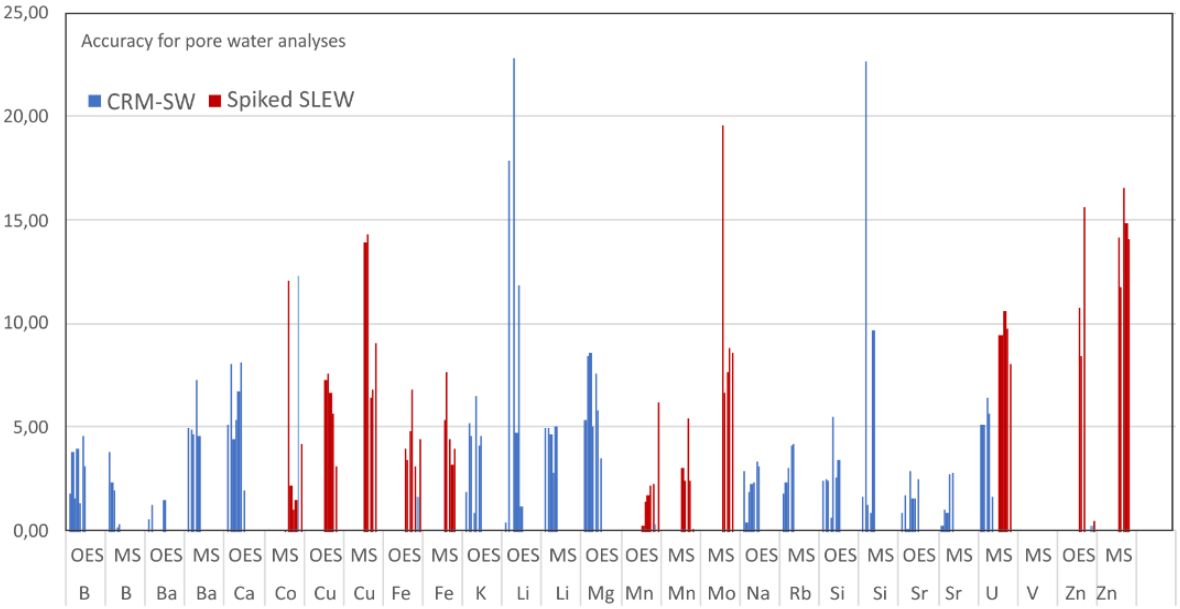

(above) Graphic representation of the accuracies and precisions for the pore water analyses. Example: B element was measured on ICP-OES and ICP-MS, in the seven batches, with 1 CRM-SW, 1 SLEZ and 1Spiked SLE and 2 RTS1 samples in each batch. Therefore, for each batch, I've obtained 1 accuracy and precision values for MESS1, and 2 accuracy and precision values for RTS1. In total, the three blue lines represents each a MESS1 value of a batch (3 for three batches), and the six yellow lines represents each a RTS1 value of a batch (2 samples * three batches). All accuracy values are less than 10 and all precisions values are less than 2.

(next page) Solid phase precisions for each elements, in each batch and on each instrument. Green numbers are values between 0 and 5, yellow for between 5 and 10 and red for higher than 10%RSD. Av. is for average value, Instr. for instrument and El. for element.

El.	Inst. (down)	CRM-SW	CRM-SW	CRM-SW	CRM-SW	CRM-SW	CRM-SW	Spiked SLEW	Spiked SLEW	Spiked SLEW	Spiked SLEW	Spiked SLEW	Spiked SLEW	Normal SLEW	Normal SLEW	Normal SLEW	Normal SLEW	Normal SLEW	Normal SLEW	Av.
	Batch (right)	7	6	5	3	2	1	7	6	5	3	2	1	7	6	5	3	2	1	
B	OES	0.83	0.29	1.05	0.55	0.27	1.29	0.04	0.80	0.99	1.37	0.17	1.37	0.83	0.29	1.05	0.55	0.27	1.29	0.75
B	MS	1.40	3.17	0.74	3.55	2.37		1.59	3.76	1.87	3.32	1.58		2.04	3.71	1.63	3.05	2.01		2.34
Ba	OES	7.38			2.46	2.25	1.53	1.25			5.79	6.25	4.61	7.38			2.46	2.25	1.53	3.94
Ba	MS	0.74	0.71	0.61	2.24	0.42		0.83	0.62	1.16	2.01	0.72		0.34	0.41	0.68	2.51	0.41		1.01
Ca	OES	0.32	2.00	0.52	0.49	3.40	0.43	0.40	1.72	2.10	0.66	3.31	0.57	0.32	2.00	0.52	0.49	3.40	0.43	1.33
Co	MS	2.67	2.56	3.72	2.74	4.54		1.56		2.76	1.85	3.17		4.06	2.63					2.84
Cu	OES							2.59	8.19	9.41	8.59	8.33	2.31							6.57
Cu	MS	1.53	1.58	3.50	0.14	0.97		1.63	1.12	1.56	0.57	3.31			3.96	3.68	4.76	4.71		1.59
Fe	OES							1.33	1.59	2.66	7.45	4.74	5.20							3.83
Fe	MS	9.23		2.23	2.50	2.48		1.04	1.50	1.36	1.49	1.30								2.57
K	OES	0.33	0.35	0.75	0.44	0.70	1.24	0.64	0.51	0.08	1.17	0.10	2.31	0.33	0.35	0.75	0.44	0.70	1.24	0.72
Li	OES	0.37	2.91	4.23		2.05	1.85	0.79	1.20	2.50			2.06	0.37	2.91	4.23		2.47	1.85	2.00
Li	MS	0.71	0.90	2.28	2.02	0.50		0.49	0.61	1.83	2.26	1.10		0.34	0.41	1.99	2.23	0.46		1.27
Mg	OES	0.28	0.50	0.82	0.36	0.31	0.75	0.33	0.22	0.83	0.29	0.64	0.89	0.28	0.50	0.82	0.36	0.31	0.75	0.52
Mn	OES	4.32	2.30	1.61	11.10	17.33	5.38	1.40	0.47	1.24	1.32	1.14	2.12	4.32	2.30	1.61	11.10	17.33	5.38	4.14
Mn	MS	1.24	2.18	1.55	1.09	1.80		1.14	2.06	1.60	1.18	1.98		1.32	2.83	1.51	1.31	1.98		1.58
Mo	MS	4.80	3.54	3.15	7.57	4.87		0.64	0.83	1.55	1.26	2.38		1.03	1.30	2.04	2.57	1.68		3.06
Na	OES	0.13	1.27	1.11	1.11	0.13	1.36	1.39	1.27	1.08	2.64	1.11	0.70	0.13	1.27	1.11	1.11	0.13	1.36	1.11
Rb	MS	0.42	0.67	1.37	0.65	1.08		0.83	1.60	1.03	0.67	1.02		1.05	1.35	1.28	0.75	1.26		0.93
Si	OES	0.96	0.99	1.88	1.20	1.57	1.32	3.38	3.87	4.70	3.92	3.76	1.40	0.96	0.99	1.88	1.20	1.57	1.32	2.41
Si	MS	9.20	19.11	2.65	5.87	2.60		7.77	5.57	6.58	10.53	7.17		12.30	8.36	6.85	22.76	13.88		7.70
Sr	OES	0.22	0.58	1.19	0.36	0.47	0.83	0.29	0.12	1.23	0.94	0.42	0.37	0.22	0.58	1.19	0.36	0.47	0.83	0.59

El.	Inst. (down)	CRM-SW	CRM-SW	CRM-SW	CRM-SW	CRM-SW	CRM-SW	Spiked SLEW	Spiked SLEW	Spiked SLEW	Spiked SLEW	Spiked SLEW	Spiked SLEW	Normal SLEW	Normal SLEW	Normal SLEW	Normal SLEW	Normal SLEW	Normal SLEW	Av.
Sr	MS	0.48	0.90	2.27	0.80	0.98		0.89	1.53	0.97	0.73	0.96		0.99	1.46	1.18	0.73	1.14		1.05
U	MS	2.16	2.16	0.00	1.71	1.89		0.87	0.61	1.49	1.87	1.50		1.23	0.95	0.97	2.01	1.41		**1.43**
V	MS	5.56	1.70	1.32	4.87	0.65		0.34	3.24	2.55	3.84	1.68		3.04	3.21	2.19	3.59	2.26		**2.57**
Zn	OES							1.04	7.98		16.20	8.81	6.74							8.16
Zn	MS	1.50		5.09	1.87	1.81		1.84	7.45	1.91	0.73	2.02								**2.69**

(below) Solid phase accuracies. No data refers to the unavailability of a CRM concentration. Green numbers are values between 0 and 5, yellow for between 5 and 10 and red for higher than 10%RE.

El.	Inst. (down)	CRM-SW	CRM-SW	CRM-SW	CRM-SW	CRM-SW	CRM-SW	CRM-SW	Spiked SLEW	Spiked SLEW	Spiked SLEW	Spiked SLEW	Spiked SLEW	Spiked SLEW	Spiked SLEW	Av. CRM-SW	Av. Sp. SLEW
	Batch (right)	1	2	3	4	5	6	7	1	2	3	4	5	6	7		
B	OES	1.84	3.81	1.58	3.98	1.37	4.62	3.15								2.91	
B	MS	3.80	2.37	2.03	0.19	0.39										1.76	
Ba	OES	0.62	1.27					1.53								1.14	
Ba	MS	5.02	4.89	4.68	7.33	4.59										5.30	
Ca	OES	5.13	8.08	4.44	5.39	6.74	8.17	1.96								5.70	
Cu	OES								0.05	12.12	2.22	1.05	1.49	12.30	4.19		4.77
Cu	MS								7.32	7.65	6.73	5.72	3.15				6.11
Co	MS								13.97	14.35	6.50	6.89	9.10				10.16
Fe	OES								3.96	3.42	4.87	6.89	3.16	1.71	4.45		4.07
Fe	MS								5.40	7.72	4.45	3.26	4.03				4.97
K	OES	1.94	5.24	4.61	0.91	6.57	4.15	4.59								4.00	

El.	Inst. (down)	CRM-SW	CRM-SW	CRM-SW	CRM-SW	CRM-SW	CRM-SW	CRM-SW	Spiked SLEW	Spiked SLEW	Spiked SLEW	Spiked SLEW	Spiked SLEW	Spiked SLEW	Spiked SLEW	Av. CRM-SW	Av. Sp. SLEW
Li	OES	0.46	17.92		22.85	4.80	11.85	1.18								9.84	
Li	MS	5.02	5.03	4.66	2.85	5.07										4.53	
Mg	OES	5.35	8.45	8.63	5.11	7.60	5.84	3.50								6.35	
Mn	OES								0.27	1.48	1.77	2.20	2.33	0.39	6.26		2.10
Mn	MS								3.05	2.48	5.46	2.42	0.15				2.71
Mo	MS								19.58	6.70	7.73	8.87	8.60				10.29
Na	OES	2.90	0.42	1.88	2.28	2.34	3.36	3.14								2.33	
Rb	MS	1.85	2.34	3.09	4.16	4.21										3.13	
Si	OES	2.45	2.54	2.42	0.71	5.51	2.59	3.45								2.81	
Si	MS	1.71	22.70	1.33	0.89	9.73										7.27	
Sr	OES	0.92	1.72	0.10	2.93	1.56	1.58	2.51								1.62	
Sr	MS	0.29	1.07	0.94	2.77	2.84										1.58	
U	MS	5.13	5.16	6.49	5.68	1.65			9.51	9.46	10.61	9.77	8.08			**4.82**	9.49
V	MS																
Zn	OES								10.81	8.47	15.68			0.27	0.52		7.15
Zn	MS								14.20	11.78	16.62	14.90	14.14				14.33

Appendix B **Supplementary material to CHAPTER 4**

B.1 **Photography of the cores**

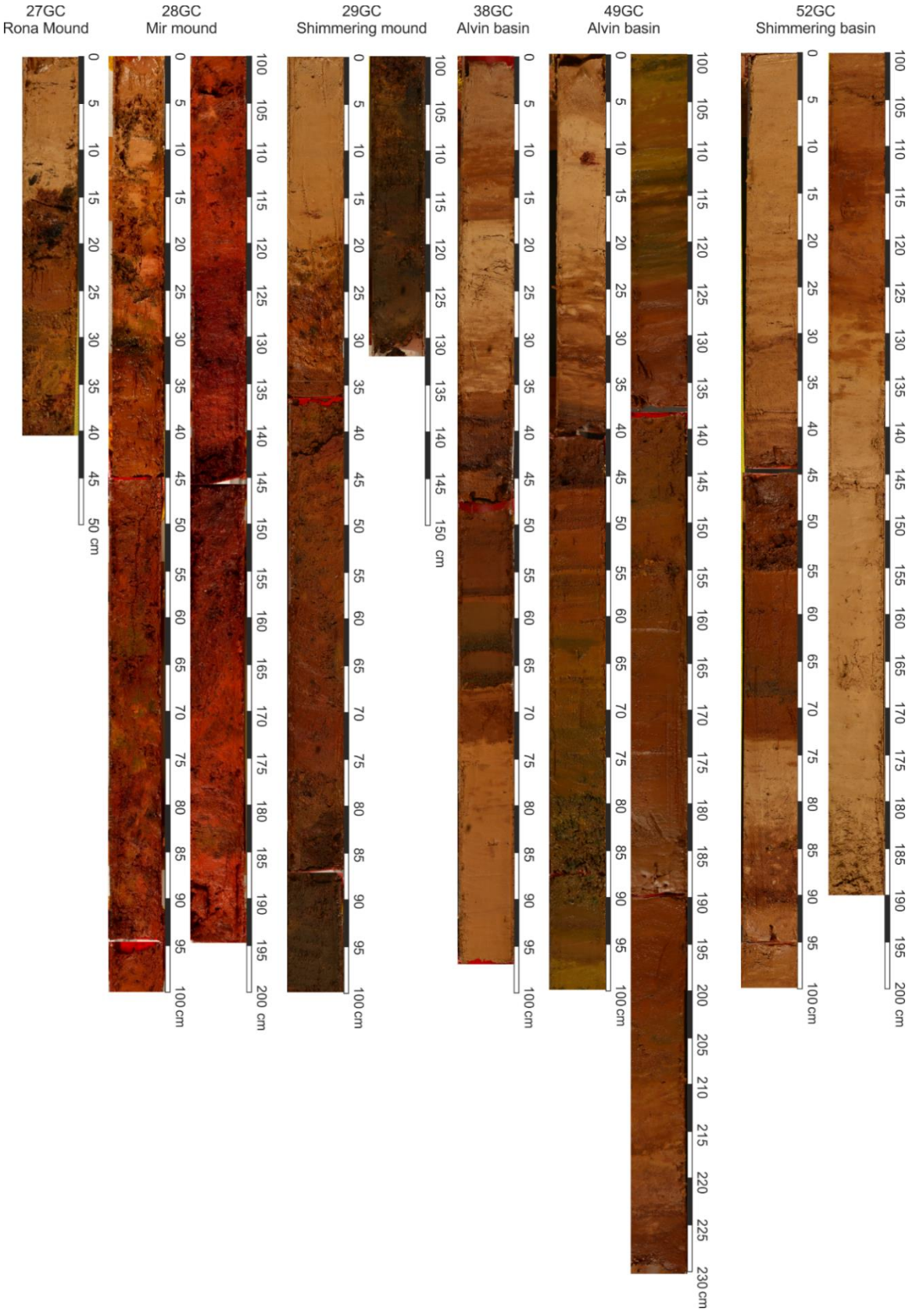

B.2 Down-core variation in Fe and Ca content and Eu anomaly in the six sediment cores

From the weight content in Ca and Fe and the Eu anomaly four different lithological classes can be distinguished: collapse, debris-flow, hydrothermal plume and pelagic sediments.

Core	Depth (cm)	Ca (wt%)	Fe (wt%)	Eu/Eu*	Lithological class
27GC	39	0.15	36.43	5.96	collapse
27GC	21	0.37	30.15	0.88	collapse
27GC	21	0.43	33.26	0.87	collapse
27GC	17	0.89	14.69	0.83	collapse
27GC	7	26.38	6.82	0.82	pelagic
27GC	1	24.30	8.54	0.81	pelagic
28GC	180	0.45	48.87	7.81	collapse
28GC	160	0.21	52.80	14.86	collapse
28GC	137	0.18	53.30	8.48	collapse
28GC	117	0.27	45.44	13.98	collapse
28GC	92	0.19	34.85	9.67	collapse
28GC	72	0.50	32.76	3.12	collapse
28GC	52	0.52	33.08	3.03	collapse
28GC	42	0.46	34.38	2.51	collapse
28GC	30	0.54	25.25	1.20	collapse
28GC	18	8.04	21.28	1.48	collapse
28GC	6.5	23.61	11.31	0.97	pelagic
29GC	130	3.31	18.57	1.14	collapse
29GC	125	0.67	20.17	1.07	collapse
29GC	120	0.39	35.97	2.25	collapse
29GC	115	0.28	26.77	3.41	collapse
29GC	110	0.20	32.17	3.46	collapse
29GC	105	0.32	30.85	3.51	collapse
29GC	95	0.42	24.08	2.88	collapse
29GC	85	0.17	23.08	5.63	collapse
29GC	75	0.43	39.84	7.04	collapse
29GC	65	0.19	37.92	7.19	collapse
29GC	55	0.28	29.68	3.92	collapse
29GC	45	0.50	19.59	4.53	collapse
29GC	35	0.34	34.76	3.82	collapse
29GC	30	0.38	37.53	5.29	collapse
29GC	25	13.44	23.03	1.62	collapse
29GC	20	16.00	18.81	1.06	collapse

Core	Depth (cm)	Ca (wt%)	Fe (wt%)	Eu/Eu*	Lithological class
29GC	15	26.14	7.23	0.84	pelagic
29GC	10	29.15	5.43	0.81	pelagic
29GC	5	27.85	5.14	0.80	pelagic
38GC	92	19.40	11.95	0.91	mixture
38GC	87	18.18	13.45	0.94	mixture
38GC	82	19.52	11.36	0.89	mixture
38GC	77	19.42	12.05	0.90	mixture
38GC	72	1.85	33.37	1.69	debris-flow
38GC	67	1.83	33.64	1.29	debris-flow
38GC	62	0.17	36.72	3.02	debris-flow
38GC	57	0.64	28.89	1.64	debris-flow
38GC	52	0.64	32.20	1.50	debris-flow
38GC	45	0.62	32.65	1.23	debris-flow
38GC	40	0.73	28.65	1.21	debris-flow
38GC	35	20.77	12.59	0.82	pelagic
38GC	30	23.25	11.64	0.88	pelagic
38GC	25	29.93	3.69	0.76	pelagic
38GC	20	33.21	2.37	0.73	pelagic
38GC	15	23.54	14.12	0.98	plume
38GC	10	14.89	23.28	1.40	plume
38GC	5	24.64	11.22	0.95	pelagic
49GC	222	12.18	23.24	1.56	debris-flow
49GC	206	0.64	32.37	1.63	debris-flow
49GC	185	0.43	35.08	1.40	debris-flow
49GC	175	0.38	38.37	2.39	debris-flow
49GC	175	0.33	34.48	2.29	debris-flow
49GC	172	0.45	38.20	2.66	debris-flow
49GC	165	0.34	35.95	2.30	debris-flow
49GC	165	0.36	36.98	2.50	debris-flow
49GC	159	0.25	32.82	2.50	debris-flow
49GC	155	0.32	37.62	2.30	debris-flow
49GC	155	0.31	36.88	2.30	debris-flow
49GC	154	0.28	35.86	2.58	debris-flow
49GC	147	0.26	27.79	3.43	debris-flow
49GC	145	0.25	33.69	3.03	debris-flow
49GC	135	0.48	35.41	2.22	debris-flow
49GC	124	2.51	22.78	1.51	debris-flow
49GC	120	3.86	24.78	2.21	debris-flow
49GC	117	1.06	27.03	3.35	debris-flow

Core	Depth (cm)	Ca (wt%)	Fe (wt%)	Eu/Eu*	Lithological class
49GC	115	2.86	27.32	2.46	debris-flow
49GC	105	2.97	24.20	2.16	debris-flow
49GC	96	8.77	25.91	1.58	debris-flow
49GC	93	0.60	30.90	9.09	debris-flow
49GC	83	0.20	30.53	5.93	debris-flow
49GC	78	0.22	31.98	5.32	debris-flow
49GC	73	0.18	30.14	4.77	debris-flow
49GC	68	0.29	36.64	2.59	debris-flow
49GC	63	0.15	31.24	4.22	debris-flow
49GC	58	0.29	32.58	2.33	debris-flow
49GC	52	0.43	31.54	2.11	debris-flow
49GC	48	0.41	30.38	2.51	debris-flow
49GC	44	0.49	26.14	2.74	debris-flow
49GC	34	11.12	19.92	1.04	plume
49GC	29	10.60	16.51	1.05	plume
49GC	24	17.16	15.39	0.97	plume
49GC	19	24.49	9.38	0.86	pelagic
49GC	14	29.16	4.80	0.76	pelagic
49GC	9	29.37	6.02	0.86	pelagic
49GC	4	24.76	12.45	1.01	plume
52GC	184	20.83	3.47	0.74	pelagic
52GC	164	28.02	2.31	0.73	pelagic
52GC	143	27.90	1.99	0.72	pelagic
52GC	132	18.20	14.27	0.96	pelagic
52GC	128	16.05	14.77	0.90	pelagic
52GC	122	4.71	25.81	1.15	plume
52GC	118	15.07	24.05	1.82	plume
52GC	112	10.93	25.37	2.27	plume
52GC	108	22.09	17.65	1.21	plume
52GC	102	15.07	14.62	1.09	plume
52GC	94	21.13	12.60	1.01	plume
52GC	90	10.93	22.41	2.13	plume
52GC	79	22.09	7.86	0.89	pelagic
52GC	69	0.23	30.70	4.32	debris-flow
52GC	65	0.43	33.81	3.34	debris-flow
52GC	59	0.38	32.47	1.98	debris-flow
52GC	50	0.51	30.57	2.74	debris-flow
52GC	38	14.76	18.61	1.10	plume
52GC	28	19.47	11.95	0.86	pelagic

Core	Depth (cm)	Ca (wt%)	Fe (wt%)	Eu/Eu*	Lithological class
52GC	18	25.54	8.01	0.82	pelagic
52GC	8	30.34	5.80	0.80	pelagic
52GC	3	28.69	4.32	0.75	pelagic

B.3 Radiocarbon raw and calibrated results

Raw conventional radiocarbon ages as provided by the NRCF and calibrated radiocarbon ages with their mean, standard deviation and the 95.4% probability range, calculated using OxCal 4.3 (Bronk Ramsey, 2009) with the Marine13 calibration curve (Reimer *et al.*, 2013) with an assumed open ocean marine reservoir effect of 405 years (*i.e.* $\Delta R = 0$). *Estimated $\delta^{13}C_{VPDB}$‰.

Publication code	Core	Depth below sediment surface (cm)	$\delta^{13}C_{VPDB}$‰ ± 0.1	Conventional radio-carbon Age (years BP)	+/- 1σ (14C years BP)	Mean cal age (years Cal BP)	+/- 1σ (years cal BP)	95.4% likelihood from	95.4% likelihood to
SUERC-86734	38GC	10	1.8	4066	37	4099	66	4225	3971
SUERC-86735	38GC	18.5	1.0	8139	38	8615	64	8757	8501
SUERC-86736	38GC	29	0.6	10698	39	12097	109	12347	11892
SUERC-86737	38GC	37	1.0	12243	41	13700	77	13847	13539
SUERC-86738	38GC	75	1.3	16895	53	19891	106	20287	19672
SUERC-86739	49GC	6	1.3 *	7416	37	7878	43	7958	7789
SUERC-86740	49GC	21	1.3 *	11657	39	13154	60	13281	13035
SUERC-86744	49GC	36	1.3 *	16524	52	19451	94	19620	19254
SUERC-86745	52GC	30	1.3 *	19255	66	22708	115	22932	22490
SUERC-86746	52GC	40	1.3 *	31057	240	34590	233	34118	35044
SUERC-86747	52GC	84	1.3 *	43108	1036	46306	1086	48656	44338
SUERC-86748	52GC	92	1.3 *	45292	1364	48081	1093	46182	>48464
SUERC-86749	52GC	149	1.3 *	>48464					
SUERC-86750	27GC	15	1.4	11142	37	12651	43	12738	12569
SUERC-86754	28GC	10	1.3	5548	36	5937	46	6047	5852

Publication code	**Core**	**Depth below sediment surface (cm)**	**$\delta^{13}C_{VPDB}$‰ ± 0.1**	**Conventional radio-carbon Age (years BP)**	**+/- 1σ (14C years BP)**	**Mean cal age (years Cal BP)**	**+/- 1σ (years cal BP)**	**95.4% likelihood from**	**95.4% likelihood to**
SUERC-86755	29GC	20	2.2	11315	42	12778	63	12904	12661

B.4 Oxygen isotope data in function of depth and age

Ages are obtained from interpolation with the software AnalySeries. I assume that the uncertainty is < 5 ka. The standard deviation is given as sigma.

Core	Depth (cm)	Age (ka)	bulk_$\delta^{18}O$ (‰)	Standard deviation
38GC	2	1.00	0.11	0.09
38GC	5	1.43	0.22	0.08
38GC	8	3.02	0.13	0.07
38GC	12	5.15	0.48	0.06
38GC	15	6.75	0.48	0.08
38GC	18	8.34	0.52	0.08
38GC	21	9.44	0.79	0.08
38GC	25	10.76	1.19	0.08
38GC	28	11.75	1.17	0.08
38GC	31	12.49	1.29	0.07
38GC	34	13.10	1.29	0.08
38GC	37	13.71	1.41	0.07
38GC	68	13.80	1.39	0.08
38GC	75	19.62	1.63	0.08
38GC	78	22.12	1.66	0.07
38GC	81	24.61	1.78	0.08
38GC	85	27.94	1.71	0.07
38GC	88	30.44	0.97	0.08
38GC	91	32.93	1.68	0.08
38GC	94	35.43	1.72	0.07
38GC	97	37.92	1.66	0.08
49GC	3	3.50	0.57	0.07
49GC	6	7.87	0.56	0.07
49GC	9	8.93	0.97	0.07
49GC	12	9.97	1.31	0.07
49GC	15	11.01	1.37	0.07
49GC	18	12.05	1.33	0.09
49GC	21	13.09	1.22	0.08
49GC	24	14.35	1.17	0.07
49GC	28	16.03	2.26	0.07

Core	Depth (cm)	Age (ka)	bulk_$\delta^{18}O$ (‰)	Standard deviation
49GC	31	17.29	1.95	0.08
49GC	34	18.55	2.13	0.08
49GC	37	19.81	1.6	0.08
49GC	39	20.65	1.11	0.08
28GC	2	0.62	0.39	0.09
28GC	5	2.60	0.06	0.07
28GC	8	4.57	-0.02	0.07
28GC	11	6.55	0.55	0.07
28GC	14	8.52	0.36	0.08
28GC	17	10.50	1.02	0.08
28GC	20	12.47	1.31	0.07
27GC	2	0.05	0.12	0.08
27GC	5	2.96	0.34	0.08
27GC	8	5.87	0.5	0.07
27GC	11	8.78	0.44	0.08
27GC	14	11.69	0.91	0.09
52GC	3	1.41	0.4	0.04
52GC	8	5.37	0.69	0.08
52GC	13	9.33	1.54	0.17
52GC	18	13.29	1.41	0.16
52GC	23	17.25	1.93	0.21
52GC	28	21.21	1.59	0.17
52GC	33	26.32	1.53	0.17
52GC	38	32.18	1.21	0.13
52GC	79	42.54	1.23	0.14
52GC	83	45.58	1.31	0.14
52GC	90	47.64	1.08	0.12
52GC	94	51.37	1.46	0.16
52GC	98	56.49	1.05	0.12
52GC	102	57.89	1.53	0.17
52GC	108	60.00	1.5	0.17
52GC	112	61.41	1.66	0.18
52GC	118	64.59	1.62	0.18
52GC	122	67.16	1.37	0.15

Core	Depth (cm)	Age (ka)	bulk_$\delta^{18}O$ (‰)	Standard deviation
52GC	128	71.01	1.22	0.13
52GC	132	76.40	0.86	0.09
52GC	138	89.29	0.68	0.07
52GC	143	100.03	0.71	0.08
52GC	146	106.48	0.77	0.08
52GC	150	115.07	0.58	0.06
52GC	155	119.20	0.73	0.08
52GC	160	123.24	0.3	0.03
52GC	164	126.47	0.6	0.07
52GC	170	131.32	1.53	0.17
52GC	175	135.36	2.01	0.22
52GC	180	139.39	1.75	0.19
52GC	184	142.63	1.85	0.20
52GC	190	147.47	1.89	0.21
29GC	2	0.06	0.46	0.07
29GC	5	2.16	0.35	0.08
29GC	8	4.27	0.77	0.08
29GC	11	6.37	0.38	0.07
29GC	15	9.17	1.48	0.07
29GC	18	11.27	1.53	0.08
29GC	21	13.37	1.52	0.08
29GC	24	15.47	1.95	0.07

B.5 52GC RPI as function of depth and age

(A) Mean RPI of core 52GC in the Shimmering sedimentary basin as a function of depth. Results show two low magnetic excursions, one enclosing a horizon derived from a turbidity event (around 40 cm bsf) and one at the bottom end of the core, around 180 cm. Those excursions are interpreted as the Laschamp and Blake events respectively at 41 ka and ~115-120 ka. The age-depth model (FIGURE 4.4) built from the RPI suggests the last 60 cm (130 cm to 190 cm) have ages younger than those interpolated from the $\delta^{18}O$ model. This age difference is an effect particularly encountered in sediments where the sedimentation rate is low (1 cm/ka or less), and it is called the lock-in age. This is interpreted as a delay in permanent

remanence from magnetic minerals in the sediments until sediments are buried below the burrowing zone and by immobilized (Kent, 1973; Suganuma *et al.*, 2011).

(B), (C), (D) Mean RPI stacks from high-resolution HINAPIS (Xuan *et al.*, 2016) and PISO (Channell *et al.*, 2009) and low resolution SINT stack (Valet *et al.*, 2005) respectively. (E) 52GC mean RPI as a function of age after interpolation.

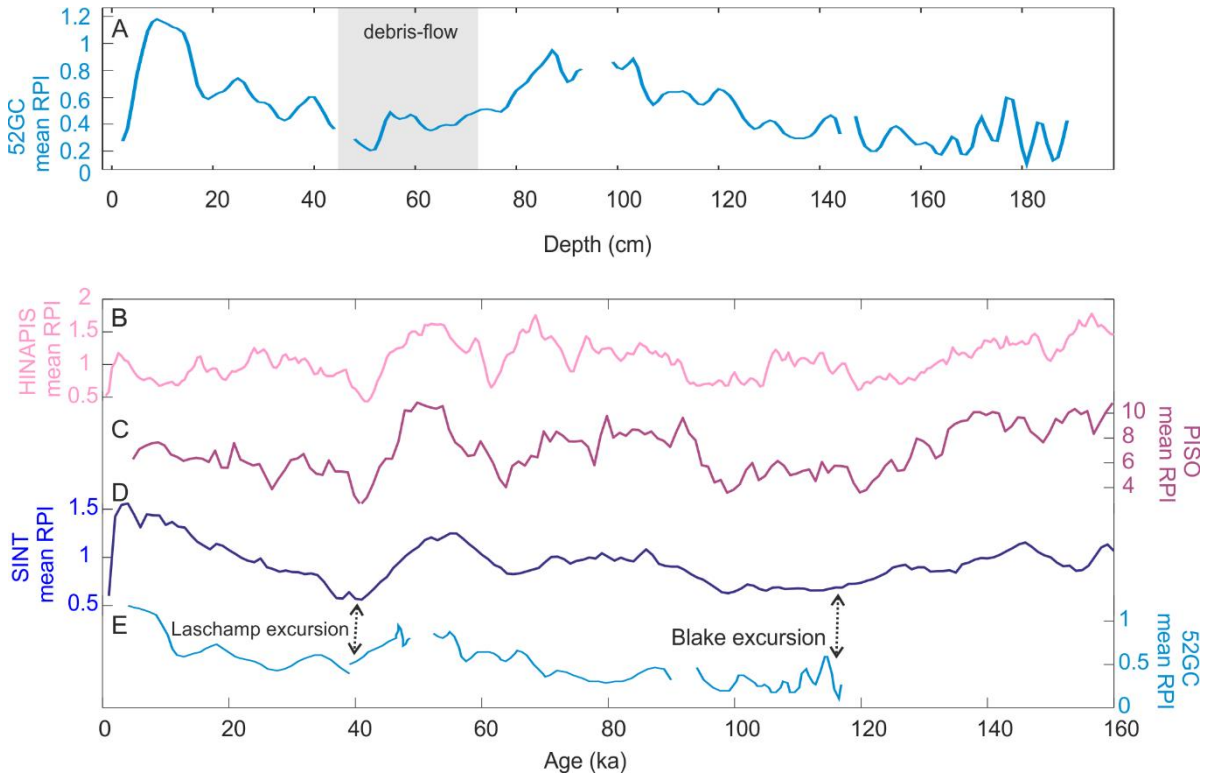

B.6 Fe as function of Eu/Eu*

Relationship between Fe and the Eu anomaly. Eu anomaly increases slowly from pelagic sediments (pink cross) to sediments with presence of hydrothermal plume fall-out (green diamond) while it reaches a maximum in the Ca-devoid hydrothermal sediments originated from collapse (purple triangle) and debris-flows (red dots). The 'mixture' represents four samples from 77 to 92 cm in 38GC (depositional basin) where Fe content increases, although Ca content is high too (~ 20 wt%). Therefore, the pelagic component prevents and smooths the positive Eu/Eu anomaly.

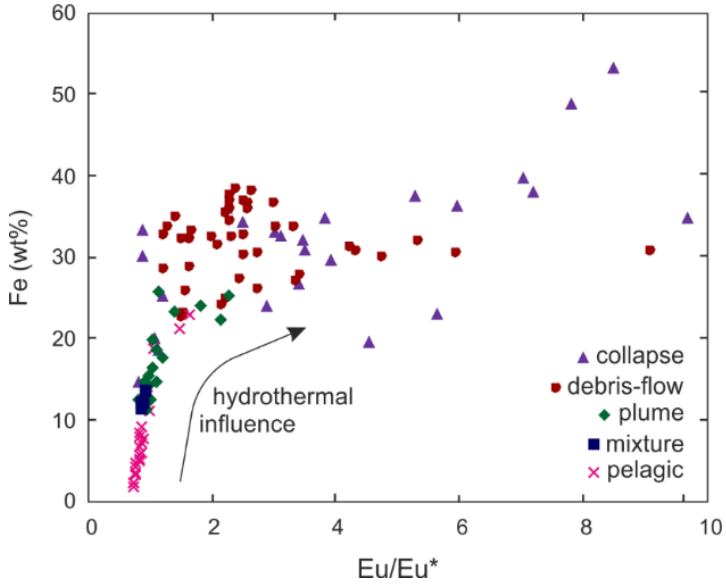

B.7 Basaltic and glass fragments

Photography of basaltic and glass fragments found in the core catcher at 52GC (Shimmering zone).

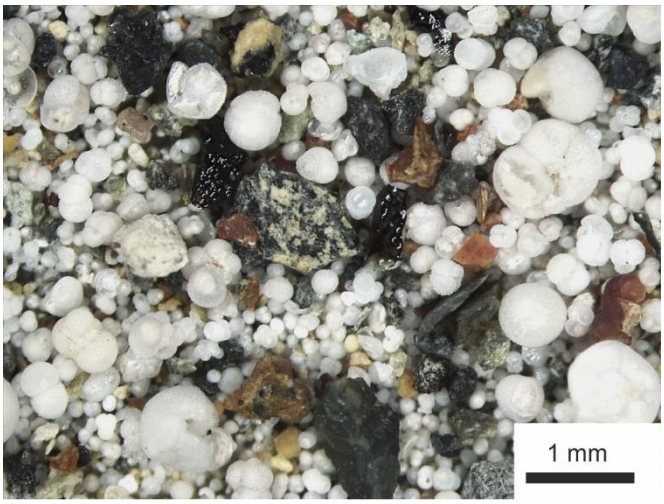

B.8 Detrital input in 52GC bottom of the core

High-resolution chemostratigraphy of 52GC core in the Shimmering basin for the elements Si, Ni, Zr and Ti/Ca ratio along with the core photography. Below 130 cm the carbonates are dominating (*cf.* FIGURE 4.3), which clearly indicates a return to pelagic sedimentation with no hydrothermal input (Fe content is close to 0). However, a down-core abundance increase of the elements Si, Ni, Zn and Ti indicates an increased input of volcanic material, most likely suggesting a close proximity to the basaltic seafloor crust.

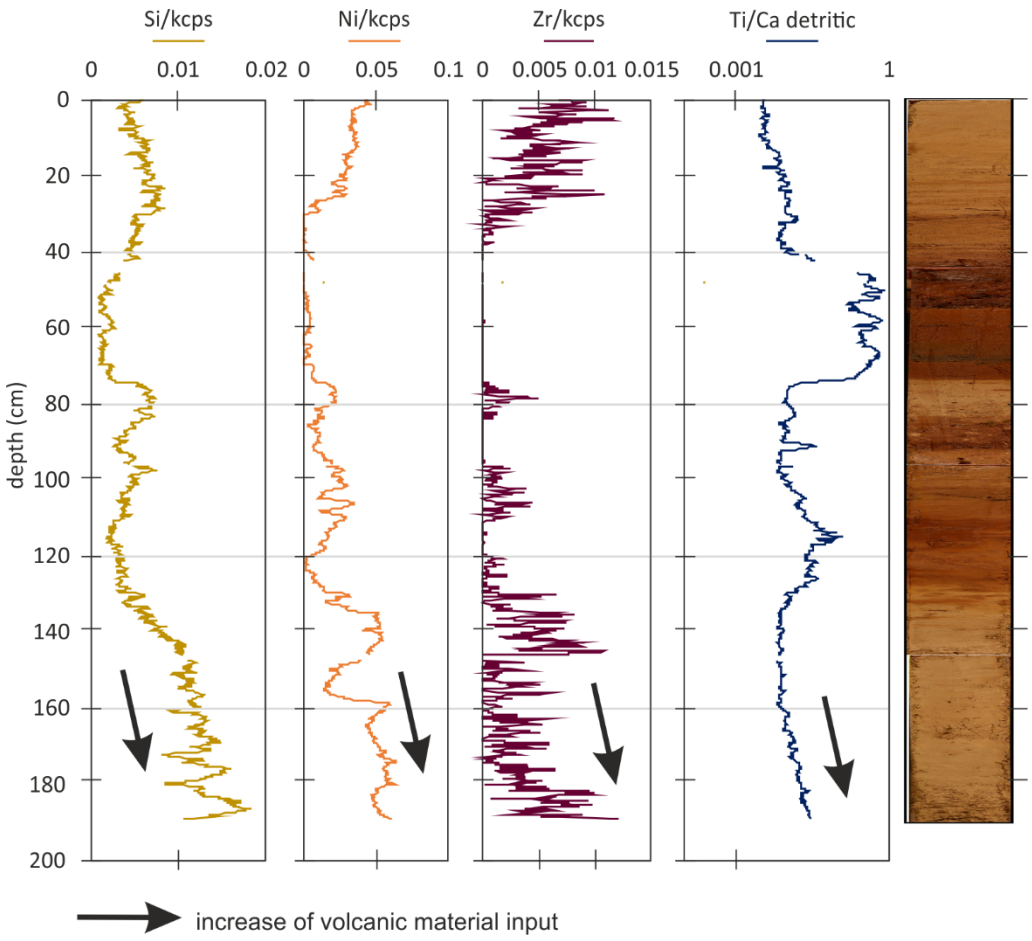

B.9 Sedimentation rate in 52GC

Age-depth model pointers referring to FIGURE 4.4, as known as lithological boundaries between two sedimentary units, with their respective sedimentary rates and the type of stratigraphy unit (FIGURE 4.3). The age-depth model correlation coefficient for Shimmering basin (52GC) built with AnalySeries is of 0.87 and therefore the obtained ages of hydrothermal events are confident. Confidence decreases for the other cores.

Depth (cm)	Time (ka)	Sedimentary rate (cm/ka)	Type of stratigraphy class
3	1.6	1.26	Pelagic
30	22.8	0.85	Pelagic
40	34.6	0.9	Plume fall out
44	38.9	Instant	Plume fall out
74	38.9	1.3	Debris-flow
84	46.4	4.7	Pelagic
92	48.1	0.6	Plume fall out
97	56.1	2.8	Plume fall out
114	62.2	1.55	Plume fall out
130	72.4	0.46	Plume fall out
0	115.2	1.2	Pelagic
180	139.4	1.2	Pelagic (with volcanogenic input)

B.10 Compiled age database for the TAGHF

This database is used to model the age summary in FIGURE 10. MS = massive sulphide.

Age (a)	Uncertainty (a)	Material	Dating method	Reference
19600	900	Massive sulphide	230Th/234U	Lalou *et al*. (1995)
18000	730	Massive sulphide	230Th/234U	Lalou *et al*. (1995)
18400	680	Massive sulphide	230Th/234U	Lalou *et al*. (1995)
102000	7000	Massive sulphide	230Th/234U	Lalou *et al*. (1995)
50000	2000	Massive sulphide	230Th/234U	Lalou *et al*. (1995)
2690	390	Massive sulphide	230Th/234U	Lalou *et al*. (1995)
1900	150	Massive sulphide	230Th/234U	Lalou *et al*. (1995)
670	45	Massive sulphide	230Th/234U	Lalou *et al*. (1995)
1400	700	Massive sulphide	230Th/234U	Lalou *et al*. (1995)
870	200	Massive sulphide	230Th/234U	Lalou *et al*. (1995)
2370	720	Massive sulphide	230Th/234U	Lalou *et al*. (1995)
1770	90	Massive sulphide	230Th/234U	Lalou *et al*. (1995)
9400	1300	Massive sulphide	230Th/234U	Lalou *et al*. (1995)
140000	20000	Birnessite	230Th/234U	Lalou *et al*. (1995)
15000-28000		Pelagic sediments	14C, δ18O	Middleton *et al*. (2016)

Age (a)	Uncertainty (a)	Material	Dating method	Reference
2500-7000		Pelagic sediments	14C, δ18O	Middleton *et al*. (2016)
16000-25000		Pelagic sediments	14C	Lisitsyn *et al*. (1989)
TAGHF: Alvin zone				
47000	4000	Massive sulphide	230Th/234U	Lalou *et al*. (1995)
48500	4000	Massive sulphide	230Th/234U	Lalou *et al*. (1995)
48000	2500	Massive sulphide	230Th/234U	Lalou *et al*. (1995)
45000	4000	Massive sulphide	230Th/234U	Lalou *et al*. (1995)
74000	10000	Birnessite	230Th/234U	Lalou *et al*. (1995)
6000-8500		Pelagic sediments	14C	Metz *et al*. (1988)
TAGHF: Mir zone				
40000-50000		Massive sulphide	230Th/234U	Lalou *et al*. (1995)
18000-26000		Massive sulphide	230Th/234U	Lalou *et al*. (1995)
14000-16000		Massive sulphide	230Th/234U	Lalou *et al*. (1995)
9500-11500		Massive sulphide	230Th/234U	Lalou *et al*. (1995)
4000-4500		Massive sulphide	230Th/234U	Lalou *et al*. (1995)
2150	180	Sub-seafloor MS	230Th/234U	Lalou *et al*. (1998)
2380	170	Sub-seafloor MS	230Th/234U	Lalou *et al*. (1998)
3000	380	Sub-seafloor MS	230Th/234U	Lalou *et al*. (1998)
2590	130	Sub-seafloor MS	230Th/234U	Lalou *et al*. (1998)
14800	1200	Sub-seafloor MS	230Th/234U	Lalou *et al*. (1998)
20000	2300	Sub-seafloor MS	230Th/234U	Lalou *et al*. (1998)
3800	700	Sub-seafloor MS	230Th/234U	Lalou *et al*. (1998)
3420	400	Sub-seafloor MS	230Th/234U	Lalou *et al*. (1998)
5400	260	Sub-seafloor MS	230Th/234U	Lalou *et al*. (1998)
4600	300	Sub-seafloor MS	230Th/234U	Lalou *et al*. (1998)
4400	200	Sub-seafloor MS	230Th/234U	Lalou *et al*. (1998)
3500	170	Sub-seafloor MS	230Th/234U	Lalou *et al*. (1998)
5600	300	Sub-seafloor MS	230Th/234U	Lalou *et al*. (1998)
6470	730	Sub-seafloor MS	230Th/234U	Lalou *et al*. (1998)

Appendix C **Supplementary material to CHAPTER 5**

C.1 Supplementary tables

C.1.1 Grain size analyses (digital)

Grain size was analysed on a Malvern grain size analyzer on 23 samples and the dataset is available in the electronic annexes (DIGITAL MATERIAL 4).

C.1.2 EDS analyses on SEM selected samples (digital)

Semi-quantitative EDS analyses were obtained on 3 selected areas on FIGURE 5.4D and chemical data are available in the electronic annexes (DIGITAL MATERIAL 8).

C.1.3 XRD mineralogy results for Southern mound, Rona mound and Mir zone

Spectra for each sample are available in the electronic annexes (DIGITAL MATERIAL 7).

Core	Depth (cm)	Identified minerals
16GC (Southern mound)	15	Todorokite, Ferripyrophyllite, Nontronite
16GC (Southern mound)	38	Hematite, Goethite
16GC (Southern mound)	66	Goethite
16GC (Southern mound)	113	Hematite, Goethite
22RD (Southern mound)	172	Nontronite, Goethite
22RD (Southern mound)	215	Goethite
22RD (Southern mound)	284	Goethite, Nontronite
22RD (Southern mound)	335	Hematite
27GC (Rona mound)	8	Calcite, Goethite
27GC (Rona mound)	24	Montmorillonite, Quartz
27GC (Rona mound)	30	Nontronite
28GC (Mir mound)	4	Calcite, Quartz
28GC (Mir mound)	28	Goethite, Birnessite, Nontronite, Todorokite
28GC (Mir mound)	75	Nontronite, Goethite
28GC (Mir mound)	129	Hematite, Goethite
28GC (Mir mound)	190	Hematite, Goethite
31RD (Southern mound)	11	Nontronite, Montmorillonite
31RD (Southern mound)	71	Nontronite, Montmorillonite
31RD (Southern mound)	125	Quartz, Goethite, Nontronite
31RD (Southern mound)	154	Hematite, Quartz, Goethite

C.1.4 ITRAX chemostratigraphy (digital)

ITRAX chemostratigraphy data for 16GC, 38GC and 39GC are available in the electronic annexes (DIGITAL MATERIAL 9). The elements analysed are Ca, Mn, Fe, Co, Cu, Zn, Ba and S. Correlation tables between those elements are also showed in the DIGITAL MATERIAL 9.

C.1.5 Mn calibration from ITRAX data (digital)

ITRAX data for 16GC, 38GC and 39GC were calibrated against whole rock geochemistry data for Mn in order to get more quantitative results and the calibrations are available in the electronic annexes (DIGITAL MATERIAL 9). Correlation coefficients were better than 0.96.

C.1.6 Solid phase concentrations

Solid phase concentration for 16GC (Southern mound), 38GC (depositional channel) and 39GC (Mir zone fan) relating to FIGURE 5. Ca, Fe, Mn, and Cu (39GC, 38GC) are measured on ICP-OES. Co, Ba and Cu (16GC) are measured on ICP-MS. The comprehensive database is available in the electronic annexes (DIGITAL MATERIAL 10).

Depth (cm)	Ca wt%	Fe wt%	Mn wt%	Co ppm	Cu wt%	Zn wt%	Ba ppm
16GC – Southern mound							
120	0.13	45.71	0.20	0.5	0.007	0.10	10
100	0.18	39.01	0.11	0.5	0.01	0.14	460
81	0.18	38.09	0.09	0.3	0.007	0.12	0
64	0.16	42.02	0.11	0.2	0.004	0.12	0
50	0.17	40.03	0.14	0.6	0.04	0.13	22890
25	0.25	32.30	0.08	0.9	0.03	0.16	30
15	0.73	20.29	15.91	19.6	0.437	0.14	2610
38GC – Depositional channel							
92	19.40	11.95	0.14	25	0.83	0.08	231
87	18.18	13.45	0.13	23	1.01	0.09	271
82	19.52	11.36	0.15	22	0.83	0.08	231
77	19.42	12.05	0.12	23	0.75	0.09	246
72	1.85	33.37	0.11	52	1.76	0.23	438
67	1.83	33.64	0.04	137	3.34	0.30	1100
62	0.17	36.72	0.01	159	6.42	0.88	815
57	0.64	28.89	0.83	52	7.23	0.24	467
52	0.64	32.20	0.44	38	4.03	0.23	521
45	0.62	32.65	0.85	58	3.75	0.30	1717
40	0.73	28.65	1.66	214	5.12	0.23	1166
35	20.77	12.59	0.28	50	0.90	0.11	586

Depth (cm)	Ca wt%	Fe wt%	Mn wt%	Co ppm	Cu wt%	Zn wt%	Ba ppm
30	23.25	11.64	0.21	29	0.67	0.10	318
25	29.93	3.69	0.11	20	0.17	0.03	230
20	33.21	2.37	0.12	27	0.10	0.02	60
15	23.54	14.12	0.05	19	1.01	0.08	42
10	14.89	23.28	0.17	52	1.66	0.12	53
5	24.64	11.22	0.13	38	0.59	0.04	50
39GC – Mir zone fan							
36	0.14	34.48	0.04	99	16.21	0.37	1
30	0.11	30.50	0.03	104	18.85	0.19	4
26	0.12	28.22	0.03	11	28.10	0.07	1
21	0.67	29.05	0.04	79	10.78	0.13	4
16	0.34	29.58	0.04	6	16.81	0.16	7
11	0.19	32.34	0.04	4	1.99	0.19	11
6	0.21	33.96	0.05	12	6.65	0.16	5

C.1.7 Y-REE data

Y-REE data for sulphide rich layers and carbonate sediments with and without hydrothermal plume fall-out in the depositional channel (38GC); Fe oxides in the deepest layer on top of the Southern mound (22RD), Fe oxides and 'fresh' sulphides in the Mir zone fan (39GC), pelagic sediments at the surface (less than 5 cm in depth), Mn oxide layers (this study and Goulding *et al*., 1998) and active TAG Mound sulphides (Mills et Elderfield, 1995). Reference data for North-Atlantic Deep Waters (Douville *et al*., 1999), black smokers (Douville *et al*. 1999), white smokers (Mitra *et al*. 1994) and chondrites C1 (Palme, 1988) are given. This table is relating to FIGURE 5.7. Excel spreadsheet of the database is available in the electronic annexes (DIGITAL MATERIAL 10).

Element/ Description	La ppm	Ce ppm	Pr ppm	Nd ppm	Sm ppm	Eu ppm	Gd ppm	Tb ppm	Dy ppm	Ho ppm	Er ppm	Tm ppm	Yb ppm	Lu ppm	Y ppm
Seawater	4.03E-06	7.71E-07	6.20E-07	3.09E-06	4.10E-06	1.10E-06	6.30E-06	9.20E-07	6.40E-06	1.70E-06	5.50E-06		5.40E-06	8.80E-07	1.70E-04
Black smoker	0.000649	0.00114	0.000159	0.000622	0.000133	0.000391	0.000123	1.78E-05	8.87E-05	1.65E-05	4.49E-05		3.82E-05	4.99E-06	6.04E-4
White smoker	0.00034	0.000479		0.000214	3.58E-05	0.001321	2.57E-05		1.79E-05		7.96E-06		6.68E-06	8.08E-07	
Chondrite C1	0.245	0.638	0.096	0.474	0.154	0.058	0.204	0.037	0.254	0.057	0.166	0.026	0.165	0.025	1.57
Mn crusts															
Goulding *et al*. 1998	10.7	18.4	2.7	12.4	2.6	2.41	2.54	0.35	2.02	0.45	1.24	0.17	1.02	0.17	
31RD	2.77	1.53	0.39	1.63	0.28	0.37	0.39	0.05	0.32	0.08	0.23	0.03	0.21	0.03	3.68
31RD	2.29	1.92	0.45	1.89	0.38	0.20	0.43	0.06	0.41	0.09	0.25	0.04	0.23	0.04	3.25
27GC	6.92	5.50	1.14	4.70	0.95	0.28	1.09	0.16	0.95	0.20	0.56	0.08	0.48	0.08	8.08
16GC	5.60	8.05	1.41	5.84	1.24	0.66	1.29	0.19	1.14	0.23	0.67	0.10	0.60	0.09	6.73

22RD	2.52	3.06	0.75	3.32	0.74	1.18	0.69	0.10	0.58	0.12	0.34	0.05	0.32	0.05	3.71
28GC	11.63	14.11	2.79	11.55	2.49	0.80	2.58	0.41	2.49	0.53	1.55	0.22	1.40	0.21	18.33
38GC	10.73	16.03	2.74	11.54	2.60	1.45	2.64	0.41	2.42	0.48	1.35	0.20	1.25	0.19	15.61
27GC	13.01	16.58	3.08	12.65	2.69	0.80	2.85	0.44	2.51	0.50	1.42	0.19	1.22	0.18	17.53
27GC	15.56	17.16	3.66	15.02	3.18	0.94	3.42	0.51	2.98	0.59	1.63	0.23	1.41	0.20	20.40
49GC	6.08	9.04	1.57	6.69	1.58	1.41	1.57	0.24	1.43	0.28	0.78	0.12	0.73	0.11	8.933
Sulphides															
Black smoker S average	0.06647	0.08850		0.06493	0.01361	0.03356	0.01081		0.0329		0.00589		0.005317		
39GC	0.28	0.63	0.09	0.42	0.08	0.06	0.07	0.01	0.09	0.02	0.06	0.01	0.06	0.01	0.48
39GC	0.13	0.32	0.05	0.27	0.10	0.08	0.14	0.03	0.17	0.04	0.10	0.02	0.11	0.02	0.93
39GC	0.24	0.61	0.13	0.68	0.22	0.12	0.28	0.05	0.34	0.07	0.20	0.03	0.21	0.03	1.41
38GC - layer	5.75	8.76	1.63	6.91	1.63	0.69	1.66	0.27	1.59	0.31	0.87	0.13	0.82	0.12	8.48
38GC - layer	2.01	2.99	0.60	2.74	0.73	0.75	0.80	0.13	0.77	0.15	0.42	0.06	0.42	0.06	4.24
Oxyhydroxides															
39GC	0.95	2.22	0.49	2.59	0.83	0.41	1.02	0.19	1.21	0.26	0.75	0.12	0.80	0.12	5.57
39GC	0.65	1.33	0.29	1.54	0.49	0.29	0.63	0.11	0.75	0.16	0.46	0.07	0.49	0.07	2.75
39GC	0.98	1.72	0.36	1.76	0.50	0.36	0.59	0.10	0.61	0.12	0.36	0.06	0.37	0.05	2.66
22RD, 308 cm	2.17	5.90	1.10	5.49	1.50	8.50	1.06	0.13	0.61	0.11	0.29	0.04	0.28	0.05	3.87
Pelagic sediments															
38GC	12.11	18.38	2.97	12.01	2.62	0.83	2.73	0.42	2.53	0.51	1.45	0.21	1.30	0.19	17.87
49GC	10.42	14.61	2.50	10.31	2.19	0.75	2.32	0.36	2.13	0.44	1.24	0.18	1.10	0.17	15.58
27GC	12.79	18.02	3.16	12.97	2.79	0.75	2.82	0.44	2.59	0.53	1.48	0.21	1.32	0.19	17.16
27GC	18.16	26.60	4.66	18.87	4.03	1.05	3.95	0.61	3.58	0.69	1.92	0.27	1.69	0.24	22.10

28GC	11.63	14.11	2.79	11.55	2.49	0.80	2.58	0.41	2.49	0.53	1.55	0.22	1.40	0.21	18.33
28GC	7.11	7.45	1.77	7.64	1.72	0.84	1.75	0.27	1.63	0.34	1.01	0.15	0.95	0.15	11.64
38GC	19.72	29.59	4.98	20.30	4.42	1.32	4.48	0.70	4.06	0.81	2.24	0.32	1.98	0.29	26.27
38GC	19.30	28.52	4.81	19.87	4.27	1.33	4.35	0.68	3.95	0.78	2.16	0.31	1.94	0.28	25.55
38GC	20.21	30.49	5.08	20.82	4.52	1.32	4.53	0.70	4.07	0.80	2.22	0.32	1.97	0.29	26.29
38GC	20.75	31.02	5.18	21.33	4.62	1.36	4.66	0.72	4.17	0.82	2.26	0.33	2.02	0.29	26.43
Pelagic sediment with hydrothermal plume fall out															
38GC – 10 cm	8.52	12.21	2.16	9.20	2.03	0.95	2.13	0.34	2.00	0.41	1.16	0.17	1.08	0.16	14.06
Severmann *et al.* 2000	15.9	23.6	3.89	14.8	3.13	1.6	3.03	0.41	2.54	0.52	1.4	0.2	1.3	0.21	

C.1.8 Pore water concentrations

Pore water concentrations for 16GC (Southern mound), 39GC (Mir zone fan) and 38GC (depositional channel) relating to FIGURE 5.8. ND = not determined, LD = below detection limit. LOD = limit of detection. Excel spreadsheet of the database is available in the electronic annexes (DIGITAL MATERIAL 15).

Depth (cm)	Cl mol/L	Mg mmol/L	Ca mmol/L	Fe µmol/L	Mn µmol/L	Co nmol/L	Cu µmol/L	Zn µmol/L	TA mmol/L	SO_4 mmol/L	NO_3 µmol/L
LOD				1.0	0.1	3	0.1	0.1			
16GC – Southern mound											
130	579	56	11.0	1.2	0.2	ND	0.3	1.2	2.7	28.0	5.9
120	594	56	10.9	2.0	0.4	ND	0.6	2.7	ND	28.6	24.4
110	586	56	10.9	0.8	0.2	ND	0.3	0.7	2.6	28.4	9.5
100	588	56	10.8	0.8	0.1	ND	0.1	0.6	2.6	28.4	8.8
90	584	56	10.7	1.0	0.1	ND	0.9	2.2	ND	28.6	11.1
82	585	57	10.9	3.9	0.7	ND	0.4	2.6	ND	28.4	14.9
70	581	57	10.8	0.9	0.1	ND	0.1	0.9	2.6	28.3	11.6
65	581	58	10.9	0.9	0.1	ND	0.1	0.6	2.7	28.0	13.7
60	591	58	11.0	2.4	0.2	ND	0.5	6.1	2.5	28.9	13.2
59	587	58	10.8	12.7	0.3	ND	0.4	1.1	ND	28.6	19.9
51	580	58	10.6	2.6	0.2	ND	0.4	0.9	ND	28.6	19.2
45	582	58	10.7	0.8	0.2	ND	0.1	1.8	ND	28.4	13.6
40	594	58	10.8	0.8	0.1	ND	0.1	2.0	ND	28.9	18.5
35	582	58	10.6	1.2	0.1	ND	0.1	0.4	ND	28.4	20.7
30	580	57	10.5	1.9	0.1	ND	0.3	0.9	ND	28.0	32.6
25	579	58	10.5	9.2	0.9	ND	0.5	7.0	2.3	28.0	22.2
20	581	57	10.4	0.6	0.1	ND	0.1	1.0	2.3	27.6	43.0
15	586	58	10.4	0.4	0.1	ND	0.1	1.3	2.2	27.9	30.6

Depth (cm)	Cl mol/L	Mg mmol/L	Ca mmol/L	Fe µmol/L	Mn µmol/L	Co nmol/L	Cu µmol/L	Zn µmol/L	TA mmol/L	SO_4 mmol/L	NO_3 µmol/L
39GC – Mir zone fan											
30	605	55	10.9	2384.3	3.2	99	27.9	39.0	0.2	30.4	5.7
25	590	55	11.0	2926.5	4.2	118	23.9	28.1	0.3	30.0	3.8
20	586	55	11.2	3052.0	6.0	149	9.5	25.2	1.2	29.8	3.8
15	585	56	11.4	2984.2	8.6	195	7.9	18.8	1.7	30.0	12.5
10	584	55	11.1	2839.1	9.7	247	4.9	15.4	1.6	29.5	5.2
5	588	55	12.2	1508.9	21.1	274	49.2	8.6	2.1	29.6	9.1
38GC – Depositional channel											
90	558	56	12.4	2.1	38.5	32	27.9	2.1	ND	26.4	4.0
85	562	56	12.2	6.5	32.5	27	14.4	4.2	ND	26.7	
80	554	56	12.2	1.6	26.2	21	24.3	1.1	3.8	26.8	6.1
80	ND	56	12.3	1.1	25.9	21	24.0	1.1	ND	ND	
75	ND	56	12.1	1.5	20.9	16	24.1	0.7	3.5	ND	3.3
70	546	54	12.2	1.6	14.2	11	15.0	0.5	3.9	24.9	3.6
65	551	55	12.3	2.4	9.2	11	7.2	1.1	ND	25.9	4.2
60	ND	55	12.3	2.3	2.5	3	4.5	1.8	3.8	ND	9.9
55	553	55	12.1	1.6	0.1	LD	0.1	0.9	3.8	25.7	5.9
50	ND	54	11.9	1.5	0.0	LD	0.2	0.8	3.8	ND	8.8
44	557	54	11.8	2.1	0.1	LD	0.3	0.8	3.7	25.7	
39	ND	55	11.9	1.6	0.4	LD	0.1	0.9	ND	ND	17.5
34	556	57	11.7	1.9	0.2	LD	0.2	4.2	3.2	26.1	19.9
29	555	58	11.7	0.9	0.4	LD	0.2	1.1	3.2	26.0	19.9
24	567	57	11.3	2.0	0.3	LD	0.2	1.2	3.0	26.3	22.4
19	570	58	11.3	2.0	0.3	LD	0.2	0.8	ND	27.2	23.9
14	555	56	11.1	1.7	0.1	LD	0.1	0.6	3.0	25.9	23.3
9	560	56	11.1	1.7	0.1	LD	0.1	0.6	2.8	25.8	27.3
4	570	56	10.8	LD	0.1	LD	0.1	0.7	2.6	25.7	26.5

Depth (cm)	Cl mol/L	Mg mmol/L	Ca mmol/L	Fe µmol/L	Mn µmol/L	Co nmol/L	Cu µmol/L	Zn µmol/L	TA mmol/L	SO_4 mmol/L	NO_3 µmol/L
Near-bottom Seawater (39MC)											
	594	57	10.8	2.3	0.1	LD	0.3	0.6	2.8	29.4	ND

C.1.9 Mn fluxes calculation (digital)

Porosity measurements, Mn diffusion, total weight of Mn, Mn concentration gradients and Mn fluxes calculations for 16GC, 38GC and 49GC are available in the electronic annexes (DIGITAL MATERIAL 15). Mn pore water profile in 49GC is also provided.

C.1.10 Correlation table in pelagic sediments (digital)

Additional correlation table on 16 bulk ICP-OES analyses from pelagic sediments (surficial carbonate ooze cover) is available in the electronic annexes (DIGITAL MATERIAL 9).

C.2 Supplementary tables for 27GC, 22RD, 31RD, 28GC and 49GC

APPENDIX C.2 presents an extensive geochemical database for solid phase and pore waters from 27GC (Rona mound), 22RD (Southern mound), 31RD (Southern mound), 28GC (Mir zone) and 49GC (depositional channel). Those data were not used or described in the CHAPTER 5. Excel spreadsheet of the database is available in the electronic annexes (DIGITAL MATERIAL 10).

C.2.1 Solid phase content

Solid phase content results for 27GC (Rona mound), 22RD (Southern mound), 31RD (Southern mound), 28GC (Mir zone) and 49GC (depositional channel). Ca, Fe, Mn, and Cu (49GC) are measured on ICP-OES. Co, Ba and Cu (16GC) are measured with ICP-MS.

Depth cm	Ca wt%	Fe wt%	Mn wt%	Co ppm	Cu ppm	Zn wt%	Ba ppm
27 GC – Rona mound							
39	0.15	36.43	0.25	2	146	0.21	10
21	0.37	30.15	0.13	9	1693	0.25	90
21	0.43	33.26	0.12	8	1728	0.24	90
17	0.89	14.69	19.58	268	13360	0.71	3230
7	26.38	6.82	0.19	24	930	0.03	60
1	24.30	8.54	0.31	28	1367	0.08	290
22RD – Southern mound							
308	0.30	42.66	0.10	1	113	0.03	10
289	0.19	51.66	0.13	0	53	0.06	10
275	0.12	41.81	0.09	0	76	0.11	0
268	0.13	46.30	0.11	0	96	0.13	40
261	0.08	37.83	0.09	0	120	0.10	2020
225	0.14	47.22	0.13	1	271	0.10	6770
210	0.12	41.80	0.10	1	119	0.06	4370
193	0.50	46.56	1.39	2	255	0.06	210
31RD – Southern mound							
239	0.36	52.69	0.39	1	60	0.04	20
229	0.32	49.35	0.22	2	58	0.03	20
155	0.09	39.82	0.20	1	297	0.07	310
135	0.14	38.69	0.12	0	133	0.06	10
115	0.17	33.07	0.08	0	61	0.04	500
92	0.17	31.35	0.07	0	59	0.04	10
71	0.22	27.76	0.13	1	208	0.03	40
52	0.30	31.01	1.15	2	167	0.03	180
32	0.61	23.68	14.90	10	1003	0.03	2230
22	1.18	11.07	11.93	7	1176	0.04	510
28GC – Mir zone							
180	0.45	48.87	0.06	0	1375	0.28	10

Depth cm	**Ca wt%**	**Fe wt%**	**Mn wt%**	**Co ppm**	**Cu ppm**	**Zn wt%**	**Ba ppm**
160	0.21	52.80	0.08	0	402	0.08	10
137	0.18	53.30	0.07	0	1061	0.10	10
117	0.27	45.44	0.05	0	87403	0.14	0
92	0.19	34.85	0.05	0	2730	0.15	0
72	0.50	32.76	1.33	3	4250	0.15	130
52	0.52	33.08	0.11	0	113	0.16	40
42	0.46	34.38	0.11	0	412	0.19	20
30	0.54	25.25	3.66	3	7424	0.19	200
18	8.04	21.28	0.22	7	339	0.16	30
6.5	23.61	11.31	1.08	14	1941	0.09	60
49GC – Depositional channel					Wt%		
222	12.18	23.24	0.20	17	1.84	0.13	144
206	0.64	32.37	0.16	95	1.92	0.34	163
185	0.43	35.08	0.20	106	3.29	0.40	114
175	0.38	38.37	0.20	98	2.18	0.43	51
175	0.33	34.48	0.15	105	3.18	0.47	44
172	0.45	38.20	0.18	73	1.80	0.39	49
165	0.34	35.95	0.16	92	2.32	0.66	67
165	0.36	36.98	0.16	101	2.15	0.65	68
159	0.25	32.82	0.12	109	4.97	0.51	34
155	0.32	37.62	0.13	126	4.09	0.55	48
155	0.31	36.88	0.13	125	4.00	0.78	41
154	0.28	35.86	0.11	104	3.33	0.52	42
147	0.26	27.79	0.05	44	1.39	0.21	105
145	0.25	33.69	0.12	185	5.75	0.46	248
135	0.48	35.41	0.14	33	2.91	0.29	347
124	2.51	22.78	0.17	23	0.65	0.12	459
120	3.86	24.78	0.14	39	0.25	0.17	278
117	1.06	27.03	0.16	32	0.11	0.17	133

Depth cm	Ca wt%	Fe wt%	Mn wt%	Co ppm	Cu ppm	Zn wt%	Ba ppm
115	2.86	27.32	0.13	40	0.17	0.25	319
105	2.97	24.20	0.08	25	0.54	0.30	98
96	8.77	25.91	0.13	22	0.17	0.44	205
93	0.60	30.90	0.06	23	2.26	0.83	61
83	0.20	30.53	0.07	20	1.16	0.69	103
78	0.22	31.98	0.04	26	1.43	0.98	258
73	0.18	30.14	0.03	24	10.25	1.85	261
68	0.29	36.64	0.05	19	0.71	0.71	354
63	0.15	31.24	0.02	48	9.45	0.82	312
58	0.29	32.58	0.09	15	0.63	0.44	159
52	0.43	31.54	0.47	28	0.82	0.39	381
48	0.41	30.38	0.69	29	2.30	0.36	316
44	0.49	26.14	2.12	103	6.21	0.23	384
34	11.12	19.92	0.20	22	1.72	0.16	408
29	10.60	16.51	0.32	57	1.65	0.13	337
24	17.16	15.39	0.25	34	0.90	0.13	425
19	24.49	9.38	0.22	23	0.38	0.08	272
14	29.16	4.80	0.11	20	0.11	0.03	256
9	29.37	6.02	0.14	20	0.09	0.03	81
4	24.76	12.45	0.19	34	0.51	0.06	49

C.2.2 Pore water concentration

Pore water concentrations of cations measured with ICP-MS and ICP-OES for 27GC (Rona mound), for 22RD (Southern mound), for 31RD (Southern mound), for 28GC (Mir zone), for 49GC (depositional channel). ND = not determined, LD = below detection limit. LOD = limit of detection. Excel spreadsheet of the database is available in the electronic annexes (Digital reference #15).

Depth Cm	Cl mmol/L	Mg mmol/L	Fe µmol/L	Mn µmol/L	Co nmol/L	Cu µmol/L	Zn µmol/L	TA mmol/L	SO_4 mmol/L	NO_3 mmol/L
LOD			1.0	0.1	3	0.1	0.1			
27GC – Rona mound										
38	ND	58	0,7	0,1	LD	0,2	3,5	2,2	ND	ND
32	ND	57	0,4	0,0	LD	0,1	1,6	2,3	ND	ND
27	ND	57	LD	0,0	LD	0,3	2,0	2,2	ND	ND
21	ND	56	0,7	0,1	LD	0,1	0,8	2,2	ND	ND
17	ND	55	0,4	0,0	LD	0,2	0,4	2,4	ND	ND
12	ND	57	0,2	0,0	LD	0,3	0,3	2,8	ND	ND
7	ND	57	0,5	0,0	LD	0,5	0,4	2,5	ND	ND
2	ND	58	0,7	0,1	LD	0,2	3,5	2,2	ND	ND
2	ND	57	0,4	0,0	LD	0,1	1,6	2,3	ND	ND
22RD – Southern mound										
305	ND	56	1,0	0,1	LD	0,6	0,6	2,3	ND	ND
297	ND	56	0,5	0,0	LD	0,2	0,5	2,8	ND	ND
289	ND	56	2,2	0,1	LD	0,2	2,3	2,8	ND	ND
282	ND	56	2,1	0,2	LD	2,5	35,9	2,7	ND	ND
275	ND	56	0,6	0,1	LD	0,8	38,8	2,7	ND	ND
268	ND	57	2,4	0,1	LD	0,2	0,7	2,8	ND	ND
261	ND	56	0,8	0,0	LD	0,1	0,4	2,7	ND	ND
254	ND	56	0,6	0,1	LD	0,2	2,2	2,8	ND	ND
246	ND	57	0,5	0,1	LD	0,3	0,5	2,8	ND	ND
239	ND	56	0,7	0,1	LD	0,2	0,8	2,6	ND	ND
231	ND	56	0,4	0,1	LD	0,4	0,8	2,8	ND	ND
225	ND	56	2,7	0,3	LD	0,2	8,9	2,9	ND	ND
216	ND	56	0,7	0,1	LD	0,1	0,4	2,8	ND	ND
210	ND	56	0,2	0,1	LD	0,1	0,6	2,9	ND	ND
202	ND	57	2,3	0,3	LD	0,2	5,4	2,8	ND	ND
193	ND	55	0,7	0,1	LD	0,2	0,4	2,9	ND	ND
31RD – Southern mound										

239	ND	58	0,3	0,2	LD	0,1	0,6	2,4	ND	23
229	ND	58	0,4	0,1	LD	0,3	3,7	2,4	ND	24
155	ND	56	0,2	0,1	LD	0,1	0,6	2,6	ND	4
145	ND	57	0,3	0,1	LD	0,3	0,5	2,6	ND	6
135	ND	57	LD	0,1	LD	0,5	0,4	2,4	ND	19
125	ND	57	0,8	0,1	LD	0,2	1,9	2,6	ND	7
115	ND	57	0,3	0,1	LD	0,1	0,5	2,9	ND	6
105	ND	57	0,7	0,1	LD	0,0	0,5	2,5	ND	4
92	ND	57	LD	0,1	LD	0,1	2,4	2,6	ND	4
81	ND	57	0,2	0,1	LD	0,1	0,4	2,6	ND	5
71	ND	57	0,3	0,1	LD	0,1	0,9	2,5	ND	13
61	ND	58	0,7	0,0	LD	0,1	0,4	2,4	ND	14
52	ND	56	1,0	0,1	LD	0,1	0,4	2,5	ND	5
42	ND	56	10,5	0,1	LD	0,0	0,2	2,5	ND	8
32	ND	56	1,5	0,2	LD	0,1	0,6	2,6	ND	12
22	ND	57	1,2	0,1	LD	0,1	0,5	2,5	ND	16
28GC – Mir zone										
188	ND	58	2,3	0,2	LD	0,4	1,3	2,3	ND	5
178	ND	58	0,2	0,0	LD	0,2	1,8	2,4	ND	3
168	ND	58	1,1	0,1	LD	0,1	1,9	2,4	ND	4
158	ND	59	0,5	0,2	LD	0,2	1,5	2,3	ND	ND
142	ND	59	0,5	0,1	LD	0,2	0,9	ND	ND	ND
135	ND	59	1,8	0,2	LD	0,1	0,9	2,4	ND	4
125	ND	58	3,7	0,1	LD	0,1	1,0	2,4	ND	5
115	ND	58	1,5	0,1	LD	0,6	1,2	2,4	ND	4
105	ND	58	3,0	0,2	LD	0,2	1,2	2,4	ND	ND
97	ND	58	0,9	0,1	LD	0,1	0,3	ND	ND	ND
91	ND	58	1,1	0,1	LD	0,1	0,3	2,4	ND	5
80	ND	58	2,7	0,1	LD	0,6	3,7	2,1	ND	6
70	ND	58	2,2	0,1	LD	0,1	0,3	2,2	ND	6
60	ND	57	1,3	0,1	LD	0,1	1,8	2,1	ND	6

50	ND	58	2,0	0,1	LD	1,7	0,9	2,2	ND	7
50	ND	57	1,6	0,1	LD	0,5	1,5	2,1	ND	11
40.5	ND	58	1,7	0,1	LD	0,1	0,7	2,2	ND	17
37	ND	56	0,7	0,1	LD	0,1	0,3	2,1	ND	14
31.5	ND	57	6,1	0,1	LD	0,3	0,8	2,1	ND	17
27	ND	57	1,8	0,1	LD	0,3	0,4	2,1	ND	20
21.5	ND	57	0,5	0,1	LD	0,1	0,9	2,1	ND	16
17	ND	57	0,3	0,1	LD	0,1	0,9	2,5	ND	24
12	ND	56	0,1	0,1	LD	0,1	0,9	2,4	ND	22
6.5	ND	56	0,4	0,1	LD	0,1	0,9	2,3	ND	25
49GC – Depositional channel										
225	575	57	1,9	84,1	44	34,0	33,0	4,1	27,2	ND
209	578	57	2,6	82,8	47	44,8	43,6	4,1	27,8	ND
187	579	57	3,8	75,6	39	15,0	14,6	3,7	27,3	ND
177	575	57	2,7	72,0	35	18,2	17,7	4,3	27,2	ND
167	574	57	2,0	67,3	31	14,7	14,3	4,0	27,3	ND
157	574	56	1,2	63,6	43	7,0	6,8	3,7	27,5	ND
147	577	56	0,9	59,9	53	7,5	7,3	3,9	27,6	ND
134	ND	57	2,0	48,3	50	10,0	9,7	3,6	ND	ND
127	590	57	1,4	47,2	56	12,9	12,5	ND	28,3	ND
117	599	57	6,7	44,8	49	8,5	8,3	3,6	29,3	ND
107	581	57	23,7	39,8	50	6,4	6,2	3,6	28,4	ND
97	595	58	30,4	30,2	39	1,5	1,5	3,4	29,0	ND
87	584	58	4,3	15,2	14	0,6	0,5	ND	28,1	ND
82	597	58	42,4	18,3	34	1,1	1,0	ND	28,5	ND
77	585	58	39,2	16,6	38	2,7	2,6	ND	28,6	ND
72	584	58	38,1	13,5	21	0,7	0,7	3,2	27,9	ND
67	587	57	27,8	10,3	19	2,9	2,8	ND	28,0	ND
62	595	58	19,6	6,7	13	0,9	0,9	2,5	28,3	ND
57	590	57	8,0	3,0	3	0,9	0,9	3,0	27,8	ND
52	606	58	2,5	0,0	LD	0,2	0,2	2,9	28,6	ND

47	572	57	2,0	0,2	LD	0,1	0,1	2,9	26,1	ND
35	577	58	2,4	0,1	LD	0,2	0,2	2,8	27,0	ND
30	577	59	2,3	0,2	LD	0,7	0,7	2,7	27,0	ND
25	581	58	1,9	0,1	LD	0,1	0,1	2,6	27,0	ND
20	576	57	1,4	0,1	LD	0,1	0,1	2,5	27,4	ND
15	598	58	2,0	0,2	LD	0,2	0,2	2,5	28,6	ND
10	580	59	7,8	0,3	LD	0,3	0,3	2,4	27,9	ND
5	600	58	5,1	0,7	LD	0,5	0,4	2,2	28,2	ND

C.2.3 Complementary pore water concentrations

Complementary pore water ICP-MS and ICP-OES results for 16GC (Southern Mound), 22RD (Southern mound), 27GC (Rona mound), 28GC (Mir zone), 31RD (Southern mound), 38GC (depositional channel), 39GC (Mir zone fan), and 49GC (depositional channel). B, Ca, K, Na, Rb, Si and Sr are measured on ICP-OES. Ba, Li, U and V are measured with ICP-MS. An excel spreadsheet of the database is available in the electronic annexes (Digital reference #15).

Depth (cm)	Al µmol/L	B µmol/L	Ba µmol/L	Ca mmol /L	K mmol /L	Li µmol/L	Na mmol/L	Ni µmol/L	Rb µmol/L	Si µmol/L	Sr µmol/L	Ti µmol /L	U µmol /L	V µmol /L
16GC – Southern mound														
130	2,06	569	0,28	11.0	10,5	28,0	488	0,07	1,55	182	88,3	0,161	0,011	0,203
120	1,49	583	0,26	10.9	10,8	30,1	477	0,12	1,53	199	88,5	0,138	0,010	0,213
110	1,16	582	0,23	10.9	10,7	30,5	479	0,08	1,49	177	88,2	0,153	0,011	0,219
100	1,17	547	0,20	10.8	10,6	30,0	476	0,08	1,46	172	86,2	0,136	0,012	0,216
90	1,43	513	0,20	10.7	10,4	26,6	481	0,07	1,44	162	85,2	0,153	0,011	0,202
82	2,99	532	0,26	10.9	10,7	28,9	487	0,13	1,47	179	86,5	0,199	0,012	0,219
70	1,30	541	0,20	10.8	10,5	29,3	482	0,09	1,40	175	87,6	0,140	0,012	0,215
65	1,19	548	0,19	10.9	10,6	28,7	493	0,08	1,34	177	88,8	0,131	0,012	0,219
60	3,03	540	0,20	11.0	10,6	29,6	491	0,13	1,44	166	87,8	0,189	0,011	0,217
59	2,25	569	0,19	10.8	10,8	31,4	491	0,24	1,51	161	86,4	0,168	0,010	0,210
51	2,26	551	0,23	10.6	10,9	28,3	487	0,08	1,51	159	85,9	0,175	0,011	0,214
45	1,12	588	0,19	10.7	11,1	32,3	486	0,10	1,57	158	85,9	0,187	0,010	0,222
40	1,34	489	0,13	10.8	10,6	28,5	488	0,11	1,40	127	83,6	0,154	0,011	0,223
35	1,13	526	0,15	10.6	10,6	29,9	476	0,08	1,45	127	83,8	0,158	0,011	0,216
30	1,07	511	0,13	10.5	10,8	27,3	478	0,09	1,43	125	82,7	0,584	0,011	0,216
25	13,05	493	0,16	10.5	10,7	28,7	482	0,17	1,45	121	83,1	0,287	0,011	0,247
20	1,64	485	0,06	10.4	10,8	33,9	484	0,10	1,44	102	81,8	0,265	0,009	0,234
15	0,58	493	0,05	10.4	11,0	32,5	481	0,09	1,39	85	82,3	0,153	0,010	0,204
15	1,59	492	0,05	10.4	10,9	32,0	480	0,09	1,40	88	81,9	0,352	0,010	0,201
22RD – Southern mound														
305	1,43	623	0,20	11,5	11,4	31,6	485	0,09	1,73	325	92,8	0,232	0,017	0,212
305	1,07	622	0,20	11,4	11,6	31,4	484	0,09	1,74	316	92,2	0,146	0,017	0,207
297	1,09	618	0,20	11,4	11,5	31,4	485	0,08	1,70	328	91,5	0,171	0,018	0,208
289	1,60	574	0,20	12,4	11,2	32,1	483	0,08	1,57	325	91,1	0,206	0,018	0,217
282	3,76	567	0,25	11,4	11,3	33,5	491	0,12	1,61	315	92,2	0,175	0,017	0,210

275	1,50	569	0,20	11,4	11,1	31,8	492	0,09	1,55	304	90,8	0,198	0,018	0,219
268	3,89	576	0,20	11,5	10,7	31,4	492	0,10	1,57	302	91,6	0,231	0,018	0,211
261	1,74	579	0,20	11,4	11,3	31,0	494	0,09	1,58	298	91,7	0,156	0,019	0,206
254	1,51	606	0,20	11,4	11,2	29,1	496	0,08	1,43	297	92,9	0,155	0,021	0,212
246	1,75	570	0,20	11,2	11,3	28,8	496	0,09	1,56	274	91,2	0,144	0,020	0,209
239	1,58	590	0,20	11,3	10,8	28,3	487	0,08	1,35	266	91,9	0,154	0,020	0,212
231	1,51	598	0,20	11,4	11,1	29,3	493	0,09	1,41	255	92,2	0,152	0,020	0,205
225	4,17	611	0,31	11,1	11,2	28,1	494	0,11	1,35	266	93,5	0,200	0,019	0,217
216	0,76	622	0,20	11,2	11,4	27,8	490	0,09	1,62	235	91,5	0,174	0,018	0,210
210	0,85	594	0,19	11,4	11,1	26,0	489	0,09	1,38	227	92,7	0,160	0,018	0,207
202	4,38	613	0,18	11,1	11,5	26,5	500	0,12	1,66	224	91,5	0,265	0,017	0,271
193	1,77	614	0,13	11,5	11,7	29,8	498	0,08	1,62	220	91,9	0,175	0,017	0,211
27GC – Rona mound														
38	1,85	482	0,17	11,2	10,8	25,9	494	0,10	1,41	247	87,0	0,157	0,012	0,281
32	1,06	511	0,16	10,9	11,2	24,0	487	0,10	1,48	251	85,5	0,153	0,010	0,275
27	0,32	496	0,15	10,9	11,4	25,7	489	0,09	1,54	261	87,5	0,143	0,009	0,280
21	0,42	536	0,17	11,0	11,3	26,6	485	0,10	1,50	253	86,2	0,123	0,009	0,270
17	20,06	563	0,18	11,0	11,6	29,3	488	0,09	1,57	235	88,1	0,151	0,009	0,292
12	0,71	521	0,18	10,9	11,3	25,6	491	0,10	1,52	201	87,5	0,161	0,009	0,311
7	0,45	522	0,17	10,8	11,1	26,0	487	0,09	1,50	165	88,3	0,139	0,009	0,318
2	0,58	519	0,15	11,2	11,2	26,4	487	0,13	1,53	107	88,4	0,152	0,011	0,316
2	0,43	521	0,15	10,9	11,3	26,4	496	0,13	1,53	106	88,3	0,148	0,011	0,321
28GC – Mir zone														
188	0,64	376	0,08	13,1	10,4	24,5	500	0,13	1,18	124	95,3	0,218	0,018	0,207
178	0,61	400	0,07	12,8	10,7	24,8	495	0,09	1,21	99	93,9	0,150	0,014	0,211
168	0,83	424	0,07	12,9	10,5	24,7	496	0,10	1,24	77	96,2	0,160	0,014	0,209
158	0,71	418	0,07	12,8	10,6	25,8	498	0,11	1,30	62	94,8	0,160	0,014	0,219
142	0,69	418	0,07	12,6	10,6	26,3	495	0,10	1,29	57	93,9	0,154	0,014	0,212
135	1,22	441	0,09	12,4	10,8	27,2	495	0,10	1,30	62	93,9	0,165	0,014	0,210

125	0,64	458	0,06	12,3	10,8	27,6	498	0,13	1,33	60	94,0	0,149	0,014	0,212
115	0,68	463	0,08	12,1	10,6	24,8	502	0,11	1,28	60	92,7	0,249	0,015	0,214
105	1,10	458	0,08	11,9	10,7	27,7	503	0,11	1,29	64	89,9	0,211	0,014	0,216
97	0,58	373	0,04	11,7	10,2	24,5	498	0,10	1,15	51	86,4	0,150	0,015	0,215
91	0,68	374	0,04	11,8	10,2	24,5	495	0,09	1,15	51	86,7	0,153	0,015	0,219
80	0,67	385	0,05	11,7	10,3	25,1	503	0,12	1,18	51	86,5	0,191	0,015	0,210
70	1,33	387	0,04	11,4	10,3	25,1	502	0,10	1,19	54	82,3	0,250	0,012	0,215
60	0,58	393	0,04	11,4	10,2	24,5	498	0,08	1,20	51	83,7	0,178	0,012	0,206
50	0,81	394	0,05	11,4	10,4	24,8	508	0,10	1,22	46	82,6	0,159	0,011	0,219
50	0,68	395	0,05	11,2	10,3	24,4	498	0,11	1,22	43	83,1	0,218	0,011	0,218
40,5	1,23	408	0,05	11,3	10,3	24,8	499	0,10	1,26	45	84,1	0,139	0,011	0,223
37	0,69	417	0,04	11,1	10,5	27,6	496	0,09	1,30	45	81,4	0,150	0,011	0,217
31,5	0,71	418	0,05	11,3	10,0	27,3	501	0,14	1,28	43	84,1	0,191	0,011	0,221
27	0,61	421	0,05	11,2	10,4	26,0	498	0,11	1,30	44	84,0	0,150	0,011	0,231
21,5	0,86	424	0,05	11,3	10,1	25,5	501	0,09	1,29	43	84,3	0,133	0,011	0,227
17	0,45	426	0,05	10,8	10,6	26,8	497	0,09	1,31	44	81,7	0,191	0,010	0,225
12	0,40	428	0,05	10,5	10,6	26,6	494	0,08	1,32	45	80,5	0,115	0,010	0,232
6,5	0,52	425	0,05	10,5	10,5	26,6	498	0,09	1,32	45	80,5	0,184	0,010	0,239
31RD – Southern mound														
239	0,78	413	0,10	11,3	10,7	26,2	505	0,16	1,26	127	85,2	0,136	0,014	0,209
229	1,07	429	0,10	11,2	10,7	28,2	499	0,16	1,27	128	84,7	0,154	0,014	0,205
155	0,72	458	0,16	11,0	10,5	27,4	490	0,08	1,26	97	86,0	0,126	0,013	0,207
155	1,48	458	0,16	11,2	10,5	27,3	490	0,08	1,26	97	86,0	0,202	0,013	0,207
145	1,02	450	0,13	11,3	10,4	24,6	496	0,08	1,24	94	85,7	0,122	0,013	0,206
135	1,17	449	0,13	11,3	10,6	24,9	496	0,08	1,26	87	87,0	0,121	0,014	0,210
125	3,06	447	0,13	11,3	10,7	24,7	495	0,08	1,26	86	86,8	0,215	0,014	0,206
115	1,98	441	0,12	11,2	10,6	24,4	494	0,09	1,26	84	86,1	0,142	0,019	0,208
105	1,37	445	0,12	11,2	10,5	24,2	490	0,11	1,25	83	86,9	0,119	0,018	0,216
92	3,22	458	0,13	11,2	10,7	24,5	493	0,13	1,29	93	87,7	0,311	0,018	0,224

81	1,22	456	0,11	11,4	10,5	23,8	490	0,08	1,26	88	88,9	0,118	0,019	0,207
71	1,43	447	0,07	11,3	10,5	23,9	495	0,10	1,27	85	87,6	0,124	0,020	0,211
61	1,49	448	0,03	11,2	11,1	26,6	509	0,10	1,33	83	85,2	0,165	0,017	0,225
52	1,77	456	0,03	11,0	10,7	25,5	492	0,10	1,30	78	83,2	0,163	0,016	0,221
42	3,40	467	0,02	11,0	10,8	26,5	490	0,09	1,33	83	83,0	0,126	0,016	0,205
32	1,53	462	0,03	11,3	11,0	29,7	492	0,11	1,34	90	82,0	0,165	0,020	0,218
32	1,63	458	0,02	11,3	11,1	30,0	488	0,12	1,35	90	81,2	0,150	0,020	0,219
22	1,30	450	0,04	11,2	10,7	28,2	489	0,10	1,31	78	84,7	0,159	0,016	0,213
38GC – Depositional channel														
90	2,16	627	0,33	12.4	11,7	27,3	497	0,10	1,46	222	100,9	0,163	0,023	0,217
85	2,46	606	0,35	12.2	11,6	27,3	485	0,16	1,44	223	99,5	0,168	0,024	0,219
80	1,04	630	0,29	12.2	11,6	27,4	492	0,10	1,49	217	100,1	0,155	0,022	0,204
80	1,21	632	0,28	12.3	11,8	27,1	492	0,09	1,48	220	100,5	0,143	0,022	0,202
75	1,08	616	0,28	12.1	11,5	27,3	487	0,10	1,47	213	99,0	0,124	0,021	0,208
70	1,77	686	0,27	12.2	11,8	25,5	491	0,09	1,47	224	101,6	0,146	0,022	0,200
65	2,02	655	0,27	12.3	11,7	25,5	489	0,10	1,46	222	100,5	0,162	0,021	0,208
60	1,92	632	0,26	12.3	11,8	27,1	491	0,12	1,50	212	99,4	0,181	0,023	0,212
55	1,30	682	0,23	12.1	11,7	26,5	489	0,10	1,49	191	99,0	0,164	0,021	0,206
50	1,29	675	0,22	11.9	11,6	25,2	488	0,09	1,48	184	98,5	0,142	0,020	0,206
44	1,16	678	0,22	11.8	11,8	25,3	493	0,09	1,48	170	96,4	0,157	0,019	0,209
39	1,11	671	0,21	11.9	11,8	26,0	487	0,09	1,51	161	96,6	0,132	0,019	0,202
34	1,08	627	0,20	11.7	11,7	25,4	498	0,09	1,53	151	95,0	0,139	0,015	0,211
29	0,85	616	0,20	11.7	11,8	25,0	504	0,09	1,57	142	96,0	0,114	0,015	0,217
24	1,55	549	0,18	11.3	11,4	26,4	492	0,09	1,52	122	91,8	0,162	0,013	0,220
19	1,22	537	0,25	11.3	11,5	27,8	499	0,10	1,52	112	91,8	0,143	0,014	0,226
14	1,13	619	0,16	11.1	11,3	25,1	490	0,10	1,47	104	93,1	0,200	0,012	0,221
9	1,45	625	0,15	11.1	11,6	26,6	487	0,09	1,52	95	92,7	0,151	0,012	0,223
4	0,83	591	0,13	10.8	11,4	26,8	491	0,09	1,56	81	91,3	0,131	0,011	0,236
39GC – Mir zone delta														

30	23,88	455	0,14	10.9	11,0	22,0	485	0,21	1,37	956	83,6	0,258	0,000	0,183
25	10,79	471	0,15	11.0	11,4	23,1	489	0,21	1,40	940	84,6	0,232	0,000	0,174
20	1,09	484	0,16	11.2	11,2	23,1	492	0,17	1,41	836	85,7	0,251	0,000	0,162
15	2,29	480	0,17	11.4	11,4	23,3	491	0,17	1,38	711	87,5	0,338	0,002	0,155
10	1,99	500	0,17	11.1	11,7	23,4	488	0,17	1,44	651	86,8	0,297	0,002	0,164
5	1,70	530	0,18	12.2	11,5	23,7	491	0,12	1,44	445	90,1	0,248	0,006	0,155
49GC – Depositional channel														
225	1,75	579	0,30	11,6	10,9	24,1	486	0,10	1,35	280	90,9	0,192	0,025	0,194
209	2,09	575	0,31	11,7	11,2	25,0	485	0,09	1,42	286	92,0	0,142	0,024	0,190
187	2,06	547	0,30	11,6	10,9	25,2	480	0,12	1,37	280	89,6	0,155	0,023	0,192
177	1,40	576	0,28	11,5	11,0	25,1	486	0,09	1,36	298	90,9	0,150	0,023	0,200
167	1,28	584	0,28	11,4	10,9	25,4	479	0,08	1,38	306	90,5	0,165	0,022	0,190
157	0,84	568	0,27	12,4	11,2	24,9	493	0,09	1,33	289	94,4	0,155	0,021	0,201
147	0,98	551	0,27	12,2	11,3	25,0	493	0,09	1,36	286	93,9	0,167	0,022	0,203
134	0,60	503	0,25	11,4	10,4	23,3	471	0,09	1,23	270	83,6	0,106	0,021	0,193
127	1,58	562	0,27	12,2	11,2	24,1	502	0,11	1,36	281	95,1	0,136	0,023	0,202
117	1,31	574	0,28	12,3	11,6	24,6	499	0,09	1,46	324	96,7	0,210	0,020	0,196
107	1,34	594	0,29	12,3	11,7	24,8	509	0,08	1,48	340	96,7	0,151	0,019	0,192
97	1,10	483	0,26	12,1	10,8	23,8	502	0,10	1,27	292	92,1	0,173	0,020	0,185
97	1,19	485	0,25	12,1	10,9	24,0	506	0,10	1,26	294	92,9	0,735	0,020	0,195
87	1,86	361	0,27	12,1	11,3	23,3	506	0,16	1,32	205	90,4	0,137	0,027	0,200
82	2,85	450	0,23	11,9	10,6	23,8	509	0,20	1,22	274	91,4	0,205	0,022	0,197
77	1,30	465	0,22	12,0	10,6	23,9	503	0,10	1,21	283	90,7	0,144	0,021	0,204
72	0,85	472	0,21	11,9	10,8	24,2	503	0,09	1,23	283	90,7	0,134	0,020	0,201
67	1,71	474	0,21	12,1	10,8	24,5	500	0,09	1,24	278	89,6	0,166	0,018	0,200
62	1,29	472	0,20	11,7	10,7	24,4	516	0,10	1,25	266	89,6	0,137	0,018	0,188
57	1,83	471	0,18	11,8	10,8	24,4	507	0,09	1,24	249	88,5	0,173	0,016	0,207
52	0,94	472	0,18	11,3	10,8	25,2	517	0,08	1,26	226	88,4	0,192	0,014	0,211
47	0,68	475	0,16	11,3	10,6	24,4	505	0,09	1,22	196	84,7	0,146	0,014	0,202

35	1,34	468	0,16	11,4	10,8	25,0	498	0,09	1,24	159	85,4	0,154	0,014	0,203
30	129,30	482	0,18	11,2	11,1	26,1	508	0,10	1,29	149	87,2	0,156	0,013	0,213
25	0,74	468	0,16	10,8	10,7	24,3	498	0,09	1,25	130	85,5	0,122	0,011	0,197
20	0,62	466	0,14	11,0	10,6	24,4	484	0,08	1,28	118	83,5	0,179	0,011	0,211
20	1,98	471	0,14	11,1	10,7	24,3	484	0,08	1,26	123	84,4	0,137	0,011	0,203
15	1,04	466	0,13	10,8	10,8	24,8	491	0,09	1,27	113	84,3	0,175	0,011	0,208
10	4,21	461	0,17	11,6	11,0	25,8	502	0,16	1,29	98	86,3	0,308	0,011	0,226
5	2,20	448	0,15	11,7	10,9	25,1	492	0,12	1,27	81	83,8	0,194	0,013	0,222

C.3 Compilation of published geochemical data of TAGHF surface massive sulphides

The data are used to calculate the average Cu, Zn, Co and Fe concentrations relating to the FIGURE 5.6 and SECTION 5.6.2.1 in the main text. The respecting reference is indicated and GSC refers to Geological Survey of Canada (unpublished data, although provided here).

Alvin zone massive sulphides (Rona mound)					
Sample	**Co (ppm)**	**Cu (%)**	**Zn (ppm)**	**Description**	**Source**
JC138- 45-5	218	0.523	1830	Surface	Aclab Blue Mining
JC138- 45-6	236	0.494	1240	Surface	Aclab Blue Mining
JC138- 45-7a	6.7	0.622	2600	Surface	Aclab Blue Mining
JC138- 45-7b	45.4	10.9	1400	Surface	Aclab Blue Mining
JC138- 57-12	3	0.0182	2350	Surface	Aclab Blue Mining
JC138- 57-20	2	0.0279	84100	Surface	Aclab Blue Mining
JC138- 57-25	2	5.83	5170	Surface	Aclab Blue Mining
JC138- 57-26	132	1.28	480	Surface	Aclab Blue Mining
JC138- 65-2	74.4	2.06	490	Surface	Aclab Blue Mining
JC138- 65-4	135	0.475	1200	Surface	Aclab Blue Mining
JC138- 65-8	335	0.708	560	Surface	Aclab Blue Mining
JC138- 65-11	181	0.572	820	Surface	Aclab Blue Mining
JC138- 65-16	271	0.621	1210	Surface	Aclab Blue Mining
JC138- 65-17-(-18)	187	1.29	1920	Surface	Aclab Blue Mining
JC138- 65-21	239	3.2	1690	Surface	Aclab Blue Mining
JC138- 65-23	348	0.233	2050	Surface	Aclab Blue Mining
JC138- 68-3(-4)	50.8	0.955	3850	Surface	Aclab Blue Mining
Average	145.08	1.75	6644.71		
Alvin zone massive sulphides (Southern mound)					
Sample	**Co (ppm)**	**Cu (ppm)**	**Zn (ppm)**	**Description**	**Source**
JC138- 41-1	977	825	190	Surface	Aclab Blue Mining
JC138- 41-2	560	1640	790	Surface	Aclab Blue Mining
JC138- 41-3	635	1740	490	Surface	Aclab Blue Mining
JC138- 41-4	1030	3810	100	Surface	Aclab Blue Mining
JC138- 41-5	1610	2360	120	Surface	Aclab Blue Mining
JC138- 41-6	710	17700	150	Surface	Aclab Blue Mining
JC138- 41-7	229	840	410	Surface	Aclab Blue Mining
JC138- 45-4x	3	119	1590	Surface	Aclab Blue Mining
JC138- 45-4y	12	92	2660	Surface	Aclab Blue Mining
JC138- 45-5	169	5230	1540	Surface	Aclab Blue Mining
JC138- 45-6	182	4940	1070	Surface	Aclab Blue Mining
JC138- 21- 1- W	1480	5230	90	Surface	Aclab Blue Mining
JC138- 21- 2- W	1160	29900	70	Surface	Aclab Blue Mining
JC138- 21- 3- W	1150	13000	140	Surface	Aclab Blue Mining
JC138- 23GC- cc- W	498	4200.00	350	Surface	Aclab Blue Mining

ALV2599-9	10	57000	1400	Surface	Petersen *et al*. 2001
ALV2599-10-7/1	23	5700	4600	Surface	Petersen *et al*. 2001
ALV2599-10-7/2	20	16500	1650	Surface	Petersen *et al*. 2001
ALV2599-11-2/1	22	1200	3100	Surface	Petersen *et al*. 2001
Average	552	9054	1079		

Mir zone massive sulphides					
Sample	**Co (ppm)**	**Cu (wt%)**	**Zn (wt%)**	**Description**	**Source**
ALV2188-3-1B	1100	9.10	0.03		GSC
ALV2188-6-1	5	0.007	0.02		GSC
ALV2195-1A	230	21.70	0.05		GSC
ALV2195-1B	440	20.10	0.04		GSC
MIR-3-76-3A	12	22.40	0.04		Rona *et al*., 1993; GSC
MIR-3-76-3B	15	20.80	0.10		Rona *et al*., 1993; GSC
MIR-3-76-3BF	12	16.00	0.05		Rona *et al*., 1993; GSC
MIR-3-76-5Aavg2	7	0.53	21.85	inactive chimney	Rona *et al*., 1993; GSC
MIR-3-76-5B	12	5.10	10.70	inactive chimney	Rona *et al*., 1993; GSC
MIR-3-76-6A	10	17.70	0.80	top of inactive chimney	Rona *et al*., 1993; GSC
MIR-3-76-6B	12	11.00	22.00	top of inactive chimney	Rona *et al*., 1993; GSC
MIR-3-76-8-1	11	20.70	3.60	top of inactive chimney	Rona *et al*., 1993; GSC
MIR-3-76-8-2	12	13.90	7.10	top of inactive chimney	Rona *et al*., 1993; GSC
MIR-3-76-8-3	9	8.50	7.60	top of inactive chimney	Rona *et al*., 1993; GSC
MIR-3-76-9A	10	15.50	0.35	talus	Rona *et al*., 1993; GSC
MIR-3-76-9B	14	17.80	0.19	talus	Rona *et al*., 1993; GSC
MIR-3-76-10	13	26.80	0.08	inactive chimney	Rona *et al*., 1993; GSC
sample 13	12	18.10	0.20		Krasnov *et al*., 1995
sample 19	5.0	15.20	0.79	chimneys and massive sulphides	Krasnov *et al*., 1995
sample 7	160	12.75	0.34	massive sulphides and ore breccia	Krasnov *et al*., 1995
sample 5	9	9.28	1.54	chimneys, massive sulphides and opal. silica	Krasnov *et al*., 1995
sample 4	20	11.75	1.53	sulphide breccia	Krasnov *et al*., 1995
sample 20-1	5.0	2.40	7.55		Krasnov *et al*., 1995
sample 20-2	5.0	4.75	3.22		Krasnov *et al*., 1995
sample 6	29	1.21	15.05	chimneys and massive sulphides	Krasnov *et al*., 1995
sample 3	10	0.81	1.90	massive quartz sulphide	Krasnov *et al*., 1995
1	34	35.33	0.40		Krasnov *et al*., 1995
2	2.5	0.43	5.32		Krasnov *et al*., 1995
3	350	3.10	0.05		Krasnov *et al*., 1995
4	740	4.74	0.32		Krasnov *et al*., 1995
Average	110	12.25	3.76		

Black smokers				
Sample	**Cu (wt%)**	**Fe (wt%)**	**Zn (wt%)**	**Source**
MIR sample - 3	3.10	12.20	0.05	Krasnov *et al*., 1995
MIR sample - 4	4.74	33.13	0.32	Krasnov *et al*., 1995
ALV2179-1-1B	23.00	31.60	0.40	Tivey *et al* 1995
ALV2179-2-2A	9.50	23.20	0.13	Tivey *et al* 1995
ALV2179-4-1-1	10.80	13.30	0.07	Tivey *et al* 1995
ALV2179-4-1-4	3.96	4.80	0.01	Tivey *et al* 1995
ALV2179-4-1A1	11.60	13.40	0.03	Tivey *et al* 1995
ALV2179-4-1T1	12.10	11.19	0.01	Tivey *et al* 1995
ALV2181-1-1A2	8.50	19.20	0.24	Tivey *et al* 1995
ALV2179-1-1A	2.50	44.20	0.93	Tivey *et al* 1995
ALV2189-5-2A	1.00	40.30	0.45	Tivey *et al* 1995
ALV2183-9-1A	17.60	30.00	0.39	Tivey *et al* 1995
ALV2190-7-1A	15.90	31.70	0.92	Tivey *et al* 1995
ALV2179-4	23.50	24.27	0.04	GSC
Average	10.56	24.64	0.20	
White smokers				
Sample	**Cu (wt%)**	**Fe (wt%)**	**Zn (wt%)**	**Source**
ALV2187-1-1A	0.6	4.2	54	Tivey *et al* 1995
ALV2187-1-4A	0.6	1.3	60.4	Tivey *et al* 1995
ALV2187-1-6A	0.5	1.6	61.5	Tivey *et al* 1995
ALV2190-14-1A	0.6	0.9	62.3	Tivey *et al* 1995
ALV2190-14-1B	0.4	2.9	53.6	Tivey *et al* 1995
ALV2183-4-1A	0.40	6.00	58.40	Tivey *et al* 1995
ALV2183-4-1B	0.50	7.30	50.60	Tivey *et al* 1995
ALV2183-4-1C	0.40	5.40	52.70	Tivey *et al* 1995
ALV2190-11-1A	0.60	4.20	59.90	Tivey *et al* 1995
ALV2190-11-1B	0.70	15.00	38.10	Tivey *et al* 1995
ALV2190-13-1A	0.40	23.00	17.60	Tivey *et al* 1995
ALV2183-6-2A	1.70	36.10	6.23	Tivey *et al* 1995
ALV2190-14-1C	0.46	0.87	57.90	GSC
ALV2190-14-1D	0.70	0.83	54.50	GSC
ALV2190-14-1E	0.34	1.21	57.10	GSC
ALV2190-14-1F	0.63	1.27	57.70	GSC
ALV2584-9	0.11	32.31	8.40	Petersen *et al*. 2001
MIR sample - 2	0.43	33.85	5.32	Krasnov *et al*., 1995
Average	0.56	9.90	45.35	

C.3.1 Composition calculations (digital)

The resolution of the three equations used to calculate Fe, Cu and Zn wt% in the sediments from 49GC, 38GC and 39GC is available in the electronic annexes (DIGITAL MATERIAL 10).

C.4 Dataset summary accompanying FIGURE 5.11 and FIGURE 7.2

Location[1]	*Sed. Thickness* (cm)[2]	*Facies (Hydrothermal influence vs. sediment background)*										*Cu (%)*					*Au (ppb)*					n[5]	Core Ref	Latitude	Longitude
			Ca (%)					*Fe (%)*																Deg°DD.MMM'	
		(% of length hydrothermal)[3]	Mean	SD[4]	Min.	Max.	Median	Mean	SD[4]	Min.	Max.	Median	Mean	SD[4]	Min.	Max.	Median	Mean	SD[4]	Min.	Max.	Median				
North Shimmering Mound	80	0				28.0					3.6					0.1					17		1	M127/690GC	26°10.774'	44°49.041'
West Shimmering Mound	290	22	15.9	11.2	1.9	30.0	19.4	13.9	10.8	2.4	30.7	10.3	1.0	1.3	0.0	3.5	0.3			<2	637		10	M127/681GC	26°10.444'	44°49.076'
East Shimmering Mound	113	0	15.9	12.0	4.1	31.1	14.2	4.9	1.8	2.4	6.7	5.2	0.0	0.0	0.0	0.1	0.0			<2			4	M127/576GC	26°10.422'	44°48.318'
Shimmering Mound	120	48	10.9	12.7	0.4	30.2	3.3	11.2	8.3	3.6	27.8	8.8	0.2	0.2	0.0	0.7	0.1			<2	347		6	M127/626GC	26°10.401'	44°48.747'
Shimmering Mound	132	81	N.A.					N.A.					N.A.					N.A.					N.A.	JC138/29GC	26°10.339’	44°48.888’
Shimmering Mound	190	42	N.A.					N.A.					N.A.					N.A.					N.A.	JC138/52GC	26°10.283’	44°48.806’
East Shimmering Mound	275	39	12.1	12.1	0.3	31.8	4.7	18.4	12.7	2.6	32.3	24.8	1.4	2.9	0.0	9.2	0.3			<2	2120		14	M127/682GC	26°10.243'	44°48.706'
Shinkai Mound	130	100				8.1				26.0	34.8				0.4	2.1		N.A.					2	JC138/51GC	26°09.477’	44°49.306’
East Rona Mound	130	0	22.7	3.6	19.9	29.7	21.3	4.6	1.2	2.7	6.4	4.5	0.1	0.0	0.1	0.1	0.1			<2	86		5	M127/616GC	26°09.391'	44°48.464'
Rona Mound	41	68	8.8	12.9	0.2	26.4	0.7	21.6	13.2	6.8	36.4	22.4			0.0	1.42		N.A.					6	JC138/27GC	26°09.375’	44°48.820’
Rona Mound	278	100	N.A.					N.A.					N.A.					N.A.					N.A.	JC138/57RD	26°09.365’	44°48.786’
East Rona Mound	64	0	29.0	5.1	23.9	34.1	29.0	4.5	2.6	1.9	7.1	4.5	0.1	0.1	0.0	0.2	0.1	32	25	7	57	32	2	M127/617GC	26°09.253'	44°48.519'
North-West Southern Mound	92	100	1.6	2.2	0.0	4.8	0.1	36.8	2.2	34.5	39.7	36.3	7.1	1.1	5.7	8.5	7.0	725	46	661	768	745	3	M127/702GC	26°09.436'	44°49.063'
Southern Mound	278	100	N.A.					N.A.					N.A.					N.A.					N.A.	JC138/50RD	26°09.342’	44°48.951’
Southern Mound	300	100	0.2	0.1	0.1	0.5	0.1	44.5	4.3	37.8	51.7	44.5	0.0	0.0	0.0	0.0	0.0	N.A.					8	JC138/22RD	26°09.339’	44°48.946’
Southern Mound	245	100	0.4	0.3	0.1	1.2	0.3	33.8	12.2	11.1	52.7	32.2	0.0	0.0	0.0	0.1	0.0	N.A.					10	JC138/31RD	26°09.337’	44°48.941’
Southern Mound	133	100	0.3	0.2	0.1	0.7	0.2	36.8	8.3	20.3	45.7	39.0	0.1	0.2	0.0	0.5	0.0	N.A.					7	JC138/16GC	26°09.338’	44°48.974’
Central area	188	90	N.A.					N.A.					N.A.					N.A.					N.A.	JC138/62GC	26°09.247’	44°48.947’
Central area	230	87	5.0	8.6	0.2	29.4	0.4	28.0	8.9	4.8	38.4	30.7	2.3	2.4	0.1	10.2	1.8	370	330	10	1500	390	38	JC138/49GC	26°09.237’	44°48.902’
Central area	300	93	13.4	10.9	0.2	31.1	11.9	21.1	11.3	3.5	34.8	20.8	2.1	2.5	0.1	7.5	1.4	605	556	58	1580	314	6	M127/647GC	26°09.146’	44°48.858’
Central area	307	87	3.9	8.1	0.1	30.0	0.4	30.7	9.1	2.9	39.2	33.8	5.1	4.3	0.1	17.2	4.2	1121	546	78	1970	1210	31	M127/627GC	26°09.139'	44°48.860'
Central area	90	39	14.1	11.2	0.2	33.2	18.8	19.7	11.0	2.4	36.7	13.8	2.2	2.1	0.1	7.2	1.0	200	270.0	<2	1000	270	18	JC138/38GC	26°09.126’	44°48.814’

Central area	267	73	8.7	11.0	0.3	31.9	1.7	23.4	11.6	3.5	36.5	27.4	1.1	1.7	0.1	5.9	0.4			<2	701		10	M127/644GC	26°09.006'	44°48.695'
Central area	300	41	16.6	16.3	0.3	33.5	16.4	20.1	18.1	1.7	40.9	19.1	0.1	0.1	0.0	0.3	0.0	63	80	11	237	26	6	M127/703GC	26°08.984'	44°48.576'
West	107	0	30.3	2.0	28.4	33.1	29.4	2.4	0.4	1.9	2.8	2.5	0.0	0.0	0.0	0.0	0.0	16	4	11	20	16	3	M127/636GC	26°09.088'	44°49.540'
North-West Mir Zone	128	12	25.3	10.9	6.7	33.4	30.6	7.6	9.7	1.4	24.4	2.3	0.9	1.4	0.0	3.4	0.1	270	396	31	955	46	4	M127/645GC	26°08.713'	44°48.725'
Mir Zone delta	39	100	0.3	0.2	0.1	0.7	0.2	31.2	2.3	28.2	34.5	30.5	14.2	8.0	2.0	28.1	16.2	780	450	550	1800	600	7	JC138/39GC	26°08.619’	44°48.550’
Mir Zone	73	100	N.A.					N.A.					N.A.					N.A.					N.A.	JC138/76RD	26°08.611’	44°48.392’
Mir Zone	63	100	N.A.					N.A.					N.A.					N.A.					N.A.	JC138/73RD	26°08.602’	44°48.393’
Mir Zone	80	75	6.7	12.3	0.2	31.2	0.8	29.1	13.5	3.8	44.3	33.2	0.2	0.1	0.1	0.3	0.1			<2	96		5	M127/692GC	26°08.559'	44°48.397'
Mir Zone	194	92	3.2	7.2	0.2	23.6	0.5	35.8	13.4	11.3	53.3	34.4				8.4							11	JC138/28GC	26°08.558’	44°48.416’
West Mir Zone	180	11	24.9	5.9	16.4	34.2	23.6	4.0	2.1	1.5	7.5	3.5	0.1	0.2	0.0	0.4	0.0			<2	175		5	M127/649GC	26°08.534'	44°48.245'
Far West	70	100	0.6	0.2	0.3	0.9	0.6	17.1	1.8	15.2	19.5	16.7	0.0	0.0	0.0	0.0	0.0			<2	<2		3	M127/693GC	26°08.466'	44°49.917'
Far East	37	0				31.3					1.3					0.0					5		1	M127/666GC	26°08.593'	44°46.920'
Far East	65	0				33.0					1.3					0.0					< 2		1	M127/691GC	26°08.417'	44°47.184'
South-West TAG Mound	20	0				33.1					1.9					0.0					20		1	M127/638GC	26°08.015'	44°50.158'
South	110	0	27.7	1.3	26.1	29.2	27.8	2.3	0.1	2.2	2.4	2.4	0.0	0.0	0.0	0.0	0.0			<2	21		3	M127/615GC	26°07.863'	44°48.180'
Reference core Far East	300	0	36.0	0.2	35.8	36.1	36.0	0.3	0.1	0.2	0.4	0.3	0.0	0.0	0.0	0.0	0.0			<2	6		2	M127/711GC	26°05.485'	44°38.770'

N.A. = Not available (no sediment samples or no data); 1. The main location or the closest identified location; 2. The sediment thickness, always higher than the reported value; 3. Percentage of length influenced by hydrothermalism (expected high Fe values), calculated from stratigraphic log; 4. Standard deviation; 5. Number of samples analysed in each core; 6. Lat. and long. coordinates from Petersen and Scientific Party (2016) and Murton and Scientific Party (2018). These provided data are obtained for the Blue Mining EC program and are not previously published.

C.5 Drainage network and sediment flow accumulation

By their nature to be principally driven by gravity, sediment transport may be compared to a water drainage pattern on terrestrial topography. Watershed were therefore processed with ArcGIS (© ESRI). For this method, I first ran the hydrology tool 'Fill' on the bathymetry raster file (© GEOMAR), then applied 'flow direction' on the obtained new raster. Finally, I ran 'Flow accumulation' on the flow direction raster. The resulting map shows the intensity of flow accumulation over the Alvin zone and highlights depositional basins (FIGURE 5.12) (methodology provided by courtesy of Gavin Haughton).

Appendix D **Supplementary material to CHAPTER 6**

D.1 **Down-core solid phase profiles**

The ITRAX chemostratigraphy database is available in the electronic annexes (DIGITAL MATERIAL 9).

D.1.1 22RD core

ITRAX chemostratigraphy (solid lines) and sediment geochemistry (dots) profiles for Fe, Ca, Sr, K, Ti, Mn, Zn, Cu, Co and Ba.

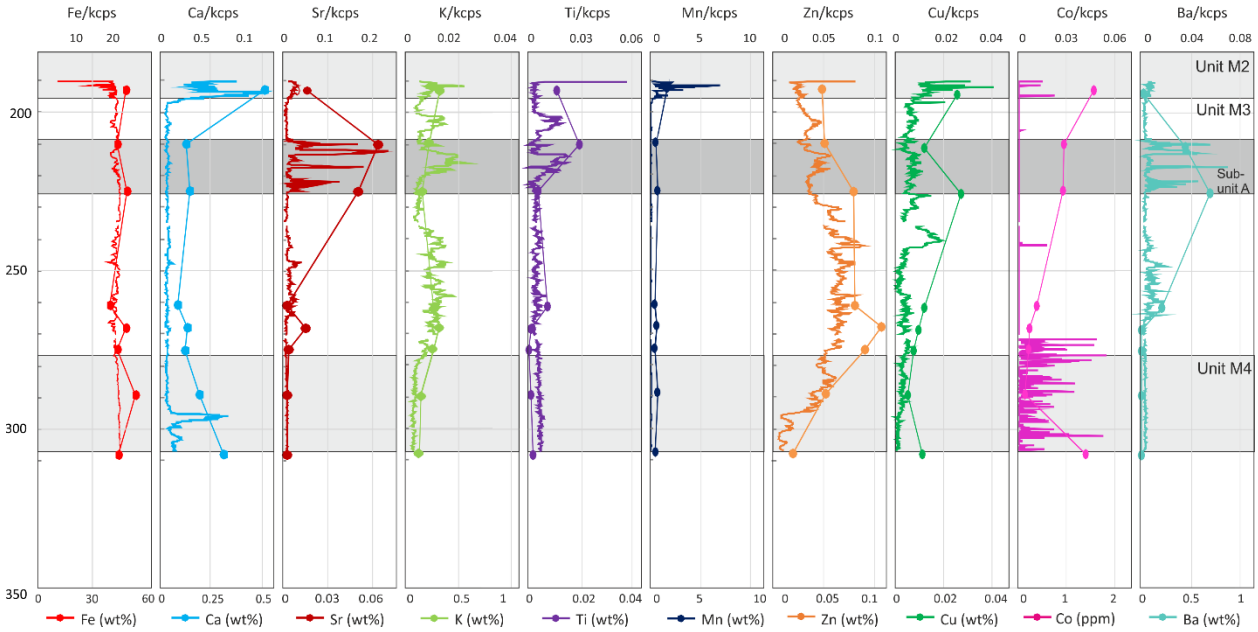

D.1.2 27GC core

ITRAX chemostratigraphy (solid lines) and sediment geochemistry (dots) profiles for Fe, Ca, Sr, K, Ti, Mn, Zn, Cu, Co and Ba.

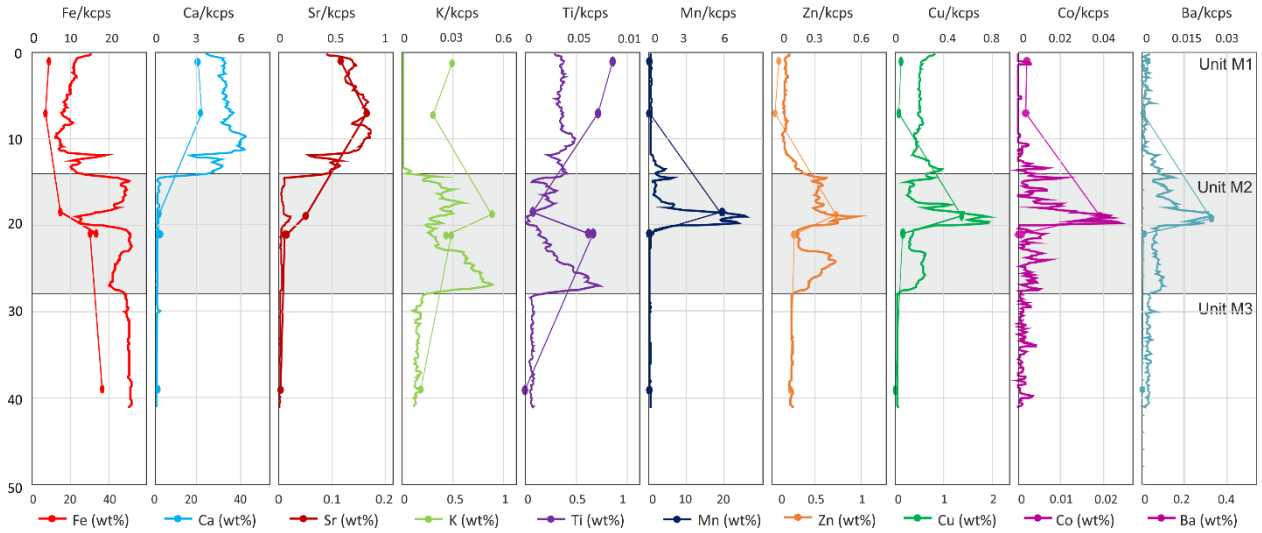

D.1.3 28GC cores

ITRAX chemostratigraphy (solid lines) and sediment geochemistry (dots) profiles for Fe, Ca, Sr, K, Ti, Mn, Zn, Cu, Co and Ba.

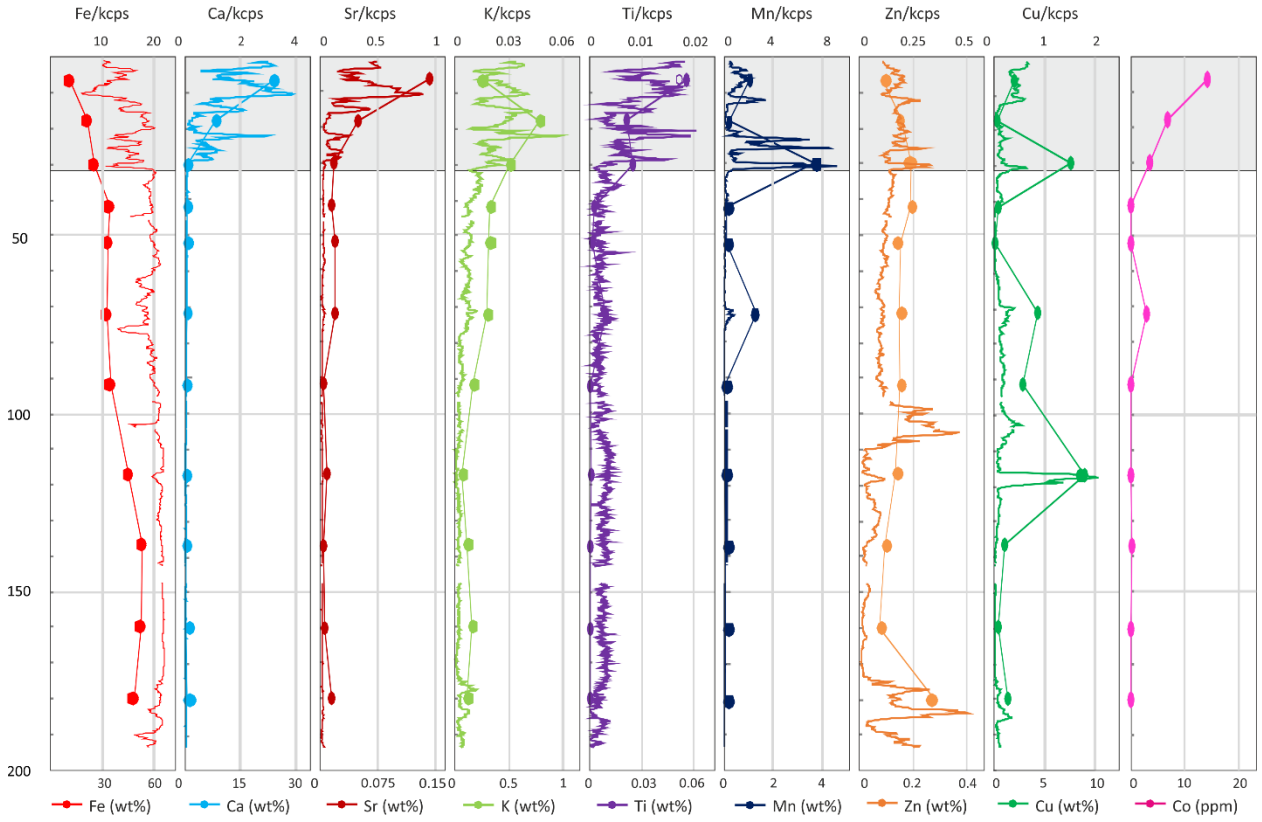

D.1.4 31RD core

ITRAX chemostratigraphy (solid lines) and sediment geochemistry (dots) profiles for Fe, Ca, Sr, K, Ti, Mn, Zn, Cu, Co and Ba.

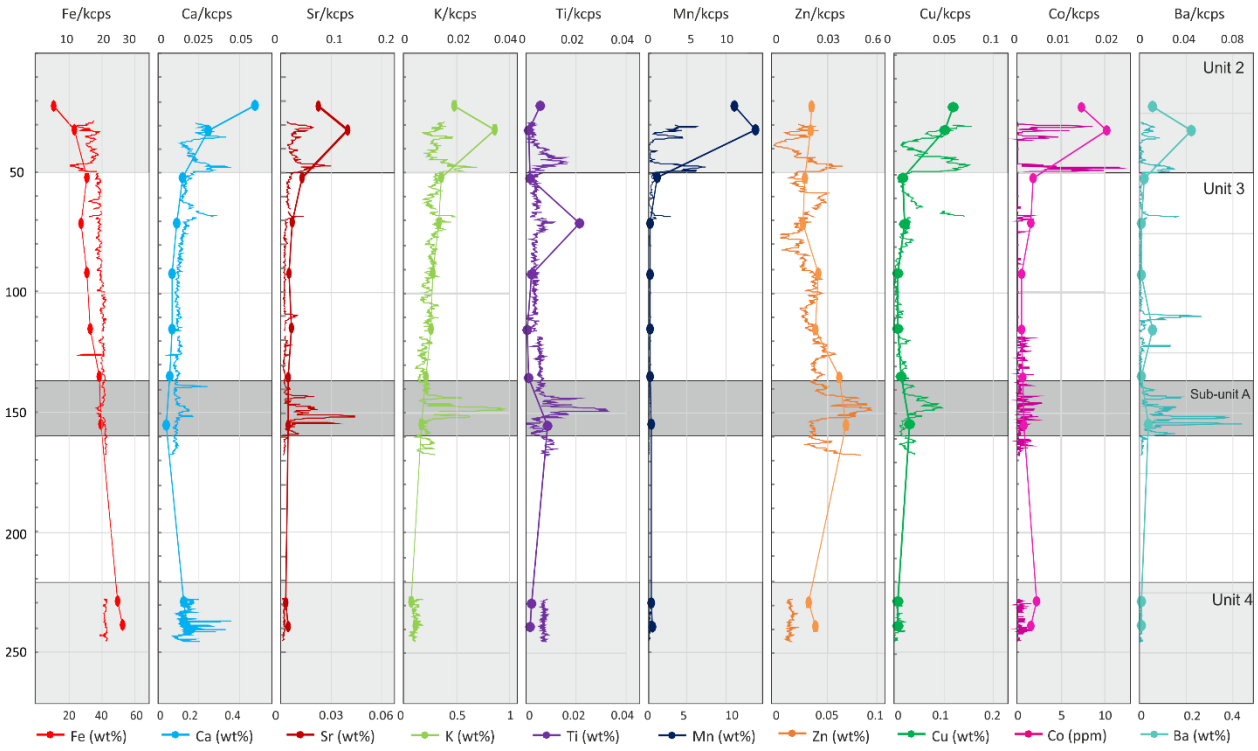

D.2 Gold concentration

The excel spreadsheet of the database is available in the electronic annexes (DIGITAL MATERIAL 10).

Coring station	Depth (cm)	Au (ppb)	Coring station	Depth (cm)	Au (ppb)
31RD	239	16	27GC	39	24
31RD	229	13	27GC	21	115
31RD	155	15	27GC	21	98
31RD	135	15	27GC	17	17
31RD	115	10	27GC	7	65
31RD	92	15	27GC	1	17
31RD	71	17	28GC	180	979
31RD	52	10	28GC	160	63
31RD	32	12	28GC	137	162
31RD	22	9	28GC	117	5482
16GC	120	15	28GC	92	404
16GC	100	8	28GC	72	41
16GC	81	7	28GC	52	141

16GC	64	11	28GC	42	136
16GC	50	23	28GC	30	13
16GC	25	13	28GC	18	74
16GC	15	26	28GC	6.5	84
22RD	308	22			
22RD	289	20			
22RD	275	17			
22RD	268	10			
22RD	261	16			
22RD	225	20			
22RD	210	12			
22RD	193	15			

D.3 FeOx sediments microscopy – M3

(A) FeOx clasts with a variable content of Si and Fe shown by the variable transparency (seemingly, ferrihydrite, goethite and quartz) in 31RD (126-130 cm) in transmitted light. (A)

(B) (Reflective light) and (C) (reflective light with crossed polarisation). Presence of rounded FeOx clasts with transparent mineral feeling spaces (seemingly silica) and thin filaments.

(D) Cluster of barite in rosette in the Ba-rich subunit in M3, 22RD.

(E) Fractured clasts of FeOx with a barite rosette in the top right corner.

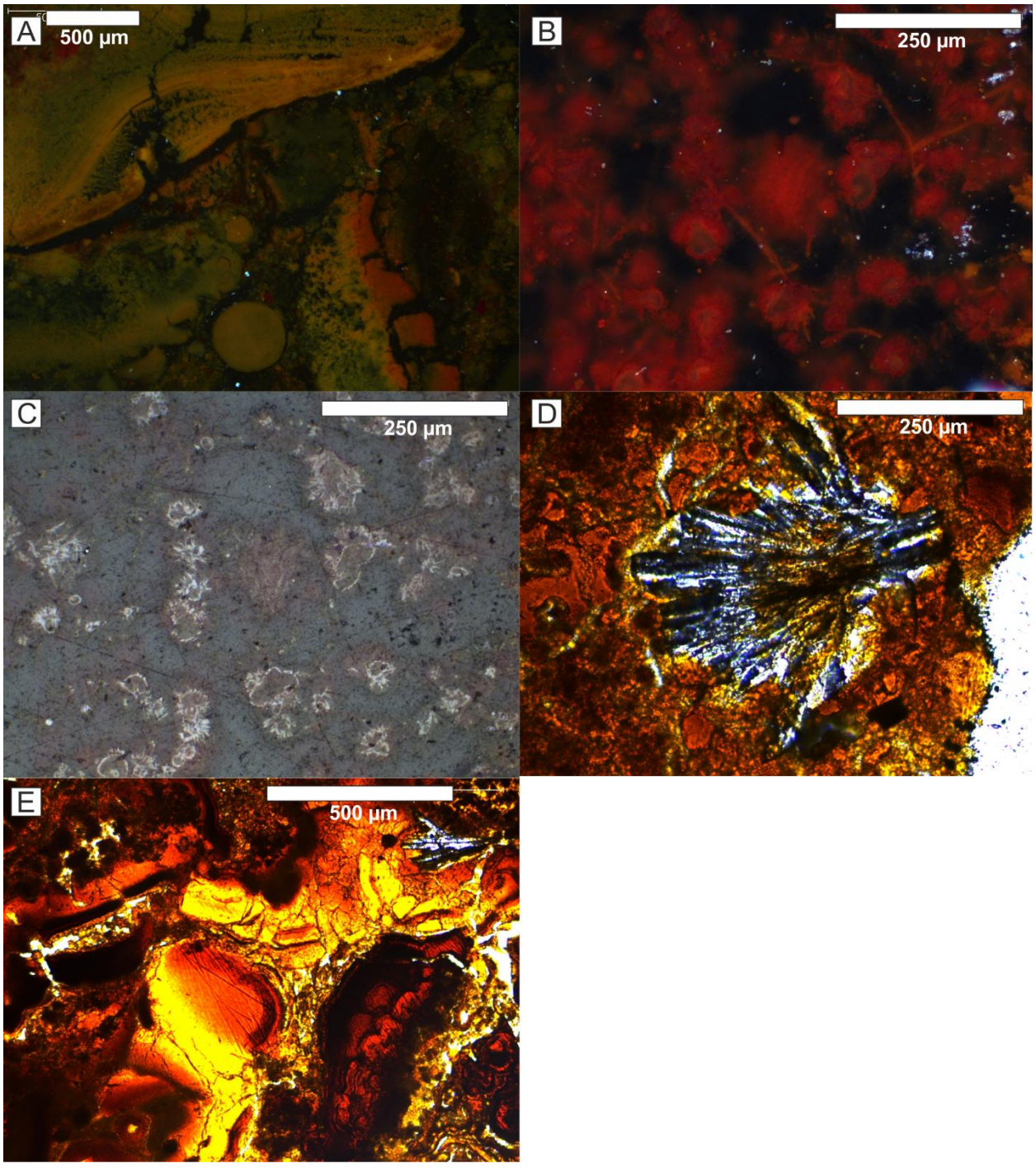

Images courtesy of Iain Stobbs.

D.4 FeOx sediments microscopy – M4

(A) Foraminifera in Unit M4, 167-168 cm. Reflective light.

(B) Hematite botryoidal growth. Reflective light.

(C) Additional backscattered microphotography (same depth as in FIGURE 6.8, showing a texture dominated by clay to silt size grains. Higher reflectivity indicates presence of higher crystallinity in hematite.

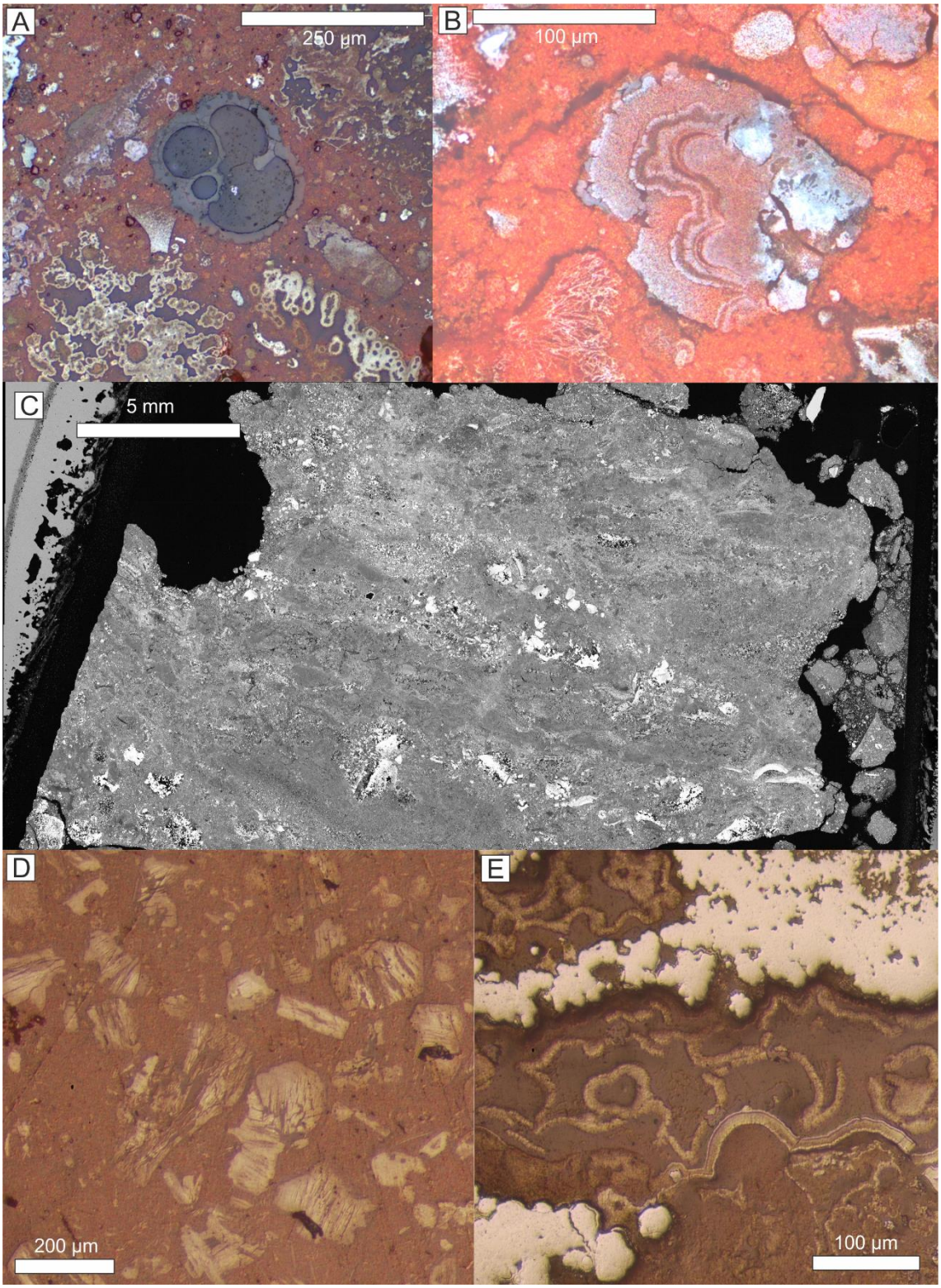

(D) Angular clasts up to 0.4 mm presenting numerous fractures within the grains. Sorting is absent and the matrix is fine grained. Reflective light microscopy of 22RD (Unit M4, 292-293 cm).

(E) Botryoidal texture of hematite, highly crystalline and partially crystalline. Note the absence of fractures. Reflective light microscopy of 22RD (Unit M4, 292-293 cm).

(A) and (B): images courtesy of Iain Stobbs.

D.6 Mineralogical XRD analyses

The analyses are re-calculated on a salt-free (halite) basis below, the minerals proportion are expressed in wt% and refers to FIGURE 6.6. The spectrum are available in the electronic annexes (DIGITAL MATERIAL 7).

Core	Depth (cm)	goethite	hematite	quartz	nontronite/todorokite	amorphous	diopside	magnesioferrite
22RD	193	36.0				64.0		
22RD	225	100.0						
22RD	261	57.9				42.1		
22RD	275	72.2			4.6	23.2		
22RD	289	35.1	64.9					
22RD	305		91.2	8.8				
28GC	75		23.9			76.1		
28GC	99	60.4	39.6					
28GC	127	27.7	22.2			50.2		
28GC	150	26.6	62.4				11.0	
28GC	190		89.4	10.6				
31RD	52				100.0			
31RD	105	51.1				48.9		
31RD	125	29.4	15.5			55.1		
31RD	155	69.7				30.3		
31RD	229		93.9	6.1				
16GC	40	12.8	10.8			76.4		
16GC	69	100.0						
16GC	131	71.0	20.8					8.2

Raw quantitative mineralogical XRD analyses on 22 samples. Diop = diopside, Goet = goethite, Hal = halite, Hem = hematite, Mgf = magnesioferrite, Qtz = quartz, S.D. = standard deviation.

Sample	Diop	1 S.D.	Goet	1 S.D.	Hal	1 S.D.	Hem	1 S.D.	Mgf	1 S.D.	Quartz	1 S.D.	Smectite /nontronite	1 S.D.	Amorphous oxides	1 S.D.	SUM
a-16gc-69			90.2	1.02	9.8	0.44											100
b-16gc-40			12.3	0.40	4.2	0.10	10.3	0.30							73.2	0.80	100
c-16gc-131			71.0	1.15			20.8	0.67	8.2	0.63							100
d-31rd-125			28.6	0.60	2.7	0.20	15.1	0.70							53.6	1.50	100
e-31rd-52					4.1	0.06							95.9				100
f-31rd-155			66.0	0.70	5.3	0.30									28.7	2.30	100
g-31rd-105			47.9	0.70	6.3	0.60									45.8	1.60	100
h-31rd-229							93.9	0.92			6.1	0.42					100
i-28gc-130							89.4	0.75			10.6	0.36					100
j-28gc-150	10.8	0.79	26.1	1.60	2.0	0.27	61.1	1.29									100
k-28gc-127			25.8	0.70	6.7	0.20	20.7	0.60							46.8	1.70	100
l-28gc-99			57.0	0.97	5.6	0.14	37.3	1.00									100
m-28gc-75					3.8	0.10	23.0	0.40							73.2	0.70	100
q-22rd-289			32.8	1.01	6.6	0.43	60.6										100
r-22rd-scrath							91.3				8.8	0.57					100
s-22rd-440			68.2	1.20	5.6	0.20							4.3	1.50	21.9	3.00	100
t-22rd-442a			55.3	0.60	4.5	0.30									40.2	1.70	100
u-22rd-446			94.4	0.71	5.7	0.20											100
v-22rd-193			34.3	0.4	4.7	0.2									61.0	1.0	100

D.7 **EDS-SEM mapping**

The three next tables below refer to FIGURE 6.7 (31RD, 126 cm). The standard deviation is expressed as 1 σ. [1] The atomic percentage is the number of atoms of that element, at that weight, divided by the total number of atoms in the sample, and multiplied by 100. The excel spreadsheet of the database is available in the electronic annexes (digital reference #8)

Element	Wt%	Wt% σ	Atomic % [1]	Oxide	Oxide %	Oxide % σ
Map A						
O	38.46		62.27			
Na	1.04	0.02	1.17	Na_2O	1.4	0.03
Mg	1.32	0.02	1.4	MgO	2.19	0.02
Al	0.19	0.01	0.19	Al_2O_3	0.37	0.02
Si	16.25	0.02	14.99	SiO_2	34.76	0.05
P	0.18	0.01	0.15	P_2O_5	0.4	0.02
S	0.08	0.01	0.06	SO_3	0.19	0.02
K	0.21	0.01	0.14	K_2O	0.26	0.01
Ca	0.12	0.01	0.07	CaO	0.16	0.01
Mn	0.03	0.01	0.02	MnO	0.04	0.02
Fe	42.13	0.04	19.54	Fe_2O_3	60.24	0.05
Map B						
O	32.83		60.89			
Na	0.26	0.05	0.33	Na_2O	0.34	0.07
Mg	0.48	0.03	0.58	MgO	0.79	0.05
Al	0.17	0.02	0.18	Al_2O_3	0.32	0.04
Si	5.17	0.03	5.46	SiO_2	11.06	0.07
P	0.14	0.02	0.14	P_2O_5	0.33	0.05
S	0.06	0.02	0.05	SO_3	0.14	0.04
K	0.08	0.02	0.06	K_2O	0.1	0.02
Ca	0.05	0.02	0.04	CaO	0.07	0.02
Fe	60.62	0.1	32.2	Fe_2O_3	86.67	0.15
Zn	0.14	0.05	0.06	ZnO	0.18	0.06

The following table refers to phase mapping (3 identified phases highlighted in a different colour: pink, dark purple and red) presented in right panel of the FIGURE 6.7.

Box B phase analysis			
Element	**Pink Weight %**	**Dark purple Weight %**	**Red Weight %**
Fe	57.9	25.1	61.9
O	33.8	44.1	32.7
Si	7.3	28.2	5.3

Mg	0.7	1.3	
K	0.1	0.4	0.1
Ca	0.1		
Zn	0.1		
Na		0.9	

The areas w, x and y are presented in the middle panel of the FIGURE 6.7.

w		
Element	**Weight %**	**σ**
Fe	61.8	0.3
O	32.5	0.3
Si	4.6	0.1
Mg	1.1	0.1
x		
O	42.5	0.3
Fe	29.8	0.3
Si	24.8	0.2
Mg	1.4	0.1
Na	1.1	0.1
K	0.4	0.1
O	42.5	0.3
y		
O	44.7	0.9
Si	29.6	0.7
z (rim)		
Fe	62.6	0.8
O	32.5	0.8
Si	4.9	0.4
z (nucleus)		
Fe	57.7	1.7
O	34.1	1.7
Si	8.2	0.9

The three next tables below refer to FIGURE 6.8 (22RD, 292 cm). [1] The atomic percentage is the number of atoms of that element, at that weight, divided by the total number of atoms in the sample, and multiplied by 100.

Element	**Wt%**	**Wt% σ**	**Atomic % [1]**	**Oxide**	**Oxide %**	**Oxide % σ**
Map A						
O	31.56		60.41			

Element	Wt%	Wt% σ	Atomic % [1]	Oxide	Oxide %	Oxide % σ
Na	0.23	0.02	0.3	Na2O	0.31	0.03
Mg	0.24	0.01	0.3	MgO	0.4	0.02
Al	0.18	0.01	0.21	Al_2O_3	0.35	0.02
Si	2.38	0.01	2.59	SiO_2	5.09	0.02
P	0.37	0.01	0.36	P_2O_5	0.84	0.02
S	0.06	0.01	0.05	SO_3	0.14	0.02
K	0.07	0.01	0.06	K_2O	0.09	0.01
Ca	0.54	0.01	0.41	CaO	0.75	0.01
Fe	64.35	0.04	35.29	Fe_2O_3	92	0.06
Cu	0.02	0.02	0.01	CuO	0.03	0.02
Total	100		100		100	
Map B						
O	31.46		60.41			
Na	0.18	0.02	0.25	Na_2O	0.25	0.02
Mg	0.16	0.01	0.21	MgO	0.27	0.02
Al	0.27	0.01	0.31	Al_2O_3	0.51	0.02
Si	2.35	0.01	2.57	SiO_2	5.03	0.02
P	0.21	0.01	0.21	P_2O_5	0.49	0.02
S	0.04	0.01	0.04	SO_3	0.11	0.02
K	0.07	0.01	0.06	K_2O	0.09	0.01
Ca	0.22	0.01	0.17	CaO	0.3	0.01
Mn	0.13	0.01	0.07	MnO	0.16	0.01
Fe	64.9	0.03	35.71	Fe_2O_3	92.79	0.05
Map C						
O	32.13		60.51			
Na	0.35	0.02	0.46	Na_2O	0.48	0.02
Mg	0.22	0.01	0.28	MgO	0.37	0.02
Al	0.14	0.01	0.16	Al_2O_3	0.27	0.02
Si	2.28	0.01	2.45	SiO_2	4.88	0.02
P	1.34	0.01	1.3	P_2O_5	3.06	0.02
S	0.19	0.01	0.18	SO_3	0.48	0.02
K	0.08	0.01	0.06	K_2O	0.1	0.01
Ca	2.16	0.01	1.62	CaO	3.02	0.01
Mn	0.15	0.01	0.08	MnO	0.2	0.01
Fe	60.95	0.04	32.89	Fe_2O_3	87.14	0.05

The following table refers to phase mapping (3 identified phases highlighted in a different colour, pink, purple and green) presented in right panel of the FIGURE 6.8.

Phase analysis			
Box B			
Elements	**Pink Weight %**	**Purple Weight %**	**Green Weight %**
Fe	65.3	66.2	1.6
O	31.5	31.2	40.4
Si	2.6	2.1	
Al	0.3	0.2	
P	0.2	0.1	16.1
Ca	0.1	0.1	38.2
S			2.1
Na			1.6
Box C			
Elements	**Pink Weight %**	**Purple Weight %**	**Green Weight %**
Fe	65.6	66.5	14.7
O	31.5	31.2	38.2
Si	2.6	2.1	0.5
P	0.2	0.1	12.8
Ca	0.1		28.1
K		0.1	
F			2.1
Al			0.1
Na			1.6

The areas w, x, y and z are presented in the middle panel of the FIGURE 6.8.

	Wt%	**Wt% σ**	**Atomic % [1]**	**Oxide**	**Oxide %**	**Oxide % σ**
w						
O	31.46		60.62			
Si	2.83	0.54	3.11	SiO2	6.06	1.15
Fe	65.71	1.31	36.27	Fe2O3	93.94	1.87
x						
O	31.06		60.45			
Si	2.02	0.29	2.24	SiO2	4.32	0.63
Fe	66.92	0.9	37.31	Fe2O3	95.68	1.28
y						
Fe	66.6	1				
O	31.2	1				
Si	2.2	0.3				
z						
O	40.87		61.37			
P	15.11	1.53	11.72	P2O5	34.61	3.51
S	3.45	0.82	2.58	SO3	8.61	2.05
Ca	40.58	1.98	24.32	CaO	56.77	2.78

Bibliography

Alt J. C. (1988) Hydrothermal oxide and nontronite deposits on seamounts in the eastern Pacific. *Mar. Geol.* **81**, 227–239.

Alt J. C. and Jiang W.-T. (1991) Hydrothermally precipitated mixed-layer illite-smectite in recent massive sulphide deposits from sea floor. *Geology* **19**, 570–573.

Andreu E., Torró L., Proenza J. A., Domenech C., García-Casco A., Villanova de Benavent C., Chavez C., Espaillat J. and Lewis J. F. (2015) Weathering profile of the Cerro de Maimón VMS deposit (Dominican Republic): Textures, mineralogy, gossan evolution and mobility of gold and silver. *Ore Geol. Rev.* **65**, 165–179.

Anschutz P. and Blanc G. G. G. (1995) Geochemical dynamics of the Atlantis II Deep (Red Sea): silica behavior. *Mar. Geol.* **128**, 25–36.

Anschutz P., Blanc G. G. G., Monnin C. and Boulègue J. (2000) Geochemical dynamics of the Atlantis II Deep (Red Sea): II. Composition of metalliferous sediment pore waters. *Geochim. Cosmochim. Acta* **64**, 3995–4006.

Aquilina A., Connelly D. P., Copley J. T., Green D. A. D. R. H., Hawkes J. A., Hepburn L. E., Huvenne V. A. I., Marsh L., Mills R. A. and Tyler P. A. (2013) Geochemical and Visual Indicators of Hydrothermal Fluid Flow through a Sediment-Hosted Volcanic Ridge in the Central Bransfield Basin (Antarctica). *PLoS One* **8**, e54686.

Aquilina A., Homoky W. B., Hawkes J. a., Lyons T. W. and Mills R. A. (2014) Hydrothermal sediments are a source of water column Fe and Mn in the Bransfield Strait, Antarctica. *Geochim. Cosmochim. Acta* **137**, 64–80.

Augustin N. (2007) The Logatchev Hydrothermal Field (MAR, 15°N): High-and Low-Temperature Alteration of Ultramafic Oceanic Crust– Geology, Geochemistry, Mineralogy. .

Bach W. and Fruh-Green G. L. (2010) Alteration of the oceanic lithosphere and implications for seafloor processes. *Elements* **6**, 173–178.

Balistrieri L. S. and Murray J. W. (1986) The surface chemistry of sediments from the Panama Basin: The influence of Mn oxides on metal adsorption. *Geochim. Cosmochim. Acta* **50**, 2235–2243.

Barrett T. J., Taylor P. N. and Lugowski J. (1987) Metalliferous sediments from DSDP Leg 92: The East Pacific Rise transect. *Geochim. Cosmochim. Acta* **51**, 2241–2253.

Barriga F. J. A. S. and Carvalho D. (1983) Carboniferous volcanogenic sulphide mineralizations in South Portugal (Iberian Pyrite Belt). *Carbonif. Port.*, 99–113.

Barton P. B. and Bethke P. M. (1987) Chalcopyrite disease in sphalerite: pathology and epidemiology. *Am. Mineral.* **72**, 451–467.

Bau M. and Dulski P. (1999) Comparing yttrium and rare earths in hydrothermal fluids from the Mid-Atlantic Ridge: Implications for Y and REE behaviour during near-vent mixing and for the Y/Ho ratio of proterozoic seawater. *Chem. Geol.* **155**, 77–90.

Beaulieu S. E., Baker E. T. and German C. R. (2015) Where are the undiscovered hydrothermal vents on oceanic spreading ridges? *Deep Sea Res. Part II Top. Stud. Oceanogr.* **121**, 1–11.

Beaulieu S. E. and Szafranski K. (2018) InterRidge Global Database of Active Submarine Hydrothermal Vent Fields, Version 3.4. Available at: http://vents-data.interridge.org [Accessed May 16, 2019].

Becker K. and Von Herzen R. P. (1996) Pre-drilling observations of conductive heat flow at the TAG active mound using Alvin. *Proc. Ocean Drill. Program, Initial Reports* **158**, 23–29.

Benedetti M. and Boulègue J. (1991) Mechanism of gold transfer and deposition in a supergene environment. *Geochim. Cosmochim. Acta* **55**, 1539–1547.

Bennett S. a., Achterberg E. P., Connelly D. P., Statham P. J., Fones G. R. and German C. R.

(2008) The distribution and stabilisation of dissolved Fe in deep-sea hydrothermal plumes. *Earth Planet. Sci. Lett.* **270**, 157–167.

Bertram C., Krätschell A., O'Brien K., Brückmann W., Proelss A. and Rehdanz K. (2011) Metalliferous sediments in the Atlantis II Deep—Assessing the geological and economic resource potential and legal constraints. *Resour. Policy* **36**, 315–329.

Bischoff J. L. (1969) Red Sea geothermal brine deposits: their mineralogy, chemistry, and genesis. In *Hot Brines and Recent Heavy Metal Deposits in the Red Sea* (eds. E. T. Degens and D. A. Ross). Springer, New York. pp. 368–401.

Blanchon P. (2011) Meltwater pulses. In *Encyclopedia of modern coral reefs: structure, form and process* (ed. D. Hopley). Springer-Verlag Berlin Heidelberg. pp. 683–690.

Blue Mining Eu-7th FP (2018) *Blue mining Public Report 2014-2018.*, Available at: http://www.bluemining.eu/download/project_results/public_reports/Blue-mining-Public-Report-2018.pdf.

Bodeï S., Buatier M. D., Steinmann M., Adatte T., Wheat C. G. and Bode\"i S. (2008) Characterization of metalliferous sediment from a low-temperature hydrothermal environment on the Eastern Flank of the East Pacific Rise. *Mar. Geol.* **250**, 128–141.

Bogdanov Y. A., Gurvich E. G., Lisitzin A. P., Serova V. V. and Gorbunova Z. N. (1997) Sediments of the active rift zone in the western Woodlark Basin and the development of hydrothermal and volcanic activity. *Mar. Geol.* **142**, 143–170.

Bortnikov N. S., Genkin A. D., Dobrovol'skaya M. G., Muravitskaya G. N. and Filimonova A. A. (1991) The nature of chalcopyrite inclusions in sphalerite: exsolution, coprecipitation, or "disease''?" *Econ. Geol.* **86**, 1070–1082.

Boström K., Peterson M. N. A., Joensuu O. and Fisher D. E. (1969) Aluminum-Poor Ferromanganoan Sediments on Active Oceanic Ridges. *J. Geophys. Res.* **74**, 3261–3270.

Bouma A. (1962) *Sedimentology of some Flysch deposits: A graphic approach to facies interpretation.* Elsevier. ed. A. Bouma,

Boyle J. F. (1984) The origin and geochemisry of the metalliferous sediments of the Troodos massif, Cyprus. University of Edinburgh.

Brathwaite R. L., Sewell R. J. and Christie A. B. (2008) Nature and tectonic setting of massive sulfide mineralisation and associated sediments and volcanics in the matakaoa volcanics, Raukumara Peninsula, New Zealand. *New Zeal. J. Geol. Geophys.* **51**, 349–366.

BRAVEX (1994) Bravex/94: Joint British–Russian Expedition to the Broken Spur and TAG Hydrothermal Vent Sites on the Mid-Atlantic Ridge. *Bridg. Newsl.* **7**, 6–9.

Bronk Ramsey C. (2009) Bayesian Analysis of Radiocarbon Dates. *Radiocarbon* **51**, 337–360.

Burdige D. J. (1993) The biogeochemistry of manganese and iron reduction in marine sediments. *Earth Sci. Rev.* **35**, 249–284.

Campbell A. C. (1991) Mineralogy and Chemistry of Marine Particles by Synchrotron X-Ray Spectroscopy, Mössbauer Spectroscopy, and Plasma-Mass Spectrometry. **02139**, 375–390.

Campbell A. C., Palmer M. R., Klinkhammer G. P., Bowers T. S., Edmond J. M., Lawrence J. R., Casey J. F., Thompson G., Humphris S. E., Rona P. A. and Karson J. A. (1988) Chemistry of hot springs on the Mid-Atlantic Ridge. *Nature* **335**, 514–519.

Cann J. and Gillis K. (2004) Hydrothermal insights from the Troodos ophiolite, Cyprus. In *Hydrogeology of the oceanic lithosphere* (eds. E. E. Davis and H. Elderfield). Cambridge University Press.

Cathles L. M. (2011) What processes at mid-ocean ridges tell us about volcanogenic massive sulfide deposits. *Miner. Depos.* **46**, 639–657.

Cave R. R., German C. R., Thomson J. and Nesbitt R. W. (2002) Fluxes to sediments underlying the Rainbow hydrothermal plume at 36 14'N on the Mid-Atlantic Ridge. *Geochim. Cosmochim. Acta* **66**, 1905–1923.

Channell J. E. T., Xuan C. and Hodell D. A. (2009) Stacking paleointensity and oxygen isotope data for the last 1 . 5 Myr (PISO-1500). *Earth Planet. Sci. Lett.* **283**, 14–23.

Chavagnac V., German C. R., Milton J. A. and Palmer M. R. (2005) Sources of REE in

sediment cores from the Rainbow vent site (36°14′N, MAR). *Chem. Geol.* **216**, 329–352.
Cherkashev G. A., Ivanov V. N., Bel'tenev V. I., Lazareva L. I., Rozhdestvenskaya I. I., Samovarov M. L., Poroshina I. M., Sergeev M. B., Stepanova T. V., Dobretsova I. G. and Kuznetsov V. Y. U. (2013) Massive sulfide ores of the northern equatorial Mid-Atlantic Ridge. *Oceanology* **53**, 607–619.
Cherkashov G. A. (1995) Hydrothermal input into sediments of the Mid-Atlantic Ridge. *Geol. Soc. London, Spec. Publ.* **87**, 223–229.
Cherkashov G. A., Kuznetsov V. Y. U., Kuksa K., Tabuns E. V, Maksimov F. and Bel'tenev V. (2017) Sulfide geochronology along the Northern Equatorial Mid-Atlantic Ridge. *Ore Geol. Rev.* **87**, 147–154.
Chiba H., Masuda H., Lee S. young and Fujioka K. (2001) Chemistry of hydrothermal fluids at the TAG active mound, MAR 26. *Geophys. Res. Lett.* **28**, 2919–2922.
Clark M. R., Desbruyères D., Fisher C., Hein J. R., Petersen S., Rowden A., Smith S., Baker E. and Beaudoin Y. (2013) *Sea-Floor Massive Sulphides: A physical, biological, environmental, and technical review*. eds. E. Baker and Y. Beaudoin,
Cline J. D. (1969) Spectrophotometric Determination of Hydrogen Sulfide in Natural Waters. *Limnol. Oceanogr.* **14**, 454–458.
Constantinou G. and Govett G. J. S. (1973) Geology, geochemistry and genesis of cyprus sulfide deposits. *Econ. Geol.* **68**, 843–858.
Corliss J. B., Dymond J., Gordon L. I., Edmond J. M., Von Herzen R. P., Ballard R. D., Green K., Williams D., Bainbridge A., Crane K. and Van Andel T. H. (1979) Submarine thermal springs on the Galápagos Rift. *Science (80-.).* **203**, 1073–1083.
Costa K. M., McManus J. F., Middleton J. L., Langmuir C. H., Huybers P. J., Winckler G. and Mukhopadhyay S. (2017) Hydrothermal deposition on the Juan de Fuca Ridge over multiple glacial–interglacial cycles. *Earth Planet. Sci. Lett.* **479**, 120–132.
Cowen J. P., Massoth G. J. and Feely R. A. (1990) Scavenging rates of dissolved manganese in a hydrothermal vent plume. *Deep Sea Res. Part A, Oceanogr. Res. Pap.* **37**, 1619–1637.
Cronan D. S. (1976) Basal metalliferous sediments from the eastern Pacific. *Bull. Geol. Soc. Am.* **87**, 928–934.
Cronan D. S. (1981) Technical report on metalliferous sediments in the CCOP/SOPAC region of the southwest pacific, with particular reference to geochemical exploration for the deposits. *Econ. Soc. commision Asia Pacific Tech. Rep.* **17**, 77.
Cronan D. S., Varnavas S. P. and Hodkinson R. (2000) Hydrothermal Mineralizing Processes and Associated Sedimentation in the Santorini Hydrothermal Embayments. *Mar. Georesources Geotechnol.* **18**, 77–118.
Croudace I. W., Rindby A. and Rothwell R. G. (2006) ITRAX : description and evaluation of a new multi-function X-ray core scanner. *Geol. Soc. London, Spec. Publ.* **267**, 51–63.
Cudennec Y. and Lecerf A. (2006) The transformation of ferrihydrite into goethite or hematite, revisited. *J. Solid State Chem.* **179**, 716–722.
Von Damm K. L. (1995) Controls on the Chemistry and Temporal Variability of Seafloor Hydrothermal Fluids. In *Seafloor Hydrothermal Systems: Physical, Chemical, Biological and Geological Interactions, Geophysical Monograph Series* (eds. S. E. Humphris, R. A. Zierenberg, L. S. Mullineaux, and R. E. Thomson). Washington, DC: American Geophysical Union. pp. 222–247.
Von Damm K. L., Edmond J. M., Measures C. I. I. and Grant B. (1985) Chemistry of submarine hydrothermal solutions at Guaymas Basin, Gulf of California. *Geochim. Cosmochim. Acta* **49**, 2221–2237.
Damyanov Z. K., Dekov V. M., Lisitzin A. P., Bogdanov Y. A., Aidanliiski G. and Dimov V. I. (1998) Mineralogical features of the near sulfide mound sediments: MIR zone, TAG Hydrothermal Field (Mid-Atlantic Ridge, 26N). *N Jb Miner. Abh.*, 43–78.
Dash E. J., Dymond J. R. and Ross H. G. (1971) Isotopic analysis of metalliferous sediment from the East Pacific Rise. *Earth Planet. Sci. Lett.* **13**, 175–180.
Dekov V. M., Cuadros J., Kamenov G. D., Weiss D., Arnold T., Basak C. and Rochette P.

(2010) Metalliferous sediments from the H.M.S. Challenger voyage (1872-1876). *Geochim. Cosmochim. Acta* **74**, 5019–5038.

Dekov V. M., Damyanov Z. K. K., Kamenov G. D., Bonev I. K. K. and Bogdanov K. B. B. (1999) Native copper and a-copper-zinc in sediments from the TAG hydrothermal field (Mid-Atlantic Ridge , 26°N) : nature and origin. *Mar. Geol.* **161**, 229–245.

Dekov V. M., Kamenov G. D., Stummeyer J., Thiry M., Savelli C., Shanks W. C., Fortin D., Kuzmann E. and Vértes A. (2007) Hydrothermal nontronite formation at Eolo Seamount (Aeolian volcanic arc, Tyrrhenian Sea). *Chem. Geol.* **245**, 103–119.

Dekov V. M., Scholten J., Garbe-schönberg D., Botz R., Cuadros J., Schmidt M. and Stoffers P. (2008) Hydrothermal sediment alteration at a seafloor vent field: Grimsey Graben, Tjornes Fracture Fracture Zone, north of Iceland. *J. Geophys. Res. Solid Earth* **113**.

DeMaster D. J. (1981) The supply and accumulation of silica in the marine environment. *Geochim. Cosmochim. Acta* **45**, 1715–1732.

Dias Á. S. and Barriga F. J. A. S. (2006) Mineralogy and geochemistry of hydrothermal sediments from the serpentinite-hosted Saldanha hydrothermal field (36°34′N; 33°26′W) at MAR. *Mar. Geol.* **225**, 157–175.

Dias A. S., Mills R. A., Taylor R. N., Ferreira P. and Barriga F. J. a S. (2008) Geochemistry of a sediment push-core from the Lucky Strike hydrothermal field, Mid-Atlantic Ridge. *Chem. Geol.* **247**, 339–351.

Dill H. G. (1994) Mineralogy and chemistry of metalliferous muds forming the topstratum of a massive sulphide metalliferous sediment sequence from East Pacific Rise 18°S: its origin and implications concerning the formation of ochrous sediments in Cyprus-Type deposits. *Mar. Georesources Geotechnol.* **159–180**, 159–180.

Ditchburn R. G., De Ronde C. E. J. and Barry B. J. (2012) Radiometric dating of volcanogenic massive sulfides and associated iron oxide crusts with an emphasis on 226Ra/Ba and 228Ra/226Ra in volcanic and hydrothermal processes at intraoceanic Arcs. *Econ. Geol.* **107**, 1635–1648.

Douville E., Bienvenu P., Charlou J.-L., Donval J.-P., Fouquet Y., Appriou P. and Gamo T. (1999) Yttrium and rare earth elements in fluids from various deep-sea hydrothermal systems - evidence for heat extraction from magma chambers or cracking fronts? *Geochim. Cosmochim. Acta* **63**, 627–643.

Van Dover C. L., Arnaud-Haond S., Gianni M., Helmreich S., Huber J. A., Jaeckel A. L., Metaxas A., Pendleton L. H., Petersen S., Ramirez-Llodra E., Steinberg P. E., Tunnicliffe V. and Yamamoto H. (2018) Scientific Rationale and International Obligations for Protection of Active Hydrothermal Vent Ecosystems From Deep-Sea Mining. *Mar. Policy* **90**, 20–28.

Dubinin A. V., Uspenskaya T. Y., Gavrilenko G. M. and Rashidov V. A. (2009) Geochemistry and genesis of Fe-Mn mineralization in island arcs in the west Pacific Ocean. *Geochemistry Int.* **46**, 1206–1227.

Dunk R. M. and Mills R. A. (2006) The impact of oxic alteration on plume-derived transition metals in ridge flank sediments from the East Pacific Rise. *Mar. Geol.* **229**, 133–157.

Dutrieux A. M., Lichtschlag A., Martins S., Milinovic J., Barriga F. J. A. S. and Murton B. J. Metal preservation in hydrothermal sediments at the TAG hydrothermal field (26°N). *In preparation*.

Dymond J. and Roth S. (1988) Plume dispersed hydrothermal particles : A time-series record of settling flux from the Endeavour Ridge using moored sensors. *Geochim. Cosmochim. Acta* **52**, 2525–2536.

Edmond J. M., Campbell A. C., Palmer M. R., Klinkhammer G. P., German C. R., Edmonds H. N., Elderfield H., Thompson G. and Rona P. A. (1995) Time series studies of vent fluids from the TAG and MARK sites (1986, 1990) Mid-Atlantic Ridge: a new solution chemistry model and a mechanism for Cu/Zn zonation in massive sulphide orebodies. *Hydrothermal Vent. Process.* **87**, 77–86.

Edmonds H. N., German C. R., Green D. A. D. R. H., Huh Y., Gamo T. and Edmond J. M.

(1996) Continuation of the hydrothermal fluid chemistry time series at TAG, and the effects of ODP drilling. *Geophys. Res. Lett.* **23**, 3487.

Edwards K. J., McCollom T. M., Konishi H. and Buseck P. R. (2003) Seafloor bioalteration of sulfide minerals: Results from in situ incubation studies. *Geochim. Cosmochim. Acta* **67**, 2843–2856.

Elderfield H., Mills R. A. and Rudnicki M. D. (1993) Geochemical and thermal fluxes, high-temperature venting and diffuse flow from mid-ocean ridge hydrothermal systems: the TAG hydrothermal field, Mid-Atlantic Ridge 26 N. *Geol. Soc. London, Spec. Publ.* **76**, 295–307.

Elderfield H. and Schultz A. (1996) Mid-Ocean Ridge Hydrothermal Fluxes and the Chemical Composition of the Ocean. *Annu. Rev. Earth Planet. Sci.* **24**, 191–224.

Evensen N. M., Hamilton P. J. and O'Nions R. K. (1978) Rare-earth abundances in chondritic meteorites. *Geochim. Cosmochim. Acta* **42**, 1199–1212.

Fallon E. K., Petersen S., Brooker R. A. and Scott T. B. (2017) Oxidative dissolution of hydrothermal mixed-sulphide ore: An assessment of current knowledge in relation to seafloor massive sulphide mining. *Ore Geol. Rev.* **86**, 309–337.

Feely R. A., Gendron J. F., Baker E. T. and Lebon G. T. (1994a) Hydrothermal plumes along the East Pacific Rise: 8°40′ to 11°50′N: Particles distribution and composition. *Earth Planet. Sci. Lett.* **128**, 19–36.

Feely R. A., Massoth G. J., Baker E. T., Lebon G. T. and Geiselman T. L. (1992) Tracking the dispersal of hydrothermal plumes from the Juan de Fuca Ridge using suspended matter compositions. *J. Geophys. Res.* **97**, 3457–3468.

Feely R. A., Massoth G. J., Trefry J. H., Baker E. T., Paulson A. J. and Lebon G. T. (1994b) Composition and sedimentation of hydrothermal plume particles from north Cleft segment, Juan de Fuca Ridge. *J. Geophys. Res.* **99**, 4985–5006.

Fisher A. and Wheat C. G. (2011) Seamounts as Conduits for Massive Fluid, Heat, and Solute Fluxes on Ridge Flanks. *Oceanography* **23**, 74–87.

Fisher C., Rowden A., Clark M. R. and Desbruyères D. (2013) Biology Associated with Sea-Floor Massive Sulphide Deposits. In *Seafloor massive sulphides: a physical, biological, environmental and technical review* p. 52.

Fouquet Y. (1997) Where are the large hydrothermal sulphide deposits in the oceans? *Philos. Trans. R. Soc. London Ser. a-Mathematical Phys. Eng. Sci.* **355**, 427–440.

Fouquet Y., Henry K., Knott R. and Cambon P. (1998) Geochemical Section of the TAG Hydrothermal Mound. *Proc. Ocean Drill. Program, Sci. Results* **158**, 363–38.

Frank M., Eisenhauer A., Kubik P. W., Dittrich-hannen B. and Segl M. (1994) Beryllium 10, thorium 230, and protactinium 231 in Galapagos microplate sediments: implications of hydrothermal activity and paleoproductivity changes during the last 100,000 years. *Paleoceanography* **9**, 559–578.

Franklin J. M. M., Gibson H., Jonasson I. R. and Galley A. G. (2005) Volcanogenic Massive Sulfide Deposits. *Econ. Geol. 100th Anniv. Vol.*, 523–560.

Froelich P. N., Klinkhammer G. P., Bender M. L., Luedtke N. A., Heath G. R., Cullen D., Dauphin P., Hammond D., Hartman B. and Maynard V. (1979) Early oxidation of organic matter in pelagic sediments of the eastern equatorial Atlantic: suboxic diagensis. *Geochim. Cosmochim. Acta* **43**, 1075–1090.

Fujioka K., Chiba H., Naganuma T., Masuda H., Oomori T., Rona P. A., Tucholke B. E., Ishihara T., Kato K., Lee S., Green D. A. D. R. H., Aoki M. and Yakamoto H. (1999) Hydrothermal activity and architecture of slow-spreading Ridge at TAG and Rainbow hydrothermal fields and Dante's Domes Megamullion in the Mid-Atlantic Ridge. *J. Deep Sea Res.* **15**, 39–49.

Gablina I. F., Semkova T. A., Stepanova T. V. and Gor'kova N. V. (2006) Diagenetic alterations of copper sulfides in modern ore-bearing sediments of the Logatchev-1 hydrothermal field (Mid-Atlantic Ridge 14°45′ N). *Lithol. Miner. Resour.* **41**, 27–44.

Le Gal V., Lucazeau F., Cannat M., Poort J., Monnin C., Battani A., Fontaine F., Goutorbe

B., Rolandone F., Poitou C., Blanc-Valleron M. M., Piedade A. and Hipólito A. (2018) Heat flow, morphology, pore fluids and hydrothermal circulation in a typical Mid-Atlantic Ridge flank near Oceanographer Fracture Zone. *Earth Planet. Sci. Lett.* **482**, 423–433.

Galley A. G. and Koski R. A. (1997) Chapter 10 Setting and Characteristics of Ophiolite-Hosted Volcanogenic Massive Sulfide Deposits. In *Volcanic Associated Massive Sulfide Deposits: Processes and Examples in Modern and Ancient Settings, Reviews in Economic Geology* Society of Economic Geologists. pp. 221–246.

Gamberi F., Marani M. and Savelli C. (1997) Tectonic, volcanic and hydrothermal features of a submarine portion of the Aeolian arc (Tyrrhenian Sea). **140**, 167–181.

Gamo T., Chiba H., Masuda H., Edmonds H. N., Fujioka K., Kodama Y., Nanba H. and Sano Y. (1996) Chemical characteristics of hydrothermal fluids from the TAG mound of the mid-Atlantic Ridge in August 1994: implications for spatial and temporal variability of hydrothermal activity. *Geophys. Monogr. Ser.* **23**, 3483–3486.

Gehrmann R. A. S., North L. J., Graber S., Szitkar F., Petersen S., Minshull T. A. and Murton B. J. (2019) Marine Mineral Exploration With Controlled Source Electromagnetics at the TAG Hydrothermal Field, 26°N Mid-Atlantic Ridge. *Geophys. Res. Lett.*, 1–9.

German C. R., Casciotti K. A., Dutay J.-C., Heimbürger L. E., Jenkins W. J., Measures C. I., Mills R. A., Obata H., Schlitzer R., Tagliabue A., Turner D. R. and Whitby H. (2016a) Hydrothermal impacts on trace element and isotope ocean biogeochemistry. *Philos. Trans. R. Soc. A Math. Phys. Eng. Sci.* **374**, 20160035.

German C. R., Colley S., Palmer M. R., Khripounoff A. and Klinkhammer G. P. (2002) Hydrothermal plume-particle fluxes at 13 degrees N on the East Pacific Rise. *Deep. Res. Part I-Oceanographic Res. Pap.* **49**, 1921–1940.

German C. R., Hergt J., Palmer M. R., Edmond J. M., Moeller P., Fouquet Y. and Shepherd T. J. (1999) Geochemistry of a hydrothermal sediment core from the OBS vent-field, 21 degrees N East Pacific Rise. *Chem. Geol.* **155**, 65–75.

German C. R., Higgs N. C., Thomson J., Mills R. A., Elderfield H., Blusztajn J., Fleer a. P. and Bacon M. P. (1993) A geochemical study of metalliferous sediment from the TAG Hydrothermal Mound, 26°08′N, Mid-Atlantic Ridge. *J. Geophys. Res.* **98**, 9683.

German C. R., Klinkhammer G. P., Edmond J. M., Mura a. and Elderfield H. (1990) Hydrothermal scavenging of rare-earth elements in the ocean. *Nature* **345**, 516–518.

German C. R., Petersen S. and Hannington M. D. (2016b) Hydrothermal exploration of mid-ocean ridges: Where might the largest sulfide deposits be forming? *Chem. Geol.* **420**, 114–126.

German C. R. and Seyfried W. E. J. (2014) Hydrothermal Processes. In *Treatise on Geochemistry* Elsevier Ltd. pp. 191–233.

German C. R., Yoerger D. R., Jakuba M. V, Shank T. M., Langmuir C. H., ichi Nakamura K. and Nakamura K. (2008) Hydrothermal exploration with the Autonomous Benthic Explorer. *Deep. Res. Part I Oceanogr. Res. Pap.* **55**, 203–219.

Germanovich L. N., Hurt R. S., Smith J. E., Genc G. and Lowell R. P. (2015) Measuring fluid flow and heat output in seafloor hydrothermal environments. *J. Geophys. Res. - Solid Earth* **120**, 8031–8055.

Glynn S., Mills R. A., Palmer M. R., Pancost R. D., Severmann S. and Boyce A. (2006) The role of prokaryotes in supergene alteration of submarine hydrothermal sulfides. *Earth Planet. Sci. Lett.* **244**, 170–185.

Goulding H. C., Mills Rachel A and Nesbitt R. W. (1998) Precipitation of hydrothermal sediments on the active TAG Mound; implications for ochre formation. In *Modern ocean floor processes and the geological record.* (eds. R A Mills and K. Harrison). Geological Society of London. pp. 201–216.

Grant K. M., Rohling E. J., Bronk Ramsey C., Cheng H., Edwards R. L., Florindo F., Heslop D., Marra F., Roberts A. P., Tamisiea M. E. and Williams F. (2014) Sea-level variability over five glacial cycles. *Nat. Commun.* **5**, 1–9.

Grasshoff K., Ehrhardt M. and Kremling K. (1983) *Methods of Seawater Analysis*. eds. K. Grasshoff, M. Ehrhardt, and K. Kremling, Verlag Chemic GmbH, Weinheim.

Grenne T. and Slack J. F. (2003) Bedded jaspers of the Ordovician Løkken ophiolite, Norway: Seafloor deposition and diagenetic maturation of hydrothermal plume-derived silica-iron gels. *Miner. Depos.* **38**, 625–639.

Griffith E. M. and Paytan A. (2012) Barite in the ocean - occurrence, geochemistry and palaeoceanographic applications. *Sedimentology* **59**, 1817–1835.

Gurvich E. G. (2006) *Metalliferous sediments of the world ocean: fundamental theory of deep-sea hydrothermal sedimentation*, Springer-Verlag Berlin Heidelberg, Berlin Heidelberg New York.

Hajash A. (1975) Hydrothermal processes along mid-ocean ridges: An experimental investigation. *Contrib. to Mineral. Petrol.* **53**, 205–226.

Halbach P., Blum N., Münch U., Plüger W., Garbe-Schönberg D. and Zimmer M. (1998) Formation and decay of a modern massive sulfide deposit in the Indian Ocean. *Miner. Depos.* **33**, 302–309.

Hannington M. D. (1993) The formation of atacamite during weathering of sulfides on the modern sea-floor. *Can. Mineral.* **31**, 945–956.

Hannington M. D., Galley A. G., Herzig P. M. and Petersen S. (1998) Comparison of the TAG Mound and stockwork complex with Cyprus-type massive sulphide deposits. *Proc. Ocean Drill. Program, Sci. Results* **158**, 389–415.

Hannington M. D., Jamieson J. W., Monecke T., Petersen S. and Beaulieu S. E. (2011) The abundance of seafloor massive sulfide deposits. *Geology* **39**, 1155–1158.

Hannington M. D., Petersen S., Herzig P. M. and Jonasson I. (2004) *A global database of seafloor hydrothermal systems, including a digital database of geochemical analyses of seafloor polymetallic sulfides: Geological Survey of Canada, Open File 4598, 1 CD-ROM.* Available at: http://oceanrep.geomar.de/33243/1/Hannington.pdf.

Hannington M. D., Petersen S. and Krätschell A. (2017) Subsea mining moves closer to shore. *Nat. Geosci.* **10**, 158–159..

Hannington M. D., De Ronde C. E. J. and Petersen S. (2005) Sea Floor Tectonics and Submarine Hydrothermal Systems. *Econ. Geol.*, 111–141.

Hannington M. D., Thompson G., Rona P. A. and Scott S. D. (1988) Gold and native copper in supergene sulphides from the Mid-Atlantic Ridge. *Nature* **333**, 64–66.

Hannington M. D., Tivey M. K., Larocque A. C. L. L., Petersen S. and Rona P. A. (1995) The Occurance of Gold in Sulfide Deposits of the TAG Hydrothermal Field, Mid-Atlantic Ridge. *Can. Mineral.* **33**, 1285–1310.

Hansell D. A. and Follows M. J. (2008) Nitrogen in the Atlantic Ocean. In *Nitrogen in the Marine Environment (2nd Edition)* pp. 597–630.

Hayes C. T., Anderson R. F., Fleisher M. Q., Huang K., Robinson L. F., Lu Y., Cheng H., Edwards R. L. and Moran S. B. (2015) 230Th and 231Pa on GEOTRACES GA03 , the U . S . GEOTRACES North Atlantic transect , and implications for modern and paleoceanographic chemical fluxes. *Deep. Res. Part II* **116**, 29–41.

Heath G. R. and Dymond J. R. (1977) Genesis and transformation of metalliferous sediments from the East Pacific Rise , Bauer Deep , and Central Basin , northwest Nazca plate. *Geol. Soc. Am. Bull.* **88**, 723–733.

Hein J. R., Clague D. A., Koski R. A., Embley R. W. and Dunham R. E. (2008) Metalliferous sediment and a silica-hematite deposit within the Blanco fracture zone, Northeast Pacific. *Mar. Georesources Geotechnol.* **26**, 317–339.

Herzig P. M. and Hannington M. D. (1995) Polymetallic massive sulfides at the modem seafloor A review. *Ore Geol. Rev.* **10**, 95–115.

Herzig P. M., Hannington M. D., Scott S. D., Maliotis G., Rona P. A. and Thompson G. (1991) Gold-rich sea-floor gossans in the troodos ophiolite and on the mid-Atlantic ridge. *Econ. Geol.* **86**, 1747–1755.

Herzig P. M., Humphris S. E., Miller D. J. and Zierenberg R. A. (1998a) *Proceedings of the*

Ocean Drilling Program, Scientific Results, Vol. 158-2.,

Herzig P. M., Petersen S. and Hannington M. D. (1998b) Geochemistry and Sulfur-Isotopic Composition of the TAG Hydrothermal Mound, Mid-Atlantic Ridge, 26°N. In *Proceedings of the Ocean Drilling Program, Scientific Results* pp. 47–70.

Hodgkinson M. R. S., Webber A. P., Roberts S., Mills R. A., Connelly D. P. and Murton B. J. (2015) Talc-dominated seafloor deposits reveal a new class of hydrothermal system Talc-dominated seafloor deposits reveal a new class of hydrothermal system. *Nat. Commun.*, 1–11.

Hodkinson R., Cronan D. S., Glasby G. P. and Moorby S. A. (1986) Geochemistry of marine sediments from the Lau Basin, Havre Trough, and Tonga—Kermadec Ridge. *New Zeal. J. Geol. Geophys.* **29**, 335–344.

Houghton J. L., Shanks W. C. and Seyfried Jr W. E. (2004) Massive sulfide deposition and trace element remobilization in the Middle Valley sediment-hosted hydrothermal system, northern Juan de Fuca Rdge. *Geochim. Cosmochim. Acta* **68**, 2863–2873.

Hovland M., Gardner J. V. and Judd A. G. (2002) The significance of pockmarks to understand fluid flow processes and geohazards. *Geofluids* **2**, 127–136.

Hrischeva E. and Scott S. D. (2007) Geochemistry and morphology of metalliferous sediments and oxyhydroxides from the Endeavour segment , Juan de Fuca Ridge. *Geochim. Cosmochim. Acta* **71**, 3476–3497.

Hu Q., Zhang X., Jiang F., Wang B., Luan Z., Chen C. and Yan J. (2017) Geochemical characteristics of hydrothermal sediments from Iheya North Knoll in the Okinawa Trough. *Chinese J. Oceanol. Limnol.* **35**, 947–955.

Humphris S. E., Bach W., Hole W. and Hole W. (2005) On the Sr isotope and REE compositions of anhydrites from the TAG seafloor hydrothermal system. *Geochim. Cosmochim. Acta* **69**, 1511–1525.

Humphris S. E., Herzig P. M., Miller D. J., Alt J. C., Becker K., Brown D., Brugmann G., Chiba H., Fouquet Y., Gemmell J. B., Guerin G., Hannington M. D., Holm N. G., Honnorez J. J., Knott R., Ludwig; R. J., Nakamura K., Petersen S., Reysenbach A. L., Rona P. A., Smith S., Sturz A. A, Tivey M. K., Zhao X. and Iturrino G. J. (1995) The internal structure of an active sea-floor massive sulfide deposit. *Nature* **377**, 713–716.

Humphris S. E., Herzig P. M., Miller D. J. and Party S. (1996) ODP Initial reports Leg 158 TAG Hydrothermal Field. In *Proc. ODP, Init. Repts., 158*

Humphris S. E., Tivey M. K. and Tivey M. A. (2015) The Trans-Atlantic Geotraverse hydrothermal field: A hydrothermal system on an active detachment fault. *Deep Sea Res. Part II Top. Stud. Oceanogr.* **121**, 1–9.

Iizasa K. (1993) Assessment of the hydrothermal contribution to seafloor sediments in the Myojinsho submarine caldera, Shichito-Iwojima ridge, Izu-Ogasawara arc, Japan. *Mar. Geol.* **114**, 119–132.

Ishibashi J., Okino K. and Sunamura M. (2015) *Subseafoor Biosphere Linked to Hydrothermal Systems.*,

Iyer S. D., Prasad M. S., Gupta S. M. and Charan S. N. (1997) Evidence for recent hydrothermal activity in the Central Indian Basin. *Deep. Res. Part I Oceanogr. Res. Pap.* **44**, 1167–1173.

Jamieson J. W., Hannington M. D., Clague D. A., Kelley D. S., Delaney J. R., Holden J. F., Tivey M. K. and Kimpe L. E. (2013) Sulfide geochronology along the Endeavour Segment of the Juan de Fuca Ridge. *Geochemistry, Geophys. Geosystems* **14**, 2084–2099.

Jamieson J. W., Petersen S. and Bach W. (2016) Hydrothermalism. In *Encyclopedia of Marine Geosciences* (eds. J. Harff, M. Meschede, S. Petersen, and Jö. Thiede). Springer Netherlands, Dordrecht. pp. 344–357.

Johns S. M., Ditchburn R. G., Barry B. J. and Yeats C. J. (2014) Episodic subseafloor hydrothermal activity within the eastern Manus back-arc basin determined by uranium-series disequilibrium in barite. *Econ. Geol.* **109**, 2227–2241.

Johnson A. and Cronan D. S. (2001) Hydrothermal Metalliferous Sediments and Waters Off

the Lesser Antilles. *Mar. Georesources Geotechnol.* **19**, 65–83.

Jørgensen B. B. and Boetius A. (2007) Feast and famine - Microbial life in the deep-sea bed. *Nat. Rev. Microbiol.* **5**, 770–781.

Josso P., Roberts S., Teagle D. A. H., Pourret O., Herrington R. and Ponce de Leon Albarran C. (2018) Extraction and separation of rare earth elements from hydrothermal metalliferous sediments. *Miner. Eng.* **118**, 106–121.

Kemp A. E. S., Pearce R. B., Pike J. and Marshall J. E. A. (1998) Microfabric and Microcompositional Studies of Pliocene and Quaternary Sapropels From the Eastern Mediterranean. *Proc. Ocean Drill. Program, Sci. Results* **160**, 1–16.

Kent D. V. (1973) Post-depositional remanent magnetisation in deep-sea sediment. *Nature* **246**, 32–34.

Khripounoff A. and Alberic P. (1991) Settling of particles in a hydrothermal vent field (East Pacific Rise 13°N) measured with sediment traps. *Deep Sea Res. Part A. Oceanogr. Res. Pap.* **38**, 729–744.

Kimura M., Uyeda S., Kato Y., Tanaka T., Yamano M., Gamo T., Sakai H., Kato S., Izawa E. and Oomori T. (1988) Active hydrothermal mounds in the Okinawa Trough backarc basin, Japan. *Tectonophysics* **145**, 319–324.

Klinkhammer G. P., Elderfield H., Edmond J. M. and Mitra A. (1994) Geochemical implications of rare earth elements patterns in hydrothermal fluids from mid-ocean ridges. *Geochim. Cosmochim. Acta* **58**, 5105–5113.

Klinkhammer G. P., Elderfield H., Greaves M., Rona P. A. and Nelsen T. A. (1986) Manganese geochemistry near high-temperature vents in the Mid-Atlantic Ridge rift valley. *Earth Planet. Sci. Lett.* **80**, 230–240.

Klinkhammer G. P. and Hudson A. (1986) Dispersal patterns for hydrothermal plumes in the South Pacific using manganese as a tracer. *Earth Planet. Sci. Lett.* **79**, 241–249.

Knight R. D., Roberts S. and Cooper M. J. (2017) Investigating monomineralic and polymineralic reactions during the oxidation of sulphide minerals in seawater: Implications for mining seafloor massive sulphide deposits. *Appl. Geochemistry* **90**, 63–74.

Koschinsky A., Garbe-schönberg D., Sander S., Schmidt K., Gennerich H. and Strauss H. (2008) Hydrothermal venting at pressure-temperature conditions above the critical point of seawater , 5°S on the Mid-Atlantic Ridge. *Geology*, 615–618.

Koski R. A., Jonasson I. R., Kadko D. C., Smith V. K. and Wong F. L. (1994) Compositions, growth mechanisms, and temporal relations of hydrothermal sulfide-sulfate-silica chimneys at the northern Cleft segment, Juan de Fuca Ridge. *J. Geophys. Res.* **99**, 4813–4832.

Krasnov S. G., Cherkashov G. A., Stepanova T. V., Batuyev B. N., Krotov a. G., Malin B. V., Maslov M. N., Markov V. F., Poroshina I. M., Samovarov M. S., Ashadze a. M., Lazareva L. and Ermolayev I. K. (1995) Detailed geological studies of hydrothermal fields in the North Atlantic. *Hydrothermal Vent. Process.* **87**, 43–64.

Kurnosov V. B. (2018) Variation of the chemical composition of sediments under middle- and low-temperature hydrothermal conditions in the southern trough of Guaymas Basin, Gulf of California: Communication 2. Results of the study of grain size fractions of sediments. *Lithol. Miner. Resour.* **53**, 76–90.

Kuznetsov V. Y. U., Arslanov K. a, Shilov V. V and Cherkashov G. A. (2002) 230Th-excess and 14C dating of pelagic sediments from the hydrothermal zone of the North Atlantic. *Geochronometria* **21**, 33–40.

Kuznetsov V. Y. U., Cherkashov G. A., Lein A. Y., Shilov V. V and Maksimov F. (2006) Th/U dating of massive sulphides from the Logatchev and Rainbow hydrothermal fields. *Geochronometria* **25**, 51–55.

Kuznetsov V. Y. U. and Maksimov F. E. (2012) Geochronometrical Methods of the Quaternary Deposits in Paleogeography and Marine Geology. In *Nauka SPb (in Russian)* p. 191.

Kuznetsov V. Y. U., Maksimov F., Zheleznov A., Cherkashov G. A., Bel'tenev V., Lazareva L. and Bel'Tenev V. (2011) 230Th/U chronology of ore formation within the semyenov hydrothermal district (13°31′ N) at the Mid-Atlantic Ridge. *Geochronometria* **38**, 72–76.

Kuznetsov V. Y. U., Tabuns E., Kuksa K., Cherkashov G. A., Maksimov F., Bel'Tenev V., Lazareva L., Zherebtsov I., Grigoriev V., Baranova N. and Bel'Tenev V. (2015) The oldest seafloor massive sulfide deposits at the Mid-Atlantic Ridge: 230Th/U chronology and composition. *Geochronometria* **42**, 100–106.

Kuznetsov V. Y. U., Tabuns E. V., Cherkashov G. A., Bel'tenev V. E., Maksimov F. E., Kuksa K., Lazareva L. I., Levchenkoa S. B. and Zherebtsov I. E. (2018a) 230Th/U Chronology and Geochemistry of Irinovskoe Hydrothermal Field (Mid-Atlantic Ridge). *Dokl. Earth Sci.* **478**, 26–30.

Kuznetsov V. Y. U., Tabuns E. V, Bel'Tenev V., Cherkashov G. A., Maksimov F. E., Kuksa K., Levchenko S. B. and Lyan K. L. (2013) 230Th/U chronology of seafloor massive sulfides formation within the "Zenith-Victory" ore field (20°08. N) at the Mid-Atlantic ridge. *Vestn. Sankt-Peterburgskogo Univ. Seriya Geol. i Geogr.* **4**, 119–130.

Kuznetsov V. Y. U., Tabuns E. V, Kuksa K., Cherkashov G. A. and Bel'Tenev V. (2018b) Chronology of Hydrothermal Activity Within the Yubileynoye Ore Field. *Dokl. Earth Sci.* **480**, 700–704.

Laj C. and Channell J. E. T. (2007) Geomagnetic Excursions. *Treatise Geophys.*, 373–416.

Lalou C. and Brichet E. (1982) Ages and implications of East Pacific Rise sulphide deposits at 21 °N. *Nature* **300**, 169–171.

Lalou C., Brichet E. and Hekinian R. (1985) Age dating of sulfide deposits from axial and off-axial structures on the East Pacific Rise near 12°50'N. *Earth Planet. Sci. Lett.* **75**, 59–71.

Lalou C., Thompson G., Arnold M., Brichet E., Druffel E. and Rona P. A. (1990) Geochronology of TAG and Snakepit hydrothermal fields, Mid-Atlantic Ridge: witness to a long and complex hydrothermal history. *Earth Planet. Sci. Lett.* **97**, 113–128.

Lalou C., Münch U., Halbach P. and Reyss J. L. (1998a) Radiochronological investigation of hydrothermal deposits from the MESO zone, Central Indian Ridge. *Mar. Geol.* **149**, 243–254.

Lalou C., Reyss J.-L. and Brichet E. (1998b) Age of Sub-Bottom Sulfide Samples At the Tag Active Mound. In *Proceedings of the Ocean Drilling Program, Scientific Results* (eds. P. M. Herzig, S. E. Humphris, D. J. Miller, and R. A. Zierenberg). pp. 111–117.

Lalou C., Reyss J.-L., Brichet E., Arnold M., Thompson G., Fouquet Y. and Rona P. A. (1993) New Age Data for Mid-Atlantic Ridge Hydrothermal Sites: TAG and Snakepit Chronology Revisited. *J. Geophys. Res.* **98**, 9705–9713.

Lalou C., Reyss J.-L., Brichet E., Rona P. A. and Thompson G. (1995) Hydrothermal activity on a 10^5-year scale at a slow spreading ridge, TAG hydrothermal field, Mid-Atlantic Ridge 26N. *J. Geophys. Res.* **100**, 17,855-17,862.

Lalou C., Reyss J. L., Brichet E., Krasnov S., Stepanova T., Cherkashev G. and Markov V. (1996) Initial chronology of a recently discovered hydrothermal field at 14°45′N, Mid-Atlantic Ridge. *Earth Planet. Sci. Lett.* **144**, 483–490.

Laurila T. E., Hannington M. D., Leybourne M., Petersen S., Devey C. W. and Garbe-Schönberg D. (2015) New insights into the mineralogy of the Atlantis II Deep metalliferous sediments, Red Sea. *Geochemistry, Geophys. Geosystems* **16**, 1–30.

Laurila T. E., Hannington M. D., Petersen S. and Garbe-Schönberg D. (2014) Early depositional history of metalliferous sediments in the Atlantis II Deep of the Red Sea: Evidence from rare earth element geochemistry. *Geochim. Cosmochim. Acta* **126**, 146–168.

Lehrmann B., Stobbs I., Lusty P. and Murton B. J. (2018) Insights into Extinct Seafloor Massive Sulfide Mounds at the TAG, Mid-Atlantic Ridge. *Minerals* **8**, 302.

Liang J., Tao C., Yang W., Liao S. and Huang W. (2018) 230Th/238U Dating of Sulfide

Chimneys in the Longqi-1 Hydrothermal Field, Southwest Indian Ridge. *Acta Geol. Sin.* **93**, 77–78.

Liao S., Tao C., Li H., Zhang G., Liang J., Yang W. and Wang Y. (2018) Surface sediment geochemistry and hydrothermal activity indicators in the Dragon Horn area on the Southwest Indian Ridge. *Mar. Geol.* **398**, 22–34.

Lichtschlag A., James R. H., Stahl H. and Connelly D. P. (2015) Effect of a controlled sub-seabed release of CO2 on the biogeochemistry of shallow marine sediments, their pore waters, and the overlying water column. *Int. J. Greenh. Gas Control* **38**, 80–92.

Lin T. J., Eecke H. C. Ver, Breves2 E. A., Dyar M. D., Jamieson J. W., Hannington M. D., H. Dahle J., Bishop L., Lane M. D., Butterfield D. A., Kelley D. S., Lilley M. D., Baross J. A. and Holden J. F. (2016) Linkages between mineralogy, fluid chemistry, and microbial communities within hydrothermal chimneys from the Endeavour Segment, Juan de Fuca Ridge T. *Geochemistry, Geophys. Geosystems* **17**, 1–21.

Lisiecki L. E. and Raymo M. E. (2005) A Pliocene-Pleistocene stack of 57 globally distributed benthic δ 18O records. *Paleoceanography* **20**, 1–17.

Lisitzin A. P., Bogdanov Y. A., Mudmaa I. O., Serova V. V, Zverinskaya I. B., Lebedev A. I., Lukashin V. N. and Gordeev V. V (1976) Metalliferous sediments and their genesis. In *Geological and geophysical research in the Southeast Pacific* (ed. A. P. Lisitzin). pp. 289–379.

Longnecker K., Sievert S. M., Sylva S. P., Seewald J. S. and Kujawinski E. B. (2018) Organic Geochemistry Dissolved organic carbon compounds in deep-sea hydrothermal vent fluids from the East Pacific Rise at 9 ° 50 0 N. *Org. Geochem.* **125**, 41–49.

Lough A. J. M., Homoky W. B., Connelly D. P., Nakamura K., Abyaneh M. K., Kaulich B. and Mills R. A. (2019) Soluble iron conservation and colloidal iron dynamics in a hydrothermal plume. *Chem. Geol.* **511**, 225-237.

Lowell R. P., Farough A., Hoover J. and Cummings K. (2013) Characteristics of magma-driven hydrothermal systems at oceanic spreading centers. *Geochemistry, Geophys. Geosystems* **14**, 1756–1770.

Ludwig K. A., Shen C. C., Kelley D. S., Cheng H. and Edwards R. L. (2011) U-Th systematics and 230 Th ages of carbonate chimneys at the Lost City Hydrothermal Field. *Geochim. Cosmochim. Acta* **75**, 1869–1888.

Lund D. C. and Asimow P. D. (2011) Does sea level influence mid-ocean ridge magmatism on Milankovitch timescales? *Geochemistry, Geophys. Geosystems* **12**, 1–26.

Lund D. C., Asimow P. D., Farley K. A., Rooney T. O., E S., Jackson E. W. and Durham Z. M. (2016) Enhanced East Pacific Rise hydrothermal activity during the last two glacial terminations. *Science (80-.).* **351**, 478–482.

Lund D. C., Seeley E. I., Asimow P. D., Lewis M. J., McCart S. E. and Mudahy A. A. (2018) Anomalous Pacific-Antarctic Ridge Volcanism Precedes Glacial Termination 2. *Geochemistry, Geophys. Geosystems* **19**, 2478–2491.

Lupton J. E. (1995) Hydrothermal plumes: near and far field. In *Seafloor hydrothermal systems: physical, chemical, biological and geological interactions Geophysical Monograph. Vol 91* (eds. S. E. Humphris, R. A. Zierenberg, L. S. Mullineaux, and T. R. E.). AGU, Washington DC. pp. 317–346.

Lusty P., Graber S., Stobbs I., Dutrieux A. and Martins S. (2017) Blue Mining D2.11 Surface geology report.

MacLachlan S. E., Hunt J. E. and Croudace I. W. (2015) An empirical assessment of variable water content and grain-size on X-ray fluoresence core-scanning measurements of deep-sea sediments. In *Micro-XRF studies of sediment cores: Applications of a non-destructive tool for the environmental sciences* (eds. I. W. Croudace and R. G. Rothwell). Springer Dordrecht. pp. 173–185.

Maslennikov V. V., Ayupova N. R., Herrington R. J., Danyushevskiy L. V. and Large R. R. (2012) Ferruginous and manganiferous haloes around massive sulphide deposits of the Urals. *Ore Geol. Rev.* **47**, 5–41.

Massoth G. J., Baker E. T., Lupton J. E., Feely R. A., Butterfield D. A., Von Damm K. L., Roe

K. K. and Lebon G. T. (1994) Temporal and spatial variability of hydrothermal manganese and iron at Cleft segment, Juan de Fuca Ridge. *J. Geophys. Res. - Solid Earth* **99**, 4905–4923.

McCarthy M. D., Beaupré S. R., Walker B. D., Voparil I., Guilderson T. P. and Druffel E. R. M. (2011) Chemosynthetic origin of 14C-depleted dissolved organic matter in a ridge-flank hydrothermal system. *Nat. Geosci.* **4**, 32–36.

McGregor B. A., Harrison C. G. A., Lavelle J. W. and Rona P. A. (1977) Magnetic anomaly patterns on Mid-Atlantic Ridge crest at 26°N. *J. Geophys. Res.* **82**, 231–238.

Metz S. and Trefry J. H. (1993) Field and laboratory studies of metal uptake and release by hydrothermal precipitates. *J. Geophys. Res.* **98**, 9661–9666.

Metz S., Trefry J. H. and Nelsen T. A. (1988) History and geochemistry of a metalliferous sediment core from the Mid-Atlantic Ridge at 26°N. *Geochim. Cosmochim. Acta* **52**, 2369–2378.

Michard A., Michard G., Stuben D., Stoffers P., Cheminee J. and Binard N. (1993) Submarine thermal springs associated with young volcanoes: The Teahitia vents, Society Islands, Pacific Ocean. *Geochim. Cosmochim. Acta* **57**, 4977–4986.

Middleton J. L., Langmuir C. H., Mukhopadhyay S., McManus J. F. and Mitrovica J. X. (2016) Hydrothermal iron flux variability following rapid sea-level changes. *Geophys. Res. Lett.*

Milani A., Statham P. J., Mowlem M. C. and Connelly D. P. (2015) Development and application of a microfluidic in-situ analyzer for dissolved Fe and Mn in natural waters. *Talanta* **136**, 15–22.

Milinovic J., Barriga F. J. A. S., Martins S., Pereira M. F. and Janeiro A. I. (2017) Offshore assessment of minerals in deep-sea sediments from the TAG-area (26°N, 44°W). In *Goldschmidt 2017 Paris Abstract* p. 1.

Miller A. R., Densmore C. D., Degens E. T., Hathaway J. C., Manheim F. T., Mcfarlin P. F. and Jokela A. (1966) Hot brines and recent iron deposits in deeps of the Red Sea. *Geochim. Cosmochim. Acta* **30**, 341–359.

Mills R. A., Clayton T. and Alt J. C. (1996) Low-temperature fluid flow through sulfidic sediments from TAG: modification of fluid chemistry and alteration of mineral deposits. *Geophys. Res. Lett.* **23**, 3495–3498.

Mills R. A. and Dunk R. M. (2010) Tracing low-temperature fluid flow on ridge flanks with sedimentary uranium distribution. *Geochemistry, Geophys. Geosystems* **11**, 1–15.

Mills R. A. and Elderfield H. (1995a) Hydrothermal activity and the geochemistry of metalliferous sediment. *Geophys. Monogr. Ser. 91*, 392–407.

Mills R. A. and Elderfield H. (1995b) Rare earth element geochemistry of hydrothermal deposits from the active TAG Mound, 26 N Mid-Atlantic Ridge. *Geochim. Cosmochim. Acta* **59**, 3511–3524.

Mills R. A., Elderfield H. and Thomson J. (1993) A dual origin for the hydrothermal component in a metalliferous sediment core from the Mid-Atlantic Ridge. *J. Geophys. Res.* **98**, 9671–9681.

Mills R. A., Taylor S. L., Plike H. and Thomson J. (2010) Hydrothermal sediments record changes in deep water oxygen content in the SE Pacific. *Paleoceanography* **25**, 1–16.

Mills R. A., Thomson J., Elderfield H., Hinton R. W. and Hyslop E. (1994) Uranium enrichment in metalliferous sediments from the Mid-Atlantic Ridge. *Earth Planet. Sci. Lett.* **124**, 35–47.

Mills R. A., Wells D. M. and Roberts S. (2001) Genesis of ferromanganese crusts from the TAG hydrothermal fields. *Chem. Geol.* **176**, 283–293.

Mitra A., Elderfield H. and Greaves M. J. (1994) Rare-earth elements in submarine hydrothermal fluids and plumes from the Mid-Atlantic Ridge. *Mar. Chem.* **46**, 217–235.

Miyashiro A., Shido F. and Ewing M. (1969) Composition and origin of serpentinites from the Mid-Atlantic Ridge near 24° and 30° North Latitude. *Contrib. to Mineral. Petrol.* **23**, 117–127.

Mottl M. J. (2003) Partitioning of energy and mass fluxes between mid-ocean ridge axes and flanks at high and low temperature. In *Energy and Mass transfer in marine hydrothermal systems* (ed. P. Halbach). pp. 271–286.

Mottl M. J. and Wheat C. G. (1994) Hydrothermal circulation through mid-ocean ridge flanks : fluxes of heat and magnesium. *Geochim. Cosmochim. Acta* **58**, 2225–2237.

Müller M., Handley K. M., Lloyd J., Pancost R. D. and Mills R. A. (2010) Biogeochemical controls on microbial diversity in seafloor sulphidic sediments. *Geobiology* **8**, 309–326.

Münch U., Lalou C., Halbach P. and Fujimoto H. (2001) Relict hydrothermal events along the super-slow Southwest Indian spreading ridge near 63°56'E- Mineralogy, chemistry and chronology of sulfide samples. *Chem. Geol.* **177**, 341–349.

Murray J. and Renard A. F. (1891) *Report of deep-sea deposits based on the speciments collected during the voyage of the H.M.S Challenger in the years 1872 to 1876.*,

Murray J. W. (1975) The interaction of metal ions at the manganese dioxide solution interface. *Geochim. Cosmochim. Acta* **39**, 505–519. Available at: https://ac.els-cdn.com/0016703775901039/1-s2.0-0016703775901039-main.pdf?_tid=1cabb46c-a844-11e7-9bac-00000aacb35f&acdnat=1507039795_7fd26775b82b29f3b893fdf6c63f8fe3.

Murton B. J., Lehrmann B., Dutrieux A. M., Martins S., Gil de la Iglesia A., Stobbs I. J., Barriga F. J. A. S., Bialas J., Dannowski A., Vardy M. E., North L. J., Yeo I. A. L. M., Lusty P. A. J. and Petersen S. (2019) Geological fate of seafloor massive sulphides at the TAG hydrothermal field (Mid-Atlantic Ridge). *Ore Geol. Rev.* **107**, 903–925. Available at: https://doi.org/10.1016/j.oregeorev.2019.03.005.

Murton B. J., Redbourn L. J., German C. R. and Baker E. T. (1999) Sources and fluxes of hydrothermal heat, chemicals and biology within a segment of the Mid-Atlantic Ridge. *Earth Planet. Sci. Lett.* **171**, 301–317.

Murton B. J. and Scientific Party S. (2018) Cruise Report : Expedition JC 138 : 29 th June – 8 th August 2016, Mid Atlantic Ridge, 26° 8.38'N; 44° 49.92'W.

Nielsen S. G., Rehkämper M., Teagle D. A. H., Butterfield D. A., Alt J. C. and Halliday A. N. (2006) Hydrothermal fluid fluxes calculated from the isotopic mass balance of thallium in the ocean crust. *Earth Planet. Sci. Lett.* **251**, 120–133.

Olive J.-A., Behn M. D., Ito G., Buck W. R., Escartin J. and Howell S. (2015) Sensitivity of seafloor bathymetry to climate-driven fluctuations in mid-ocean ridge magma supply. *Science (80-.).* **350**, 310–313.

Paillard D., Labeyrie L. and Yiou P. (1996) Macintosh Program Performs Time-Series Analysis. *Eos, Trans. Am. Geophys. Union* **77**, 379.

Palme H. (1988) Chemical Abundances in Meteorites. In *Cosmic Chemistry* (ed. G. Klare). Springer Berlin Heidelberg, Berlin, Heidelberg. pp. 28–51.

Pan A., Yang Q., Zhou H., Ji F., Wang H. and Pancost R. D. (2018) Geochemical impacts of hydrothermal activity on surface deposits at the Southwest Indian Ridge. *Deep. Res. Part I Oceanogr. Res. Pap.* **139**, 1–13.

Papavassiliou K., Voudouris P., Kanellopoulos C., Glasby G., Alfieris D. and Mitsis I. (2017) New geochemical and mineralogical constraints on the genesis of the Vani hydrothermal manganese deposit at NW Milos island, Greece: Comparison with the Aspro Gialoudi deposit and implications for the formation of the Milos manganese mineralization. *Ore Geol. Rev.* **80**, 594–611.

Pelleter E., Fouquet Y., Etoubleau J., Cheron S., Labanieh S., Josso P., Bollinger C. and Langlade J. (2017) Ni-Cu-Co-rich hydrothermal manganese mineralization in the Wallis and Futuna back-arc environment (SW Pacific). *Ore Geol. Rev.* **87**, 126–146.

Petersen S. (2000) The Geochemical and Mineralogical Evolution of the TAG Hydrothermal Field, Mid-Atlantic Ridge, 26°N. Technischen Universität Bergakademie Freiberg.

Petersen S. (2019a) Bathymetric data products from AUV dives during METEOR cruise M127 (TAG Hydrothermal Field, Atlantic). *PANGAEA*. Available at: https://doi.pangaea.de/10.1594/PANGAEA.899415.

Petersen S. (2019b) Raw multibeam EM122 data and data products: METEOR cruise M127

(TAG Hydrothermal Field, Atlantic). *PANGAEA*. Available at: https://doi.org/10.1594/PANGAEA.899408.

Petersen S., Augustin N., Cherkashov G. A., Fisher S., Franz L., Han X., Klein F., Maggiulli M., Ockert C., Perner M., Peters M., Rahders E., Rudzitis E., Smith D., Stepanova T. V, Storm S., Strauss H. and Zhou N. (2007) Shallow-drilling of the ultramafic-hosted Logatchev hydrothermal field at 14°45′N on the Mid-Atlantic Ridge using a new lander-type seafloor drill. *InterRidge News* **16**, 11–13.

Petersen S., Herzig P. M. and Hannington M. D. (2000) Third dimension of a presently forming VMS deposit: TAG hydrothermal mound, Mid-Atlantic Ridge, 26°N. *Miner. Depos.* **35**, 233–259.

Petersen S., Krätschell A., Augustin N., Jamieson J. W., Hein J. R. and Hannington M. D. (2016) News from the seabed – Geological characteristics and resource potential of deep-sea mineral resources. *Mar. Policy* **70**, 1–13.

Petersen S., Kuhn K., Kuksa K., Augustin N., Hékinian R., Franz L. and Borowski C. (2009) The geological setting of the ultramafic-hosted Logatchev hydrothermal field (14°45′N, Mid-Atlantic Ridge) and its influence on massive sulfide formation. *Lithos* **112**, 40–56.

Petersen S., Lehrmann B. and Murton B. J. (2018) Modern seafloor hydrothermal systems: New perspectives on ancient ore-forming processes. *Elements* **14**, 307–312.

Petersen S., Monecke T., Westhues A., Hannington M. D., Gemmell J. B., Sharpe R., Peters M., Strauss H., Lackschewitz K., Augustin N., Gibson H. and Kleeberg R. (2014) Drilling Shallow-Water Massive Sulfides at the Palinuro Volcanic Complex, Aeolian Island Arc, Italy. *Econ. Geol.* **109**, 2129–2158.

Petersen S. and Scientific Party S. (2016) *RV METEOR Fahrtbericht / Cruise Report M127 - Extended Version: Metal fluxes and Resource Potential at the Slow-spreading TAG Midocean Ridge Segment (26°N, MAR) – Blue Mining@Sea.*, Kiel.

Plank T. (2014) 4.17 - The Chemical Composition of Subducting Sediments. In *Treatise on Geochemistry (Second Edition)* pp. 607–629.

Prichard H. M. and Maliotis G. (2007) Gold mineralization associated with low-temperature, off-axis, fluid activity in the Troodos ophiolite, Cyprus. *J. Geol. Soc. London.* **155**, 223–231.

Purdy G. M., Sempere J.-C., Schouten H., Dubois D. L. and Goldsmith R. (1990) Bathymetry of the mid-atlantic ridge, 24°-31°N: A map series. *Mar. Geophys. Res.* **12**, 247–252.

Reimer P. J., Bard E., Bayliss A., Beck J. warren, Blackwell P. G., Ramsey C. B., Buck C. E., Cheng H., Edwards R. L., Friedrich M., Grootes P. M., Guilderson Th. P., Haflidason H., Hajdas I., Hatte C., Heaton T. J., Hoffmann D. L., Hogg A. G., Hughen K. A., Kaiser K. F., Kromer B., Manning S. W., Niu M., Reimer R. W., Richards D. A., Scott E. M., Southon J. R., Staff R. A., Turney C. S. M. and van der Plicht J. (2013) Intcal13 and Marine13 Radiocarbon Age Calibration Curves 0–50,000 Years Cal Bp. *Radiocarbon* **55**, 1869–1887.

Resing J. A., Sedwick P. N., German C. R., Jenkins W. J., Moffett J. W., Sohst B. M. and Tagliabue A. (2015) Basin-scale transport of hydrothermal dissolved metals across the South Pacific Ocean. *Nature* **523**, 200–203.

Revan M. K., Genc Y., Delibas O., Maslennikov V. V., Ayupova N. R. and Zimitoglu O. (2019) Mineralogy and geochemistry of metalliferous sedimentary rocks from the Upper Cretaceous VMS deposits of the Eastern Pontides (NE Turkey). *Turkish J. Earth Sci.* **28**, 299–327.

Ridley W. I. (2012) Weathering Processes. In *Volcanogenic Massive Sulfide Occurrence Model: U.S. Geological Survey Scientific Investigations Report 2010–5070 –C* pp. 191–201.

Robertson A. and Degnan P. (2008) Significance of modern and ancient oceanic Mn-rich hydrothermal sediments, exemplified by Jurassic Mn-cherts from Southern Greece. *Geol. Soc. London, Spec. Publ.* **148**, 217–240.

Robertson A. and Fleet A. J. (1976) The Origins of Rare Earths in Metalliferous Sediments of the Troodos Massif, Cyprus. *Earth Planet. Sci. Lett.* **28**, 385–394.

Robertson A. H. F. (1975) Cyprus umbers: basalt-sediment relationships on a Mesozoic ocean ridge. *J. Geol. Soc. London* **131**, 511–531.

Robertson A. H. F. and Varnavas S. P. (1993) The origin of hydrothermal metalliferous sediments associated with the early Mesozoic Othris and Pindos ophiolites, mainland Greece. *Sediment. Geol.* **83**, 87–113.

Rona P. A. (1984) Hydrothermal Mineralization At Seafloor Spreading Centers: Atlantic Ocean And Indian Ocean. *Earth-Science Rev.* **20**, 1–104.

Rona P. A. (1980) TAG Hydrothermal Field: Mid-Atlantic Ridge crest at latitude 26 N. *J. Geol. Soc. London.* **137**, 385–402.

Rona P. A., Bogdanov Y. A., Gurvich E. G., Rimski-Korsakov N. A., Sagalevitch A. M., Hannington M. D. and Thompson G. (1993a) Relict hydrothermal zones in the TAG Hydrothermal Field, Mid-Atlantic Ridge 26°N, 45°W. *J. Geophys. Res. Solid Earth* **98**, 9715–9730.

Rona P. A., Devey C. W., Dyment J. and Murton B. J. (2010) Diversity of hydrothermal systems on slow spreading ocean ridges. In *Geophysical Monograph Series 188* pp. 1–3.

Rona P. A., Fujioka K., Chiba H., Masuda-Nakaya H., Oomori T., Kleinrock M. C., Tivey M. A. and Lalou C. (1998) An active low-temperature mound and a large inactive sulphide mound found in the TAG Hydrothermal Field, Mid-Atlantic Ridge, 26°N, 45°W. In *AGU abstract December 1998* p. 2.

Rona P. A., Hannington M. D., Raman C. V., Thompson G., Tivey M. K., Humphris S. E., Lalou C. and Petersen S. (1993b) Active and relict sea-floor hydrothermal mineralization at the TAG hydrothermal field, mid-Atlantic ridge. *Econ. Geol.* **88**, 1989–2017.

Rona P. A., Klinkhammer G. P., Nelsen T. A., Trefry J. H. and Elderfield H. (1986) Black smokers, massive sulphides and vent biota at the Mid-Atlantic ridge. *Nature* **321**, 33–37.

Rona P. A., Petersen S., Becker K., Von Herzen R. P., Hannington M. D., Herzig P. M., Naka J., Lalou C. and Thompson G. (1996) Heat flow and mineralogy of TAG relict high-temperature hydrothermal zones: Mid-Atlantic Ridge 26°N, 45°W. *Geophys. Res. Lett.* **23**, 3507–3510.

de Ronde C. E. J., Hannington M. D., Stoffers P., Wright I. C., Ditchburn R. G., Reyes A. G., Baker E. T., Massoth G. J., Lupton J. E., Walker S. L., Greene R. R., Soong C. W. R., Ishibashi J., Lebon G. T., Bray C. J. and Resing J. A. (2005) Evolution of a submarine magmatic-hydrothermal system: Brothers volcano, southern Kermadec Arc, New Zealand. *Econ. Geol.* **100**, 1097–1133.

Rouxel O., Toner B., Germain Y. and Glazer B. (2018) Geochemical and iron isotopic insights into hydrothermal iron oxyhydroxide deposit formation at Loihi Seamount. *Geochim. Cosmochim. Acta* **220**, 449–482.

Ruhlin D. E. and Owen R. M. (1986) The rare earth element geochemistry of hydrotermal sediments from the East Pacific Rise: Examination of a seawater seavenging mechanism. *Geochim. Cosmochim. Acta* **50**, 393–400.

Rusakov V. Y., Shilov V. V., Ryzhenko B. N., Gablina I. F., Roshchina I. A., Kuz'mina T. G., Kononkova N. N. and Dobretsova I. G. (2013) Mineralogical and geochemical zoning of sediments at the Semenov cluster of hydrothermal fields, 13°31′-13°30′ N, Mid-Atlantic Ridge. *Geochemistry Int.* **51**, 646–669.

Sajih M., Bryan N. D., Livens F. R., Vaughan D. J., Descostes M., Phrommavanh V., Nos J. and Morris K. (2014) Adsorption of radium and barium on goethite and ferrihydrite: A kinetic and surface complexation modelling study. *Geochim. Cosmochim. Acta* **146**, 150–163.

Schaap A., Papadimitiou S., Mawji E., Loucaides S. and Mowlem M. (2019) *An autonomous sensor for in situ measurement of total alkalinity*. Goldschmidt Conference 2019, Barcelona, Abstract.

Schwertmann U., Friedl J. and Stanjek H. (1999) From Fe (III) Ions to Ferrihydrite and then

to Hematite. *Jounral colloid interface Sci.* **209**, 215–223.
Schwertmann U. and Murad E. (1983) Effect of pH on the Formation of Goethite and Hematite from Ferrihydrite. *Clays Clay Miner.* **31**, 277–284. Available at:
Schwertmann U., Stanjek H. and Becher H.-H. (2004) Long-term in vitro transformation of 2-line ferrihydrite to goethite/hematite at 4, 10, 15 and 25°C. *Clay Mineral.* **39**, 433–438.
Sclater J. G., Jaupart C. and Galson D. (1980) The heat flow through oceanic and continental crust and the heat loss of the Earth. *Rev. Geophys.* **18**, 269–311.
Scott M. R., Scott R. B., Morse J. W., Betzer P. R., Butler L. W. and Rona P. A. (1978) Metal-enriched sediments from the TAG Hydrothermal Field. *Nature* **276**, 811–813.
Scott R. B., Rona P. A., McGregor B. A. and Scott M. R. (1974) The TAG hydrothermal field. *Nature* **248**, 81–82.
Seeberg-Elverfeldt J., Schluter M., Feseker T. and Kolling M. (2005) Rhizon sampling of porewaters near the sediment-water interface of aquatic systems. *Limnol. Oceanogr.* **3**, 361–371.
Sempéré J.-C., Lin J., Brown H. S., Schouten H. and Purdy G. M. (1993) Segmentation and morphotectonic variations along a slow-spreading center: The Mid-Atlantic Ridge 24°00′N-- 30°40′N). *Mar. Geophys. Res.* **15**, 153–200.
Sempéré J.-C., Purdy G. M. and Schouten H. (1990) Segmentation of the Mid-Atlantic Ridge between 24° N and 30°40′ N. *Nature* **344**, 427–431.
Severmann S., Mills R. A., Palmer M. R. and Fallick A. E. (2004) The origin of clay minerals in active and relict hydrothermal deposits. *Geochim. Cosmochim. Acta* **68**, 73–88.
Severmann S., Mills R. A., Palmer M. R., Telling J. P., Cragg B. A. and John Parkes R. (2006) The role of prokaryotes in subsurface weathering of hydrothermal sediments: A combined geochemical and microbiological investigation. *Geochim. Cosmochim. Acta* **70**, 1677–1694.
Shanmugam G. (2018) Slides, Slumps, Debris Flows, Turbidity Currents, Hyperpycnal Flows, and Bottom Currents. In *Reference Module in Earth Systems and Environmental Sciences* Elsevier.
Shearme S., Cronan D. S. and Rona P. A. (1983) Geochemistry of sediments from the TAG Hydrothermal Field, M.A.R. at latitude 26° N. *Mar. Geol.* **51**, 269–291.
Skornyakova I. S. (1965) Dispersed iron and manganese in Pacific Ocean sediments. *Int. Geol. Rev.* **7**, 2161–2174.
Spiess F. N., Macdonald K. C., Atwater T., Ballard R. D., Carranza A., Cordoba D., Cox C., Diaz Garcia V. M., Francheteau J., J G., Hawkins J., Haymon R., Hessler R., Juteau T., Kastner M., Larson R., Luyendyk B., Macdougall J. D., Miller S., Normark W., Orcutt J. and Rangin C. (1980) East Pacific Rise: Hot Springs and Geophysical Experiments. *Science (80-.).* **207**, 1421–1433.
Stein A. and Stein S. (1994) Constraints on hydrothermal heat flux through the oceanic lithopshere from global heat flow.pdf. *J. Geophys. Res.* **99**, 3081–3095.
Steinmann M., Bodeï S. and Buatier M. D. (2012) Nd-Sr isotope and REY geochemistry of metalliferous sediments in a low-temperature off-axis hydrothermal environment (Costa Rica margin). *Mar. Geol.* **315–318**, 132–142.
Stobbs I. J. (2020) Origins and implications of Si-Fe cap rocks from extinct seafloor massive sulphide deposits from the TAG hydrothermal Field, 26˚N, Mid-Atlantic Ridge. *Thesis*. University of Southampton.
Stobbs I. J., Murton B. J., Boyce A., Pearce R. B. and Petersen S. (2019) Origins of Si-Fe cap rocks at extinct seafloor massive sulphide (eSMS) deposits from the TAG Hydrothermal Field (26°N), Mid-Atlantic Ridge. In *SGA Abstract* pp. 1–4.
Stuiver M. and Polach H. (1977) Discussion of 14C Data. *Radiocarbon* **19**, 355–363.
Suganuma Y., Okuno J., Heslop D., Roberts A. P., Yamazaki T. and Yokoyama Y. (2011) Post-depositional remanent magnetization lock-in for marine sediments deduced from 10Be and paleomagnetic records through the Matuyama-Brunhes boundary. *Earth Planet. Sci. Lett.* **311**, 39–52.

Suzuki Y., Inagaki F., Takai K., Nealson K. H. and Horikoshi K. (2004) Microbial diversity in inactive chimney structures from deep-sea hydrothermal systems. *Microb. Ecol.* **47**, 186–196.

Ta K., Peng X., Chen S., Xu H., Li J., Du M., Hao J. and Lin Y. (2017) Hydrothermal nontronite formation associated with microbes from low-temperature diffuse hydrothermal vents at the South Mid-Atlantic Ridge. *J. Geophys. Res. Biogeosciences* **122**, 2375–2392.

Tenzer R. and Gladkikh V. (2014) Assessment of density variations of marine sediments with ocean and sediment depths. *Sci. World J.* **2014**.

Thompson G., Humphris S. E., Schroeder B., Sulanowska M. and Rona P. a (1988) Active vents and massive sulfides at 26°N (TAG) and 23°N (Snakepit) on the mid-Atlantic ridge. *Can. Mineral.* **26**, 697–711.

Thompson G., Mottl M. J. and Rona P. A. (1985) Morphology, mineralogy and chemistry of hydrothermal deposits from the TAG area, 26 degrees N, Mid-Atlantic Ridge. *Chem. Geol.* **49**, 243–257.

Thomson J., Higgs N. C., Croudace I. W., Colley S. and Hydes D. J. (1993) Redox zonation of elements at an oxic/post-oxic boundary in deep-sea sediments. *Geochim. Cosmochim. Acta* **57**, 579–595.

Tivey M. K. (2007) Generation of Seafloor Hydrothermal Vent Fluids and Associated Mineral Deposits. *Oceanography* **20**, 50–65.

Tivey M. K. and Humphris S. E. (2000) A synthesis of geological and geochemical investigations of the TAG hydrothermal fluid: insights into fluid flow and mixing processes in a hydrothermal system. In *Ophiolites and oceanic crust: new insights from field studies and the Ocean Drilling Program* (eds. Y. Dilek, E. M. Moores, D. Elthon, and A. Nicolas). Geological Society of America Special Paper 349, Boulder, Colorado. pp. 213–235.

Tivey M. K., Humphris S. E., Thompson G., Hannington M. D. and Rona P. A. (1995) Deducing patterns of fluid flow and mixing within the TAG active hydrothermal mound using mineralogical and geochemical data. *J. Geophys. Res.* **100**, 12527.

Toner B. M., Santelli C. M., Marcus M. A., Wirth R., Chan C. S., McCollom T. M., Bach W. and Edwards K. J. (2009) Biogenic iron oxyhydroxide formation at mid-ocean ridge hydrothermal vents: Juan de Fuca Ridge. *Geochim. Cosmochim. Acta* **73**, 388–403.

Tucholke B. E., Humphris S. E. and Dick H. J. B. (2013) Cemented mounds and hydrothermal sediments on the detachment surface at Kane Megamullion: A new manifestation of hydrothermal venting. *Geochemistry, Geophys. Geosystems* **14**, 3352–3378.

Valet J. P., Meynadier L. and Guyodo Y. (2005) Geomagnetic dipole strength and reversal rate over the past two million years. *Nature* **435**, 802–805.

Velasco F., Herrero J. M., Suárez S., Yusta I., Alvaro A. and Tornos F. (2013) Supergene features and evolution of gossans capping massive sulphide deposits in the Iberian Pyrite Belt. *Ore Geol. Rev.* **53**, 181–203.

Walter P. and Stoffers P. (1985) Chemical characteristics of metalliferous sediments from eight areas on the Galapagos Rift and East Pacific Rise between 2°N and 42°S. *Mar. Geol.* **65**, 271–287.

Wang Y., Han X., Jin X., Qiu Z., Ma Z. and Yang H. (2012) Hydrothermal Activity Events at Kairei Field, Central Indian Ridge 25°S. *Resour. Geol.* **62**, 208–214.

Webber A. P., Roberts S., Murton B. J. and Hodgkinson M. R. S. (2015) Geology, sulfide geochemistry and supercritical venting at the Beebe Hydrothermal Vent Field, Cayman Trough. *Geochemistry, Geophys. Geosystems* **16**, 2661–2678.

Webber A. P., Roberts S., Murton B. J., Mills R. A. and Hodgkinson M. R. S. (2017) The formation of gold-rich seafloor sulfide deposits: Evidence from the Beebe hydrothermal vent field, Cayman Trough. *Geochemistry, Geophys. Geosystems* **18**, 2011–2027.

Weisener C. G., Smart R. S. C. and Gerson A. R. (2004) A comparison of the kinetics and mechanism of acid leaching of sphalerite containing low and high concentrations of iron. *Int. J. Miner. Process.* **74**, 239–249.

Wheat C. G. and Fisher A. T. (2008) Massive, low-temperature hydrothermal flow from a basaltic outcrop on 23 Ma seafloor of the Cocos Plate: Chemical constraints and implications. *Geochemistry, Geophys. Geosystems* **9,** 1-16.

Wheat C. G., Fisher A. T., McManus J., Hulme S. M. and Orcutt B. N. (2017) Cool seafloor hydrothermal springs reveal global geochemical fluxes. *Earth Planet. Sci. Lett.* **476**, 179–188.

White S. N., Humphris S. E. and Kleinrock M. C. (1998) New observations on the distribution of past and present hydrothermal activity in the TAG area of the Mid-Atlantic Ridge (26N08'). *Mar. Geophys. Res.* **20**, 41–56.

Xuan C., Channell J. E. T. and Hodell D. A. (2016) Quaternary magnetic and oxygen isotope stratigraphy in diatom-rich sediments of the southern Gardar Drift (IODP Site U1304 , North Atlantic) IS. *Quat. Sci. Rev.* **142**, 74–89.

Xuan C. and Oda H. (2015) UDECON: Deconvolution optimization software for restoring high-resolution records from pass-through paleomagnetic measurements. *Earth, Planets Sp.* **67**.

Yang W., Tao C., Li H., Liang J., Liao S., Long J., Ma Z. and Wang L. (2017) 230Th/238U dating of hydrothermal sulfides from Duanqiao hydrothermal field, Southwest Indian Ridge. *Mar. Geophys. Res.* **38**, 71–83.

You C. F. and Bickle M. J. (1998) Evolution of an active sea-floor massive sulphide deposit. *Nature* **394**, 668–671.

Yu Z., Li H., Li M. and Zhai S. (2018) Hydrothermal signature in the axial-sediments from the Carlsberg Ridge in the northwest Indian Ocean. *J. Mar. Syst.* **180**, 173–181.

Zierenberg R. A., Fouquet Y., Miller D. J., Bahr J. M. M., Baker P. A. A., Bjerkgård T., Brunner C. A. A., Duckworth R. C., Gable R., Gieskes J. M., Goodfellow W. D. D., Gröschel-Becker H. M. M., Guèrin G., Ishibashi J., Iturrino G. J., James R. H., Lackschewitz K., Marquez L. L. L., Nehlig P., Peter J. M., Rigsby C. a., Schultheiss P., Shanks W. C. P. I., Simoneit B. R. T. R. T., Summit M., Teagle D. A. H., Urbat M., Zuffa G. G. G. and Iturrino; G. J. (1998) The deep structure of a sea-floor hydrothermal deposit. *Lett. to Nat.* **392**, 485–488.

Zierenberg R. A. and Miller D. J. (2000) Overview of ocean drilling program leg 169: Sedimented Ridges II. In *Proceedings of the Ocean Drilling Program, Scientific Results* (eds. R. A. Zierenberg, Y. Fouquet, D. J. Miller, and N. W. R). pp. 1–39.

Zonenshain L. P., Kuzmin M. I., Lisitzin A. P., Bogdanov Y. A. and Baranov B. V. (1989) Tectonics of the Mid-Atlantic rift valley between the TAG and MARK areas (26-24N): Evidence for vertical tectonism. *Tectonophysics* **159**, 1–23.